

THE UNIVERSITY OF HULL

**Theranostic porphyrin conjugates for the
combined treatment and diagnosis of cancer**

being a thesis submitted for the Degree of
Doctor of Philosophy in the University of Hull

By

Steven Yong-Yi Yap

April 2019

Abstract

The development of theranostic agents capable of the combined treatment of diagnosis of disease has seen a growing interest within the research community. The combination of diagnostic and treatment modality onto a single construct will allow the careful monitoring of the biodistribution of drug molecules, allowing optimisation of treatment, paving a way towards personalised medicines.

Photodynamic therapy (PDT) is a promising treatment technique for cancer. It is minimally invasive and shows little or no toxicity which proves advantageous over traditional anti-cancer techniques. It involves the administration of a non-toxic drug known as photosensitiser and the irradiation with visible light to activate the photosensitisers. The activated photosensitiser will generate reactive oxygen species that can deal oxidative damage to surrounding tissues, culminating in cell death. Hence, the selective accumulation of the photosensitiser into diseased tissues is of utmost importance for photodynamic therapy.

This make photosensitisers for photodynamic therapy an ideal candidate to be combined with a diagnostic modality, allowing the monitoring of accumulation of photosensitisers, improving treatment outcomes by irradiation when photosensitiser levels are maximal. Therapeutic abilities of porphyrin as a photosensitiser are undisputed, their ease of synthesis and functionalisation made them the photosensitiser of choice to combine with a diagnostic modality. Magnetic resonance imaging (MRI), positron emission tomography (PET), and single photon emission tomography (SPECT) are of particular interest as they are routinely used in clinics and allow the imaging of the distribution of the imaging agent.

In this thesis, molecular- and nano-theranostic agents were investigated to combine PDT with MRI contrast agent, PET radioisotope, or SPECT radioisotope. A brief introduction of these treatment and diagnostic techniques along with the current advances in theranostic is given in chapter 1. The bioconjugation of cowpea mosaic virus, a biological nanoplatform, with porphyrin is described in chapter 2. Synthesis of polyacrylamide nanoparticles for the encapsulation and functionalisation of porphyrin and MRI contrast molecules is described in chapter 3. Molecular-theranostic agents is described in chapter 4 and chapter 5; chapter 4 describes a PDT/PET theranostic agent and chapter 5 describe two molecular theranostics. prostate-targeted and non-targeted PDT/SPECT theranostic agents.

Successful synthesis and evaluation of these theranostic agents led to the *in vitro* and *in vivo* analysis to evaluate their efficacy in PDT treatment and MR/PET/SPECT imaging.

Parts of this thesis have been published in the following journal articles:

“Selective radiolabelling with ^{68}Ga under mild conditions: a route towards a porphyrin PET/PDT theranostic agent.”

S. Yap, T. W. Price, H. Savoie, R. W. Boyle and G. J. Stasiuk, *Chem. Commun.*, 2018, **54**, 7952-7954, DOI:10.1039/C8CC03897J.

Acknowledgement

I would like to express my most sincere appreciation to my supervisors Prof. Ross Boyle and Dr Graeme Stasiuk. Ross has given me the opportunity to work on this research project, has shown endless patience in reviewing the work and presentations I have prepared. His feedback, constructive criticism, and advice on my project are of utmost importance and without it, this project would not have been possible. Graeme, an indispensable mentor, teaches and educates me to be a better researcher, whom I will always be in debt to.

Secondly, I would like to thank Prof. Dave Evans and Dr Sachin Shah whom have opened up a completely new field for me, introducing the world of virology which prove to be ever so exciting to work on.

Thirdly, I would like to thank our fellow collaborators within our university and from Hull and East Yorkshire Hospitals NHS Trust, Imperial College London, and University of Toronto; Dr Lawrence Kenning for phantom MRI, Dr James Wilton-Ely and Hannah Perry for the relaxivity studies, Prof. Gang Zheng, Dr Juan Chen, and Lili Ding for the *in vivo* studies, Prof. Steve Archibald and Dr Ben Burke for making ^{99m}Tc work a possibility, Ann Lowry for the TEM image.

I would like to thank Dr Thomas Price for being a friend, colleague, and ^{68}Ga trainer. His advice, expertise, and contribution led to the success and publication of one of the projects describe in this thesis. I would particularly like to thank Huguette Savoie for her biology expertise and the cell work she has carried out for me throughout my PhD, without which this thesis would just be a synthetic letter. I would also like to thank both my master students, Saul Michues and Harry Sample, whom have paved the way for one of my PhD projects. Many thanks to Dr Rob Lewis for his continuous battle with the NMR machine and the National Mass Spectrometry, Swansea for performing mass spectrometry analyses on my compounds.

Special thanks to Jordon Sandland, Aimie Rendle, Michelle Kinnon, Mitchell Clark, Charlotte Eling, Beatrix Brito, and Tom included again for being my friends and more than just a colleague in the lab, making my long enduring PhD journey bearable.

Last but not least, I would like to thank my family, my close friends, and my partner, Sherlyn Khaw, for their continuous support, love, and encouragement, while I am studying and working abroad. For without them, I would not have enjoyed such opportunity.

Abbreviation

2CPP	5, 15-bis[3,4-bis(carboxymethyleneoxy)phenyl] porphyrin
ADPA	Anthracene-9,10-dipropionic acid
AIBN	2,2'-azobis(isobutyronitrile)
AIDS	Acquired immunodeficiency syndrome
ALA	5-aminolevulinic acid
APMA	<i>N</i> -(3-aminopropyl)methacrylamide
APS	Ammonium persulfate
BOP	Benzotriazol-1-yloxytris(dimethylamino)phosphonium salt
BSA	Bovine serum albumin
CIC	<i>N</i> -cyclohexyl- <i>N'</i> -isopropylcarbodiimide
CP256	Tris(hydroxypyridinone) chelator
CPMV	Cowpea mosaic virus
CT	X-ray computed tomography
CuAAC	Copper-catalysed azide-alkyne cycloaddition
DCM	Dichloromethane
DIC	dicyclohexylcarbodiimide
DLS	Dynamic light scattering
DMAP	4-dimethylaminopyridine
DMF	<i>N,N</i> -dimethylformamide
DMSO	<i>N,N</i> -dimethyl sulfoxide
DOTA	1,4,7,10-Tetraazacyclododecane-1,4,7,10-tetraacetic acid
DOX	Doxorubicin
Dpaa	Picolinic acid-amino acid based chelators
DTPA	Diethylenetriaminepentaacetic acid
DTPA-DA	Diethylenetriaminepentaacetic acid dianhydride
DTTA	Diethylenetriaminetetraacetic acid
DU145	Human prostate carcinoma
DU145-PSMA	Human prostate carcinoma - PSMA expressing variant
EDC	<i>N</i> -ethyl- <i>N'</i> -(3-dimethylaminopropyl)carbodiimide
EMA	European Medicines Agency
EPR	Enhanced permeation and retention
ESI	Electrospray ionisation
FBS	Foetal bovine serum

FDA	Food and Drugs Administration
FDG	¹⁸ F-fluorodeoxyglucose
Gd-MP	Gadolinium mesoporphyrin
H&E	Haemotoxylin and Eosin
HBED	<i>N,N'</i> -bis(2-hydroxybenzyl)ethylenediamine- <i>N,N'</i> -diacetic acid
HHDPD	3-(1-hydroxyheptyl)-deutero-porphyrin dimethylester
HMPAO	Hexamethyl propyleneamine oxime
HOAt	1-hydroxy-7-azabenzotriazole
HOBt	1-hydroxybenzotriazole
Hp	Hematoporphyrin
HpD	Hematoporphyrin derivatives
HPLC	High performance liquid chromatography
HT-29	Human colorectal adenocarcinoma
k_{ex}	Water exchange rate
L	Large subunit
LDL	Low-density lipoproteins
Ln	Lanthanides
LUMO	Lowest unoccupied molecular orbital
mAb	monoclonal antibodies
MCOTMDHPD	[(2 <i>R</i>)-2-methoxycarbonylmethyl]-3-oxo-2,7,12,18-tetramethyl-2,3-dihydro-2 <i>H</i> ,23 <i>H</i> -dihydroporphyrinato-13,17-diyl]dipropionic acid dimethylester
MIBI	Methoxyisobutylisonitrile
MRI	Magnetic resonance imaging
NET	Neuroendocrine tumour
NHS	<i>N</i> -hydroxysuccinimide
NMR	Nuclear magnetic resonance
NMRD	Nuclear magnetic relaxation dispersion
NOTA	1,4,7-Triazacyclononane-1,4,7-triacetic acid
PAN	Polyacrylamide nanoparticle
PBS	Phosphate buffered saline
PDI	Polydispersity index
PDT	Photodynamic therapy
PEG	Polyethylene glycol
PET	Positron emission tomography
PIC	Photoimmunoconjugates

PPIX	Protoporphyrin IX
PS-3	^{99m} Tc-labelled HpD
PSMA	Prostate specific membrane antigen
PTT	Photothermal therapy
q	Hydration number
r_1	Relaxivity
RCY	Radiochemical yield
r_{GdH}	Electron spin-proton distance
S	Small subunit
SBM	Solomon-Bloembergen-Morgan
S _N	Singlet state, where N = positive integer
SPECT	Single photon emission computed tomography
T_1 relaxation time	Spin-lattice relaxation time
T_2/T_2^* relaxation time	Spin-spin relaxation time
T4CPP	5,10,15,20-tetrakis[3,4-bis(carboxymethyleneoxy)phenyl] porphyrin
TCPP	5,10,15,20-tetrakis-(p-carboxymethyleneoxyphenyl)porphyrin
TEA	Triethylamine
TEM	Transmission electron microscopy
TEMED	<i>N,N,N',N'</i> -tetramethylethylenediamine
TFA	Trifluoroacetic acid
TFPP	5,10,15,20-tetrakis(pentafluorophenyl)porphyrin
THPTA	Tris(3-hydroxypropyltriazolylmethyl)amine
TLC	Thin layer chromatography
TM	Targeting molecule
TMPP	5,10,15,20-tetrakis(4-methoxyphenyl)porphyrin
T _N	Triplet state, where N = positive integer
TPP	5,10,15,20-tetraphenylporphyrin
TUNEL	Terminal deoxynucleotidyl transferase dUTP Nick-End Labeling
VIPERdb	Virus particle explorer database
W/O	Water-in-oil
wAMD	Wet age-related macular degeneration
γ_H	Gyromagnetic ratio of proton
τ_{ci}	Correlation time, $i = 1,2$
τ_m	Lifetime of water molecule in inner sphere

τ_R

Rotational correlation time

COSHH statement

All experiments were carried out in accordance with the University of Hull's Health and Safety guidelines. A full COSHH and risk assessment was carried out for each new experiment, signed by the undertaking student, supervisor (Prof. Ross Boyle) and the departmental safety officer (Dr Tom McCreedy, Dr Rob MacDonald, and Dr Rob Lewis) before any practical work started. The COSHH forms carry the reference numbers YY01-YY52.

Table of contents

Abstract.....	ii
Acknowledgement	iv
Abbreviation	v
COSHH statement.....	ix
Table of contents.....	x
List of figures.....	xiv
List of Schemes.....	xx
List of Tables	xxiii
Chapter 1 Introduction	1
1.1 Photodynamic therapy	1
1.1.1 Photophysical and photochemical processes of photodynamic therapy	2
1.1.2 Cell death	4
1.2 Photosensitisers for photodynamic therapy	5
1.2.1 Evolution of photosensitisers: porphyrins and other tetrapyrrolic macrocycles	6
1.2.2 First generation photosensitisers.....	7
1.2.3 Second-generation photosensitisers	8
1.2.4 Third- and/or fourth-generation photosensitisers.....	11
1.3 Medical imaging	14
1.3.1 Fluorescence imaging	15
1.3.2 Magnetic resonance imaging	15
1.3.3 Positron emission tomography imaging.....	25
1.3.4 Single-photon emission computed tomography imaging.....	32
1.4 Theranostic.....	37
1.4.1 Gd-based MRI/PDT theranostic porphyrin.....	37
1.4.2 ⁶⁸ Ga-based PET/PDT theranostic porphyrin.....	41
1.4.3 ^{99m} Tc-based SPECT/PDT theranostic porphyrin.....	46
1.5 Conjugation strategies.....	49
1.5.1 Peptide coupling and reagents.....	49
1.5.2 Copper-catalysed azide-alkyne cycloaddition (CuAAC) “click” reaction.....	51

1.6 Objective of this study	51
Chapter 2 Bioconjugation of cowpea mosaic virus (CPMV).....	52
2.1 Porphyrin synthesis	53
2.1.1 Carboxylate-reactive porphyrin	53
2.1.2 Amine-reactive porphyrin	54
2.1.3 Azide-porphyrin for CuAAC	56
2.2 Bioconjugation of CPMV with cationic porphyrin.....	57
2.2.1 Conjugating carboxylic acid groups on CPMV	58
2.2.2 Conjugating amine groups on CPMV	59
2.2.3 Modification of CPMV for CuAAC	61
2.3 Summary	64
Chapter 3 Polyacrylamide nanoparticles synthesis and conjugation	66
3.1 Polyacrylamide nanoparticle.....	66
3.1.1 Free radical polymerisation.....	67
3.2 Synthesis of bifunctional acryloyl monomers and conjugatable molecules	69
3.2.1 Alkyne-bearing monomer	69
3.2.2 Azido-bearing monomer	70
3.2.3 Porphyrin synthesis for covalent incorporation	71
3.2.4 Porphyrin synthesis for covalent conjugation.....	73
3.2.5 Synthesis of conjugatable metal chelator.....	74
3.3 Synthesis of polyacrylamide nanoparticle (PAN).....	75
3.3.1 Synthesis of blank PAN.....	76
3.3.2 Synthesis of mono-functionalised PAN.....	76
3.3.3 Synthesis of dual functional PAN <i>via</i> covalent-encapsulation of porphyrin	79
3.3.4 Synthesis of dual-functional PAN for orthogonal conjugation.....	87
3.4 <i>In vitro</i> cytotoxicity evaluation.....	92
3.5 Relaxivity studies and phantom MRI.....	93
3.6 Hydration state evaluation	95
3.7 <i>In vivo</i> evaluation – PDT and MRI	99
3.8 Summary	104

Chapter 4 Radiolabelling of porphyrin conjugates with ^{68}Ga , a route towards a PDT/PET theranostic agent	105
4.1 Synthesis and evaluation of porphyrin- H_3Dpaa conjugate	106
4.2 ^{68}Ga radiolabelling	108
4.3 <i>In vitro</i> phototoxicity evaluation.....	111
4.4 Summary	112
Chapter 5 Porphyrins and amino acids “clicked” conjugates for $^{99\text{m}}\text{Tc}$ radiolabelling as PDT/SPECT theranostic agent.....	114
5.1 Synthesis of bifunctional and trifunctional porphyrin-amino acid conjugates	115
5.1.1 Synthesis and characterisation of porphyrin-Gly conjugate and porphyrin- $[\text{natRe}(\text{Gly})]$ complex.....	115
5.1.2 Synthesis and characterisation of porphyrin-Lys-TM conjugate and porphyrin- $[\text{natRe}(\text{Lys})]$ -TM complex.....	117
5.2 $^{99\text{m}}\text{Tc}$ radiolabelling.....	121
5.3 <i>In vitro</i> phototoxicity evaluation.....	126
5.4 Summary	129
Chapter 6 Conclusion and Future Outlook	130
Chapter 7 Experimental Section	131
7.1 Materials and methods	131
7.2 HPLC conditions.....	131
7.3 ^{68}Ga radiochemistry	132
7.4 $^{99\text{m}}\text{Tc}$ radiochemistry	132
7.4.1 Synthesis of $[\text{natRe}(\text{CO})_3(\text{H}_2\text{O})_3]^+$	132
7.4.2 $^{99\text{m}}\text{Tc}$ radiolabelling	132
7.5 <i>In vitro</i> cytotoxicity evaluation (MTT assay)	133
7.5.1 General procedure for phototoxicity and toxicity assay	133
7.5.2 Phototoxicity and toxicity evaluation of PAN described in Chapter 3	133
7.5.3 Phototoxicity and toxicity evaluation of porphyrin conjugate described in Chapter 4	133
7.5.4 Phototoxicity and toxicity evaluation of porphyrin conjugate described in Chapter 5	134

7.6 CPMV purification and characterisation.....	134
7.6.1 Ultrafiltration	134
7.6.2 Dialysis	134
7.6.3 Agarose gel electrophoresis	134
7.6.4 UV-vis analysis of CPMV	135
7.6.5 TEM sample preparation and imaging.....	135
7.7 PAN characterisation and evaluation.....	135
7.7.1 Dynamic light scattering and zeta potential measurements	135
7.7.2 TEM sample preparation and imaging.....	135
7.7.3 Phantom MRI.....	136
7.7.4 T1 measurements and Evans magnetic susceptibility measurement.....	136
7.7.5 Luminescence measurements and hydration states calculation	136
7.8 Synthesis and bioconjugation described in chapter 2	137
7.9 Synthesis and PAN functionalisation described in chapter 3.....	149
7.10 Synthesis described in Chapter 4	168
7.11 Synthesis described in Chapter 5	173
Chapter 8 Reference.....	183

List of figures

Figure 1.1 Schematic for the clinical procedure for PDT.	2
Figure 1.2 A simplified Jablonski diagram, showing the photochemical mechanism of a typical photosensitiser.	2
Figure 1.3 Schematic for cell death via necrosis and apoptosis. Image adapted and redrawn from <i>Alcohol Res. Health</i> , 2001, 25 , 175–184. ¹⁰	5
Figure 1.4 Examples of non-macrocyclic photosensitisers.	6
Figure 1.5 Structure of porphyrin and some other tetrapyrrolic molecules.	6
Figure 1.6 Structure of metal-free protohaem (left), hematoporphyrin (middle), protohaem (right).	7
Figure 1.7 Photofrin® the first clinically approved photodynamic drug.	7
Figure 1.8 Structure of Visudyne® (top left), Purytin® (top right), Foscan® (bottom left), and Tookad® (bottom right).	8
Figure 1.9 Structure of Levulan®, Metvix®, and Benvix®.	9
Figure 1.10 Schematic representation of haem synthesis pathway and the usage of exogenous ALA which leads to synthesis and accumulation of PPIX. Scheme was modified from <i>Chem. Rev.</i> , 2010, 110 , 2795–2838. ³	10
Figure 1.11 Structures of water soluble porphyrin, top left: tetra(<i>N</i> -methyl-4-pyridinium)porphyrin, top right: tetra(4-sulfonatophenyl)porphyrin sodium, bottom left: meso-tetrakis(4-PEG ₁₀₀₀ thioxytetra-2,3,5,6-fluorophenyl)- porphyrinato]zinc(II), bottom right: tetra(3,5-dihydroxyphenyl)porphyrin.	11
Figure 1.12 Schematic of the difference between normal vasculature and tumour vasculature.	12
Figure 1.13 Electromagnetic spectrum. ⁶¹	15
Figure 1.14 A rotating nucleus with a positive charge produce a magnetic field known as magnetic moment. This can be described to be analogous to a bar of magnet.	16
Figure 1.15 Schematic of Zeeman interaction. In the absence of magnetic field (left), B_0 , the collection of spin will have no preferential alignment. In the presence of magnetic field (right), the parallel orientation is lower energy, and contains more nuclei compared to the higher energy antiparallel orientation. The difference in energy between the two levels is ΔE .	17
Figure 1.16 Protons with a net magnetisation, M_0 , upon excitation with a 90° pulse, de-align the vector M_0 by 90° into the transverse plane.	18
Figure 1.17 T_2 relaxation also known as spin-spin relaxation.	19
Figure 1.18 In the presence of a magnetic field, a proton precesses around the magnetic field. The rate of precession is known as the Larmor frequency, ω_0 .	19
Figure 1.19 Schematic to show the lost in uniformity of after 90° excitation pulse, which is also known as T_2 or T_2^* relaxation.	20
Figure 1.20 FDA and/or EMA approved gadolinium-based contrast agents.	22

Figure 1.21 Gd-based contrast agent with a bound water molecule surrounded by bulk water. τR stands for rotational correlation time of the contrast agent and k_{ex} is the water exchange rate and τM is the lifetime of water molecule in the inner sphere	24
Figure 1.22 Schematic of the radioactive decay of a positron emitting isotope follow by the annihilation of positron and electron to produce gamma rays	26
Figure 1.23 Production of ^{68}Ge from ^{69}Ga shown in dashed arrow. The decay of ^{68}Ge to ^{68}Ga and to ^{68}Zn is shown in solid arrows. ^{85,86}	27
Figure 1.24 Structure of ^{68}Ga -DOTATATE, which was approved by FDA in July 2016. ⁹¹	28
Figure 1.25 PET maximum-intensity-projection images of 60 years old patient with typical endobronchial carcinoid. (a) PET imaging with ^{18}F -FDG, (b) PET imaging with ^{68}Ga -DOTATATE, in which ^{68}Ga -DOTATATE showed higher accumulation in tumour. Image taken from <i>J. Nucl. Med.</i> , 2009, 50 , 1927–1932. ⁹²	28
Figure 1.26 Some macrocyclic chelators for ^{68}Ga .	29
Figure 1.27 Structures of HBED, HBED-CC, and HBED-CC-PSMA.	30
Figure 1.28 Structure of H ₂ dedpa and derivatives.	30
Figure 1.29 Structure of AAZTA and derivatives reported by Waldron <i>et al.</i> ^{104,105}	31
Figure 1.30 Structure of CP256 and its derivatives. ^{107,108}	32
Figure 1.31 Structure of H ₃ Dpaa and its derivatives, H ₃ Dpaa.dab and H ₄ Dpaa.ga. ¹⁰⁹	32
Figure 1.32 Radioactive decay scheme of ^{99}Mo to generate $^{99\text{m}}\text{Tc}$ and the subsequent decay to $^{99\text{m}}\text{Tc}$ and ^{99}Ru .	33
Figure 1.33 FDA-approved brain perfusion agent, $^{99\text{m}}\text{Tc}$ -HMPAO and $^{99\text{m}}\text{Tc}$ -bicisate.	34
Figure 1.34 SPECT image of a patient with stroke in the top left area of the brain. Image obtained from <i>Chem. Soc. Rev.</i> , 1998, 27 , 43. ¹¹²	35
Figure 1.35 FDA-approved myocardial agent, $^{99\text{m}}\text{Tc}$ -sestamibi and $^{99\text{m}}\text{Tc}$ -tetrofosmin.	35
Figure 1.36 FDA-approved phosphonate ligands for $^{99\text{m}}\text{Tc}$ complexation for bone imaging.	36
Figure 1.37 Structure of FDA-approved $^{99\text{m}}\text{Tc}$ -tilmanocept.	37
Figure 1.38 Structure of patented gadolinium mesoporphyrin (Gd-MP).	38
Figure 1.39 Sedstructure of Gd ₂ (DTPA) ₄ TPP and Gd(DTPA)TPyP.	39
Figure 1.40 Tetrasubstituted DTTA porphyrin reported by Luo <i>et al.</i> (a) and Sour <i>et al.</i> (b). ^{137,138}	39
Figure 1.41 Porphyrin-DOTA conjugate reported by Schmitt <i>et al.</i> ^{141,142}	40
Figure 1.42 Platinated Gd ³⁺ metalloporphyrin reported by Wu <i>et al.</i> ¹⁴⁵	41
Figure 1.43 Structure of [^{68}Ga (TFPP)], reported by Fazaeli <i>et al.</i> ¹⁴⁷	42
Figure 1.44 Structure of [^{68}Ga (Hp)], [^{68}Ga (PPIX)], [^{68}Ga (TPP)], [^{68}Ga (HHDPP)], and [^{68}Ga (MCOTMDHPD)], reported by Zoller <i>et al.</i> ^{148,149}	43
Figure 1.45 Structure of targeted [Ga(PPIX-RGD)], reported by Behnam Azad <i>et al.</i> ¹⁵⁰	44
Figure 1.46 Structure of targeted dodecapeptide [Ga(TPyP-TWYKIAFQRNRK)], reported by Bryden <i>et al.</i> ¹⁵²	44

Figure 1.47 Structure of GaporRu reported by Pan <i>et al.</i> . ¹⁵⁴	45
Figure 1.48 Structure of [⁶⁸ Ga(TCPP-DOTA)] (top) and [⁶⁸ Ga(TCPP-NOTA)] (bottom), reported by ¹⁵⁵	46
Figure 1.49 Structure of TMPP (left) and phytochlorin (right) used for ^{99m} Tc radiolabelling as reported by Motaleb <i>et al.</i> . ^{158,159}	47
Figure 1.50 Structure of [^{99m} Tc(T4CPP)] and [^{99m} Tc(2CPP)], reported by Subbarayan <i>et al.</i> and Santos <i>et al.</i> , respectively. ^{161,162}	48
Figure 1.51 Structure of hematoporphyrin-histidine conjugate, reported by Lie <i>et al.</i> . ¹⁶⁴	48
Figure 1.52 Structure of [^{99m} Tc(Porphyrin-BiPy)] and [^{99m} Tc(Porphyrin-DETA)], reported by Spagnul <i>et al.</i> . ^{165,166}	49
Figure 1.53 Peptide bond formation.	50
Figure 1.54 Scheme showing the formation of <i>O</i> -acylisourea and acid chloride from carboxylic acid, subsequent formation of activated ester using NHS, and formation of peptide bond.	50
Figure 1.55 Comparison between Huisgen reaction and CuAAC.	51
Figure 2.1 Space filling crystal structure of CPMV obtained from VIPERdb. ¹⁷⁴	52
Figure 2.2 UV-vis spectra of porphyrin 10 and porphyrin 11 .	57
Figure 2.3 Native agarose gel electrophoresis of CPMV1 and CPMV2 . 1,3 = wtCPMV, 2 = modified CPMV1 , 4 = modified CPMV2 .	58
Figure 2.4 UV-vis spectra of wtCPMV, porphyrin 7 , and CPMV . UV-vis spectrum of CPMV3 shows clear indication of the presence of porphyrin after purification <i>via</i> dialysis.	60
Figure 2.5 Native agarose gel electrophoresis of modified CPMV3 under Coomassie blue stain. 1 = wtCPMV, 2 = unpurified CPMV3 , 3 = 4 hr dialysis of CPMV3 , 4 = 8 hr dialysis of CPMV3 .	60
Figure 2.6 2% (w/v) uranyl acetate stained TEM images obtained for modified CPMV3 .	61
Figure 2.7 Native agarose gel electrophoresis of modified CPMV4 under ethidium bromide stain. 1= wtCPMV, 2,3,4,5 = CPMV4 with 10,000, 20,000, 50,000, and 100,000 molar excess of propionic acid, respectively.	62
Figure 2.8 UV-vis absorption spectrum of purified modified CPMV5 and wtCPMV. The absence of absorption at 494 nm indicates the absence or a negligible amount of conjugatable amine.	63
Figure 2.9 UV-vis spectra of wtCPMV, porphyrin 11 , and CPMV6 after 6 hours dialysis. UV-vis spectrum of CPMV6 shows clear indication of the presence of porphyrin after purification <i>via</i> dialysis.	64
Figure 2.10 Native agarose gel electrophoresis with ethidium bromide stain for viral nanoparticles of 1 = wtCPMV, 2 = CPMV4 , 3 = CPMV6 . Lane 3 shows high absorption in loading well, indicating aggregation of viral particles.	64
Figure 3.1 Structural formula of acrylamide and <i>N,N'</i> -methylenebisacrylamide. Carbon-carbon double bond in bold to highlight the site of attack for free radicals.	66
Figure 3.2 Acrylamide monomers bearing reactive functionality.	67

Figure 3.3 Schematic of a reverse micelle (water-in-oil micelle).	67
Figure 3.4 Magnevist® and technetium-99m pentetate.	74
Figure 3.5 PAN_{blank} prepared by polymerisation of acrylamide, and <i>N,N'</i> -methylenebisacrylamide.	76
Figure 3.6 DLS size distribution by intensity of PAN_{blank} .	76
Figure 3.7 PAN-(amine) prepared by co-polymerisation of APMA, acrylamide, and <i>N,N'</i> -methylenebisacrylamide.	76
Figure 3.8 PAN-(porphyrin) prepared by co-polymerisation of porphyrin 23 , acrylamide, and <i>N,N'</i> -methylenebisacrylamide.	77
Figure 3.9 z_{ave} and zeta potential of PAN_{blank} , PAN-(porphyrin_{0.05}) , and PAN-(porphyrin_{0.5}) .	78
Figure 3.10 DLS size distribution by intensity of PAN-(porphyrin_{0.05}) (left) and PAN-(porphyrin_{0.5}) (right).	78
Figure 3.11 PAN-(porphyrin-amine) prepared by co-polymerisation of porphyrin 23 , APMA, acrylamide, and <i>N,N'</i> -methylenebisacrylamide.	79
Figure 3.12 DLS Size distribution by intensity of PAN-(porphyrin _{0.02} -amine _{0.5}), PAN-(porphyrin _{0.05} -amine _{0.5}), and PAN-(porphyrin _{0.5} -amine _{0.5}).	80
Figure 3.13 z_{ave} and zeta potential of PAN-(porphyrin _{0.02} -amine _{0.5}), PAN-(porphyrin _{0.05} -amine _{0.5}), and PAN-(porphyrin _{0.5} -amine _{0.5}).	80
Figure 3.14 DLS Size distribution by intensity of PAN-(porphyrin_{0.05}-amine_{1.0}) and PAN-(porphyrin_{0.05}-amine_{2.0}) .	81
Figure 3.15 z_{ave} and zeta potential of PAN-(porphyrin _{0.05} -amine _{0.5}), PAN-(porphyrin _{0.05} -amine _{1.0}) and PAN-(porphyrin _{0.05} -amine _{2.0}).	81
Figure 3.16 z_{ave} and zeta potential of PAN-(porphyrin _{0.05} -amine _{0.5}) and DTPA _{0.5} -PAN-(porphyrin _{0.05}) (left), and PAN-(porphyrin _{0.5} -amine _{0.5}), DTPA _{0.5} -PAN-(porphyrin _{0.5})-triethylamine, and DTPA _{0.5} -PAN-(porphyrin _{0.5})-NaHCO ₃ (right).	83
Figure 3.17 DLS Size distribution by intensity of PAN-(porphyrin _{0.5} -amine _{0.5}), (DTPA _{0.5})-PAN-(porphyrin _{0.5})-triethylamine, and (DTPA _{0.5})-PAN-(porphyrin _{0.5})-NaHCO ₃ .	83
Figure 3.18 DLS Size distribution by intensity of PAN synthesised with primary monomer ratio of 100:1 acrylamide: <i>N,N'</i> -methylenebisacrylamide (left) and (right).	84
Figure 3.19 Difference between size distribution by number (left), volume (middle), and intensity (right). Figure was redrawn with reference from <i>Zetasizer Nano Series User manual</i> , Malvern Instrument, Series 1.1., 2013. ²⁵⁴	85
Figure 3.20 DLS size distribution by number of PAN-(porphyrin _{0.05}), PAN-(porphyrin _{0.5}), PAN-(porphyrin _{0.5} -amine _{0.5}), (DTPA _{0.5})-PAN-(porphyrin _{0.5})-triethylamine, and (DTPA _{0.5})-PAN-(porphyrin _{0.5})-NaHCO ₃ .	86
Figure 3.21 DLS size distribution by intensity of PAN-(amine_{1.0}-alkyne_{1.0}) .	87

Figure 3.22 z_{ave} and zeta potential of PAN-(amine _{1.0} -alkyne _{1.0}), (porphyrin _{1.0})-PAN-(amine _{1.0}), (porphyrin _{1.0} -DTPA _{1.0})-PAN, and (Porphyrin _{1.0} -[Gd(DTPA)] _{1.0})-PAN.	90
Figure 3.23 TEM images of nanoparticles negatively stained using 1% aqueous uranyl acetate. (a) PAN-(amine _{1.0} -alkyne _{1.0}), (b) (porphyrin _{1.0})-PAN-(amine _{1.0}), (c) (porphyrin _{1.0} -DTPA _{1.0})-PAN, (d) (Porphyrin _{1.0} -[Gd(DTPA)] _{1.0})-PAN.	91
Figure 3.24 UV-vis absorbance spectrum of the porphyrin 28 and PAN after porphyrin conjugation.	91
Figure 3.25 % cell survival after incubation with (porphyrin_{1.0}-[Gd(DTPA)]_{1.0})-PAN with and without light irradiation with varying porphyrin concentrations.	93
Figure 3.26 NMRD profile of (porphyrin_{1.0}-[Gd(DTPA)]_{1.0})-PAN and Magnevist® in varying magnetic field.	94
Figure 3.27 Phantom MRI obtained on 3 T MRI scanner of (porphyrin_{1.0}-[Gd(DTPA)]_{1.0})-PAN and Magnevist® at different concentrations, with water as a control.	94
Figure 3.28 Luminescence emission spectrum of ([Eu(DTPA)]_{1.0})-PAN-(alkyne_{1.0}) . ($\lambda_{ex} = 395$ nm).	96
Figure 3.29 Excited state lifetime measurement of ([Eu(DTPA)]_{1.0})-PAN-(alkyne_{1.0}) , $\lambda_{ex} = 395$ nm, $\lambda_{em} = 615$ nm. Red: H ₂ O, black: D ₂ O.	96
Figure 3.30 Luminescence emission spectrum of ([Tb(DTPA)]_{1.0})-PAN-(alkyne_{1.0}) . ($\lambda_{ex} = 380$ nm).	97
Figure 3.31 Excited state lifetime measurement of ([Tb(DTPA)]_{1.0})-PAN-(alkyne_{1.0}) , $\lambda_{ex} = 380$ nm, $\lambda_{em} = 545$ nm. Red: H ₂ O, black: D ₂ O.	97
Figure 3.32 Ternary anion adducts formed at Ln ³⁺ centres.	98
Figure 3.33 Luminescence emission spectrum (left, $\lambda_{ex} = 395$ nm) and excited state lifetime measurement (right, Red: H ₂ O, black: D ₂ O, $\lambda_{ex} = 395$ nm, $\lambda_{em} = 615$ nm) of ([Eu(DTPA)]_{1.0})-PAN-(alkyne_{1.0}) prepared without the use of acetate buffer, showed similar spectra compared to Figure 3.28 and Figure 3.29.	99
Figure 3.34 FDA approved DTPA derivative, Omniscan™ and Optimark®.	99
Figure 3.35 MRI images of mice pre-administered and 24-hour post administration with (porphyrin_{1.0}-[Gd(DTPA)]_{1.0})-PAN .	100
Figure 3.36 Fluorescence Maestro imaging of mice, 24-hour post administration with (porphyrin_{1.0}-[Gd(DTPA)]_{1.0})-PAN (top) and PBS (bottom).	101
Figure 3.37 H&E evaluation of organ toxicity from each cohort. Organs include heart, liver, spleen, lung, and kidney. Histological slices do not show adverse effects on these tissues 24-hour post-PDT.	102
Figure 3.38 H&E and TUNEL staining on tumour cells, showed clear PDT effect on mice 1, 3, and 5 when compared to PBS control mice 2 and 4.	102
Figure 3.39 TUNEL quantification of tumour cells shown in Figure 3.38, shows clear PDT effect in mice 1, 3, and 5 when compared to PBS control mice 2 and 4.	103

- Figure 3.40 ICP-MS biodistribution analysis of mice 1, 3, and 5, shows major deposition of Gd in liver and spleen, and significant Gd uptake in tumour cells. 103
- Figure 4.1 UV-vis HPLC chromatograms of porphyrin **32**, conjugate **33**, and complex [^{nat}Ga]-**34**. 108
- Figure 4.2 Radio-HPLC chromatograms of radiolabelling mixtures of [⁶⁸Ga(Dpaa.ga)] (left) and porphyrin **32** (right). Red line indicates radiolabelling at pH 7.4 and blank line indicates radiolabelling at pH 4.5. Reaction conditions: [H₄Dpaa.ga] = 100 μM, T = 25 °C, t = 15 mins. [**32**] = 100 μM, T = 99 °C, t = 45 mins. 109
- Figure 4.3 Radio-HPLC chromatograms of radiolabelling mixture [⁶⁸Ga]-**34** and UV-vis HPLC chromatograms of [^{nat}Ga]-**34**. (top) pH 4.5, 0.1 M acetate buffer, (bottom) pH 7.4, 0.1 M phosphate buffer. Red dashed line indicates radio-HPLC of [⁶⁸Ga]-**34**. Black solid line indicates UV-HPLC of [^{nat}Ga]-**34**. Reaction conditions: [**33**] = 100 μM, T = 25 °C, t = 15 mins. 110
- Figure 4.4 Radio-TLC of radiolabelling mixture [⁶⁸Ga]-**34** at pH 4.5 (A) and pH 7.4 (B), [⁶⁸Ga(Dpaa.ga)] at pH 4.5 (C) and pH 7.4 (D), and porphyrin **32** at pH 4.5 (E) and pH 7.4 (F). Dotted lines indicate baseline (left, R_f = 0) and solvent front (right, R_f = 1). Radio-TLC were carried out on aluminium-backed silica TLC plates with 0.1 M aqueous 1:1 trisodium citrate: citric acid as the mobile phase. Reaction conditions: (A-D) [L] = 100 μM, t = 15 mins, T = 25 °C. (E,F) [L] = 100 μM, t = 45 min, T = 99 °C. 111
- Figure 4.5 UV-vis absorbance spectrum of **33** and [^{nat}Ga]-**34**. 112
- Figure 4.6 % cell survival of HT-29, irradiated cell and non-irradiated cells (control), determined using MTT assay. Cells were incubated with varying concentration of conjugate **33** (left) and [^{nat}Ga]-**34** (right) for 1 hour and irradiated cells received 20 J cm⁻¹ white light. 112
- Figure 5.1 UV-vis HPLC chromatograms of porphyrin **11**, conjugate **35**, and complex **36**. 116
- Figure 5.2 UV-vis HPLC chromatograms of conjugate **45**, conjugate **46**, and complex [^{nat}Re]-**47**. 120
- Figure 5.3 Radio-HPLC chromatogram of [^{99m}TcO₄]⁻ and [^{99m}Tc(CO)₃]⁺. 121
- Figure 5.4 Radio-TLC chromatograms of reduction of [^{99m}TcO₄]⁻ to [^{99m}Tc(CO)₃]⁺. Dotted lines indicate baseline (10 cm, R_f = 0) and solvent front (90 cm, R_f = 1). Radio-TLC were carried out on aluminium-backed silica TLC plates with 1% HCl in methanol as the mobile phase. 122
- Figure 5.5 Overlays of radio-HPLC of [^{99m}Tc]-**36** and [^{99m}Tc]-**47** and UV-vis HPLC chromatograms [^{nat}Re]-**36** and [^{nat}Re]-**47**. Reaction conditions: [L] = 150 μM, t = 30 mins, T = 99 °C, pH 7.4. 123
- Figure 5.6 RCY for the [^{99m}Tc(CO)₃]⁺ radiolabelling of conjugate **35** and conjugate **46** with varying concentration. Reaction conditions: t = 30 mins, T = 99 °C, pH 11. 124
- Figure 5.7 RCY for the [^{99m}Tc(CO)₃]⁺ radiolabelling of conjugate **35** and conjugate **46** with varying concentration. Reaction conditions: t = 30 mins, T = 99 °C, pH 7.4. 124
- Figure 5.8 Radio-TLC of radiolabelling mixture of [^{99m}Tc(CO)₃]⁺ (A), [^{99m}Tc]-**36** (B), and [^{99m}Tc]-**47** (C). Dotted lines indicate baseline (left, R_f = 0) and solvent front (right, R_f = 1). Radio-

TLC were carried out on aluminium-backed silica TLC plates with 0.1 M 1:1 citric acid:trisodium citrate as the mobile phase. Reaction conditions: (A) $t = 30$ mins, $T = 99$ °C. (B,C) $[L] = 150$ μ M, $t = 30$ mins, $T = 99$ °C, pH 7.4. 125

Figure 5.9 Serum stability of radiolabelled conjugates, [^{99m}Tc]-**36** and [^{99m}Tc]-**47**. 126

Figure 5.10 Percentage cell survival of HT-29, irradiated cell and non-irradiated cells (control), determined using MTT assay. Cells were incubated with varying concentration of conjugate **35** (left) and [^{nat}Re]-**36** (right) for 1 hour and irradiated cells received 20 J cm^{-1} white light. 127

Figure 5.11 Percentage cell survival of DU145 (circle) and DU145-PSMA (triangle) cells, irradiated (red) and non-irradiated (black) cells. Cells were incubated with varying concentration of conjugate **46** (top) and [^{nat}Re]-**47** (bottom) for 30 mins and irradiated cells received 20 J cm^{-1} white light. 128

List of Schemes

Scheme 2.1 Synthesis of 5-[4-aminophenyl]-10,15,20-tri-(N-methyl-4-pyridinium)porphyrin **3**. Reagents and conditions: (i) propionic acid, 170 °C, 1 hour, (ii) DMF, methyl iodide, 40 °C, overnight, (iii) 6 M HCl, 90 °C, 3 hours. 53

Scheme 2.2 Reaction scheme for synthesis of 5-[4-(Succinimide-N-oxycarbonyl)phenyl]-10,15,20-tri(N-methyl-4-pyridinium)porphyrin **7**. Reagents and conditions: (i) propionic acid, 170 °C, 1 hour, (ii) EtOH, H₂O, potassium hydroxide, room temperature, overnight, (iii) dry pyridine, thionyl chloride, *N*-hydroxysuccinimide, 50 °C, 3 hours, (iv) DMF, methyl iodide, 40 °C, overnight. 55

Scheme 2.3 Reaction scheme for the synthesis of 5-[4-azidophenyl]-10,15,20-tri-(N-methyl-4-pyridinium)porphyrin **11**. Reagents and conditions: (i) 6 M HCl, 90 °C, 2 hours, (ii) Trifluoroacetic acid (TFA), water, sodium nitrite, sodium azide, 0 °C, 1 hour, (iii) DMF, methyl iodide, 40 °C, overnight, (iv) water, zinc acetate, room temperature, 1 hour. 56

Scheme 2.4 Bioconjugation of carboxylate-reactive porphyrin **3** with wtCPMV. Reagents and conditions: (i) 0.1 M pH 7 sodium phosphate buffer, 20% DMSO, EDC, NHS, room temperature, 2 hours, (ii) porphyrin **3**, room temperature, overnight. 58

Scheme 2.5 Bioconjugation of amine-reactive porphyrin **7** with wtCPMV. Reagents and condition: (i) 0.1 M pH 7 sodium phosphate buffer, 20% DMSO, porphyrin **7**, room temperature overnight. 59

Scheme 2.6 Reaction scheme for the bioconjugation of propiolic NHS-ester onto lysine residues on wtCPMV. Reagents and conditions: (i) 0.1 M pH 7 sodium phosphate buffer, 20% DMSO, propiolic acid, EDC, NHS, room temperature, overnight. 61

Scheme 2.7 Reaction scheme for bioconjugation of Alexafluor-488 NHS onto **CPMV4** to determine the presence of excess amine. Reagents and conditions: (i) 0.1 M pH 7 sodium phosphate buffer, 20% DMSO, Alexafluor-488 NHS, 4 °C, overnight. 62

Scheme 2.8 Reaction scheme for bioconjugation of azide-porphyrin 11 onto alkyne modified CPMV 15 via CuAAC click reaction. Reagents and conditions: (i) 0.1 M pH 7 sodium phosphate buffer, 20% DMSO, porphyrin 11 , CuSO ₄ , sodium ascorbate, THPTA, 4 °C, overnight.	63
Scheme 3.1 Dissociation of persulfate with TEMED as an accelerator to generate free radicals.	68
Scheme 3.2 Initiation and propagation reaction scheme for free radical polymerisation.	68
Scheme 3.3 Termination phase of free radical polymerisation, (Top) dimerization and (bottom) disproportionation.	68
Scheme 3.4 Synthesis of <i>N</i> -(2-(2-(prop-2-yn-1-yloxy)ethoxy)ethyl)acrylamide from commercially available 2-(2-aminoethoxy)ethanol. Reagents and conditions; (i) DCM, di- <i>tert</i> -butyl dicarbonate, 40 °C, overnight. (ii) DMF, NaH, 30 mins, propargyl bromide, room temperature, overnight. (iii) 4 N HCl in dioxane, room temperature, 1 hour. (iv) dry DCM, Ar atmosphere, TEA, acryloyl chloride, 0 °C-room temperature, 4 hours.	69
Scheme 3.5 Synthesis of <i>N</i> -(2-(2-azidoethoxy)ethyl)methacrylamide from <i>tert</i> -butyl (2-(2-hydroxyethoxy)ethyl)carbamate, described earlier in chapter 3.2.1. Reagents and materials: (i) dry DCM, <i>p</i> -toluenesulfonyl chloride, DIPEA, DMAP, inert atmosphere, 0 °C-room temperature, overnight. (ii) dry DMF, NaN ₃ , 90 °C, 48 hours. (iii) 4 N HCl in dioxane, room temperature, 1 hour. (iv) DMF, methacrylic anhydride, DIPEA, inert atmosphere, overnight.	70
Scheme 3.6 Synthesis of water-soluble acryloyl-porphyrin. Reagents and conditions: (i) DMF, EDC, HOBt, DMAP, 21 , 40 °C, overnight. (ii) DMF, MeI, 40 °C, overnight.	71
Scheme 3.7 Synthesis of acryloyl-functionalised linker 21 . Reagents and conditions: (i) dry DCM, di- <i>tert</i> -butyl decarbonate, inert atmosphere, 0 °C-room temperature, overnight. (ii) dry DCM, acryloyl chloride, 0 °C-room temperature, overnight. (iii) 4 N HCl in dioxane, room temperature, 1 hour.	72
Scheme 3.8 Synthesis of zinc complexed water-soluble azido porphyrin. Reagent and conditions: Reagents and conditions: (i) DMF, EDC, HOBt, DMAP, 25 , 40 °C, overnight. (ii) DMF, MeI, 40 °C, overnight. (iii) water, zinc acetate, 40 °C, overnight.	73
Scheme 3.9 Synthesis of azido-functionalised linker. Reagents and conditions: (i) MeOH, CuSO ₄ .5H ₂ O, K ₂ CO ₃ , Imidazole-1-sulfonyl azide hydrochloride, room temperature, overnight. (ii) 4 N HCl in dioxane, room temperature, 1 hour.	74
Scheme 3.10 Synthesis of DTPA-DA. Reagents and conditions: (i) acetic anhydride, pyridine, 65 °C, overnight.	75
Scheme 3.11 Reaction scheme for the synthesis of DTPA-PAN-(porphyrin) from PAN-(porphyrin-amine) . Reagents and conditions: (i) DTPA-DA 29 , triethylamine, room temperature, overnight. (ii) DTPA-DA 29 , saturated NaHCO ₃ , room temperature, overnight.	82
Scheme 3.12 Scheme for the synthesis of PAN-(amine_{1.0}-alkyne_{1.0}) <i>via</i> inverse microemulsion polymerisation of acrylamide, <i>N,N'</i> -methylenebisacrylamide, APMA, and 15 .	87

- Scheme 3.13 Reaction scheme for the orthogonal conjugation of PAN for the synthesis of **(porphyrin_{1.0}-[Gd(DTPA)]_{1.0})-PAN**. Reagents and conditions: (i) porphyrin **28**, CuSO₄, sodium ascorbate, microwave (50 °C, 4 hours, 75 W). (ii) DTPA-DA **29**, aq. NaHCO₃, room temperature, overnight. (iii) GdNO₃.6H₂O, pH 4.5 acetate buffer, room temperature, overnight. 88
- Scheme 3.14 Synthesis of **([Ln(DTPA)]_{1.0})-PAN-(alkyne_{1.0})**. Reagents and conditions: (i) DTPA-DA **29**, aq. NaHCO₃, room temperature, overnight. (ii) EuCl₃.6H₂O/ TbCl₃.6H₂O, pH 4.5 acetate buffer, room temperature, overnight. 95
- Scheme 4.1 Reaction scheme for the synthesis of amine-appended porphyrin **32**. Reagents and conditions: (i) DMF, EDC, HOBt, DMAP, room temperature, overnight, (ii) DMF, MeI, 40 °C, overnight, (iii) DCM, TFA, room temperature, 3 hours. 106
- Scheme 4.2 NHS esterification of H₄Dpaa.ga. (i) MeCN, Ac₂O, pyridine, r.t. 30 mins. (ii) DMF, NHS, TEA, r.t. 2 hrs. 107
- Scheme 4.3 Peptide coupling and subsequent Ga complexation of porphyrin-H₃Dpaa conjugate **33**. (i) DMF, TEA, room temperature, overnight. (ii) 0.1 M pH 4.5 acetate buffer, GaCl₃, room temperature, overnight. 107
- Scheme 5.1 Synthesis of porphyrin-Gly conjugate **35** and porphyrin-[^{nat}Re(Gly)] complex [^{nat}Re]-**36**. Reagents and conditions: (i) 1:1 *t*-butanol:water, CuSO₄, sodium ascorbate, TBTA, microwave (20 mins, 75 W, 50 °C). (ii) phosphate buffer (pH 7), [Re(CO)₃Br₃][NEt₄]₂ **37**, 65 °C, 2 hours. 115
- Scheme 5.2 Synthesis of “clickable” and conjugatable alkyne-functionalised lysine. Reagents and conditions: (i) DMF, K₂CO₃, propargyl bromide, room temperature, 48 hours. (ii) DCM, TFA, room temperature, 2 hours. (iii) DMF, disuccinimidyl suberate, TEA, room temperature, overnight. 117
- Scheme 5.3 Synthesis of small molecule dipeptide precursor **39** for the targeting molecule for PSMA. Reagents and conditions: dry DCM, triphosgene, TEA, 0 °C-room temperature, 3 hours. (ii) MeOH, Pd on C, hydrazine, room temperature, overnight. 118
- Scheme 5.4 Conjugation of **40** and **42** and subsequent *tert*-butyl deprotection. Reagents and conditions: (i) DMF, TEA, room temperature, overnight. (ii) DCM, TFA, room temperature, 3 hours. 118
- Scheme 5.5 “Click” conjugation of **44** with porphyrin **11**, methyl deprotection, and ^{nat}Re complexation. Reagents and conditions: (i) 1:1 *t*-butanol:water, CuSO₄, sodium ascorbate, TBTA, microwave (3 hours, 75 W, 70 °C). (ii) water, LiOH, room temperature 3 hours. (iii) phosphate buffer (pH 7), [Re(CO)₃Br₃][NEt₄]₂ **37**, 65 °C, 30 mins. 119
- Scheme 5.6 Radiolabelling of conjugate **35** and conjugate **46** to prepare complex [^{99m}Tc]-**36** and [^{99m}Tc]-**47**. Reaction conditions: t = 30 mins, T = 99 °C, pH 7.4 or pH 11. 122

List of Tables

Table 1.1 Properties of some of the elements commonly found in biological systems. Values obtained from <i>MRI: Basic Principles and Applications</i> . ⁶⁷	17
Table 2.1 Varying concentration of wtCPMV and molar excesses of porphyrin 7 .	59
Table 3.1 Varying molar percentage of porphyrin 23 and APMA used for the synthesis of PAN-(porphyrin-amine) .	79
Table 3.2 Effect of monomer ratio on PAN yield and PAN polydispersity.	84
Table 3.3 Rate constant, k , for the phosphorescence decay and the derived hydration state, q , for ([Eu(DTPA)]_{1,0}-PAN-(alkyne_{1,0}) and ([Tb(DTPA)]_{1,0}-PAN-(alkyne_{1,0}) .	98
Table 4.1 Radiochemical yields of ⁶⁸ Ga labelling reactions. Reaction conditions: ^{a,b} [L] = 100 μM. ^a t = 15 mins, T = 25 °C. ^b t = 45 mins, T = 99 °C. ^c I = 0.1 M acetate buffer. ^d I = 0.1 M phosphate buffer.	108

Chapter 1 Introduction

Cancer is one of the leading causes of death in the world, with 17 million new cases of cancer and 9.6 million deaths caused by cancer worldwide in 2018 (obtained from Cancer Research UK).¹ One of the keys to cancer cure is early detection and treatment. There are many techniques to diagnose and image cancer, which includes, X-rays, fluorescence imaging, magnetic resonance imaging (MRI), positron emission tomography (PET) imaging, and single photon emission computed tomography (SPECT) imaging. The subsequent treatment process can prove to be tedious, ineffective, and painful to the patient. One treatment technique is photodynamic therapy (PDT), which has been shown to achieve similar effectiveness and have many advantages over traditional cancer treatment techniques such as surgery and radiotherapy, with lower morbidity rates, improved functional, and cosmetic outcomes.² However, there is much room for improvement on specificity, sensitivity, efficiency, and efficacy of these imaging and treatment techniques.

This research will revolve around the development of molecular- or nano-theranostic conjugates for the combined treatment and diagnosis of cancer. Photodynamic therapy as a cancer treatment technique and optical imaging, magnetic resonance imaging, positron emission tomography, and single-photon emission computed tomography as cancer imaging techniques are described. The combination of multiple modalities often involves covalent conjugation, hence, some conjugation methods are also included.

1.1 Photodynamic therapy

Photodynamic therapy (PDT) is a promising treatment technique for cancer.³ PDT is minimally invasive and shows little or no toxicity which proves advantageous over traditional anti-cancer techniques, including surgery, radiation therapy, and chemotherapy. These traditional anti-cancer techniques can be inefficient, painful to the patient, and it often takes a long time for the patient to recuperate from the treatment.^{3,4}

PDT involves the administration of a non-toxic drug, known as a photosensitiser, to a patient bearing a lesion, which is often, but not limited to cancer.^{5,6} An ideal photosensitiser will selectively accumulate in diseased tissues after a period of time. Irradiation with a carefully regulated dose of light onto the target tissue/organ will activate the photosensitisers, generating reactive oxygen species *in situ*, causing oxidative damage to surrounding tissues, eventually culminating in cell death.

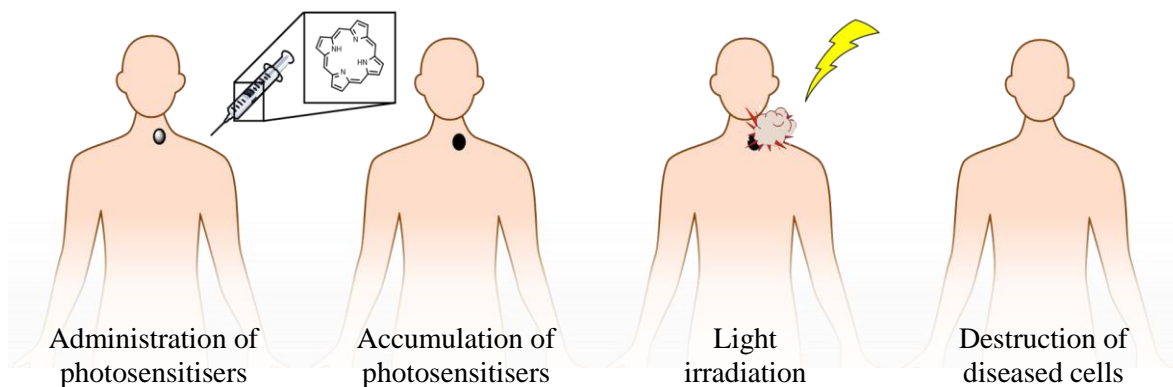


Figure 1.1 Schematic for the clinical procedure for PDT.

1.1.1 Photophysical and photochemical processes of photodynamic therapy

A photosensitiser is a molecule that, upon absorption of a photon (a packet of light energy) of sufficient energy, can transfer the energy to a substrate without itself being permanently altered. Figure 1.2 shows a simplified Jablonski diagram to illustrate the photophysical and photochemical processes involved in PDT. The photosensitiser exists in its ground singlet state (S_0) and, upon absorption of a photon of sufficient energy, an electron will be promoted to a lowest unoccupied molecular orbital. Current PDT uses light in the range of visible and near infrared light (400-800 nm) to activate photosensitisers.^{4,7} Upon light irradiation, the photosensitiser is excited into short lived excited singlet states, for instance an electron is excited to S_1 ; electrons can be excited to occupy other higher excited state depending on the wavelength of light and the photosensitiser used.⁴

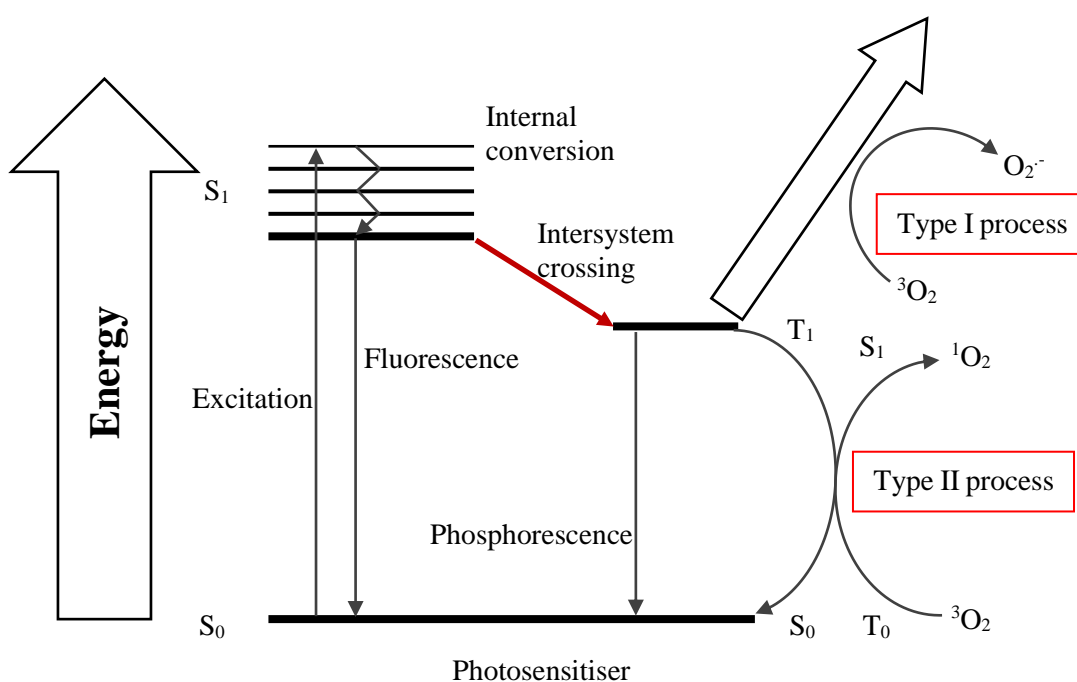


Figure 1.2 A simplified Jablonski diagram, showing the photochemical mechanism of a typical photosensitiser.

Internal conversion, sometimes also known as radiationless de-excitation, can occur. This process involves relaxation within the same excited state (S_1) *via* the release of phonon/s (a packet of vibrational energy) in the form of thermal energy. This can be followed by the relaxation back to the ground state (S_0) *via* the emission of a photon as fluorescence. Due to the nature of fluorescence, some of the energy of the initial absorbed photon is lost as phonons, the emitted photon is thus of lower energy.

Alternatively, the excited photosensitiser can undergo intersystem crossing to occupy a lower energy, longer lived, excited triplet state (T_1), a spin forbidden process. According to the spin selection rules, only transitions between the same spin states are allowed, for instance, transitions between singlet ground states to excited singlet states. Notwithstanding the spin selection rules, a good photosensitiser can still have high triplet state quantum yield. The excited triplet state photosensitiser can undergo a second spin inversion to relax back to its singlet ground state *via* phosphorescence. These spin forbidden processes are also the reason behind the longer lived excited triplet state. The typical values for photosensitisers excited singlet state lifetimes are in the nanosecond timeframe, whereas, excited triplet state lifetimes are in the micro to millisecond range.⁴

The longer-lived excited triplet state photosensitiser is predominantly responsible for causing the photodynamic effect. There are two types of photodynamic reactions and they are defined as Type I and Type II reactions.

Type I processes are electron- or hydrogen atom-transfer reactions between the excited triplet state (T_1) photosensitiser and readily oxidisable or readily reducible substrates. These substrates can be in the form of biological molecules such as cell membranes and proteins. The transfer of an electron or a hydrogen atom to or from these substrates will generate radicals.

Alternatively, the triplet state photosensitiser can undergo electron transfer directly with molecular oxygen to generate superoxide (O_2^-). Superoxide can act as reducing agent and donate an electron to metal ions such as Fe^{3+} , that will act as a catalyst to break the oxygen-oxygen bonds in hydrogen peroxide (H_2O_2) to form highly reactive hydroxyl radicals ($OH\bullet$).⁸ In addition, reaction between superoxides produces hydrogen peroxide which can lead to more generation of hydroxyl radicals.

The radicals formed *via* this type I processes, are free to react with more organic substrates, which in turns generate more radicals. This can cause a radical chain reaction with other surrounding tissues, and consequently oxidative damage to cells.

Type II processes involve energy transfer. The excited triplet state photosensitiser can undergo an electron spin exchange with molecular oxygen. Molecular oxygen (exists as a triplet ground state) is excited to its reactive singlet state (1O_2). Singlet oxygen is strong oxidant which can react

with many biological molecules, including unsaturated fatty acids, cholesterol, cell membranes, and many amino acids.⁹ The lifetime of singlet oxygen in a cellular environment is short (<40 ns)⁸ and therefore it can only react with substrates near its site of production. This is particularly useful as photosensitisers can be targeted and selectively accumulate only in diseased tissues, upon activation with light, only diseased tissues are destroyed leaving healthy tissues intact.

Type I and type II processes may occur simultaneously and play important roles in impeding cellular mechanisms and destroying cellular structure. The ratio of the two processes are dependent of the photosensitiser used and the local oxygen concentration. However, there is evidence showing type II processes predominate in causing photodynamic damage to cells.^{3,10} Most importantly, both these processes can cause oxidative damage to biomolecules, eventually culminating cell death.

1.1.2 Cell death

Cell death can occur in two ways, necrosis and apoptosis (Figure 1.3).¹¹ Apoptosis, also known as “cell suicide”, only affects individual cells. Apoptosis can occur naturally and is a form of programmed cell death in multicellular organisms.¹² However, it can also be induced by external factors – including photodynamic damage. Apoptosis begins with condensing DNA material in the cell. This is followed by breaking down of cells into multiple smaller fragments known as apoptotic bodies. These fragments will still be enclosed by a cell membrane, and be disposed of when macrophages engulf and destroy them.^{13,14} Apoptosis is therefore, in most cases, the preferred cell death method as diseased cells are removed in an organised manner without extensive inflammation. Photosensitisers that accumulate in mitochondria have been found to trigger apoptosis more efficiently.¹⁵

Necrosis, on the other hand is said to be the opposite of apoptosis. It is a form of cell injury caused by external factors such as trauma or metabolic injury. However, there is evidence showing that necrosis can be a rare form of programmed cell death with the intention to evoke an immune response by expelling their intracellular contents,¹⁴ for instance during a viral or bacterial infection. Cells undergoing necrosis initially swell (necrosis derived from the word “oncos” which means swelling)¹² and organelles break down. The cell membrane eventually ruptures and releases cytosolic constituents into its extracellular space which may induce inflammation in nearby cells and may cause cell death.¹⁴

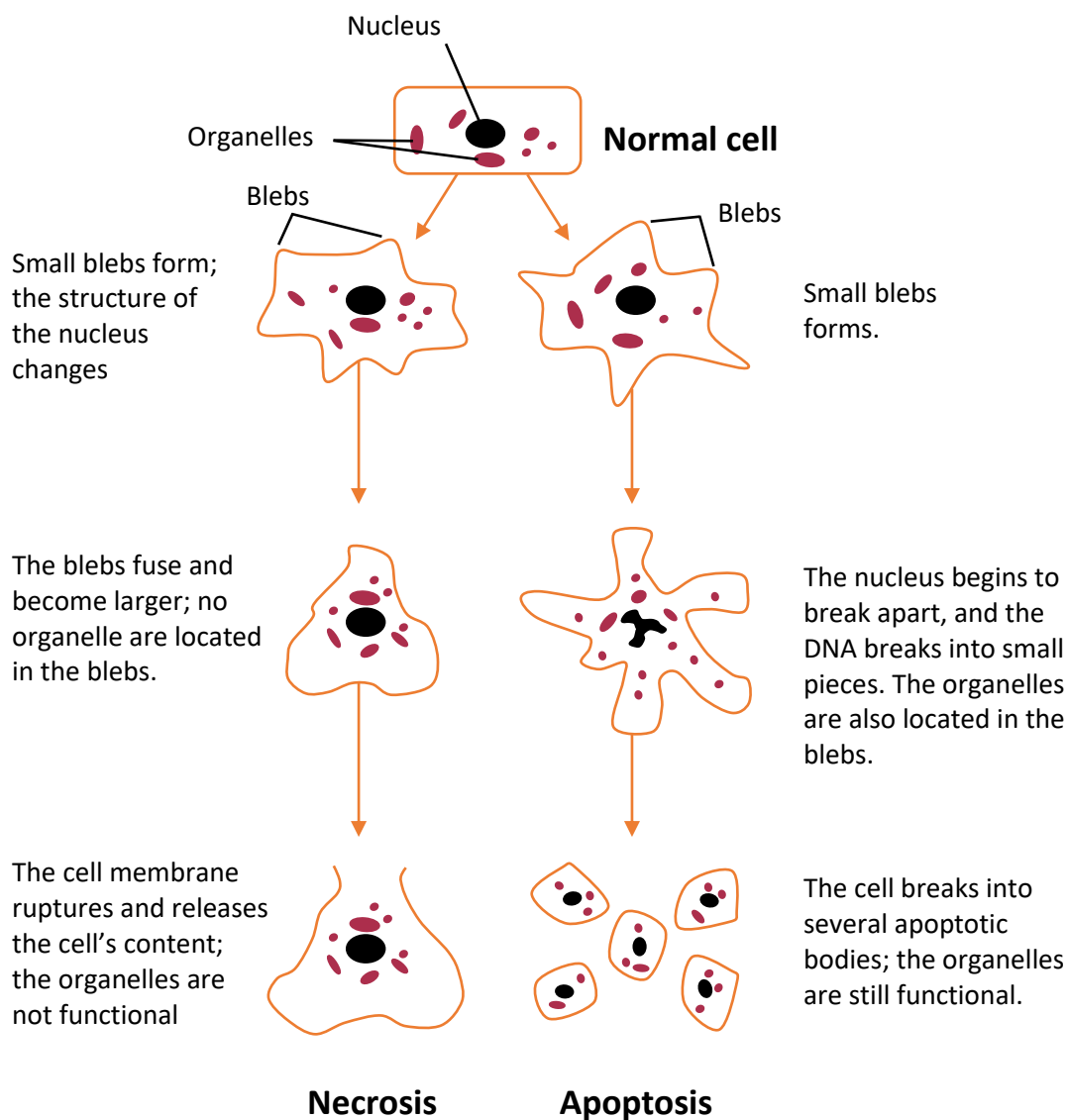


Figure 1.3 Schematic for cell death via necrosis and apoptosis. Image adapted and redrawn from *Alcohol Res. Health*, 2001, **25**, 175–184).

1.2 Photosensitisers for photodynamic therapy

As mentioned earlier, photosensitisers are molecules capable of absorbing a photon, and transferring the energy to a substrate without themselves being permanently altered. Organic photosensitisers are usually molecules that have extended conjugated π systems, capable of absorbing a photon in the visible light region. Some non-macrocyclic based photosensitisers are methylene blue, acridine, and Rose Bengal (Figure 1.4).

However, more commonly used photosensitisers are tetra-pyrrolic macrocycles, such as porphyrin, chlorin, bacteriochlorin, and phthalocyanine (Figure 1.5).

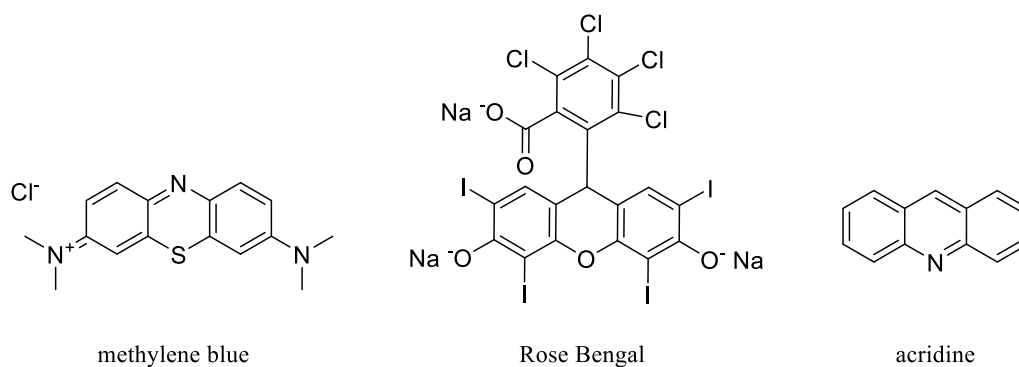


Figure 1.4 Examples of non-macrocyclic photosensitisers.

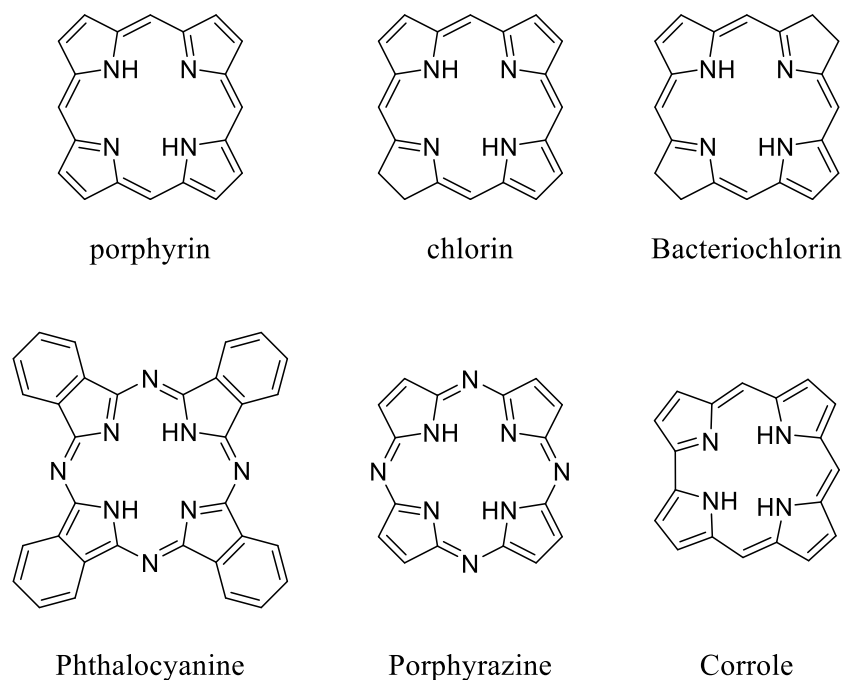


Figure 1.5 Structure of porphyrin and some other tetrapyrrolic molecules.

1.2.1 Evolution of photosensitisers: porphyrins and other tetrapyrrolic macrocycles

Phototherapy where only light is involved in the treatment of disease dates back to the late 19th century where the Nobel laureate, Niels Ryberg Finsen demonstrated the use of intense light radiation to treat *Lupis vulgaris*. Before the era of photodynamic therapy, the photosensitising ability of porphyrins and other tetrapyrrolic macrocycles had been observed, and was regarded as a disease known as photosensitivity syndrome.³ In mild cases it caused skin lesions, oedema, and erythema, but could be lethal in its severe form. The occurrence of photosensitisation in the body can be caused by a faulty biosynthesis of protohaem (essential in the formation of haemoglobin and myoglobin) resulting in accumulation of protoporphyrin IX (PPIX), which is the equivalent of protohaem without the iron metal centre. This accumulation of metal free PPIX in the blood is responsible for the photosensitivity. It has also been observed in rats that a chlorophyll related diet (alcohol-treated *Chorella* algae) can induced photosensitivity syndrome.¹⁶

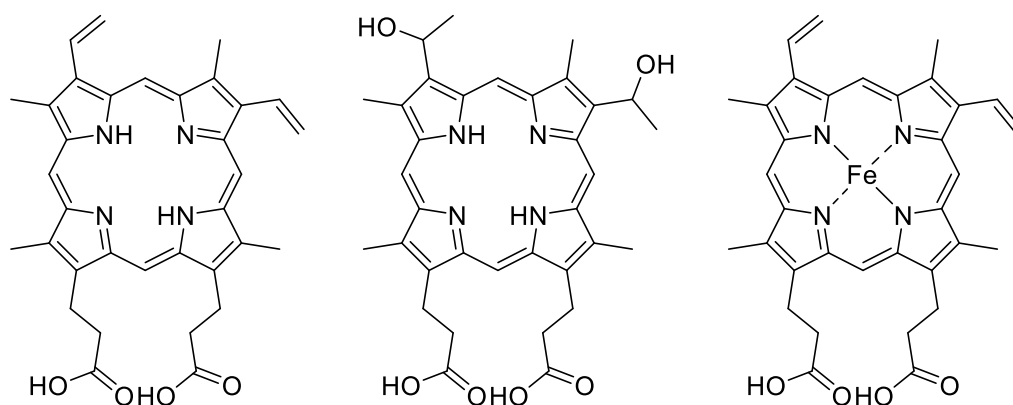


Figure 1.6 Structure of metal-free protohaem (left), hematoporphyrin (middle), protohaem (right).

However, it was not until 1903, when the photosensitising ability of these compounds was used to treat diseases. Von Tappeiner's group described the treatment of skin carcinomas using a topical fluorescein-based dye, eosin.^{3,4} Later in 1913, a German physician – Meyer Betz injected himself with 200 mg of hematoporphyrin (Hp) in saline and observed a general skin sensitivity on areas exposed to light^{3,9}. Another significant breakthrough occurred in 1942 when Hp was observed to accumulate in tumours and induced necrosis in cells upon light illumination.⁹

1.2.2 First generation photosensitisers

Subsequent research into Hp led to the first synthesis of hematoporphyrin derivatives (HpD) in 1960 by Lipson and Blades⁹ and eventually led to the first clinically approved photosensitiser, Photofrin® (a purified version of HpD) in 1993.

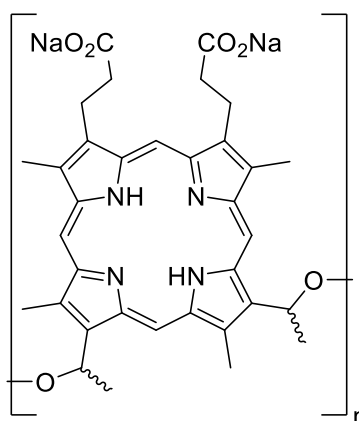


Figure 1.7 Photofrin® the first clinically approved photodynamic drug.

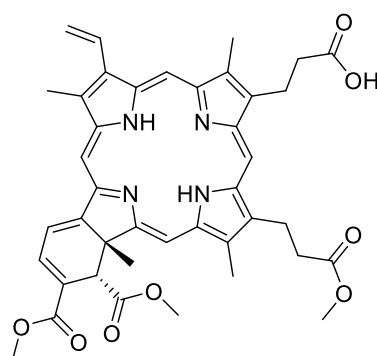
However, Photofrin® has severe drawbacks (Figure 1.7). Photofrin® is a mixture of dimers and oligomers of hematoporphyrin. Photofrin® shows prolonged photosensitivity post-treatment which can last up to 1-2 months.⁹ This can cause a great deal of discomfort and inconvenience to the patient and can limit the number treatments administered. Furthermore, these photosensitisers have weak absorption at long wavelengths, Photofrin® has an absorption spectrum that ranges between 400-630 nm with the weakest absorption Q-band at 630 nm. Despite being the weakest

absorption band, this wavelength is used for photodynamic treatment as it penetrates tissues best (a tissue depth of 5 mm).¹⁷

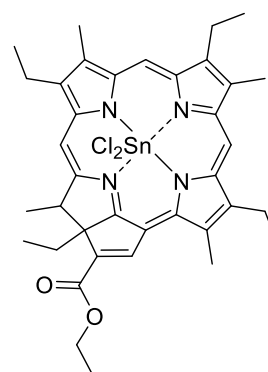
1.2.3 Second-generation photosensitisers

Problems encountered in first-generation photosensitisers led to further research in the development of second-generation photosensitisers. Second-generation photosensitisers are structurally defined photosensitisers and have been shown to tackle some of the problems that exist in first generation photosensitisers, to have improved efficacy, and broadening the types of diseases that can be treated.^{3,18}

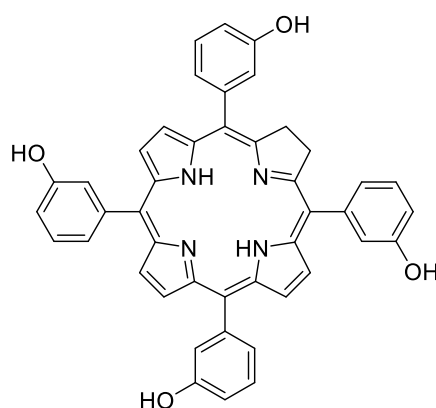
Visudyne®, a benzoporphyrin derivative, has been approved for treating wet age-related macular degeneration (wAMD) and cutaneous non-melanoma skin cancer. The success of Visudyne® is due to its intensified and red-shifted long wavelength absorption at 690 nm which has a 50% greater tissue penetration in comparison to Photofrin®'s absorption at 630 nm. Furthermore, it shows a quick accumulation time (30-150 minutes) and a fast clearance from the body (photosensitivity only lasts a few days).^{18,19}



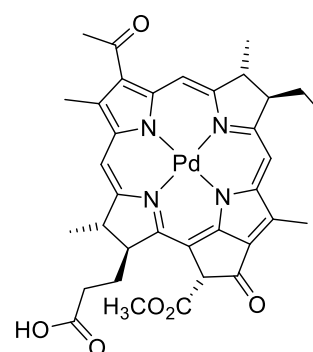
Visudyne®



Purlytin®



Foscan®



Tookad®

Figure 1.8 Structure of Visudyne® (top left), Purlytin® (top right), Foscan® (bottom left), and Tookad® (bottom right).

Tin etiopurpurin (marketed as Purlytin®) is a chlorin-based photosensitiser, which has been approved in the USA for the treatment of cutaneous metastatic breast cancer, the treatment of Kaposi's sarcoma in patients with acquired immunodeficiency syndrome (AIDS), and non-malignant conditions such as psoriasis and restenosis.^{3,18} Purlytin® has an intensified absorption at 650-680 nm. Another chlorin-based photosensitiser, tetra(*m*-hydroxyphenyl)chlorin (marketed as Foscan® or Temoporfin®), has been approved by the European Medicines Agency (EMA) for treatment of head and neck squamous cell carcinoma. Advantages of Foscan® include the low amount of drug and light required for photodynamic treatment.

Tookad®, palladium bacteriopheophorbide, is a metallo-photosensitiser, recently (2017) approved by EMA for the treatment of low-risk prostate cancer. Tookad® is used for vascular-targeted PDT, where PDT causes the destruction of blood vessels, subsequently inducing cancer cells death due to lack of nutrient supply.^{20,21} Some advantages Tookad® has as a photosensitiser are its strong absorbance at 650-750 nm and minimal skin photosensitivity.^{22,23}

An alternative approach to the utilisation of endogenous photosensitisers as photodynamic agents was described by Kennedy and Pottier in the early 1990s.²⁴ 5-aminolevulinic acid (ALA, marketed as Levulan®) is formed in mammals and is necessary for the biosynthesis of protohaem (Figure 1.10). ALA will undergo several reactions and modifications to form PPIX, and when administered as a prodrug, ALA can cause an excess of PPIX to be produced in tumours, allowing photodynamic treatment and/or fluorescence imaging.⁴ Since this early work, several ALA derivatives have been synthesised and approved – Metvix® and Benvix® (Figure 1.9).

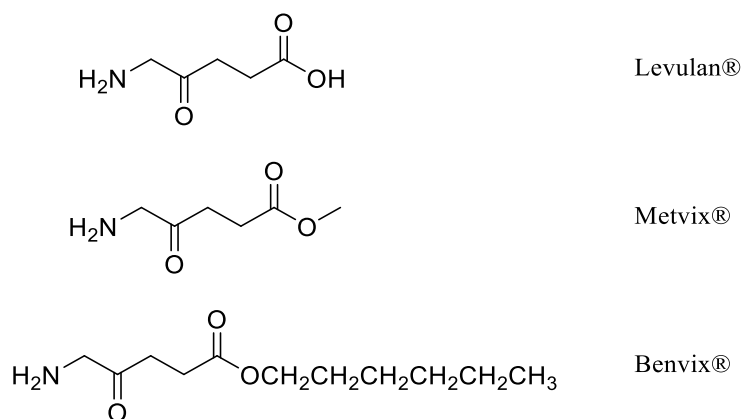


Figure 1.9 Structure of Levulan®, Metvix®, and Benvix®.

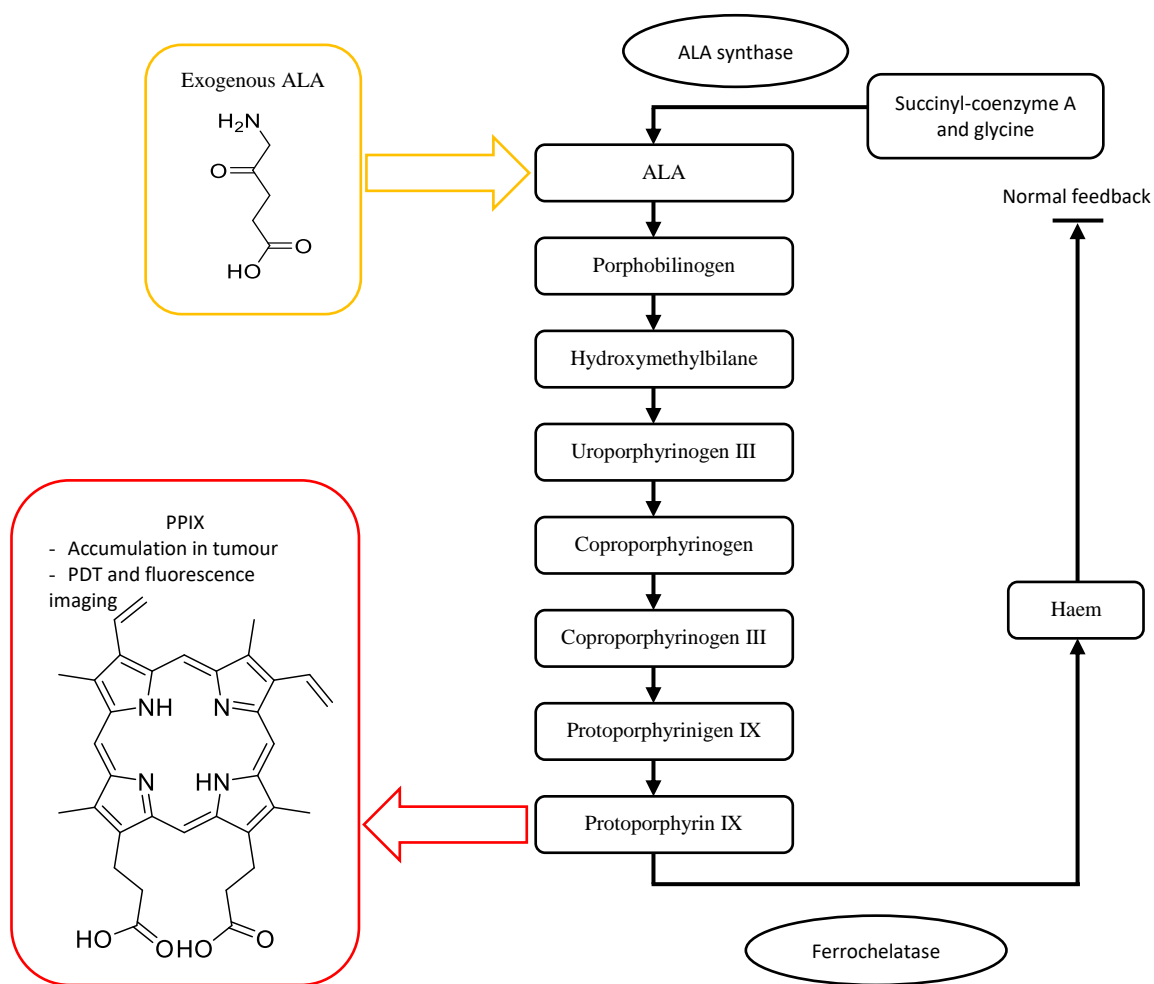


Figure 1.10 Schematic representation of haem synthesis pathway and the usage of exogenous ALA which leads to synthesis and accumulation of PPIX. Scheme was modified from *Chem. Rev.*, 2010, **110**, 2795–2838.⁴

Some of the photosensitisers described have poor solubility, for instance, Visudyne® and Purlytin®, hence, delivery vehicles for formulation of these photosensitisers were utilised.²⁵ The delivery vehicles used are often amphiphilic systems, such as phospholipid vesicles or oil emulsion, which are stable in aqueous media and possess hydrophobic/apolar regions for the dissolution of hydrophobic photosensitisers.^{26–29} Another method to overcome the solubility issues is to introduce polar water-soluble groups onto photosensitisers. Specific water-soluble moieties can be introduced on the peripheral parts of the photosensitisers, for example, water-soluble porphyrins with quaternised pyridinium groups,^{30,31} PEGylated phenyl groups,^{32,33} sulfonated groups,^{30,34} and hexahydroxy groups³⁵ have been shown in literature (Figure 1.11).

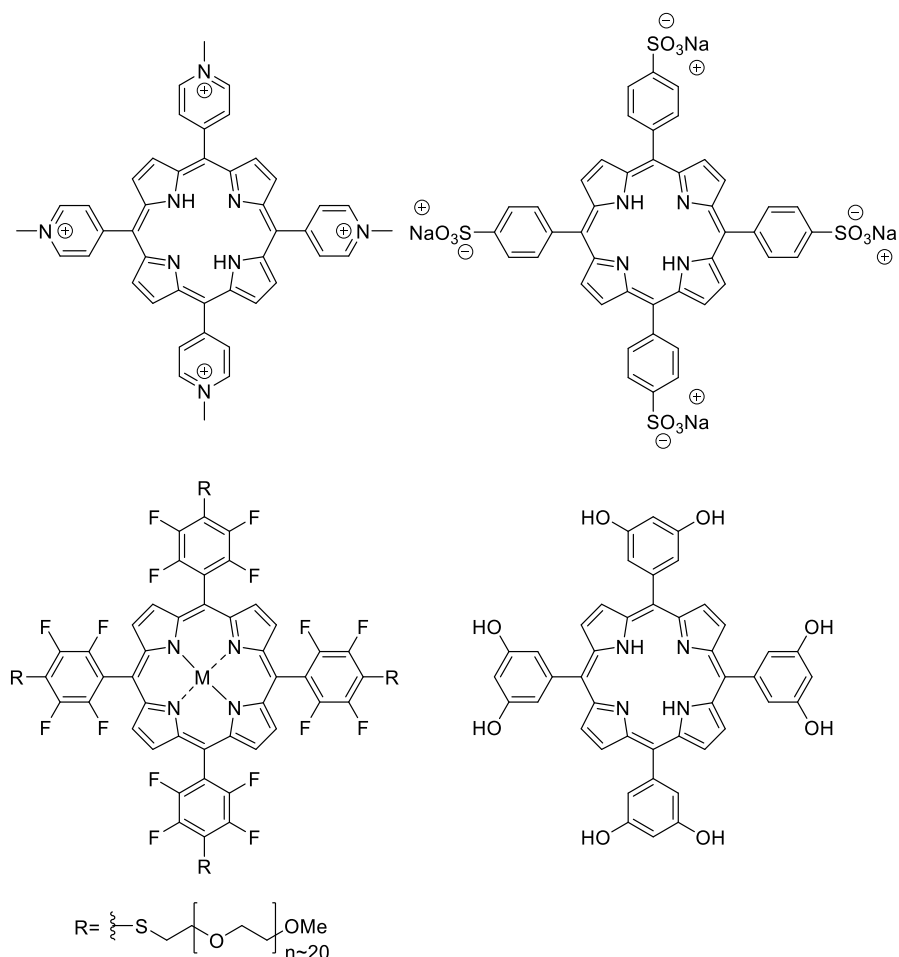


Figure 1.11 Structures of water soluble porphyrin, top left: tetra(*N*-methyl-4-pyridinium)porphyrin, top right: tetra(4-sulfonatophenyl)porphyrin sodium, bottom left: meso-tetrakis(4-PEG₁₀₀₀thioxytetra-2,3,5,6-fluorophenyl)porphyrinato]zinc(II), bottom right: tetra(3,5-dihydroxyphenyl)porphyrin.

1.2.4 Third- and/or fourth-generation photosensitisers

Second-generation photosensitisers addressed some of the problems which existed in first-generation photosensitisers. Third-generation photosensitisers focused on the selective delivery of photosensitisers to diseased tissues.

One of the ways to improve delivery of photosensitisers to tumour tissues is to use delivery vehicles such as liposomes, micelles, and emulsions, as mentioned earlier.^{25,36} These delivery vehicles not only allow the delivery of hydrophobic molecules, they also take advantage of abnormalities in their vasculature systems and has the ability to passively target tumour tissues through the enhanced permeability and retention (EPR) effect (Figure 1.12), a term first coined by Maeda.³⁷ However, recent evidence (publication of thousands of research papers) showed that EPR effect works in rodent models and not in humans, and should be used on a case-by-case basis.^{38,39} Liposomal delivery vehicles such as Cremophor EL emulsion has also been shown to have affinity towards low-density lipoproteins (LDL) and a better selectivity towards tumour cells.^{25,40} This is due to some tumour tissues overexpressing LDL receptors, which leads to photosensitiser accumulation in tumour cells.⁴¹

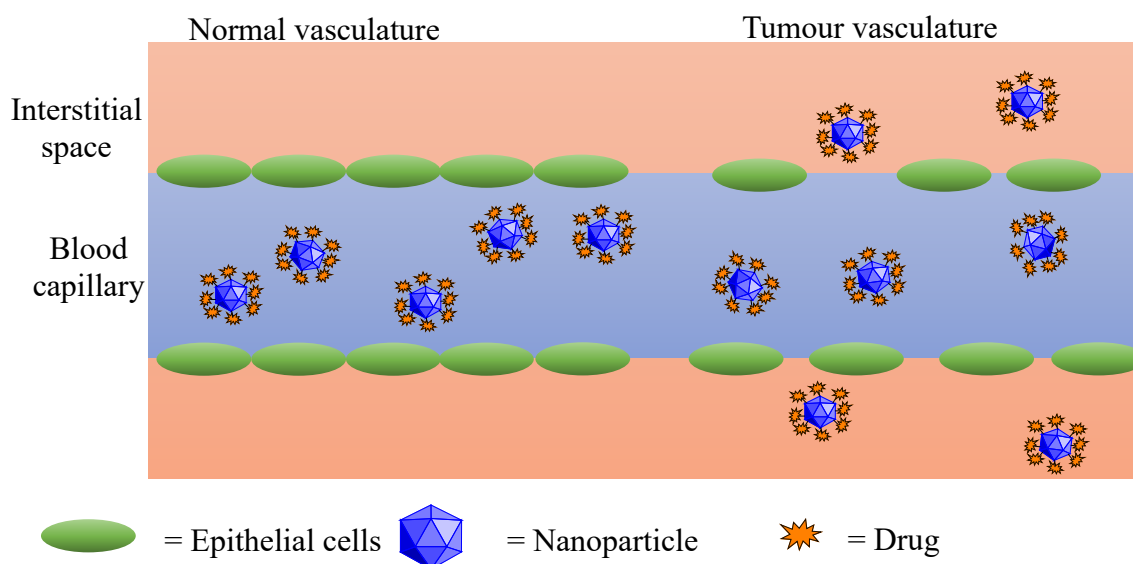


Figure 1.12 Schematic of the difference between normal vasculature and tumour vasculature.

Another way to selectively deliver photosensitisers to tumours is *via* covalent conjugation with a biomolecule capable of targeting receptors overexpressed on cancer cells. One such class of biomolecules are monoclonal antibodies (mAb); mAbs have the ability to recognise and bind to specific antigens, which are overexpressed on cancer cells.^{42,43} The covalent-conjugation of mAb with photosensitisers produces photoimmunoconjugates (PICs), which improves the selectivity of photosensitisers towards cancer cells. This attractive way of targeting photosensitisers has led to extensive research in this field and several reviews have described this.⁴²⁻⁴⁵

Steroids and hormones are another group of biomolecules that are capable of targeting cancer cells. The most common steroid in human is cholesterol, which is an important component in cell membranes, controlling their fluidity and flexibility.⁴⁶ Other steroids, such as, oestrogens, androgens, progestins, mineralocorticoids, and glucocorticoids, are signalling molecules and can bind to and activate their corresponding receptor, which can be utilised to target and deliver photosensitisers.⁴⁶ Taquet *et al.* reviewed the conjugation of phthalocyanines with cholesterol, estradiol, and estrone.⁴⁴ Osati *et al.* gave a comprehensive review on the conjugation of photosensitisers, which includes, porphyrins, chlorins, phthalocyanines, and pheophorbide with steroids and their subsequent applications.⁴⁶

Peptides and amino acids are also often used to improve photosensitisers' selectivity and accumulation in cancer cells. This can include cell penetrating,⁴⁷ nuclear localising⁴⁸ and mitochondria localising⁴⁹ peptides. By conjugating to these peptides, a large amount of photosensitiser can be delivered into the cell interior or to sensitive organelles (such as the nucleus and mitochondria), allowing more efficient and effective photodynamic treatment.^{50,51} A different class of peptide that are often used are tumour targeting peptides which selectively target tumour cells. Tumour targeting peptides are very similar to mAbs; they target a specific marker or integrin overexpressed on cancer cells. Research in to targeted peptides led to the development of a library

of peptides for targeted cancer therapy⁵² and also several reviews on the usage of peptides for targeted delivery of photosensitisers.^{53,54}

Besides improving the selectivity and the accumulation of photosensitisers in cancer cells, development of dual-/multi-functional photosensitisers (fourth-generation) have also been described.³ Incorporation of an additional functionality/modality, for example the incorporation of an additional therapy, such as, chemotherapy or photothermal therapy (PTT).

Yang *et al.* reported the use of liposomes loaded with lipophilic IR780 photosensitiser and hydrophilic tirapazamine for combined PDT and chemotherapy. Chemotherapeutic tirapazamine exhibits little toxic effect in oxygen-normal cells but exhibits high cytotoxicity under hypoxic condition. The use of IR780 for PDT depletes oxygen creating a synergistic effect, a hypoxic condition which activates tirapazamine.⁵⁵

Deng *et al.* reported the use of nitroimidazole-bearing polymer to form micelles and encapsulate chemotherapeutic doxorubicin (DOX) and chlorin e6. The nitroimidazole-based micelle is responsive to both hypoxic condition (tumour environment) and singlet oxygen (generated through PDT), which will trigger the disassembly of the micelle and the subsequent release of therapeutic agents. It was also reported that under hypoxic condition, nitroimidazole is capable of depleting glutathione,^{56,57} which is capable of preventing oxidative damage from singlet oxygen and also confer resistance to some chemotherapeutic drugs.⁵⁸

A targeted polysaccharide-based nanoparticle for the co-delivery of chemotherapeutic DOX and ALA-photosensitiser prodrug was reported by Wang *et al.*. Nanoparticle synthesis was carried out *via* layer-by-layer self-assembly of anionic and cationic polysaccharide. DOX, ALA, and anti-HER2 antibody was conjugated onto anionic polysaccharide; in which, DOX and ALA were loaded as the anionic core of nanoparticle, encapsulated by cationic polysaccharide, and decorated with anionic anti-HER2 antibody, forming a tri-layer nanoparticle capable of targeted drug release and PPIX production for combined chemotherapy and photodynamic therapy.⁵⁹

An example of combining PTT and PDT was reported by Liu *et al.*. In this study, a self-assembling iodinated aza-BODIPY nanoparticle was described. The self-assembling nanoparticle showed excellent *in vitro* photodynamic therapy with an IC_{50} of $7.91 \mu\text{g mL}^{-1}$ against HepG2 cells, and showed *in vivo* photothermal therapy *via* intratumoural injection with an increase in temperature up to $44.6 \text{ }^\circ\text{C}$.⁶⁰

Cai *et al.* reported an Fe-based metal organic framework nanoparticle conjugated with indocyanine green as the photosensitiser for combined PTT and PDT. The nanoparticle PDT capability was tested against a singlet oxygen sensor and the PTT capability was shown to increase temperature of water by $7.4 \text{ }^\circ\text{C}$. Synergistic PDT/PTT was also tested *in vivo*, and showed the nanoparticle was biocompatible and capable of inhibiting tumour growth.⁶¹

Using a different nanoplatform and an extension to the work described earlier by Wang *et al.*, the same research group reported the use of pH-sensitive gold nanorods for the loading of DOX and ALA. The gold nanorod reported is capable of dual chemotherapy/PDT (irradiation at 635 nm), dual chemotherapy/PTT (irradiation at 808 nm), or triple chemotherapy/PDT/PTT (irradiation at both wavelengths).⁶²

Instead of incorporating another therapy, research also focusses on introducing a diagnostic modality into the construct. The combination of diagnostic and therapeutic modalities into a single entity is now a growing area of research (not limited to photosensitisers), often referred to as theranostics, a term first coined by Funkhouser in 2002.³

As mentioned earlier, organic photosensitisers are molecules that have extended conjugated π system; most of which are capable of fluorescence imaging (an exception is Tookad® which has a negligible fluorescence quantum yield)²³, this makes most photosensitisers natural multimodal agents. Unsurprisingly, the use of porphyrins for fluorescence imaging and fluorescence-guided surgery in clinical settings is well-studied and established.^{3,63,64} Research into theranostics also focusses on the combination of other medical imaging techniques, such as, magnetic resonance imaging (MRI), positron emission tomography (PET) imaging, and single photon computed tomography (SPECT) imaging.

The following subchapters will describe some routinely used medical imaging techniques and the combination of these imaging methods with photosensitisers for use as fourth-generation theranostic agents.

1.3 Medical imaging

Some examples of medical imaging techniques are radiography, fluorescence imaging, magnetic resonance imaging (MRI), positron emission tomography (PET) imaging, single photon emission computed tomography (SPECT) imaging. These imaging techniques have something in common; they use electromagnetic waves (Figure 1.13).⁶⁵ Radiography, PET imaging, and SPECT imaging uses ionising radiation such as gamma rays and X-rays. Fluorescence imaging involves electromagnetic waves in the optical and near-infrared range. MRI involves probing and detecting a specific nuclei using radiofrequency and magnetic fields.

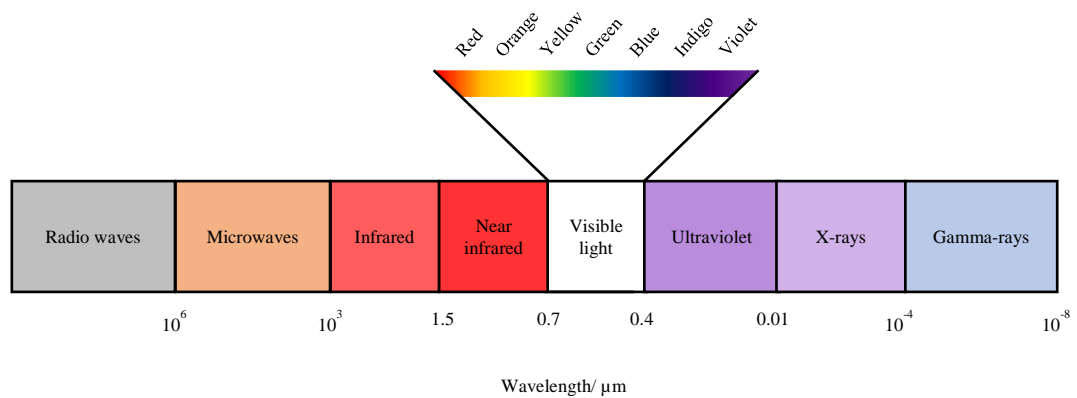


Figure 1.13 Electromagnetic spectrum.⁶⁵

These imaging techniques have their own advantages and disadvantages. Fluorescence imaging has high resolution and high sensitivity, however, it has poor tissue penetration. MRI has excellent resolution, however, it has poor sensitivity. PET and SPECT imaging both have high sensitivity, however, they lack anatomical resolution and hence are often used in conjunction with X-ray computed tomography (CT).⁶⁶

In this subchapter, medical imaging techniques that can introduce an additional imaging modality to complement PDT for cancer imaging are described, namely, fluorescence imaging, MRI, PET imaging, and SPECT imaging.

1.3.1 Fluorescence imaging

Fluorescence imaging involves illuminating the targeted area with a specific wavelength of light and detecting the emission (fluorescence) of the affected region.^{3,67} This is often carried out on surface tissues, and can be facilitated with the use of endoscopes. Contrast between diseased tissues and healthy tissues can be obtained from exogenous (drug-induced fluorescence) or endogenous molecules (autofluorescence).^{3,67,68} The difference in autofluorescence of diseased tissues can be used to distinguish between diseased and healthy cells. However, autofluorescence is only capable of detecting lesion/tumour mass and cannot show early neoplastic changes.⁶⁷

As mentioned before, photosensitisers are capable of behaving as fluorescence imaging agents. By administering an exogenous fluorophore, such as a photosensitiser, the contrast between diseased and healthy tissues can be improved, albeit, this relies on selective accumulation of the fluorophore. An example of this used indocyanine green as a fluorophore for 3D fluorescence imaging of human breast cancer *in vivo*.⁶⁹

1.3.2 Magnetic resonance imaging

MRI is a non-invasive imaging technique that is capable of providing 3D images of all parts of the human body without the use of ionizing radiation. It has a high spatial resolution and has been shown to be capable of obtaining better contrast between different types of tissues compared with

X-ray computed tomography (CT).⁷⁰ MRI is essentially a nuclear magnetic resonance (NMR) experiment of the human body; it involves applying a magnetic field across the patient and using tailored radiofrequency pulse sequence to probe a specific atom.

1.3.2.1 Principle of MRI

MRI is a measurement technique that is used to examine a specific nuclei. Hence, the structure of an atom is an important component for MRI. An atom consists of three fundamental particles, protons, neutrons, and electrons. Protons and neutrons make up the nucleus of the atom with electrons located in orbitals around the nucleus. A nuclei can be said to be rotating about an axis at a constant rate, possessing a nuclear spin, I . Every element in the periodic table except argon and cerium has a naturally occurring isotope that possess spin. This rotating nuclei produces a nuclear magnetic moment, μ , and can be described to be analogous to a bar of magnet (Figure 1.14).

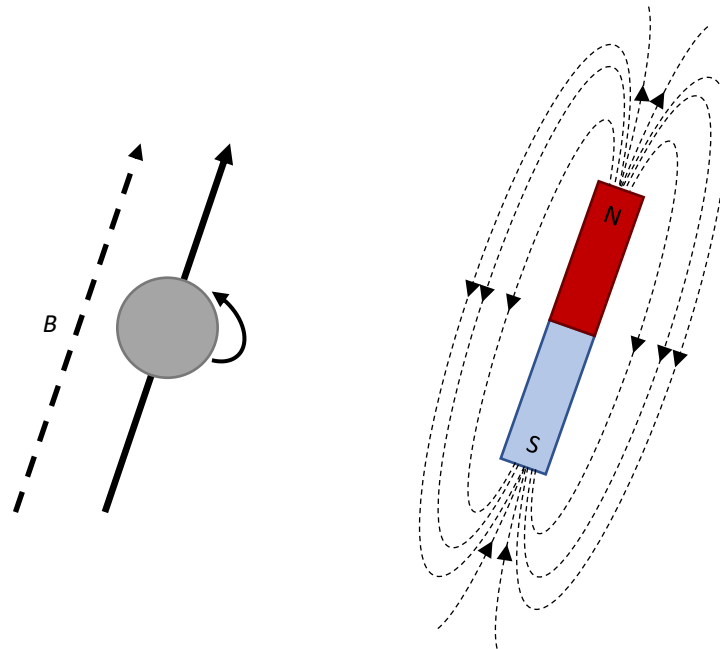


Figure 1.14 A rotating nucleus with a positive charge produce a magnetic field known as magnetic moment. This can be described to be analogous to a bar of magnet.

The ^1H nuclei, which consists of only a proton, is the most commonly examined atom in MRI. It exists in the largest concentrations in the human body as part of water molecules and fatty tissues, is the most abundant isotope of hydrogen, and has a spin, I , of $\frac{1}{2}$. Hereon, this subchapter will focus on the nucleus of ^1H , proton.

When a human body is placed in B_0 , the spin of the nuclei is polarised and aligned either parallel or antiparallel with the magnetic field (Figure 1.15), known as the Zeeman interaction. This interaction causes a difference in energy, ΔE , and hence more spins will populate the lower energy level. The vector sum of these spin in the presence of a B_0 , is therefore nonzero and will point

towards the same direction of B_0 , resulting in a net magnetisation, M_0 . The number of protons occupying these energy level can be determined using the Boltzmann distribution function (Eq. 1.1).

Element	Nuclear composition		Nuclear spin/ I	% Natural abundance
	Protons	Neutrons		
^1H	1	0	1/2	99.985
^2H	1	1	1	0.015
^{12}C	6	6	0	98.90
^{13}C	6	7	1/2	1.10
^{14}N	7	7	1	99.634
^{15}N	7	8	1/2	0.366
^{16}O	8	8	0	99.762
^{17}O	8	9	5/2	0.038
^{19}F	9	10	1/2	100
^{23}Na	11	12	3/2	100
^{31}P	15	16	1/2	100

Table 1.1 Properties of some of the elements commonly found in biological systems. Values obtained from *MRI: Basic Principles and Applications*.⁷¹

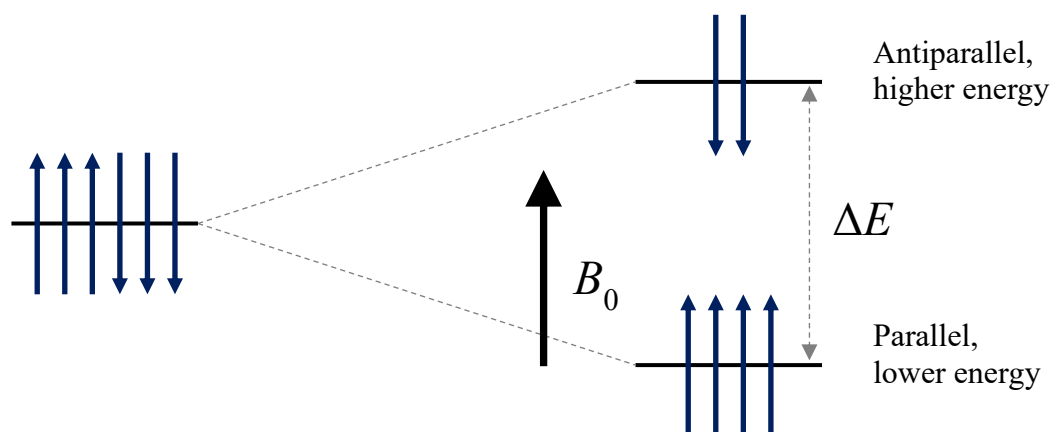


Figure 1.15 Schematic of Zeeman interaction. In the absence of magnetic field (left), B_0 , the collection of spin will have no preferential alignment. In the presence of magnetic field (right), the parallel orientation is lower energy, and contains more nuclei compared to the higher energy antiparallel orientation. The difference in energy between the two levels is ΔE .

$$\frac{N_{Antiparallel}}{N_{Parallel}} = e^{-\frac{\Delta E}{kT}} \quad \text{Eq. 1.1}$$

To probe the proton, a short burst, or excitation pulse, of radiofrequency energy is applied. The nuclei in the parallel lower energy level will absorb a portion of this energy, de-align the spin of the nuclei, and excite the nuclei to the antiparallel higher energy level. Once the excitation pulse is turned off, the nuclei will immediately realign themselves to their original equilibrium state,

reemitting a photon of radiofrequency energy. The process of re-emitting a radiofrequency pulse after absorbing a radiofrequency pulse is known as relaxation. This is an important process in MRI as this reemitted photon will then be detected by the MR machine and subsequently used to generate a 3D image of the patient. Relaxation is a time-dependent process and is characterised by a rate constant known as relaxation time. There are two relaxation times that can be measured, known as $T1$ and $T2$, which will be described briefly below.

1.3.2.2 Spin-lattice relaxation or $T1$ relaxation

$T1$ relaxation is also known as the spin-lattice relaxation, in which nuclei lose energy to their surroundings. Nuclei in a magnetic field have a net magnetisation, M_0 , upon excitation with a radiofrequency pulse (eg. 90° pulse), this will de-align the vector of M_0 by 90° into the transverse plane (Figure 1.16). The time taken for 63% of M to return to its original M_0 equilibrium state is known as the $T1$ relaxation time, which is governed by the following equation (Eq. 1.2).

$$M(t) = M_0(1 - e^{-t/T1}) \quad \text{Eq. 1.2}$$

Where t is the time following the excitation pulse.

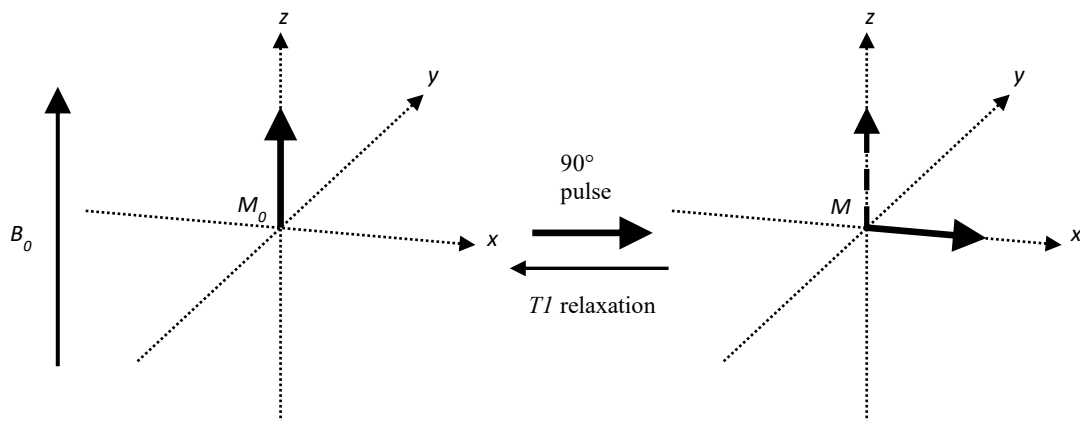


Figure 1.16 Protons with a net magnetisation, M_0 , upon excitation with a 90° pulse, de-align the vector M_0 by 90° into the transverse plane.

As mentioned, $T1$ relaxation is where nuclei lose their energy to their surroundings, hence, the protons' environment is an important factor that affects $T1$ relaxation time. For instance, metal ions such as iron and manganese can have significant magnetic moments that influence the relaxation time in their local environment. Proteins are large biomolecules that have slow tumbling frequencies which allows a more efficient energy transfer to the surrounding, resulting in a shorter $T1$. The differences in $T1$ relaxation within the human body allows MRI to differentiate/provide contrast between tissues.

1.3.2.3 Spin-spin relaxation or $T2/T2^*$ relaxation

$T2$ relaxation is also known as spin-spin relaxation, in which the energy of the excited proton is transferred to a nearby nuclei, instead of transferring to the surrounding (Figure 1.17). As

mentioned earlier, a nucleus rotates around an axis, possessing a nuclear spin, as shown in Figure 1.14; in the presence of a magnetic field, the nuclei also precesses about the magnetic field (Figure 1.18). The rate of precession is known as the Larmor frequency, ω_0 .

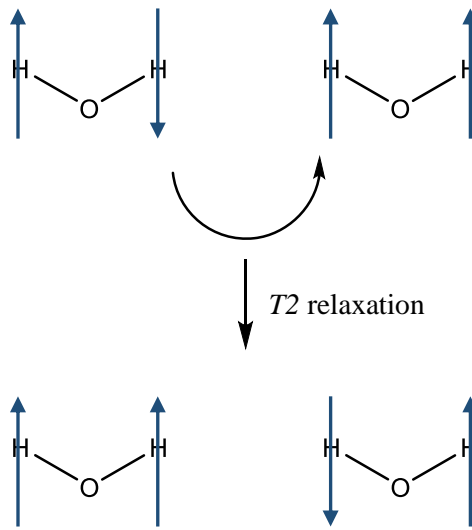


Figure 1.17 T_2 relaxation also known as spin-spin relaxation.

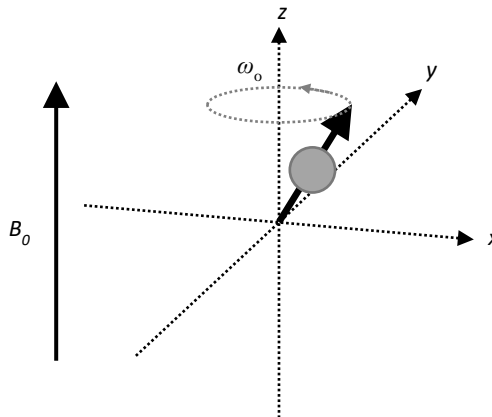


Figure 1.18 In the presence of a magnetic field, a proton precesses around the magnetic field. The rate of precession is known as the Larmor frequency, ω_0 .

Upon excitation with a 90° radiofrequency pulse, the spin of the nuclei is de-aligned by 90° as shown in Figure 1.16, these spins will possess the same ω_0 and precess around the magnetic field. However, this uniformity, where all nuclei possess with the same ω_0 , will gradually be lost. The process in which this uniformity is lost is known as the T_2 or T_2^* relaxation.

There are several factors that causes this lost in uniformity:

- (i) Molecular motions, such as, vibrations and rotations of the spins. This process is irreversible and is responsible for the true T_2 relaxation
- (ii) Non-uniform magnetic field from the MRI machine
- (iii) Differences in magnetic susceptibility, for instance, the interface between two different tissues

These sources listed above contribute to the total spin-spin relaxation time, T_2^* relaxation time:

$$\frac{1}{T2^*} = \frac{1}{T2} + \frac{1}{T2_M} + \frac{1}{T2_{MS}} \quad \text{Eq. 1.3}$$

Where $T2$ is the true irreversible $T2$ relaxation time, $T2_M$ is due to non-uniform magnetic field, and $T2_{MS}$ is due to magnetic susceptibility difference.

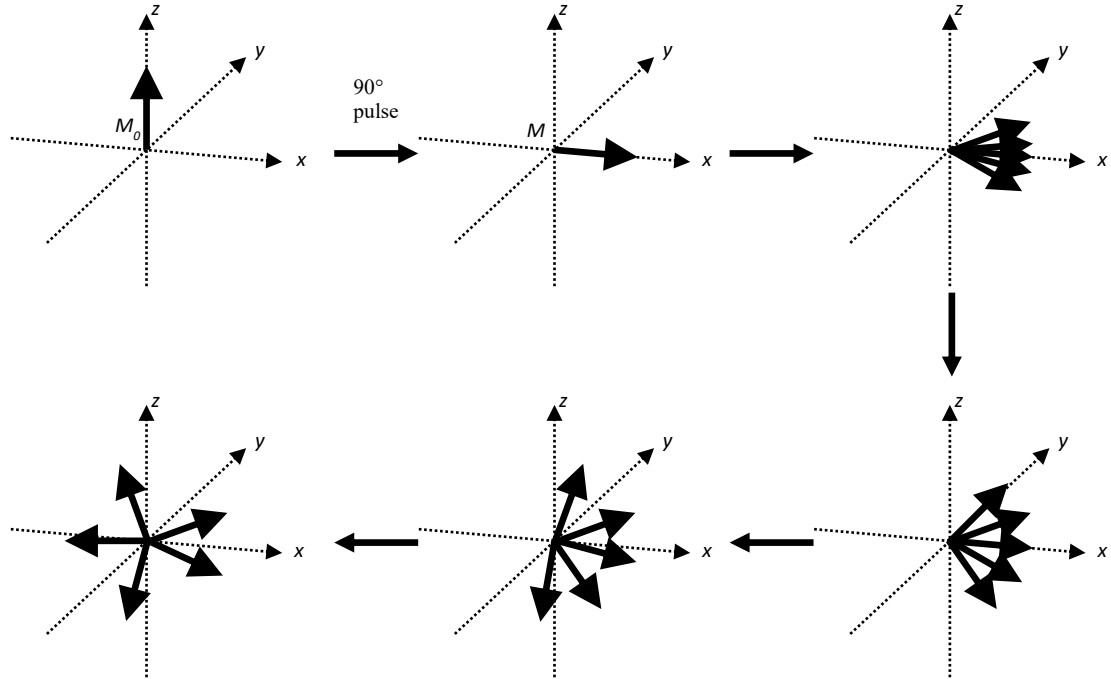


Figure 1.19 Schematic to show the lost in uniformity of after 90° excitation pulse, which is also known as $T2$ or $T2^*$ relaxation.

The lost in uniformity following a 90° pulse is governed by the following equation.

$$M_{XY}(t) = M_{XY_{max}} e^{-t/T2^*} \quad \text{Eq. 1.4}$$

Where M_{XY} is the magnetisation in the transverse plane, $M_{XY_{max}}$ is the magnetisation immediately after 90° excitation, and t is the time following the excitation pulse.

Some sources that cause the lost in uniformity can be reversed using carefully chosen pulse sequences, such as the spin-echo experiment, and $T2$ relaxation time can be used instead of $T2^*$ relaxation time in Eq. 1.4. The details of a spin-echo experiment have been described in several textbooks, and is not discussed here as they are beyond the scope of this thesis.⁷¹

1.3.2.4 MRI contrast agent

Despite MRI being a high-resolution imaging technique and capable of differentiating different tissue types due to their differences in $T1$ or $T2$ relaxation, MRI can have difficulty in distinguishing pathological tissues from healthy tissues (if they have the same relaxation). Hence, MRI contrast agents have been utilised to improve the quality and contrast of the MR image obtained, by enhancing the difference in signal intensity.

When an MRI contrast agent is administered, it affects the $T1$ relaxation and/or $T2$ relaxation times of the surrounding water proton nuclei.⁷² Contrast agents that shortens $T1$ relaxation rates are known as $T1$ contrast agents, they increase the $T1$ -weighted MRI signal, creating a brighter image. Contrast agent that shorten $T2$ relaxation times are known as $T2$ contrast agents, they decrease the $T2$ MRI signal in a T2-weighted spin echo experiment, creating a darker image. In either case, a greater contrast is achieved.

All Food and Drug Administration (FDA) and EMA approved $T1$ contrast agents to date are gadolinium-based (Figure 1.20). Gd^{3+} has 7-unpaired electrons, and is one of the most paramagnetic ions; it has a large effective magnetic moment, $\mu_{\text{eff}} = 7.94 \text{ B.M.}$.^{66,73} When a Gd^{3+} complex is administered into the human body, it will lower the $T1$ relaxation time of bound water, increasing the $T1$ -weighted MRI signal.

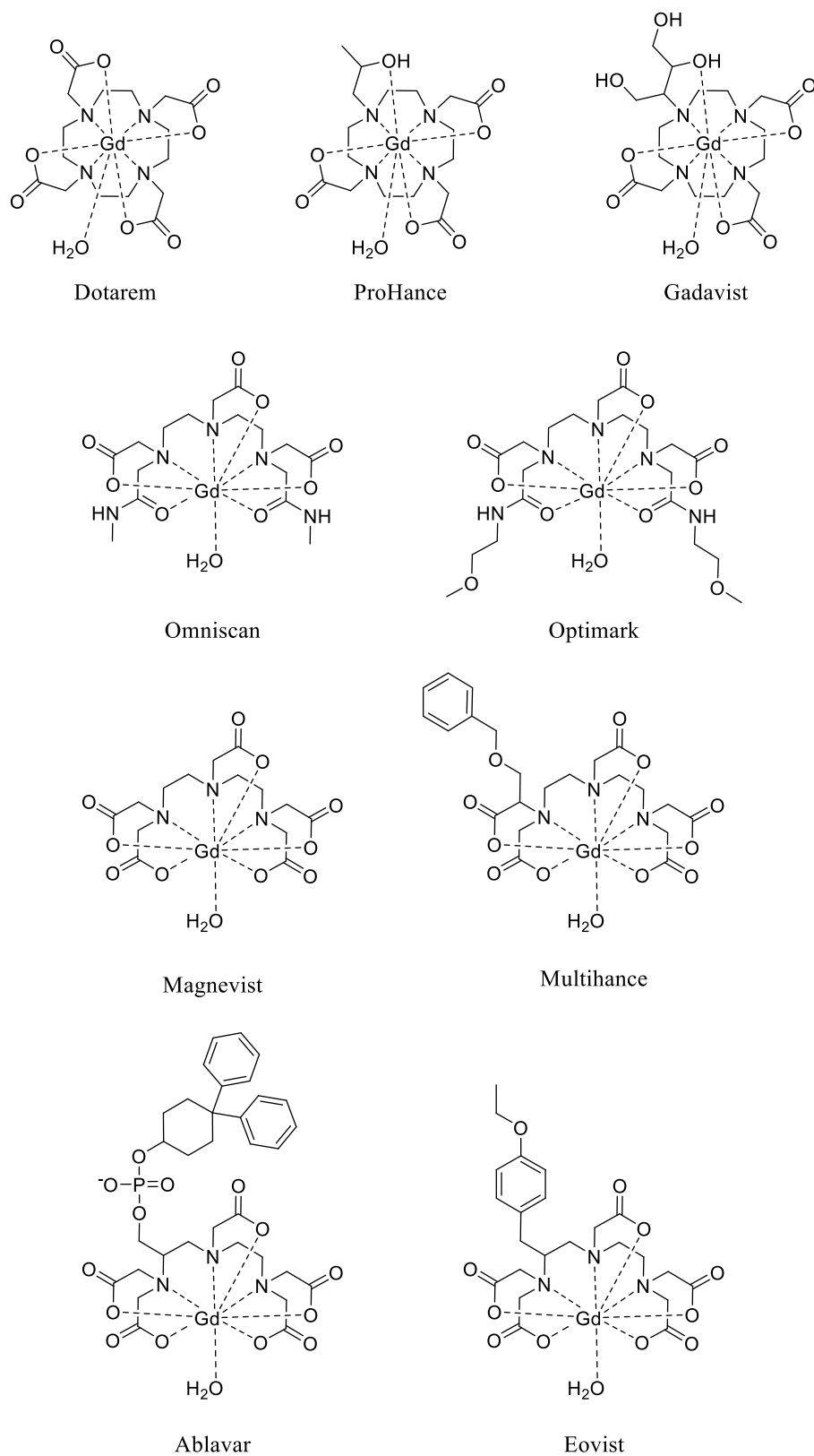


Figure 1.20 FDA and/or EMA approved gadolinium-based contrast agents.

1.3.2.5 Proton Relaxivity, r_1

As mentioned above, signal intensity of MRI depends on the relaxation time of the tissue types and this relaxation time can be altered upon administration of a contrast agent. For T_1 relaxation,

the signal intensity of $T1$ -weighted can be increased by shortening $T1$ relaxation time or increasing the $T1$ relaxation rate, $R1$ (Eq. 1.5):

$$R1 = \frac{1}{T1} \quad \text{Eq. 1.5}$$

The $T1$ relaxation rate, $R1$, can be described as the sum of a diamagnetic relaxation rate, $\frac{1}{T1_d}$, which corresponds to the relaxation rate of the solvent/tissue and a paramagnetic relaxation rate, $\frac{1}{T1_p}$, which corresponds to the relaxation rate enhancement due to a paramagnetic species, for instance, a Gd-based contrast agent (Eq. 1.6):

$$\frac{1}{T1} = \frac{1}{T1_d} + \frac{1}{T1_p} \quad \text{Eq. 1.6}$$

The paramagnetic relaxation rate is linearly proportional to the concentration of paramagnetic species, $[Gd]$:

$$\frac{1}{T1_p} = r_1[Gd] \quad \text{Eq. 1.7}$$

where r_1 is the proton relaxivity of the paramagnetic species, which has a unity of $\text{mM}^{-1} \text{s}^{-1}$ provided concentration of Gd^{3+} , $[Gd]$, is given in mM . Proton relaxivity defines the efficiency of the paramagnetic species to enhance relaxation rate of protons, thus the efficacy as a contrast agent.

This paramagnetic relaxation rate is made up of contributions from inner sphere and outer sphere relaxation mechanism (Eq. 1.8).⁷⁴ Inner sphere contribution is due to the interaction between gadolinium with directly bound water molecules (Figure 1.21). Outer sphere contribution is due to interaction with closely diffusing water molecules.

$$\frac{1}{T1_p} = \left(\frac{1}{T1_p}\right)^{IS} + \left(\frac{1}{T1_p}\right)^{OS} \quad \text{Eq. 1.8}$$

where IS refers to inner sphere and OS refers to outer sphere.

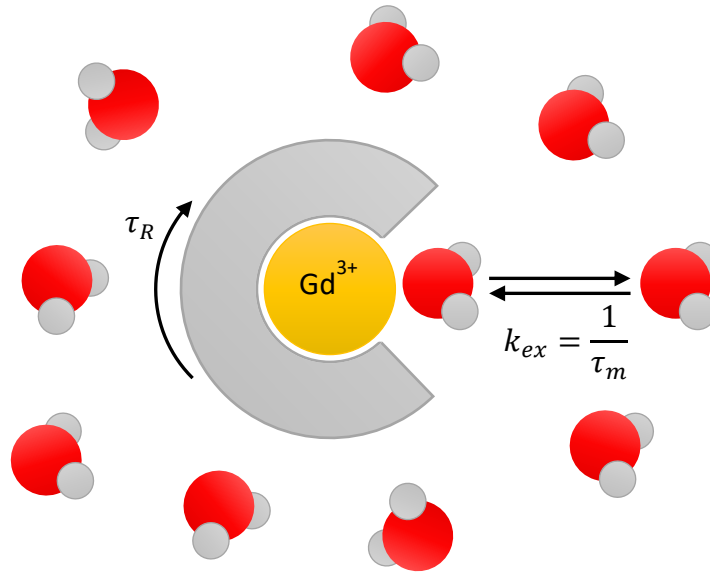


Figure 1.21 Gd-based contrast agent with a bound water molecule surrounded by bulk water. τ_R stands for rotational correlation time of the contrast agent and k_{ex} is the water exchange rate and τ_m is the lifetime of water molecule in the inner sphere

The development of high relaxivity contrast agents mainly involves improving the inner sphere contribution, as this contribution can be easily controlled and modified by careful design of contrast agent and will be discussed below.⁷⁵ Furthermore, outer sphere contribution can hardly be altered.⁷⁵ Hence, for new generation contrast agent, inner sphere contributes to 90% of the total relaxivity.⁷⁵

The inner sphere relaxation rate is defined with the following Eq. 1.9:

$$\left(\frac{1}{T_1}\right)^{IS} = \frac{[Gd]q}{55.5} \frac{1}{T_{1M} + \tau_m} \quad \text{Eq. 1.9}$$

where q is the hydration number, $1/T_{1M}$ is the T_1 relaxation rate of inner sphere water, and τ_m is the lifetime of water molecule in the inner sphere (equal to the reciprocal of water exchange rate, $1/k_{ex}$).

Eq. 1.9 shows that inner sphere relaxation is dependent on several factors, including $1/T_{1M}$ and $1/\tau_m$. This means T_{1M} and τ_m need to be as small as possible to give a contrast agent with high relaxivity. For first generation contrast agent, $T_{1M} > \tau_m$ and T_{1M} is the limiting factor for the relaxivity of these contrast agents.⁷⁶ Eq. 1.10 shows that magnetic field dependent dipole-dipole and, T_1^{DD} , scalar or contact mechanisms, T_1^{SC} , contribute to T_{1M} . For T_1 relaxation, the scalar mechanism, T_1^{SC} represents a small negligible contribution and will not be described.⁷⁵⁻⁷⁷ T_1^{DD} is governed by several factors and is given in Eq. 1.11 below:

$$\frac{1}{T_{1M}} = \frac{1}{T_1^{DD}} + \frac{1}{T_1^{SC}} \quad \text{Eq. 1.10}$$

$$\frac{1}{T_1^{DD}} = \frac{2}{15} \frac{\gamma_H^2 g_e^2 \mu_B^2}{r_{GdH}^6} S(S+1) \left(\frac{\mu_0}{4\pi}\right)^2 \left[7 \frac{\tau_{c2}}{1 + \omega_e^2 \tau_{c2}^2} + 3 \frac{\tau_{c1}}{1 + \omega_H^2 \tau_{c1}^2} \right] \quad \text{Eq. 1.11}$$

where γ_H is the gyromagnetic ratio of proton, g_e is the electron g factor, μ_B is the Bohr magneton, r_{GdH} is the electron spin (Gd^{3+} metal ion) – proton distance, S is the spin quantum number, μ_0 is the vacuum permittivity, ω_e and ω_H are electron and proton Larmor frequencies, respectively, and τ_{c1} and τ_{c2} are correlation times. The correlation times can be described with Eq. 1.12 below:

$$\frac{1}{\tau_{ci}} = \frac{1}{\tau_m} + \frac{1}{\tau_R} + \frac{1}{T_{ie}} \quad i = 1,2 \quad \text{Eq. 1.12}$$

where τ_R is the rotational correlation time and T_{1e} and T_{2e} are $T1$ and $T2$ electron spin relaxation times of the Gd^{3+} metal ion.

The electron spin relaxation rate has been described in literature.⁷⁸ The combination of these equations is often referred to as the Solomon-Bloembergen-Morgan (SBM) theory which is also discussed in detail in literature.⁷⁹

As seen above, several parameters can affect the inner sphere relaxivity, and ultimately the relaxivity of a contrast agent. Hence, optimisation and improving the relaxivity of a contrast agent can be achieved by decreasing the lifetime of inner sphere water, increasing hydration state, decreasing Gd^{3+} - proton distance, increasing the electron spin relaxation time, and decreasing the rotational correlation time. These strategies to improve MRI contrast agent have been described in literature.⁷⁶

1.3.3 Positron emission tomography imaging

Positron emission tomography (PET) is a powerful diagnostic imaging technique, and has naturally lent itself to being one of the dominant imaging methods in medicine.⁸⁰ One of the advantages of PET is its high sensitivity, hence, only a small dose of radiotracer is required for imaging; a typical ^{18}F -fluorodeoxyglucose (^{18}F -FDG) dose of 370-740 MBq is administered for clinical imaging, which correspond to 6 pmol of radiotracer.^{81,82}

Some positron emitting isotopes are ^{11}C , ^{13}N , ^{15}O , ^{18}F , ^{44}Sc , ^{64}Cu , ^{68}Ga , and ^{89}Zr , with ^{18}F being most widely employed in the form of clinically approved ^{18}F -FDG, which is routinely used in cancer imaging.^{80,83} However, PET imaging provides little or no anatomical imaging and has to be used in conjunction with X-ray computed tomography (CT), to form a hybrid imaging technique known as PET/CT.

PET is non-invasive and is capable of imaging deep tissues. In the case of photodynamic treatment, PET has been demonstrated to be capable of monitoring changes in tumour metabolism, allowing the visualisation of treatment dynamics of PDT in tumour cells in real-time.^{84,85}

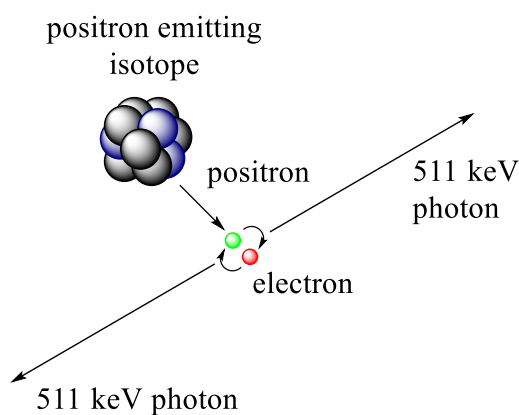


Figure 1.22 Schematic of the radioactive decay of a positron emitting isotope followed by the annihilation of positron and electron to produce gamma rays

The principle behind PET is that when a positron emitting radiotracer is administered to a patient, an ideal PET radiotracer will selectively accumulate in the diseased tissue, or the tissue of interest. The PET radiotracer undergoes radioactive decay to produce a positron. Upon collision between the positron and a nearby electron, they will annihilate each other releasing energy in the form of gamma rays, specifically, two gamma rays with an energy of 511 keV traveling 180° coincidence to each other (Figure 1.22). The two emitted photons are subsequently detected simultaneously, allowing the reconstruction of the “line-of-coincidence”, and the approximate position of the radiotracer can be determined.⁸⁰

1.3.3.1 ^{68}Ga

The ^{68}Ga radionuclide has been studied extensively as a promising PET radiotracer. It has a half-life of 68 minutes, well suited to imaging a range of biochemical processes, and has an 89% radioactive decay to positron and 11% *via* electron capture.⁸⁶ There is significant refreshed interest in the potential of ^{68}Ga with the introduction of the modern $^{68}\text{Ge}/^{68}\text{Ga}$ radionuclide generator developed by radiochemists in Obninsk, Russia (Cyclotron Co., Ltd).⁸⁷

The parent nuclide, ^{68}Ge , has a half-life of 270.95 days, and is generated in a cyclotron from gallium metal targets,⁸⁸ this allows for the production of long-lived generators (Figure 1.23). ^{68}Ge will undergo radioactive decay *via* electron capture to produce the radioactive daughter nuclei, ^{68}Ga . Combined with an efficient ion exchange chromatography column, in which the parent nuclei are held stationary and the soluble daughter nuclei are eluted off, an efficient $^{68}\text{Ge}/^{68}\text{Ga}$ radionuclide generator can be produced.⁸⁹

^{66}Zn 27.7%	^{67}Ga $T_{1/2} = 78 \text{ h}$	^{68}Ge $T_{1/2} = 270.9 \text{ d}$
^{67}Zn 4.0%	^{68}Ga $T_{1/2} = 68 \text{ min}$	
^{68}Zn 18.5%	^{69}Ga 60.1%	

p, 2n

Figure 1.23 Production of ^{68}Ge from ^{69}Ga shown in dashed arrow. The decay of ^{68}Ge to ^{68}Ga and to ^{68}Zn is shown in solid arrows.^{89,90}

Gallium is the third element (4th period) in group 13 of the Periodic Table. Its only stable oxidation state in water is +3, where the hydrated gallium 3+ ($\text{Ga}(\text{H}_2\text{O})_6^{3+}$) is only stable in strong acidic conditions. Upon neutralisation to a pH range of 3-7, it will hydrolyse to form $\text{Ga}(\text{OH})_3$ which is insoluble if the concentration exceeds the nanomolar level. While at physiological pH, gallium exists predominantly as a soluble species, $(\text{Ga}(\text{OH})_4)^-$.^{89,91}

Ga^{3+} is a hard acid metal, it will better accept hard donor ligands such as carboxylic acids, amines phosphonates, and hydroxamates.⁸⁹ Furthermore, Ga^{3+} is very similar to high spin Fe^{3+} , they have the same +3 ionic charge, similar ionic radii (62 pm for Ga^{3+} and 65 pm for Fe^{3+}), and also has the same coordination number of 6. Hence, ^{68}Ga radiopharmaceuticals need to be thermodynamically stable towards hydrolysis in physiological conditions to prevent ligand exchange, in which Ga^{3+} binds with transferrin, a blood serum protein that naturally binds Fe^{3+} .⁹² Another desirable property is that chelators should be stable in the presence of other serum cations such as Zn^{2+} , Ca^{2+} , and Mg^{2+} .

1.3.3.2 ^{68}Ga chelators

The most widely used gallium chelator is the cyclic 1,4,7,10-tetraazacyclododecane-1,4,7,10-tetraacetic acid (DOTA, Figure 1.26). DOTA has been used extensively in the radiolabelling of ^{68}Ga ; one of the most successful examples being ^{68}Ga -DOTATATE (Figure 1.24), in which DOTA is conjugated to a somatostatin derivative (Tyr³-octreotate) for the monitoring and imaging of neuroendocrine tumours (NETs). ^{68}Ga -DOTATATE has been proven to show higher lesion uptake,⁹³ and also higher *in vivo* distribution ratios of tumour to healthy tissues (Figure 1.24 and Figure 1.25).⁹⁴ These findings led to extensive clinical trials of ^{68}Ga -DOTATATE and the recent approval, 1st June 2016, by the FDA.⁹⁵

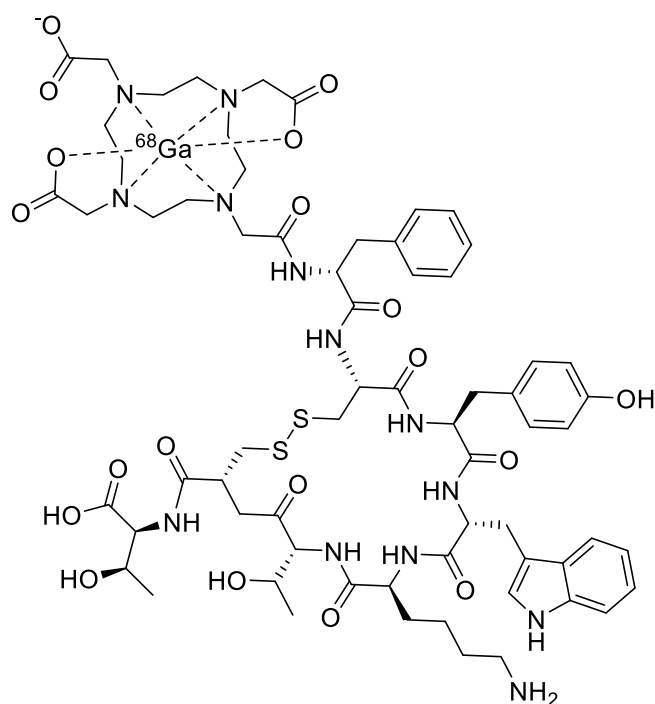


Figure 1.24 Structure of ^{68}Ga -DOTATATE, which was approved by FDA in July 2016.⁹⁵

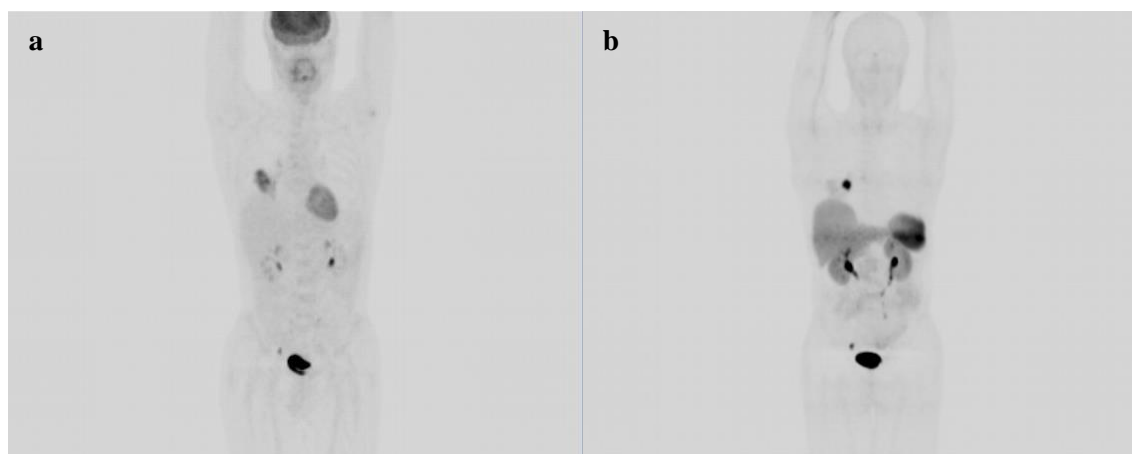


Figure 1.25 PET maximum-intensity-projection images of 60 years old patient with typical endobronchial carcinoid. (a) PET imaging with ^{18}F -FDG, (b) PET imaging with ^{68}Ga -DOTATATE, in which ^{68}Ga -DOTATATE showed higher accumulation in tumour. Image taken from *J. Nucl. Med.*, 2009, **50**, 1927–1932.⁹⁶

Another commonly used cyclic gallium chelator is 1,4,7-triazacyclononane-1,4,7-triacetic acid (NOTA, Figure 1.26), which possesses greater binding affinity for ^{68}Ga compared to DOTA and higher stability ($\log K_{\text{Ga-NOTA}} = 31.0$ and $\log K_{\text{Ga-NOTA}} = 26.1$).^{81,97} A commonly used NOTA derivative is NODAGA (Figure 1.26), which possesses an extra appended carboxylic arm for conjugation to other molecules. Similar to ^{68}Ga -DOTATATE, NODAGA has been conjugated to somatostatin agonist Tyr³-octreotate.⁹⁸ Another NOTA derivative, which involves replacing carboxylic groups with phosphonate and phosphinic acids, is known as TRAP (Figure 1.26), and has been shown to have a higher stability compared to NOTA ($\log K_{\text{Ga-TRAP}} = 35$).^{81,99,100}

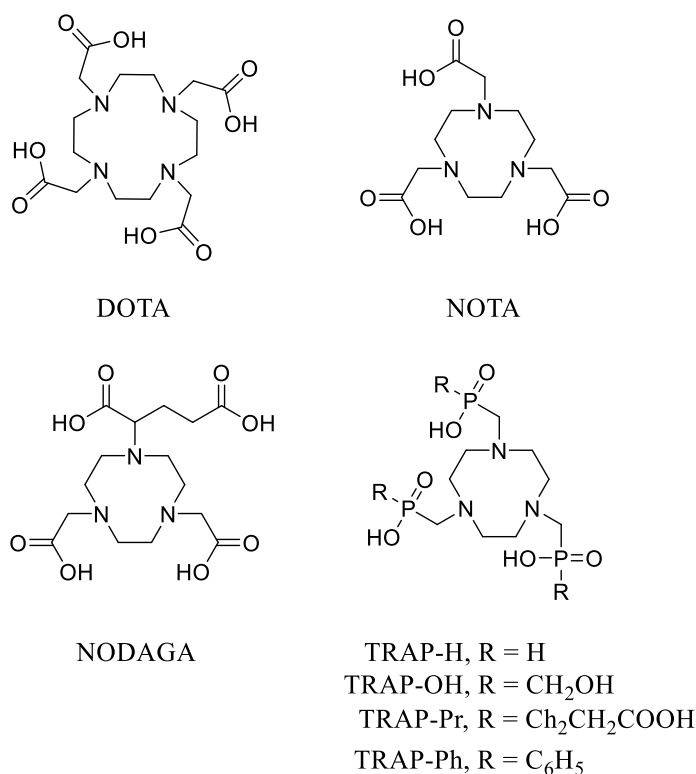


Figure 1.26 Some macrocyclic chelators for ⁶⁸Ga.

However, these macrocyclic chelators require harsh conditions for radiolabelling with ⁶⁸Ga, which involves heating to over 80 °C (required for DOTA) and acidic conditions (required for DOTA, NOTA, and TRAP).⁸¹ Hence, recent research on ⁶⁸Ga chelators features acyclic chelators, capable of rapid radiolabelling with ⁶⁸Ga under mild conditions – room temperature at neutral pH and at low chelator concentrations.

N,N'-bis(2-hydroxybenzyl)ethylenediamine-*N,N'*-diacetic acid (HBED) shows good stability with $\log K_{Ga-HBED} = 37.7$ (Figure 1.27).¹⁰¹ A derivative of HBED, HBED-CC which possesses two appended carboxylic acid moieties for further conjugation has been reported by Eder *et al.*¹⁰² The conjugation of dipeptide, a prostate-specific membrane antigen (PSMA) inhibitor, onto HBED-CC have been reported¹⁰³ and have undergone extensive clinical studies.¹⁰⁴ Radiolabelling of HBED-CC-PSMA was shown to be able to achieve 99% radiochemical yield (RCY) in 1 min at room temperature, however, at an acidic pH of 4.2.¹⁰³

chelators are capable of chelating ^{68}Ga at a pH range of 4-7; at pH 6.8, these chelator are capable of achieving a RCY of >97% in 3 minutes. Stability of these radiolabelled complexes with the exception of DATA^M were tested and showed stability in diethylenetriaminepentaacetic acid, Fe^{3+} , apotransferrin, and foetal calf serum, over a two-hour period.

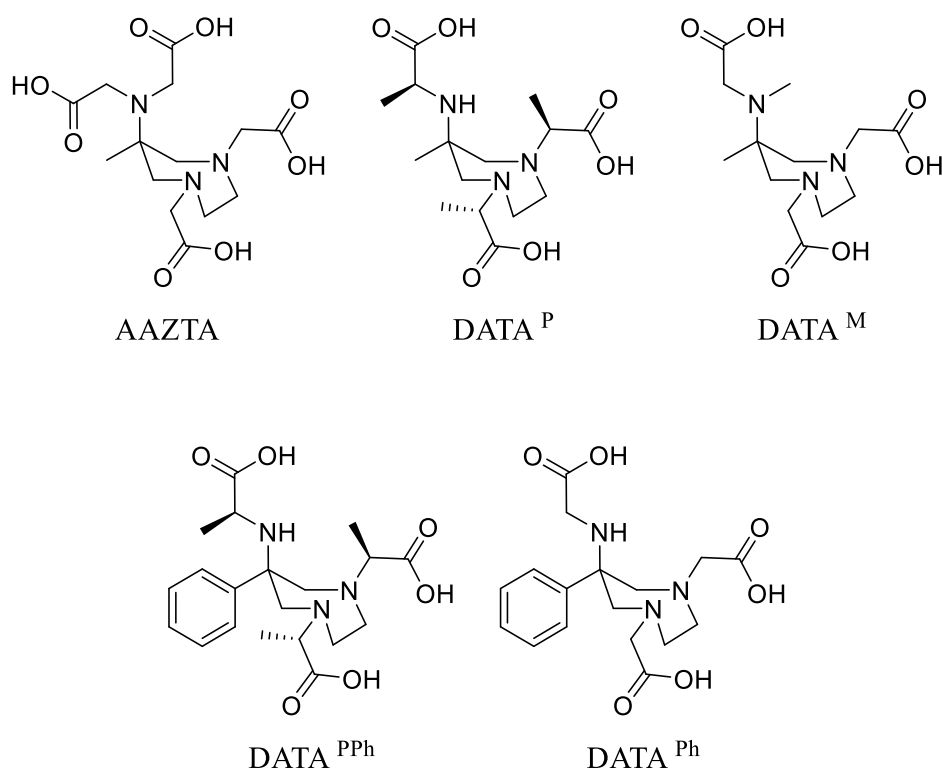


Figure 1.29 Structure of AAZTA and derivatives reported by Waldron *et al.*^{108,109}

Philip Blower's research group have reported the use of tris(hydroxypyridinone) chelator (CP-256, Figure 1.30) which is capable of achieving >95% RCY at pH ~6.5 for 2-5 minutes.¹¹¹ The ^{68}Ga -CP256 shows no evidence of protein binding or ^{68}Ga dissociation when incubated with human serum for up to four hours. The excellent radiolabelling kinetics prompted the conjugation to biomolecules. A maleimide derivative of CP256 was conjugated to protein C2Ac, showed retention of calcium-dependent binding to phosphatidylserine *in vitro*. *In vivo* studies showed the stability of the complex.¹¹¹ Two isothiocyanate derivative of CP256 were also conjugated to c(RGDfk), and *in vivo* studies carried out. Both CP256-c(RGDfk) conjugates showed *in vivo* stability and a tumour to background concentration ratio of 2.76 ± 0.18 .¹¹²

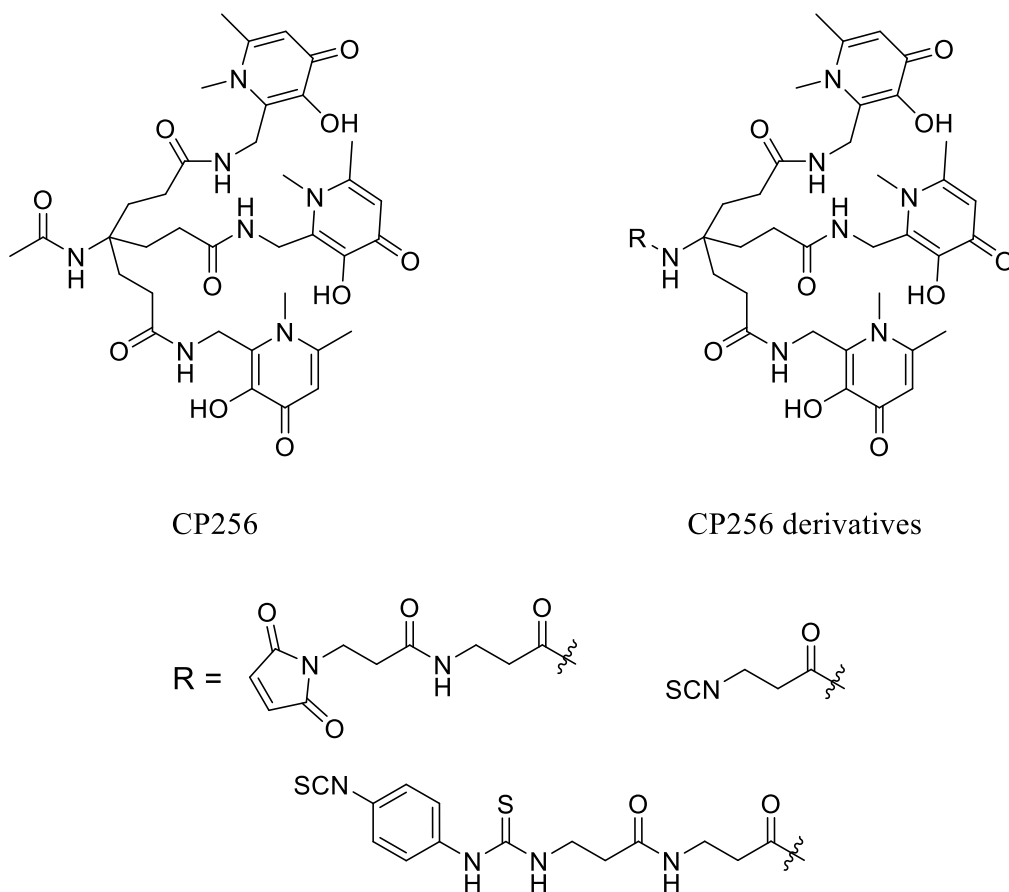


Figure 1.30 Structure of CP256 and its derivatives.^{111,112}

An example of ^{68}Ga radiolabelling above pH 7 was reported by Price *et al.*; an amino-acid based acyclic chelator (H_3Dpaa , Figure 1.31) for the mild radiolabelling of ^{68}Ga is described. H_3Dpaa is capable of ^{68}Ga radiolabelling at pH 7.4 at 37 °C with near quantitative RCY in 5 minutes. Bifunctional derivative of Dpaa were also described, conjugatable amine ($\text{H}_3\text{Dpaa.dab}$) and carboxylic acid ($\text{H}_4\text{Dpaa.ga}$) moiety were introduced onto Dpaa. $\text{H}_3\text{Dpaa.dab}$ and $\text{H}_4\text{Dpaa.ga}$ showed RCY of 84% and 94%, respectively under similar radiolabelling conditions.¹¹³

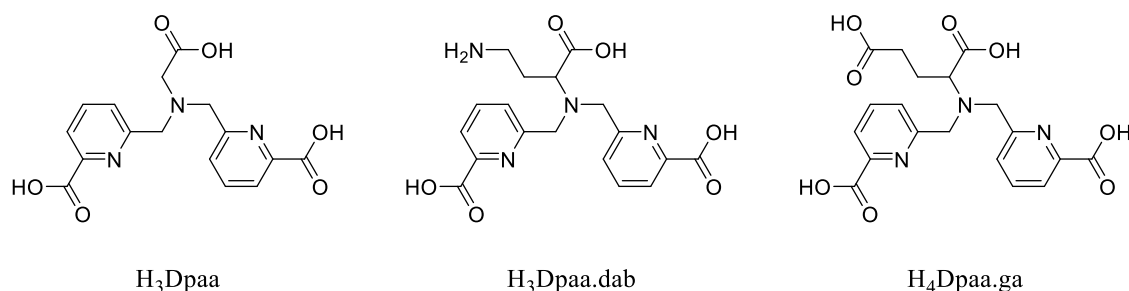


Figure 1.31 Structure of H_3Dpaa and its derivatives, $\text{H}_3\text{Dpaa.dab}$ and $\text{H}_4\text{Dpaa.ga}$.¹¹³

1.3.4 Single-photon emission computed tomography imaging

Similar to PET, single-photon emission computed tomography (SPECT) is a highly sensitive imaging technique (however, it is a few orders of magnitude less sensitive than PET)¹¹⁴ that requires the administration of a gamma emitting radioisotope. SPECT imaging relies on the

radiotracer to biodistribute/accumulate in the body. Images are then obtained using a gamma camera and computed to provide a 3D distribution of the radiotracer in the body. Similar to PET imaging, SPECT imaging does not provide any anatomical imaging and is used along with CT.

SPECT radioisotopes are usually heavy isotopes in comparison to PET, this includes ^{111}In , $^{99\text{m}}\text{Tc}$, ^{123}I , and ^{131}I . Ideally, these radioisotopes need to emit gamma radiation at the range of 100-250 keV and can only have one gamma radiation, for instance, ^{123}I and $^{99\text{m}}\text{Tc}$ only emits photons at 159 keV and 140 keV, respectively. A wide range of SPECT tracers have been developed, most notably with $^{99\text{m}}\text{Tc}$, which $^{99\text{m}}\text{Tc}$ itself has more than 15 Food and Drug Administration (FDA) approval radiopharmaceuticals.¹¹⁵ Very similar to ^{68}Ga , the generation of $^{99\text{m}}\text{Tc}$ can be achieved from a $^{99}\text{Mo}/^{99\text{m}}\text{Tc}$ generator, with saline as the eluent. Its well-established chemistry, availability from a $^{99}\text{Mo}/^{99\text{m}}\text{Tc}$ generator, and its relative low cost, made it one of the most used radioisotopes in diagnostic nuclear medicine.

1.3.4.1 $^{99\text{m}}\text{Tc}$

$^{99\text{m}}\text{Tc}$ is a SPECT imaging isotope and is currently the most used diagnostic nuclear medicine. It has a half-life of six hours, and a gamma radiation at 141 keV with virtually no α or β - emissions, with only low energy Auger electron.¹¹⁶ Its convenient half-life is enough to enable various radiopharmaceutical chemistry to be carried out prior to medical imaging and also short enough to minimise the amount of radiation dose delivered to patients.

$^{99\text{m}}\text{Tc}$ is also the first element to be produced artificially by Perrier and Segre in 1937 in Berkeley cyclotron *via* bombardment of molybdenum metal target with deuterons.^{117,118} Currently, generation of $^{99\text{m}}\text{Tc}$ is carried out using $^{99}\text{Mo}/^{99\text{m}}\text{Tc}$ generator, first developed in Brookhaven in the early 1960s.¹¹⁷ This is also one of the few reasons behind the success and continued usage of $^{99\text{m}}\text{Tc}$ in medical imaging as the inexpensive generator can be easily made available to many hospitals.

^{99}Mo , in the form of $^{99}\text{MoO}_4^{2-}$, is produced as a fission product of ^{235}U , which is subsequently extracted and adsorbed onto surface of alumina particles for the production of $^{99}\text{Mo}/^{99\text{m}}\text{Tc}$ generator.¹¹⁹ It has a half-life of 66 hours and will undergo β - decay to give 88.75% $^{99\text{m}}\text{TcO}_4^-$ (Figure 1.32). $^{99\text{m}}\text{TcO}_4^-$ can be eluted off the generator with saline solution (0.15 M NaCl) to give a concentration of $^{99\text{m}}\text{TcO}_4^-$ in the range of 10^{-8} to 10^{-6} M.¹¹⁸ Subsequent decay of $^{99\text{m}}\text{Tc}$ will give the relatively safe, minor hazard, long-lived β - emitting daughter nuclei, $^{99}\text{TcO}_4^-$.

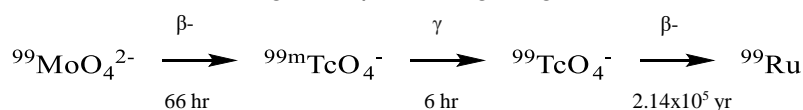


Figure 1.32 Radioactive decay scheme of ^{99}Mo to generate $^{99\text{m}}\text{Tc}$ and the subsequent decay to $^{99\text{m}}\text{Tc}$ and ^{99}Ru .

Technetium is positioned in the middle of the second row of transition metals. It can have oxidation states ranging from +1 to +7 and depending on the oxidation state, a coordination

number of 4 to 9.¹¹⁶ This allows a variety of ligands to chelate and conjugate to technetium and can be tailored to allow specificity and selectivity to image a variety of diseased tissues of interest.

1.3.4.2 ^{99m}Tc radiotracers

^{99m}Tc have been used for several decades and various kits have been developed for safe usage of ^{99m}Tc in routine operations. Kits are sterile and pyrogen-free reagents, lyophilised and stored under inert atmosphere.¹²⁰ For the case of ^{99m}Tc kits, this usually includes a reducing agent, for example, tin (II) and a chelating agent.

Hexamethyl propyleneamine oxime (HMPAO) is the first FDA-approved ^{99m}Tc brain perfusion imaging agent (Figure 1.33).¹²¹ 8 hours post administration of this ^{99m}Tc-HMPAO (Figure 1.33) complex shows accumulation of 3.4 – 5.7% of the injected activity in human brain.¹²² Reduction of ^{99m}TcO₄⁻ with tin (II) in the presence of HMPAO ligand will generate the desired complex which is used within 30-45 minutes of preparation to prevent degradation.^{120,123} ^{99m}Tc-HMPAO was also shown to be taken up by white blood cells – leucocytes, lymphocytes, and macrophages, hence it is also used for imaging infection and inflammation.¹²³

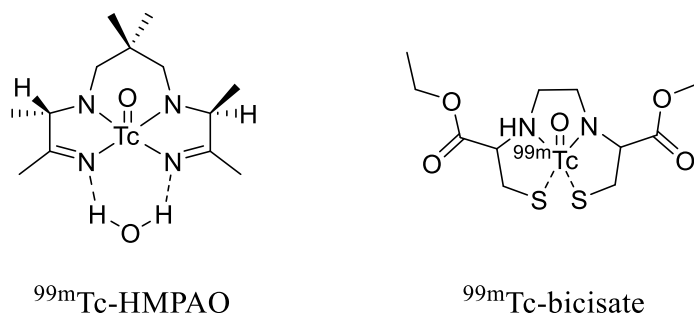


Figure 1.33 FDA-approved brain perfusion agent, ^{99m}Tc-HMPAO and ^{99m}Tc-bicisate.

Another FDA approved brain perfusion agent is ^{99m}Tc-bicisate (Figure 1.33). ^{99m}Tc-bicisate is a lipophilic molecule that is capable of diffusing through the blood-brain barrier *via* passive diffusion, it is subsequently hydrolyse by enzymes to form the more polar monoester-monocarboxylic acid metabolite which retains in the brain.¹²⁴ It is used in the assessment of neurological disease, such as stroke. Both ^{99m}Tc-HMPAO and ^{99m}Tc-bicisate are used to diagnose a wide range of brain disease such as epilepsy, strokes, to Parkinson's disease.^{122,125-127} They

provide images of cerebral blood flow; for example, Figure 1.34 shows deficient blood flow of a stroke patient with depleted blood flow in the top left area of the brain.¹¹⁷

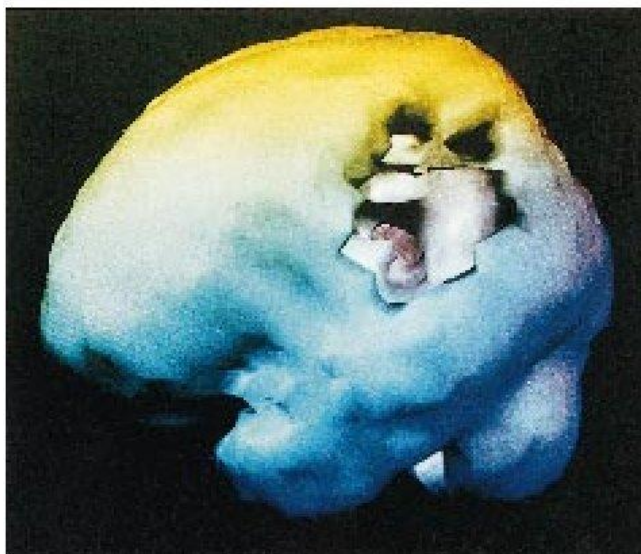


Figure 1.34 SPECT image of a patient with stroke in the top left area of the brain. Image obtained from *Chem. Soc. Rev.*, 1998, **27**, 43.¹¹⁷

^{99m}Tc are also used routinely as a myocardial perfusion agent for heart imaging. ^{99m}Tc-sestamibi and ^{99m}Tc-tetrofosmin are FDA-approved radiotracers for heart imaging. Both of this radiotracer are cationic and lipophilic (Figure 1.35). These charged complex accumulates in heart tissues *via* Na/K ATPase mechanism as a K⁺ mimics.¹¹⁷

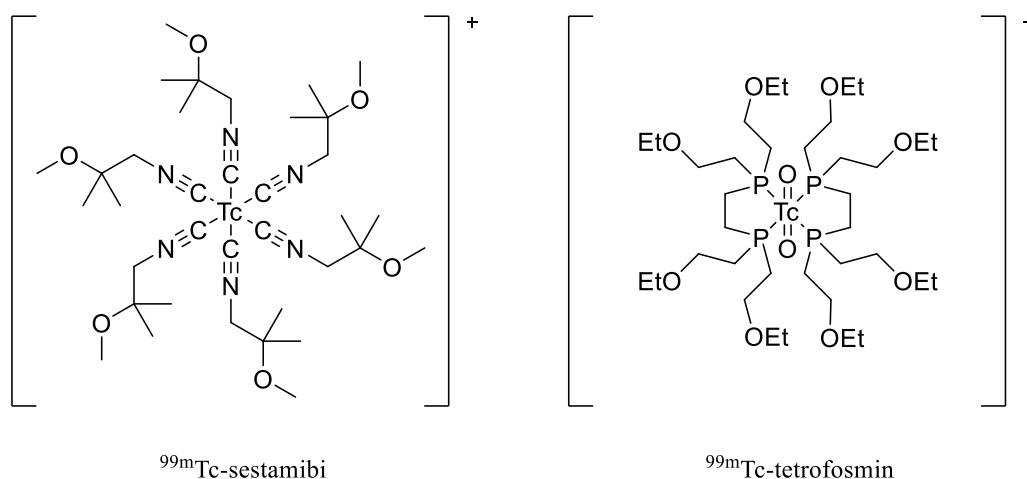


Figure 1.35 FDA-approved myocardial agent, ^{99m}Tc-sestamibi and ^{99m}Tc-tetrofosmin.

^{99m}Tc-sestamibi was first described by Jones *et al.*. *In vivo* animal studies showed promising results led to clinical trials and the subsequent FDA-approval of this radiotracer. Monodentate methoxyisobutylisonitrile (MIBI) is volatile and unstable however, is made available in the form of copper tetrafluoroborate adduct, [Cu(MIBI)₄]BF₄ for technetium labelling. Labelling of technetium with MIBI is achieved by reducing technetium from oxidation state of +7 to +1 and chelation in the presences of [Cu(MIBI)₄]BF₄ at elevated temperature for 10 minutes to form

^{99m}Tc -sestamibi.^{123,128–130} This complex is taken up by myocardium cells, tumours, and metastases, and is used to image blood perfusion, myocardial infarction, and coronary arteries.^{120,123}

Kelly *et al.* described the use of ^{99m}Tc -tetrofosmin.¹³¹ Radiolabelling of ^{99m}Tc -tetrofosmin was carried out in the presence of reducing agent SnCl_2 and diphosphine ligands (1,2-bis[bis-(2-ethoxyethyl)phosphino]ethane). ^{99m}Tc -tetrofosmin has shown good heart uptake with good retention.¹³² The presence of the alkoxy group on the bidentate phosphine ligands enable rapid clearance of the radiotracer from liver, lungs, and blood, reducing background radiation.¹¹⁷

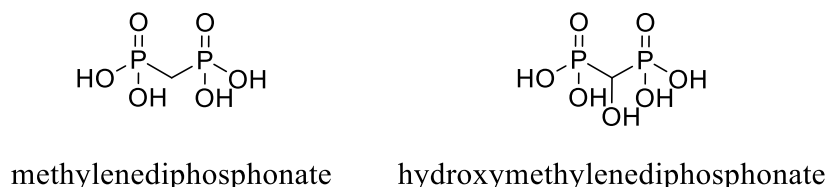


Figure 1.36 FDA-approved phosphonate ligands for ^{99m}Tc complexation for bone imaging.

Phosphonate ligands has also been employed to form ^{99m}Tc complexes for bone imaging. Figure 1.36 shows two FDA-approved bone imaging phosphonate ligands, methylenediphosphonate and hydroxymethylenediphosphonate, which complex ^{99m}Tc to form ^{99m}Tc -medronate and ^{99m}Tc -oxidronate, respectively. The free phosphoryl oxygen on these phosphonate ligands binds with Ca^{2+} on bone surfaces, allowing accumulation of these radiotracers in bone, especially at sites with high Ca^{2+} concentration. One of the main use of bone imaging is for cancer patients to identify and/or diagnose metastasis into bone.^{117,132}

A recently FDA-approved ^{99m}Tc -tilmanocept, is an example of targeted delivery of ^{99m}Tc radiopharmaceutical (Figure 1.37). ^{99m}Tc -tilmanocept was first described by Vera *et al.* and has undergone extensive clinical trials.¹³³ The molecule has a dextran backbone functionalised with a targeting moiety, mannose, and a ^{99m}Tc chelator, diethylenetriamine-pentaacetic acid (DTPA). ^{99m}Tc -tilmanocept accumulates in lymphatic tissues by binding to a macrophage-specific receptor. It has shown high specificity and retention towards lymph nodes and fast clearance from site of administration.¹³⁴ Its main use is for lymphatic mapping in patients with breast cancer or melanoma.^{134,135}

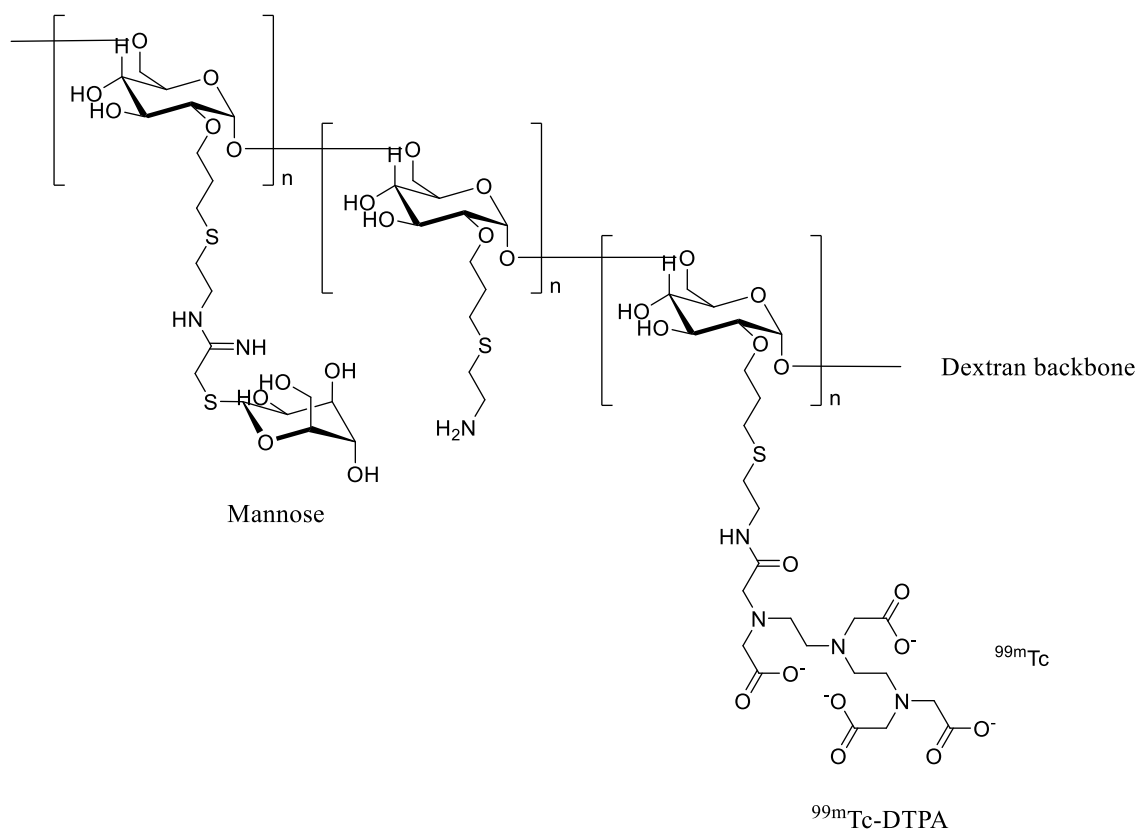


Figure 1.37 Structure of FDA-approved ^{99m}Tc -tilmanocept.

1.4 Theranostic

As mentioned earlier, the development of fourth-generation photosensitisers involved the incorporation of a diagnostic modality along with therapeutic photosensitisers. This combination of diagnostic and therapeutic modalities into a single entity is known as theranostic.

The novelty of this idea is that a single multimodal compound can contain diagnostic and therapeutic capabilities; functionality can be “switched” between diagnostic and therapeutic, facilitating detection and treatment of disease and reducing the number of drugs administered to the patient. Theranostic photosensitisers can therefore allow the careful monitoring of the degree of accumulation of photosensitiser, improving treatment outcomes by irradiation when photosensitiser levels are maximal. Subsequently, theranostic photosensitisers can also allow post-treatment imaging to evaluate treatment outcome.^{3,136}

In this subchapter, the combination of some relevant imaging techniques onto porphyrins are described. This includes the combination of a Gd-based MRI contrast agent with porphyrins, ^{68}Ga as a PET radiotracer with porphyrins, and ^{99m}Tc as a SPECT radiotracer with porphyrins.

1.4.1 Gd-based MRI/PDT theranostic porphyrin

Porphyrins are known to chelate a host of metals, which also includes gadolinium. This enables porphyrins to form Gd^{3+} complexes as MRI contrast agents. Lyon *et al.* and Furmanski *et al.* have

both reported the use of water-soluble (cationic and anionic) porphyrin Gd^{3+} complexes as MRI contrast agents, however, have both shown dissociation of Gd^{3+} within biological media.^{137,138}

Patented gadolinium mesoporphyrin (Gd-MP) is one of the earliest examples of combining Gd with a porphyrin. Two DTPA was covalently conjugated onto mesoporphyrin, allowing the complexation of two Gd^{3+} (Figure 1.38) to form Gd-MP. Gd-MP originally designed for tumour imaging when tested *in vivo* in rats showed no tumour specificity, however it showed affinity towards nonviable components such as, necrosis, thrombosis, and cystic secretion.¹³⁹ Further studies utilises Gd-MP for *in vivo* tracking of hematopoietic cells which are used in bone marrow transplantation to treat certain diseases, such as, leukemia, lymphomas, and metastasized carcinomas.¹⁴⁰ However, to date, PDT evaluation has never been carried out.

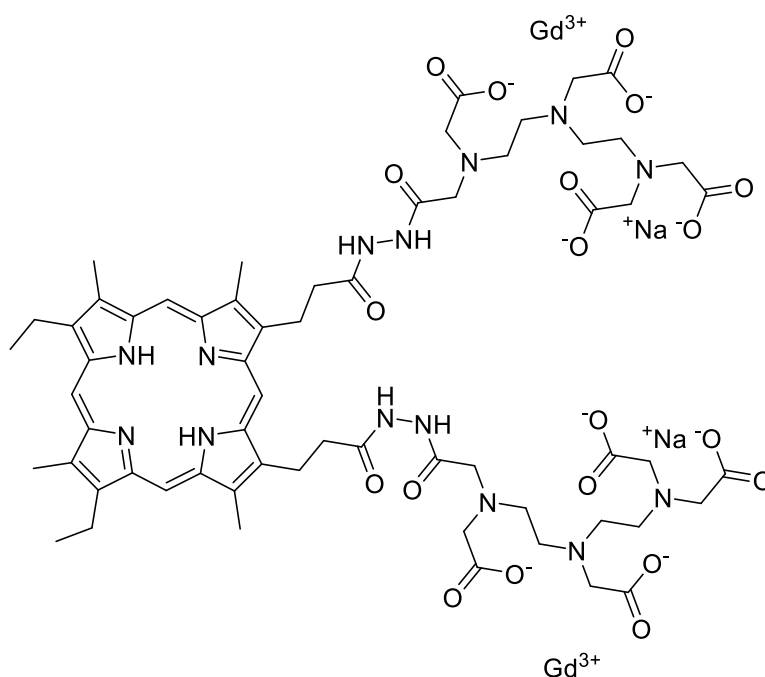


Figure 1.38 Structure of patented gadolinium mesoporphyrin (Gd-MP).

An example showing the combined use of PDT and MRI was first reported by Hindre *et al.*. Two porphyrin derivatives were described; $\text{Gd}_2(\text{DTPA})_4\text{TPP}$ contains four DTPA complexed with two Gd^{3+} , and $\text{Gd}(\text{DTPA})\text{TPyP}$ is a tricationic porphyrin with one DTPA complexed with one Gd^{3+} (Figure 1.39). *T1* measurements on $\text{Gd}_2(\text{DTPA})_4\text{TPP}$ and $\text{Gd}(\text{DTPA})\text{TPyP}$ showed both derivatives outperform Magnevist (Gd-DTPA) with a relaxivity of $14.8 \text{ mM}^{-1} \text{ s}^{-1}$ and $11.67 \text{ mM}^{-1} \text{ s}^{-1}$ at 20 MHz, respectively. *In vitro* toxicity showed both porphyrin derivatives induced less cell death in the dark when compared to HpD in HT-29 and L1210 cells. Phototoxicity was carried out with an argon laser at 25 J cm^{-1} , showed both compounds have a LD50 of 0.1 and $1 \mu\text{g mL}^{-1}$ for $\text{Gd}_2(\text{DTPA})_4\text{TPP}$ and $\text{Gd}(\text{DTPA})\text{TPyP}$, respectively in HT-29 cells and LD50 of $0.1 \mu\text{g mL}^{-1}$ for both porphyrin derivatives in L1210 cells.¹⁴¹

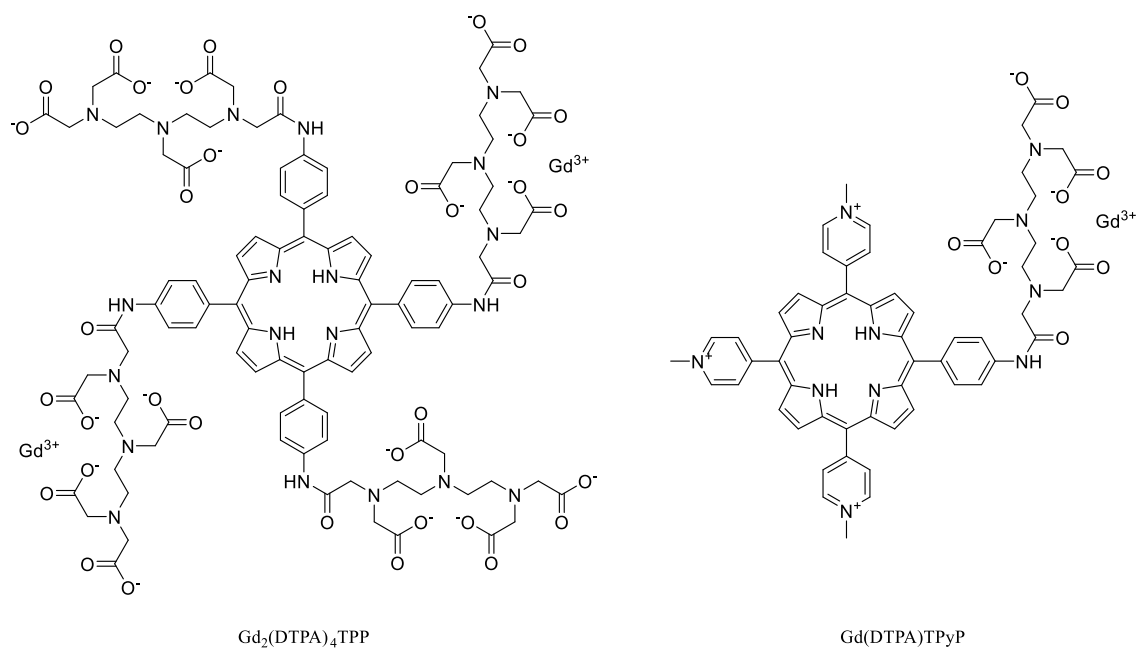


Figure 1.39 Sedstructure of Gd₂(DTPA)₄TPP and Gd(DTPA)TPyP.

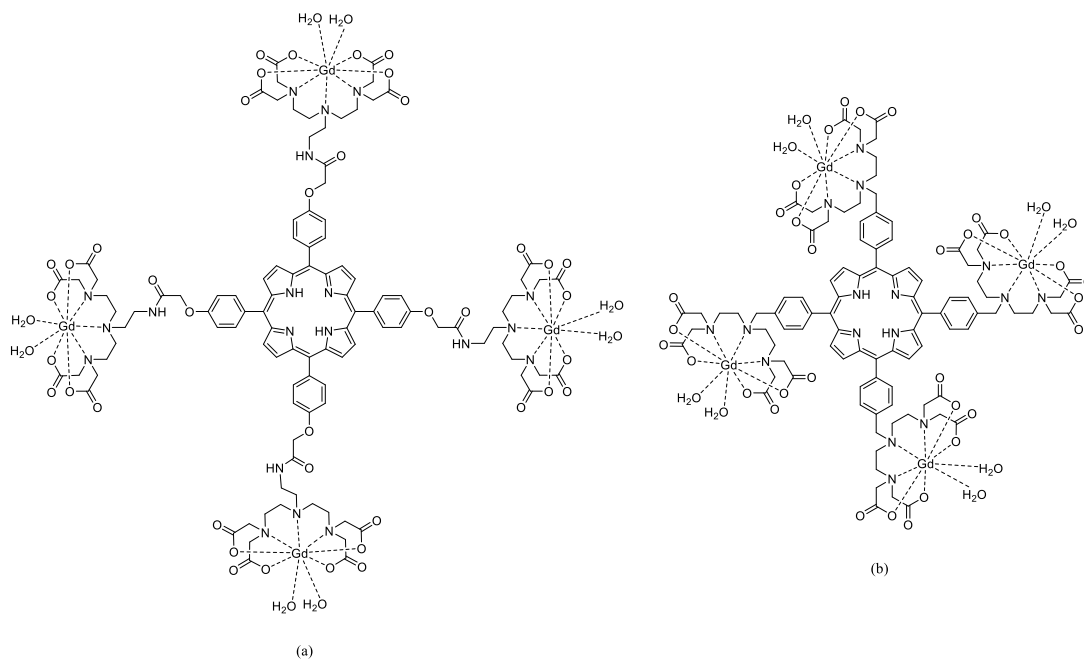


Figure 1.40 Tetrasubstituted DTTA porphyrin reported by Luo *et al.* (a) and Sour *et al.* (b).^{142,143}

Luo *et al.* reported a very similar porphyrin as Hindre *et al.*, where a porphyrin bearing four diethylenetriaminetetraacetic acid (DTTA) was synthesised and capable of forming a seven-coordinated Gd³⁺ complex (Figure 1.40). T1 measurements showed Gd₄(DTTA)₄TPP has a relaxivity of 14.1 mM⁻¹ s⁻¹ per Gd³⁺ in HEPES buffer at 23 MHz. Gd₄(DTTA)₄TPP was also shown to bind to human serum albumin, with a marked increase in relaxivity (29.2 mM⁻¹ s⁻¹) due to the association with a large molecular weight resulting in an increase in rotational correlation time, τ_R .¹⁴⁴ Gd₄(DTTA)₄TPP showed efficient singlet oxygen generation when irradiated with 650 nm light. Gd₄(DTTA)₄TPP is also capable of fluorescence imaging under the same 650 nm light irradiation and was shown to be internalised in the whole of HT29 cells.¹⁴²

Another tetrasubstituted DTTA porphyrin was reported by Sour *et al.* (Figure 1.40). The reported porphyrin-Gd³⁺ complex has a shorter and more rigid linker compared to Luo *et al.* and boasted a relaxivity of 48.59 mM⁻¹ s⁻¹ at 40 MHz. Proton nuclear magnetic relaxation dispersion (NMRD) profiles of the complex showed a characteristic of a slow tumbling molecule/structure, with an increase in relaxivity around 10-80 MHz.¹⁴⁵ Efficient singlet oxygen generation was successfully evaluated using a singlet oxygen sensor, anthracene-9,10-dipropionic acid (ADPA). This prompted the *in vitro* cytotoxicity studies. The complex showed an LD50 of 50 μM in the dark and achieved an LD50 of 6 μM with light irradiation at 8 mW cm⁻² at 636 nm.¹⁴³

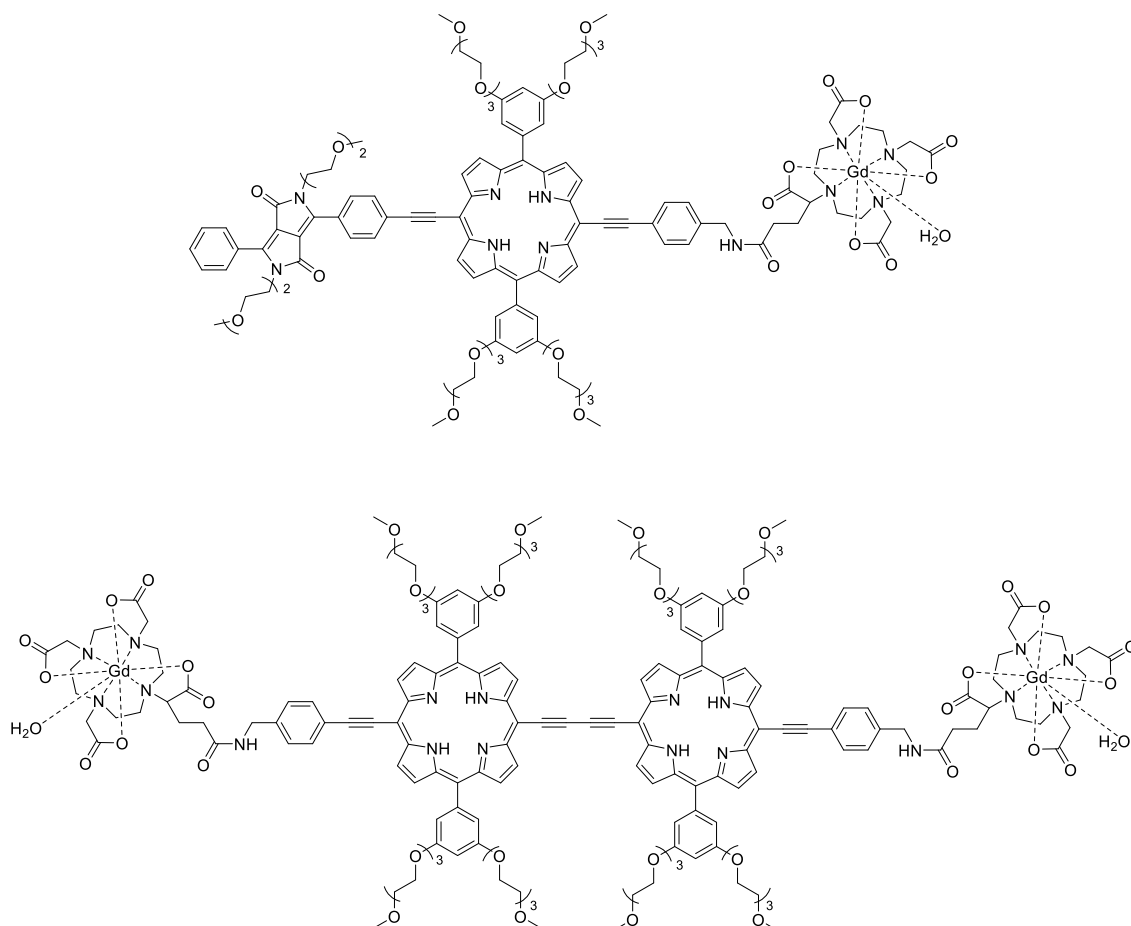


Figure 1.41 Porphyrin-DOTA conjugate reported by Schmitt *et al.*^{146,147}

Schmitt *et al.* reported the use of macrocyclic ligand, DOTA conjugated to porphyrin for Gd³⁺ complexation (Figure 1.41). One of the porphyrin conjugates described included diketopyrrolopyrrole–zinc(II) porphyrin as a one- and two-photon photosensitizer conjugated to one [Gd(DOTA)]⁻ as an MRI contrast agent. A high relaxivity of 19.91 mM⁻¹ s⁻¹ at 20 MHz was obtained for a relatively small molecule system (2.4 kDa) with one monohydrated Gd³⁺ complex. Singlet oxygen phosphorescence and singlet oxygen trap, diphenylisobenzofuran was used to detect singlet oxygen generation, which showed a singlet oxygen quantum yields, ϕ_{Δ} , of 0.24 and 0.68, respectively. The difference in ϕ_{Δ} is due to different measurement techniques carried out in

different solvent system. *In vitro* cytotoxicity showed LD50s of 10 μM in the dark and 1 μM when irradiated with 2.9 mW cm^{-2} of 660 nm light.¹⁴⁶

Schmitt *et al.* also reported a porphyrin dimer conjugated with two $[\text{Gd}(\text{DOTA})]^-$ (Figure 1.41); the porphyrin dimer was previously shown to be an efficient one- and two-photon photosensitiser.^{148,149} The complex showed a relaxivity of 14.41 $\text{mM}^{-1} \text{s}^{-1}$ at 40 MHz which increases to 29.7 $\text{mM}^{-1} \text{s}^{-1}$ in the presence of bovine serum albumin (BSA). A singlet oxygen quantum yield, ϕ_{Δ} of 0.36 was obtained in DMSO. *In vitro* cytotoxicity showed an LD50 of 12 μM in the dark and 1 μM when irradiated with 40 J cm^{-2} of 746 nm light.¹⁴⁷

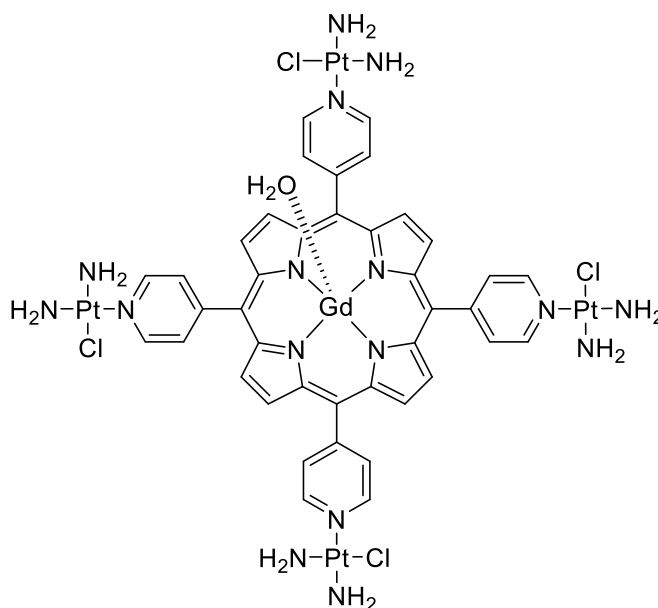


Figure 1.42 Platinated Gd^{3+} metalloporphyrin reported by Wu *et al.*¹⁵⁰

Wu *et al.* reported a trifunctional metalloporphyrin as an MRI-guided, chemo-, photodynamic therapy agent. Despite to the instability of Gd^{3+} metalloporphyrin as reported by Lyon *et al.* and Furmanski *et al.*,^{137,138} Wu *et al.* described a 5,10,15,20-tetra(4-pyridyl)porphyrin functionalised with cisplatin, as chemo-photodynamic therapy agent, and Gd^{3+} in the porphyrin core (Figure 1.42). The complex showed a relaxivity of 8.89 $\text{mM}^{-1} \text{s}^{-1}$ at 60 MHz, which is larger than the relaxivity of clinically used Magnevist at the same magnetic field ($r_1 = 5.4 \text{ mM}^{-1} \text{ s}^{-1}$).¹⁵¹ *In vitro* cytotoxicity showed minimal toxicity in the dark up to 1 μM and showed synergistic chemo-photodynamic activity when irradiated with 630 nm light at 120 J cm^{-1} , with an LD50 of <0.1 μM .¹⁵⁰

1.4.2 ^{68}Ga -based PET/PDT theranostic porphyrin

In the previous subchapter, some literature has shown the usage of the porphyrin core to complex Gd^{3+} , unsurprisingly, several examples have also shown ^{68}Ga complexation using the porphyrin core. However, complexation of ^{68}Ga within the porphyrin core often requires harsh conditions

such as the use of forcing microwave heating at temperature >100 °C. Nevertheless, there are several reports of the use of ^{68}Ga porphyrin as an imaging agent and theranostic agent.

Fazaeli *et al.* reported the use of 5,10,15,20-tetrakis(pentafluorophenyl)porphyrin (TFPP) to complex ^{68}Ga (Figure 1.43). Radiolabelling showed TFPP complexed ^{68}Ga at 100 °C for 60 mins in quantitative yield, showing the only example in literature for non-microwave mediated complexation of ^{68}Ga into the porphyrin core. Radiolabelled [$^{68}\text{Ga}(\text{TFPP})$] showed excellent serum stability with radiochemical purity of 99% up to 5 hours. Biodistribution and imaging studies was carried out in fibrosarcoma tumours bearing Swiss mice, which showed accumulation in tumour with a tumour-to-muscle ratio of 5.13.¹⁵²

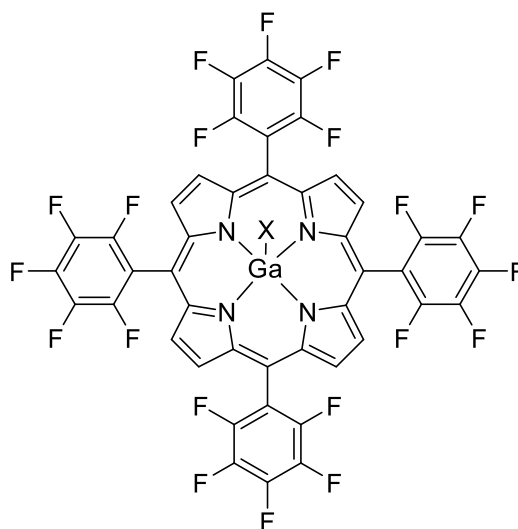


Figure 1.43 Structure of [$^{68}\text{Ga}(\text{TFPP})$], reported by Fazaeli *et al.*¹⁵²

Zoller *et al.* reported the radiolabelling and evaluation of five different porphyrins, which includes Hp, PPIX, tetraphenylporphyrin (TPP), and two other synthetic porphyrins, 3-(1-hydroxyheptyl)-deutero-porphyrin dimethylester (HHDPD) and [(2R)-2-methoxycarbonylmethyl)-3-oxo-2,7,12,18-tetramethyl-2,3-dihydro-21H,23H-dihydroporphyrinato-13,17-diyl]dipropionic acid dimethylester (MCOTMDHPD) (Figure 1.44). Hp and PPIX were radiolabelled under aqueous conditions, while water-insoluble TPP, HHDPD, and MCOTMDHPD were labelled under anhydrous organic conditions. With microwave heating at 170 °C, radiolabelling yield of 69%, 49%, 82%, 83%, and 42% were achieved for Hp, PPIX, TPP, HHDPD, and MCOTMDHPD, respectively. Purification *via* anion exchange cartridge yielded $>95\%$ purity for [$^{68}\text{Ga}(\text{Hp})$], [$^{68}\text{Ga}(\text{TPP})$], and [$^{68}\text{Ga}(\text{HHDPD})$]. [$^{68}\text{Ga}(\text{TPP})$], and [$^{68}\text{Ga}(\text{HHDPD})$] showed excellent serum stability up to 2 hours, however, [$^{68}\text{Ga}(\text{Hp})$] showed 50% dissociation of ^{68}Ga in 72 mins. Despite these results, the only *in vivo* biodistribution data was

reported for [$^{68}\text{Ga}(\text{Hp})$], showing 0.5% of the injected dose uptake in tumour and significant uptake in the kidneys due to renal clearance of [$^{68}\text{Ga}(\text{Hp})$].^{153,154}

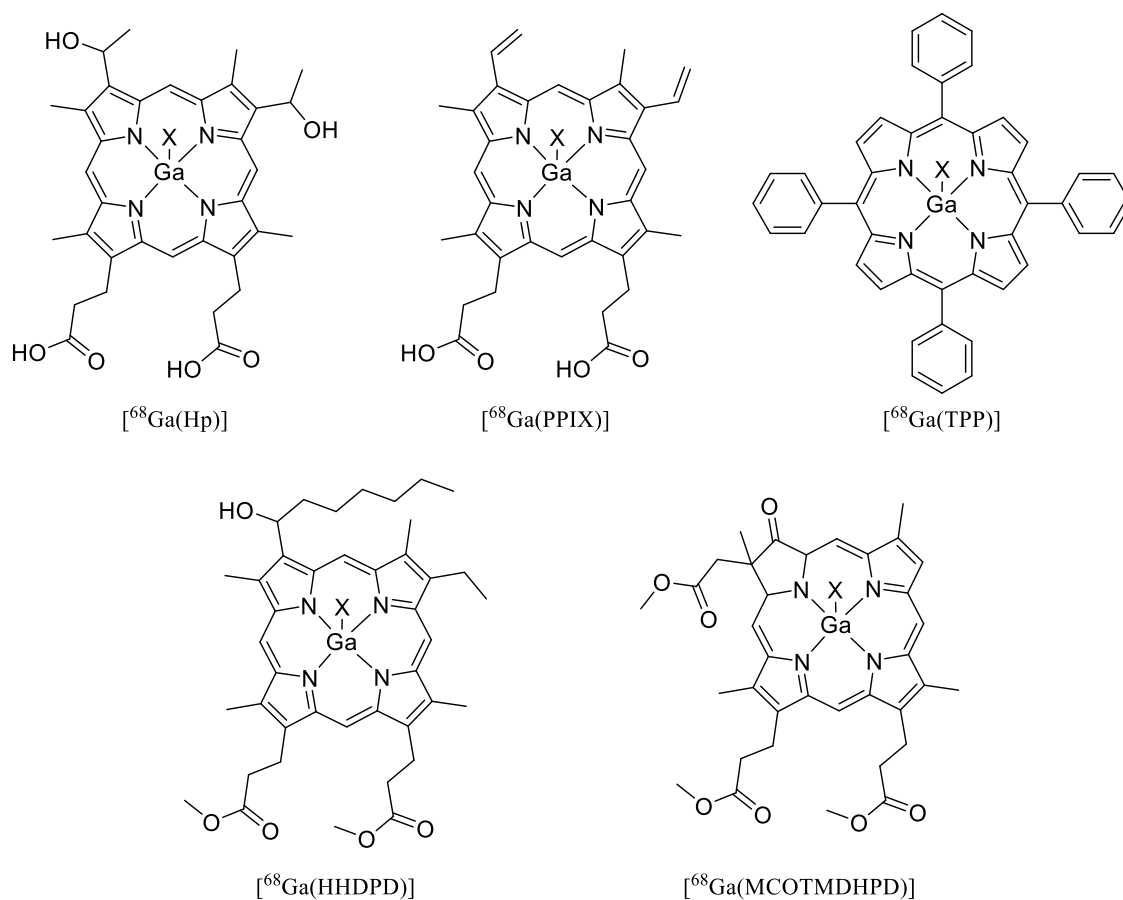


Figure 1.44 Structure of [$^{68}\text{Ga}(\text{Hp})$], [$^{68}\text{Ga}(\text{PPIX})$], [$^{68}\text{Ga}(\text{TPP})$], [$^{68}\text{Ga}(\text{HHDPD})$], and [$^{68}\text{Ga}(\text{MCOTMDHPD})$], reported by Zoller *et al.*^{153,154}

Targeted ^{68}Ga porphyrin has also been shown in the literature. Behnam Azad *et al.* reported the conjugation of tripeptide RGD, a well-known peptide for targeting the $\alpha_v\beta_3$ integrin, with PPIX. Subsequent ^{68}Ga complexation under microwave conditions (120 °C, 45 mins) yielded [$^{68}\text{Ga}(\text{PPIX-RGD})$] with RCY of 33% (Figure 1.45). Non-radioactive [$^{\text{nat}}\text{Ga}(\text{PPIX-RGD})$] was further evaluated *in vitro* via confocal microscopy. [$^{\text{nat}}\text{Ga}(\text{PPIX-RGD})$] showed significant uptake in MDA-MB-435 cells which overexpress $\alpha_v\beta_3$ integrin.¹⁵⁵

Pan et al. reported bimetallic a porphyrin containing both ^{68}Ga and Ru (GaporRu, Figure 1.47). The same porphyrin was initially reported to complex Zn^{2+} in the porphyrin core (ZnporRu) and was shown to have mitochondria specificity.¹⁵⁸ Replacing the zinc with Ga^{3+} resulted in a change in overall charge and increases the amphiphilicity. This improved the cell uptake of the molecule and specificity towards the lysosomes was observed. Radiolabelling under microwave conditions (150 °C, 15 mins, in acetic acid) gave RCY of 85%. *In vitro* toxicity studies showed GaporRu has a LD50 of 70 μM in the dark against HeLa cells, which is less than ZnporRu (LD50 = 27 μM). Phototoxicity showed that GaporRu has a LD50 of 23 μM and 18 μM in HeLa cells and MCF-7, respectively.¹⁵⁹

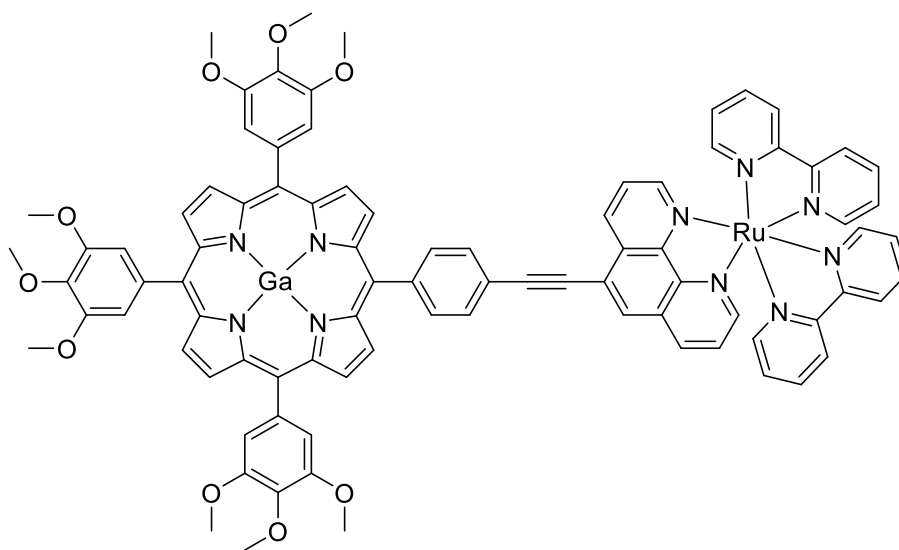


Figure 1.47 Structure of GaporRu reported by Pan *et al.*¹⁵⁹

Another strategy towards ^{68}Ga theranostic porphyrin is to conjugate a ^{68}Ga chelator onto the porphyrin. Careful choice of chelator will enable using milder radiolabelling conditions, mitigating the need for harsh and forcing microwave conditions for radiolabelling of ^{68}Ga into the porphyrin core. Guleria et al. reported the use of the traditional macrocyclic chelator, DOTA and NOTA to conjugate onto 5,10,15,20-tetrakis-(p-carboxymethyleneoxyphenyl)porphyrin (TCPP). Commercially available bifunctional, DOTA and NOTA with an amino-benzyl group on the C-backbone was utilised. The well-established carbodiimide coupling strategy was utilised to form TCPP-DOTA and TCPP-NOTA. Radiolabelling of ^{68}Ga was carried out at 100 °C for 20 mins to give RCY of 80%. A control non-radioactive reaction, carried out under similar conditions, showed that ^{nat}Ga does not occupy the porphyrin core as determined using UV-vis spectroscopy. Incubation with human serum proteins of both purified complex, [^{68}Ga (TCPP-DOTA)] and [^{68}Ga (TCPP-NOTA)] showed serum stability of >90% up to 3 hours. *In vivo* biodistribution studies showed significant tumour accumulation and retention up to 2 hours for both complexes, and both showed a major clearance through the renal pathway.¹⁶⁰

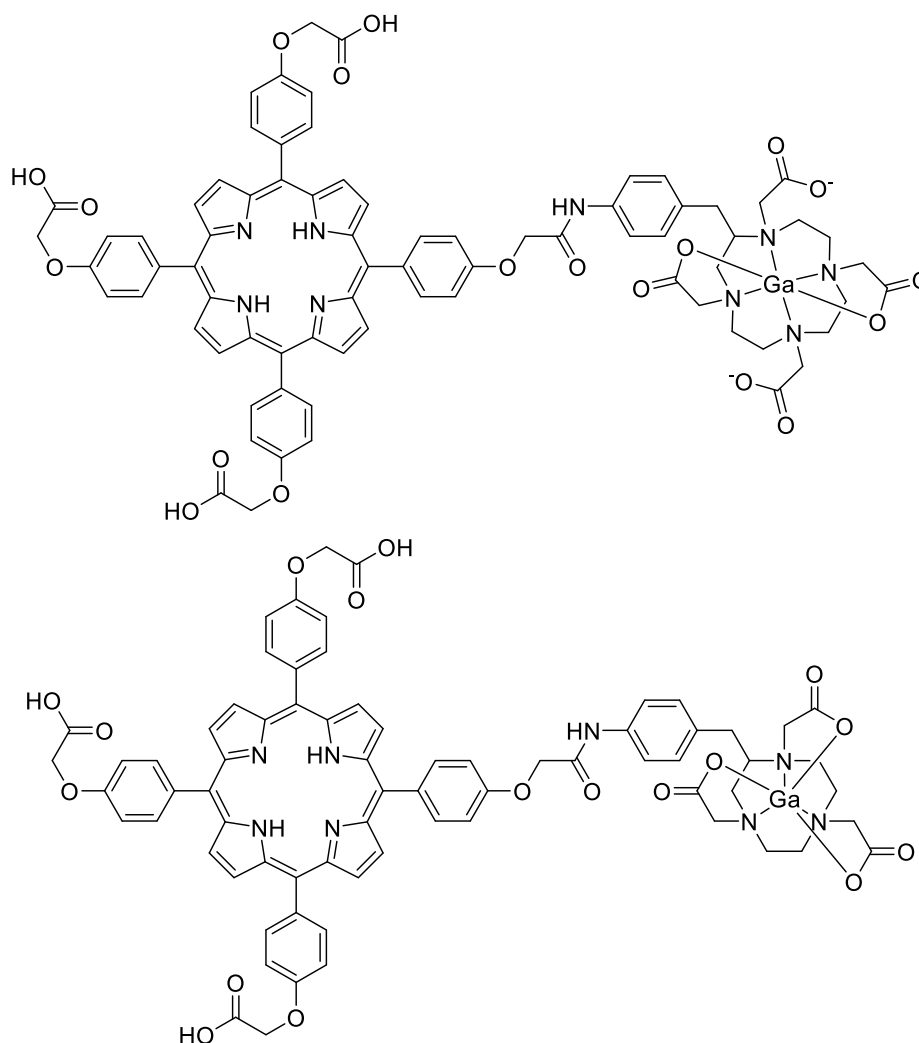


Figure 1.48 Structure of [$^{68}\text{Ga}(\text{TCPP-DOTA})$] (top) and [$^{68}\text{Ga}(\text{TCPP-NOTA})$] (bottom), reported by ¹⁶⁰

1.4.3 $^{99\text{m}}\text{Tc}$ -based SPECT/PDT theranostic porphyrin

Radiolabelling the porphyrin core with $^{99\text{m}}\text{Tc}$ has also been reported. Babbar *et al.* and Gupta *et al.* both reported the radiolabelling of HpD (PS-3) core with $^{99\text{m}}\text{Tc}$. Gupta *et al.* research also expands beyond radiolabelling and includes formulation of PS-3 into liposomes and conjugating PS-3 with carcinoembryonic-antigen mAb. Both research groups reported the use of SnCl_2 as a reducing agent for $^{99\text{m}}\text{Tc}$, and radiolabelling was carried out at pH 7, give RCY of >90%. Babbar *et al.* also included serum stability studies showing good *in vitro* serum stability up to 2 hours before gradually deteriorating to radiochemical purity of 76%.^{161,162}

Motaleb *et al.* also reported the radiolabelling of 5,10,15,20-tetrakis(4-methoxyphenyl)porphyrin (TMPP) and phytychlorin core with reduced $^{99\text{m}}\text{Tc}$. Radiolabelling of TMPP at room temperature for 30 mins at pH 3 with 100 μg SnCl_2 yielded a RCY of 95%. Radiolabelling of phytychlorin was also carried out at room temperature for 30 mins, however at pH 10 with 75 μg SnCl_2 , yielded a RCY of 98%. Both porphyrin complex showed significant tumour uptake *in vivo* and a renal clearance preference.^{163,164}

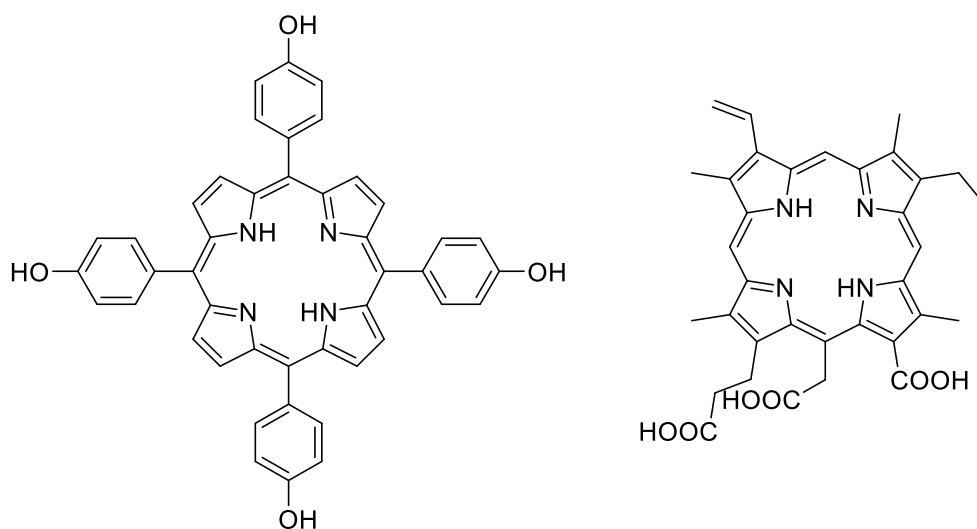


Figure 1.49 Structure of TMPP (left) and phytychlorin (right) used for ^{99m}Tc radiolabelling as reported by Motaleb *et al.*^{163,164}

Radiolabelling ^{99m}Tc on the periphery of a porphyrin with a chelator was also reported. Subbarayan *et al.* and Santos *et al.* both reported a simpler way of complexing ^{99m}Tc on the peripheral of the porphyrin using a 3,4-dicarbomethoxymethyleneoxyphenyl group on the *meso*-position of the porphyrin. Subbarayan *et al.* reported tetra-*meso*-substituted porphyrin (T4CPP), while Santos *et al.* reported a 5,10-bi-*meso*-substituted porphyrin (2CPP) (Figure 1.50). Radiolabelling efficiency was evaluated and a RCY of >95% and 93% was achieved by T4CPP and 2CPP, respectively. Serum stability studies showed [$^{99m}\text{Tc}(\text{T4CPP})$] is stable towards serum up to 4 hours and gradually decreases to 80% radiochemical purity. [$^{99m}\text{Tc}(\text{2CPP})$] showed a constant radiochemical purity of around 87% up to 6 hours. Photodynamic activity of 2CPP was evaluated on H1299 and WiDr cells; where irradiation with 10 J cm^{-1} of >560 nm light, showed cell survival of 72% and 84% in H1299 and WiDr cells respectively, at a concentration of 200 μM . The poor photodynamic activity was suspected to be due to the high number of carboxylic acids on the porphyrin which was shown to reduce cellular uptake.¹⁶⁵ T4CPP was not evaluated for its photodynamic activity. Biodistribution studies on [$^{99m}\text{Tc}(\text{2CPP})$] showed increasing tumour accumulation with time with a tumour-to-muscle ratios of 3.33 and 3.55 in WiDr-bearing mice and H1299-bearing mice respectively, 5 hours post-injection. Biodistribution studies for [$^{99m}\text{Tc}(\text{T4CPP})$] showed a greater tumour-to-muscle ratio of 9.4 in spontaneous mammary tumour in C3H/J mice, 5.4 in *N*-nitrosomethylurea-induced mammary tumour, and 4.2 in C6-Glioma in rats.^{166,167}

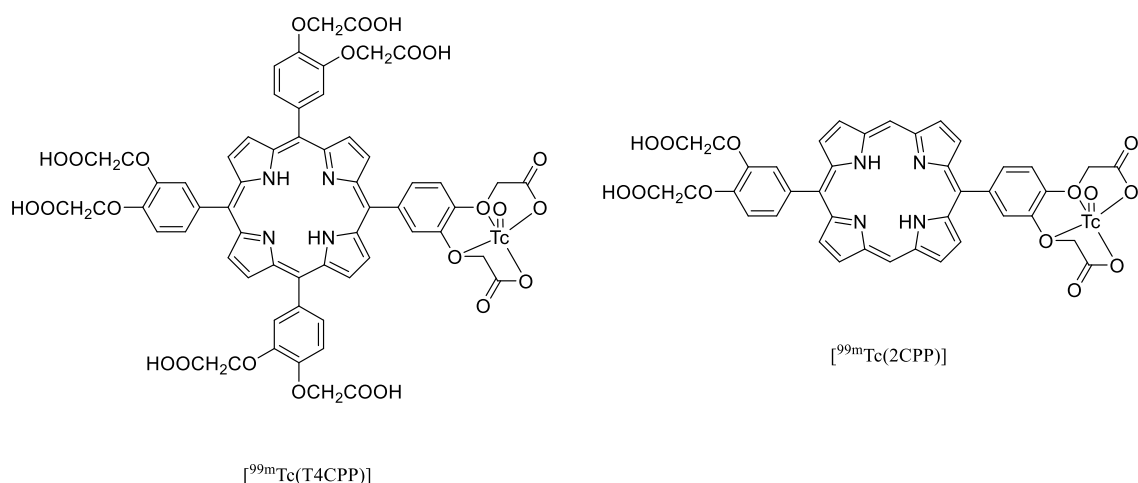


Figure 1.50 Structure of [^{99m}Tc(T4CPP)] and [^{99m}Tc(2CPP)], reported by Subbarayan *et al.* and Santos *et al.*, respectively.^{166,167}

Liu *et al.* reported the conjugation of histidine onto hematoporphyrin for the complexation of [^{99m}Tc(CO)₃]⁺ (Figure 1.51). Histidine acts as a tridentate ligand and was shown to stably chelate [^{99m}Tc(CO)₃]⁺.¹⁶⁸ Using benzotriazol-1-yloxytris(dimethylamino)phosphonium salt (BOP) coupling reagent, two histidine molecules were conjugated onto hematoporphyrin. Radiolabelling efficiency of the ligand was evaluated, and ideal conditions were determined to be at pH 9, at 75 °C for 30 mins, with an RCY of >95%. Stability of the complex was tested with excess histidine in physiological conditions, and it was shown to be stable up to 8 hours, indicating that the conjugation of histidine onto porphyrin do not affect the complex stability.¹⁶⁹

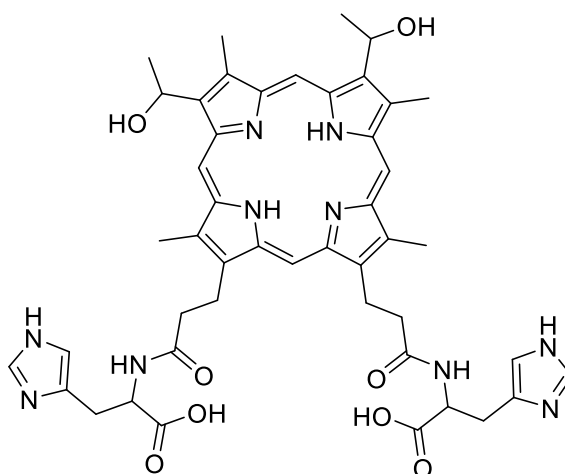


Figure 1.51 Structure of hematoporphyrin-histidine conjugate, reported by Lie *et al.*.¹⁶⁹

The complexation of [^{99m}Tc(CO)₃]⁺ onto porphyrins is also reported by Spagnul *et al.*. Two synthetic water-soluble porphyrins bearing ^{99m}Tc⁺ chelator was reported; One ligand (Porphyrin-BiPy) bears a bidentate bipyridyl chelator, and the other (Porphyrin-DETA) bears a tridentate diethylenetriamine chelator. Radiolabelling was carried out at pH 7.4, at 50 °C, for 30 mins to give both radiolabelled complexes in quantitative yield. Non-radioactive Re⁺ complexes of these ligands were synthesised as a control for HPLC and for biological studies. Cellular uptake studies

were carried out using confocal microscopy; Porphyrin-BiPy showed aggregation around cells with minimal uptake, while [Re(Porphyrin-BiPy)] showed clear cellular uptake with accumulation near the nuclear membrane. Porphyrin-DETA and [Re(Porphyrin-DETA)] do not show any cellular uptake. Toxicity and phototoxicity of the two ligands and their Re^+ complexes were also evaluated on HeLa cells; all compounds showed minimal toxicity in the dark with the exception of [Re(Porphyrin-BiPy)] which has an LD50 of 20.5 μM . Phototoxicity was also evaluated with 10 J cm^{-1} of 590-700 nm light irradiation; an LD50 of 0.2-5.8 μM were achieved for these compounds.^{170,171}

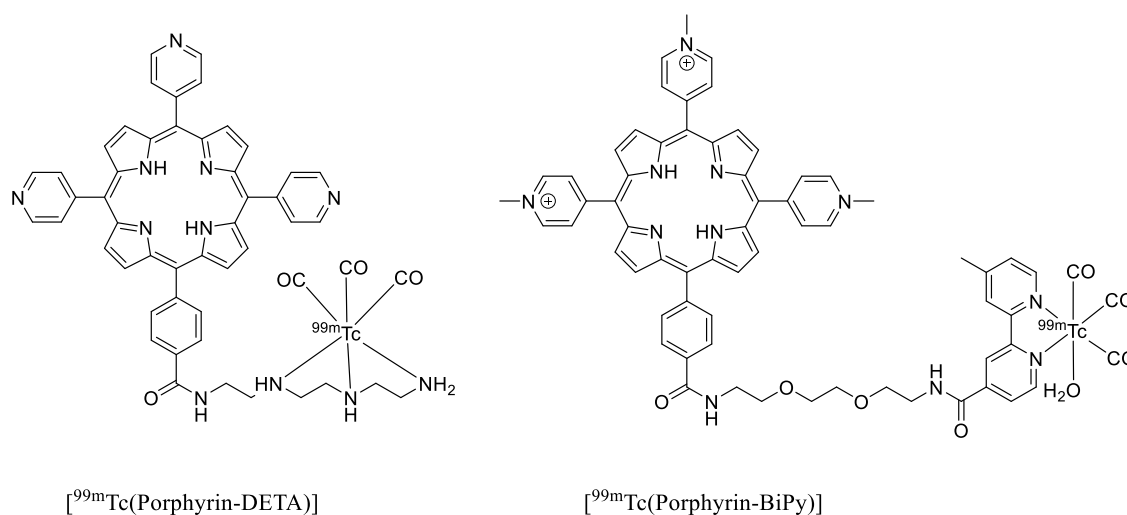


Figure 1.52 Structure of [$^{99\text{m}}\text{Tc}$ (Porphyrin-BiPy)] and [$^{99\text{m}}\text{Tc}$ (Porphyrin-DETA)], reported by Spagnul *et al.*^{170,171}

1.5 Conjugation strategies

Research into theranostic/multifunctional molecules or structures often requires the covalent conjugation of two or more molecules to form a single molecule/construct as shown in the examples in subchapter 1.4. Several strategies are available to form a covalent bond between two molecules. Hereby, in this subchapter, the commonly use peptide coupling and copper-catalysed azide-alkyne cycloaddition (CuAAC) are described.

1.5.1 Peptide coupling and reagents

Traditionally, peptide coupling is the combination of two amino acid residues together to form a peptide (amide) bond. This involve the formation of an amide bond between the amino group of one amino acid residue and the carboxylic acid group of another amino acid residue (Figure 1.53). This reaction is not limited to amino acids and can be utilised between any amino group and carboxylic acids.¹⁷²

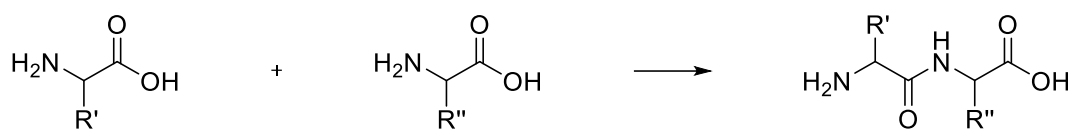


Figure 1.53 Peptide bond formation.

However, carboxylic acids have poor reactivity and often require activation of the group prior to peptide coupling. The activated form can be shelf-stable, intermediately stable (careful storage is required), and transiently stable (not isolatable or detectable and has to be generated *in situ*).

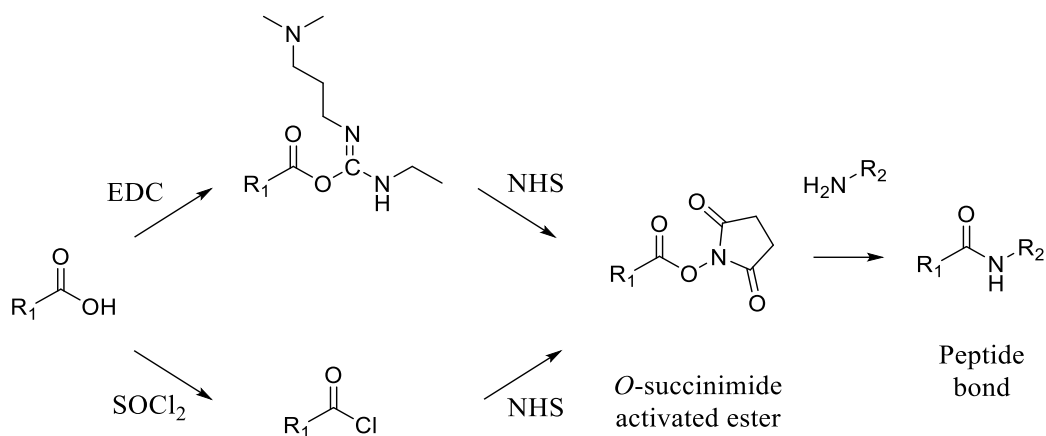


Figure 1.54 Scheme showing the formation of *O*-acylisourea and acid chloride from carboxylic acid, subsequent formation of activated ester using NHS, and formation of peptide bond.

Carbodiimides are commonly used coupling reagents. Carbodiimides has two weakly alkaline nitrogen atoms which can undergo a reaction with carboxylic acid to form a very reactive *O*-acylisourea (not isolatable, Figure 1.54).¹⁷³ The *O*-acylisourea can then undergo aminolysis in the presence of an amino acid to form a peptide bond. Some common carbodiimides reagents are dicyclohexylcarbodiimide (DIC), *N*-ethyl-*N'*-(3-dimethylaminopropyl)carbodiimide (EDC), and *N*-cyclohexyl-*N'*-isopropylcarbodiimide (CIC).

Another way of activating carboxylic acids is *via* acid chlorides. The formation of acid chlorides can be carried out using chlorinating agents such as phthaloyl dichloride, thionyl chloride, and oxalyl chloride (Figure 1.54). However, acid chlorides are often regarded as “over-activated” and are prone to undergo side reactions creating impurities.¹⁷³

A way to mitigate over-activated carboxylic acid (from *O*-acylisourea or acid chlorides) is to utilise activated esters, through the use of *N*-hydroxy derivatives (Figure 1.54). These *N*-hydroxy derivatives are less reactive than *O*-acylisourea or acid chlorides and more efficient as they suppress side reactions. Some of these *N*-hydroxy derivatives are 1-hydroxybenzotriazole (HOBT), 1-hydroxy-7-azabenzotriazole (HOAt), and *N*-hydroxysuccinimide (NHS).¹⁷³

1.5.2 Copper-catalysed azide-alkyne cycloaddition (CuAAC) “click” reaction

CuAAC is an improved Huisgen cycloaddition, is one of the few “click” reactions, and is by far the most widely used. The non-catalysed reaction was first reported in 1893 by A. Michael,¹⁷⁴ but was known as the Huisgen reaction following Huisgen’s studies on the reaction in the 1960s.¹⁷⁵ The Huisgen reaction requires harsh reaction condition (heating up to 100 °C), takes a long time to reach completion, and produces isomeric product. The improved Huisgen cycloaddition, CuAAC was reported by Sharpless¹⁷⁶ and Meldal¹⁷⁷ independently in 2002, and due to its high yielding, fast rate, and can perform efficiently in physiological condition, hence it became one of the most used “click” reaction (Figure 1.55).

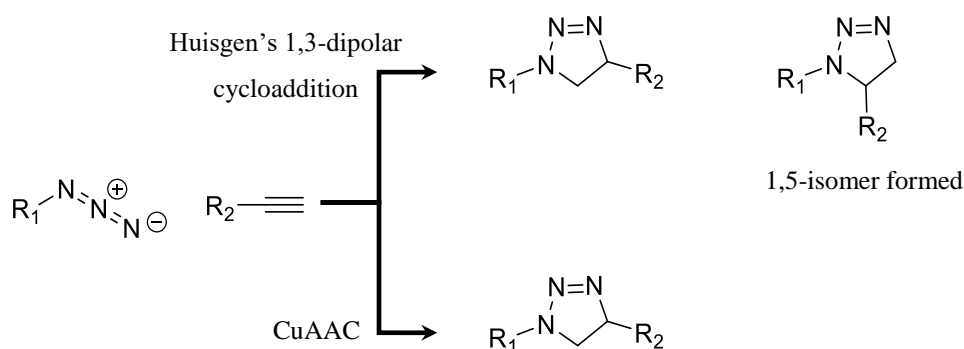


Figure 1.55 Comparison between Huisgen reaction and CuAAC.

1.6 Objective of this study

Past research into photosensitisers for photodynamic treatment had led to the development of second-, third-, and fourth-generation photosensitiser which demonstrated progressively better photodynamic capabilities, selectivity towards diseased tissues, and with additional functionality. Since the selectivity and accumulation of photosensitisers in diseased tissues are essential for photodynamic treatment, in this study, a detail investigation to combine a non-invasive imaging modality with a porphyrin-based photosensitiser aimed to develop new fourth-generation theranostic photosensitisers for cancer diagnosis and cancer therapy was carried out.

Chapter 2 will describe the utilisation of a biological nanoplatform for the loading of porphyrin to enable PDT. Chapter 3 will discuss the usage of synthetic polymeric nanoplatform for the loading of porphyrin and Gd^{3+} -based contrast agent to enable PDT and MRI. In chapter 4, a porphyrin conjugate capable of ^{68}Ga complexation to enable PDT and PET imaging is described. Chapter 5 described the utilisation of “click” chemistry to conjugate porphyrin with amino acid residues. The formation of these porphyrin-amino acid conjugates enables the complexation of ^{99m}Tc , thus allowing PDT and SPECT imaging. Chapter 3, 4, and 5 successfully described the development of fourth-generation theranostic photosensitisers capable of PDT and medical imaging, allowing the combined treatment and diagnosis of cancer, ultimately paving a way towards personalised medicine.

Chapter 2 Bioconjugation of cowpea mosaic virus (CPMV)

In this chapter, a biological nanoplatform, specifically the virus capsid of cowpea mosaic virus (CPMV) will be investigated as a drug delivery platform. Photosensitisers such as porphyrins will be conjugated onto CPMV to enable photodynamic treatment of cancers.

CPMV is the type member of the genus Comovirus within the family Comoviridae (Figure 2.1). The structure of CPMV has been characterised by X-ray crystallography at 2.8 Å,¹⁷⁸ and the structural data is available at Virus Particle ExploreR database (VIPERdb).¹⁷⁹ It has an icosahedral shape; the word *icosahedron* is derived from Greek meaning “twenty seats”. In other words, an icosahedron is a polyhedron that consists of twenty triangular faces. CPMV is approximately 30 nm in diameter and comprised 60 of two coat protein subunit each, small (S) and large (L) units. The S subunit consists of one domain and the L subunit consists of two domains.

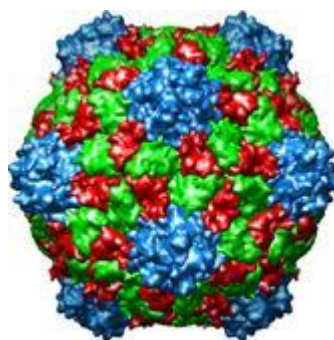


Figure 2.1 Space filling crystal structure of CPMV obtained from VIPERdb.¹⁷⁹

CPMV has five solvent-exposed exterior lysine residues on both L and S coat proteins combined. This gives a total of 300 solvent exposed lysine residues for each CPMV particles, however, only a maximum of 240 labelled lysine have been observed in the literature.¹⁸⁰ CPMV also displays nine carboxylate groups on L and S coat proteins, derived from aspartic and glutamic acids residues.¹⁸¹ The abundance of reactive groups makes CPMV a natural multifunctional nanoparticle platform; capable of orthogonal functionalisation and capable of delivering a high payload of drug molecules.

Unsurprisingly, extensive literature have shown the use of viral nanoparticles including CPMV for the bioconjugation of molecules; several reviews^{182–191} and book chapters^{192–194} have described the extensive literature available for the bioconjugation of molecules onto CPMV and other viral nanoparticles.

This chapter will describe the synthesis of suitable porphyrins – water-soluble porphyrin with conjugatable “handles”, and the subsequent bioconjugation of these porphyrins onto the amine and carboxylate groups on the exterior of wtCPMV. Several bioconjugation conditions were

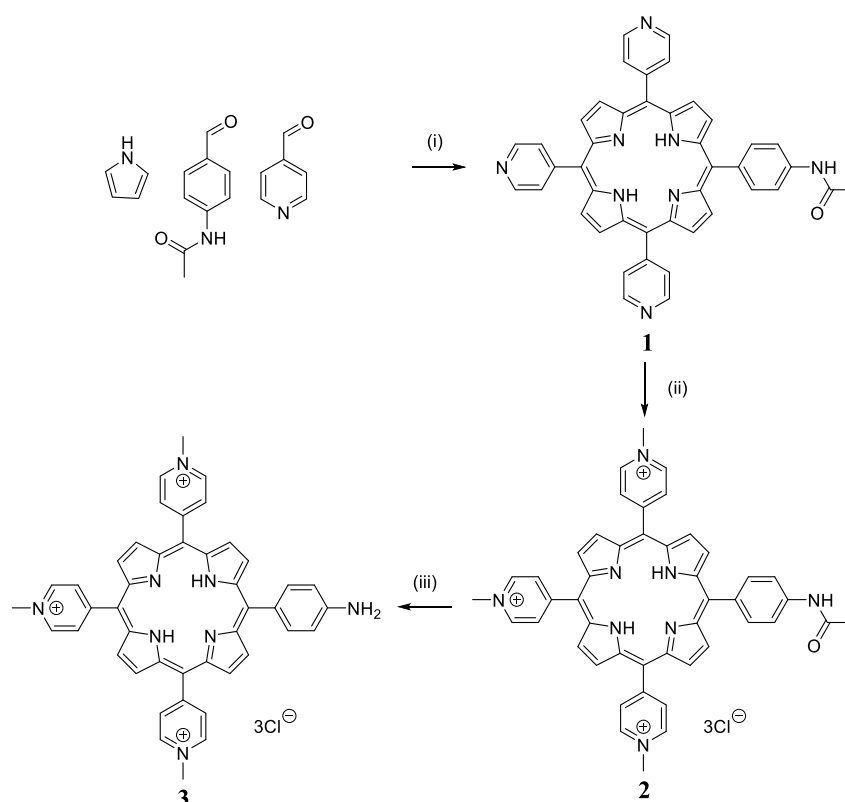
investigated, which also includes the functionalisation of CPMV with an alkyne moiety prior to copper-catalysed azide-alkyne cycloaddition (CuAAC) with azido porphyrin.

2.1 Porphyrin synthesis

In this work, synthesis of water-soluble porphyrins with reactive “handles” was carried out for the purpose of conjugating porphyrins onto CPMV. Initially, amine and carboxylate reactive porphyrins were synthesised. A porphyrin bearing an azide group has also been synthesised to enable CuAAC.

Water-solubilisation of porphyrin is of particular interest not just for the development of third- and fourth-generation photosensitisers but is a necessity for the bioconjugation of wtCPMV. Bioconjugation with CPMV can only be carried out in aqueous buffer media due to CPMV incompatibility with organic solvents. Despite being “extremely” robust, CPMV is only stable in DMSO-buffer mixtures of up to 20% (v/v) DMSO in buffer for more than two weeks, and stability will decrease with increasing DMSO. At 80% (v/v) DMSO in buffer, the half-life of CPMV particles is approximately 30 minutes.¹⁹⁵ Hence, the need for water-solubilisation of porphyrin.

2.1.1 Carboxylate-reactive porphyrin



Scheme 2.1 Synthesis of 5-[4-aminophenyl]-10,15,20-tri-(N-methyl-4-pyridinium)porphyrin **3**. Reagents, conditions, and yields: (i) propionic acid, 170 °C, 1 hour, 6.3% (ii) DMF, methyl iodide, 40 °C, overnight, 99% (iii) 6 M HCl, 90 °C, 3 hours, 79%.

Synthesis of porphyrin with an amine “handle” was carried out using the mixed-aldehyde Adler-Longo condensation described in the literature.^{196,197} However, a protected amine-aldehyde is

required as an amine group is a nucleophile and will participate in the condensation reaction in the formation of the porphyrin.

Synthesis of porphyrin **1** utilised the mixed-aldehyde Adler-Longo condensation using a modified literature method (Scheme 2.1). A ratio of 2:1 of 4-pyridinecarboxaldehyde:4-acetamidobenzaldehyde was used instead of a 3:1 ratio to form an A₃B₁ *meso*-substituted porphyrin, due to the lower reactivity of 4-acetamidobenzaldehyde. With this optimised method, the product was obtained with a yield of 6.3%, higher than the literature value of 3.9%.¹⁹⁷ The identity of porphyrin **1** was confirmed using NMR spectroscopy, mass spectrometry, and UV-vis spectroscopy, which are in agreement with literature values.¹⁹⁷

Quaternisation of *meso*-positioned pyridyl groups was carried out prior to amine deprotection to prevent methylation of the primary amine group necessary for further conjugation. By using a literature method, quaternisation of porphyrin **1** with methyl iodide at elevated temperature overnight gave cationic water-soluble porphyrin **2** in quantitative yield.^{198,199} Clear solubilisation of the porphyrin in water and polar solvents such as methanol, ethanol, *N,N*-dimethyl sulfoxide (DMSO) was observed, with NMR spectroscopy in DMSO-*d*₆ confirming the formation of porphyrin **2**.

Hydrolysis of the acetamido group to the corresponding amine group by refluxing in concentrated aqueous HCl gave porphyrin **3** in 79% yield. The successful synthesis of **3** was determined by NMR spectroscopy with ¹H NMR peaks matching literature values.¹⁹⁹ This afforded porphyrin **3** with an amine group capable of conjugating to a carboxylate moiety.

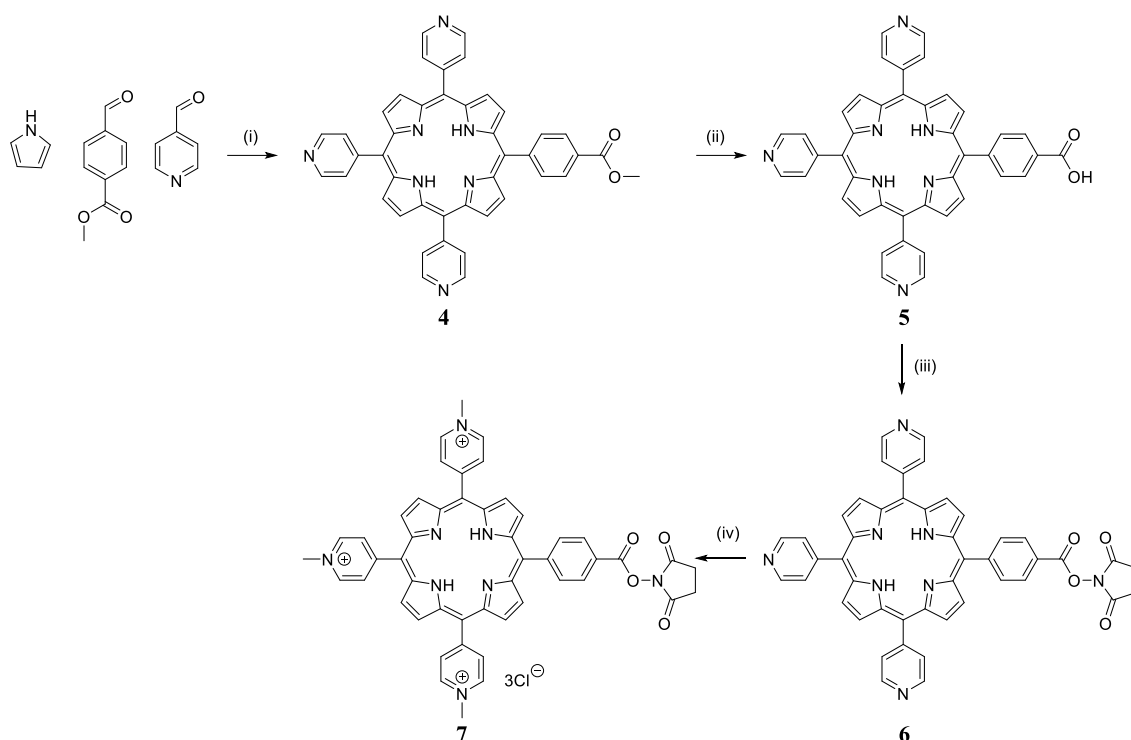
2.1.2 Amine-reactive porphyrin

Succinimide activated-ester fluorophores have previously been shown to form covalent peptide bonds with CPMV and the synthesis of succinimide activated ester porphyrin is well established.^{195,200,201} Hence, a cationic water-soluble porphyrin **7** bearing an activated succinimide ester was devised.

Synthesis of porphyrin **4** was carried out using the mixed-aldehyde Adler-Longo methodology (Scheme 2.2).^{196,202} Condensation of pyrrole, 4-pyridinecarboxaldehyde, and methyl 4-formylbenzaldehyde and subsequent purification using silica column chromatography yielded porphyrin **4** in 8.3%, a higher yield than literature at 4.7%.²⁰² The product was confirmed using NMR spectroscopy, mass spectrometry, and UV-vis spectroscopy, with these analysis matching literature values.²⁰²

Hydrolysis of porphyrin **4** was carried out using potassium hydroxide in a mixture of ethanol and water. Hydrolysis of porphyrin **4** gave a single porphyrin **5** product in quantitative yield (97%) with a simple reaction workup without the need for lengthy column chromatography. NMR

spectroscopy shows the clear removal of the alkyl group from the ester; removal of singlet peak at 4.12 ppm in ^1H NMR and removal of the peak at 52.62 ppm in ^{13}C NMR.



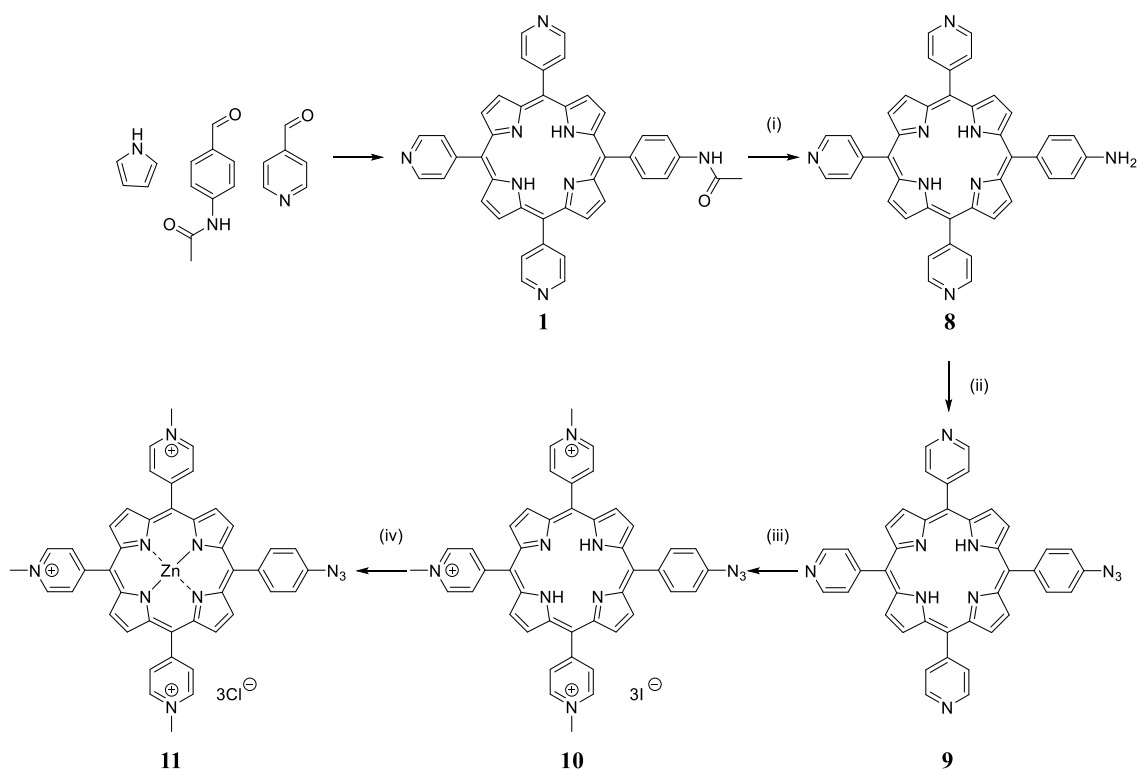
Scheme 2.2 Reaction scheme for synthesis of 5-[4-(Succinimide-N-oxycarbonyl)phenyl]-10,15,20-tri(N-methyl-4-pyridinium)porphyrin **7**. Reagents, conditions, and yields: (i) propionic acid, 170 °C, 1 hour, 8.3%, (ii) EtOH, H₂O, potassium hydroxide, room temperature, overnight, 97%, (iii) dry pyridine, thionyl chloride, *N*-hydroxysuccinimide, 50 °C, 3 hours, 66%, (iv) DMF, methyl iodide, 40 °C, overnight, 55%.

Activation of the carboxylic acid was carried out *via* the acid chloride mediated pathway to form an activated succinimide ester reactive handle on porphyrin **6**. Thionyl chloride was added to a solution of porphyrin **5** in dry pyridine to form the corresponding acid chloride, subsequent addition of *N*-hydroxysuccinimide (NHS) generated porphyrin **6** in 66% yield. Although the *O*-succinimide moiety was known to degrade under protic solvent and silica, porphyrin **6** showed sufficient stability to undergo flash silica chromatography. ^1H NMR analysis shows the formation of a singlet with a chemical shift of 3.01 ppm that integrated to four protons and indicates the protons on succinimide. ^{13}C NMR shows an extra peak in the alkyl region at 25.89 ppm and two peaks in the carbonyl regions at 162.06 and 169.45 ppm, indicating carbons on the *O*-succinimide. NMR spectroscopy gives evidence to the formation of porphyrin **6** and these analysis match literature values.²⁰³

The *meso*-positioned pyridyl groups were quaternised using a similar method for the synthesis of porphyrin **2** to afford water-soluble porphyrin **7**. The successful synthesis of porphyrin **7** was determined with NMR spectroscopy which matches literature values.²⁰³ This afforded porphyrin **7** as an amine-reactive porphyrin capable of conjugating free-amines available on CPMV.

2.1.3 Azide-porphyrin for CuAAC

The ubiquitous CuAAC often referred to as a “click” reaction, is a reaction that conjugates two molecules together through the formation of a triazole between an alkyne and an azide group. CuAAC is inert in the presence of water and capable of proceeding to completion at ambient temperature, making it an ideal strategy to conjugate molecules onto viral nanoparticles. Unsurprisingly, some literature examples have utilised CuAAC with CPMV.^{204–207} In this subchapter, the synthesis of a water-soluble azido porphyrin for the use in CuAAC bioconjugation is described.



Scheme 2.3 Reaction scheme for the synthesis of 5-[4-azidophenyl]-10,15,20-tri-(N-methyl-4-pyridinium)porphyrin **11**. Reagents, conditions, and yields: (i) 6 M HCl, 90 °C, 2 hours, 92%, (ii) Trifluoroacetic acid (TFA), water, sodium nitrite, sodium azide, 0 °C, 1 hour, 73%, (iii) DMF, methyl iodide, 40 °C, overnight, 97%, (iv) water, zinc acetate, room temperature, 1 hour, 98%.

Scheme 2.3 shows the synthesis of water-soluble azido porphyrin **11**. Porphyrin **8** can be obtained from the hydrolysis of the acetamido group on porphyrin **1** with concentrated HCl to give the product in a 90% yield. The slight improvement in yield compared to the hydrolysis of cationic porphyrin **2** to porphyrin **3** (Scheme 2.1, 78% yield) is possibly due to the easier purification of porphyrin **8** in organic solvent compared to in water. Diazotization of porphyrin **8** using sodium nitrite and sodium azide utilised a modified literature method and gave porphyrin **9** as the product in 93% yield.²⁰⁸ Quaternisation of porphyrin **9** using methyl iodide gave water-soluble porphyrin with an azide-reactive handle **10** in quantitative yield (97%).

Zinc metal insertion was carried out as porphyrin rings that contain a zinc (II) cation have been shown to enhance membrane binding efficiency,²⁰⁹ but more importantly, this prevents the

insertion of copper into the porphyrin during CuAAC.¹⁹⁸ Copper (I) can be produced *in situ* from copper (II) in the presence of sodium ascorbate and is used as a catalyst in azide and alkyne cycloadditions, however, copper can also be easily complexed by porphyrins. Upon Cu complexation with porphyrin, this will quench the fluorescence and photodynamic properties of the porphyrin,²¹⁰ hence, the necessity for zinc complexation. Zinc insertion into the porphyrin can be determined by UV-vis spectroscopy as the absorption spectrum of metallated porphyrins has two Q-bands instead of four Q-bands shown by free base porphyrins (Figure 2.2). Analysis by NMR spectroscopy and mass spectroscopy gives further evidence for the successful synthesis of porphyrin **11**, which matches literature values. This afforded porphyrin **11** as a “clickable” water-soluble azido porphyrin.

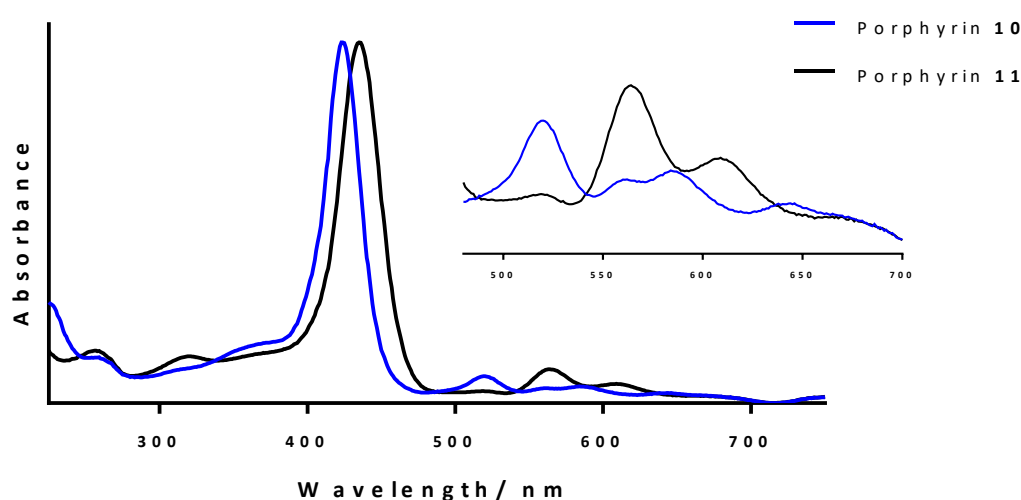


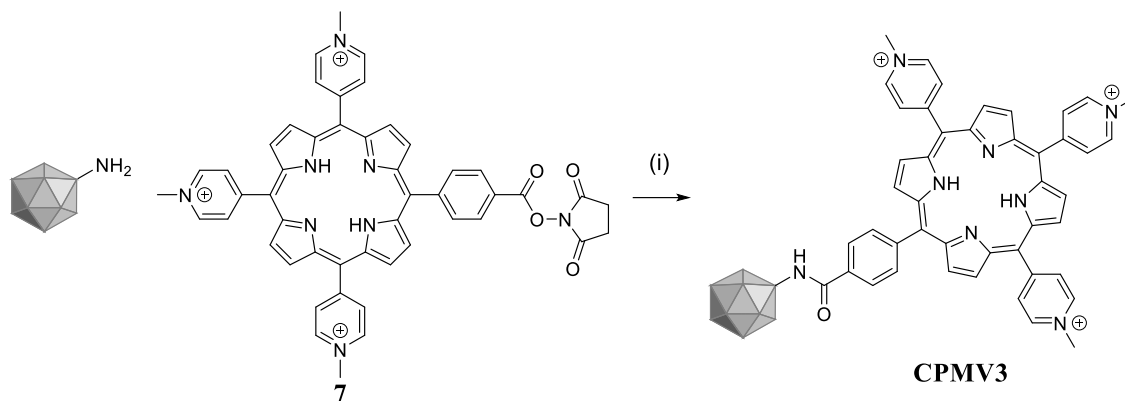
Figure 2.2 UV-vis spectra of porphyrin **10** and porphyrin **11**.

2.2 Bioconjugation of CPMV with cationic porphyrin

In this subchapter, solvent-exposed amino acid residues on CPMV will be conjugated with water-soluble cationic porphyrin. It has been shown in the literature that the innately negatively charged CPMV tends to have a short blood circulation half-life (less than 10 minutes²¹¹, whereas positively charged bacteriophages such as Q β and M13, have been shown to have circulation half-lives of 4-5 hours^{212,213}). By conjugating cationic water-soluble porphyrin onto CPMV, the water-solubilisation of the cationic charge of the porphyrin is not only a necessity, but they may also introduce a desired trait – longer circulation time *in vivo* of the viral nanoparticle. Conjugation of carboxylate-reactive porphyrin **3**, and amine-reactive porphyrin **7** are discussed. Conjugation of an alkyne linker for subsequent CuAAC of azido porphyrin **11** is also explored as an alternative strategy.

examples of peptide conjugation with water-soluble porphyrins. Literature also showed these peptide coupling reactions involved non-NHS mediated coupling reagents, this includes the usage of aminium- and uronium-based coupling reagents,^{199,216–218} anhydrides,²¹⁹ *in situ* formations of anhydrides with ethyl chloroformate,^{216,217,220,221} and acid chlorides.²²²

2.2.2 Conjugating amine groups on CPMV



Scheme 2.5 Bioconjugation of amine-reactive porphyrin **7** with wtCPMV. Reagents, condition, and yields: (i) 0.1 M pH 7 sodium phosphate buffer, 20% DMSO, porphyrin **7**, room temperature overnight, 19%.

An alternative method to conjugate porphyrins onto wtCPMV lysine residues was devised as the alkyl amine on the lysine was expected to be more reactive than the aryl-amine porphyrin **3**. To facilitate this the NHS-substituted porphyrin **7** was employed (Scheme 2.5).

Porphyrin **7** was incubated with wtCPMV at room temperature, with gentle stirring overnight. This reaction was carried out with various concentrations of wtCPMV and different molar excesses of porphyrin **7** (Scheme 2.7). The best results were obtained from 0.2 mg mL⁻¹ wtCPMV with 2000 molar excess porphyrin **7** with purification *via* dialysis membrane.

Concentration wtCPMV/ mg mL ⁻¹	Molar excesses of porphyrin 7		
	2000	2500	5000
0.10			✓
0.20	✓		
0.35			✓
0.50		✓	✓

Table 2.1 Varying concentration of wtCPMV and molar excesses of porphyrin **7**. Ticks indicate reaction conditions that have been attempted.

Precipitation and aggregation of viral nanoparticles was visible post-reaction and purification *via* centrifugal filter units led to the immediate loss of all viral nanoparticles as aggregates which were trapped by the centrifugal filters. Hence, purification through a dialysis membrane was used, combined with attempts to disperse the aggregates through pipetting.

At 0.2 mg mL^{-1} wtCPMV with 2000 molar excess of porphyrin **7**, it was possible to isolate **CPMV3**, albeit, with a poor 19% yield as determined using UV-vis spectroscopy (Figure 2.4). Typical yields of purification using a dialysis membrane were $>90\%$.

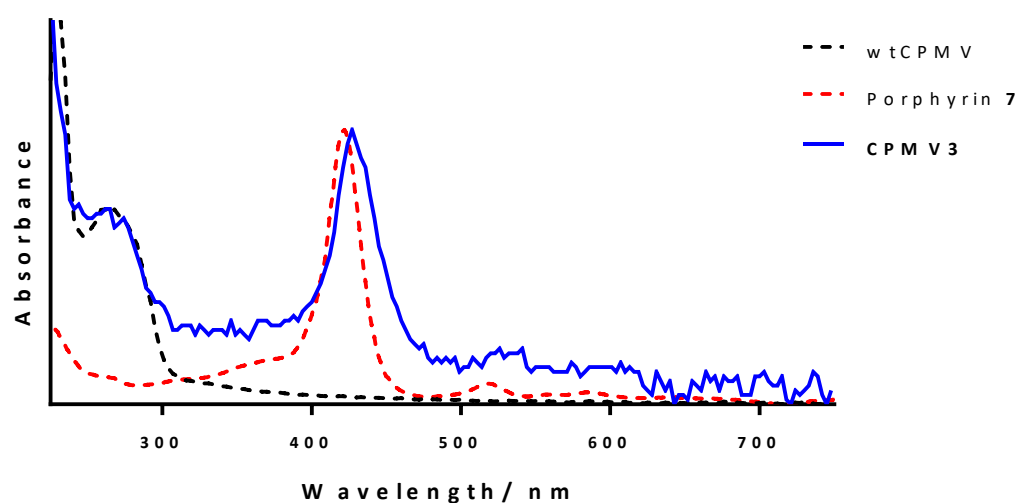


Figure 2.4 UV-vis spectra of wtCPMV, porphyrin **7**, and **CPMV**. UV-vis spectrum of **CPMV3** shows clear indication of the presence of porphyrin after purification *via* dialysis.

UV-vis spectroscopy of the dispersed aggregates gave poor UV-vis spectrum (Figure 2.4) due to the presence of dispersed solids and indicates the presence of porphyrin as an intense Soret band can be observed at 427 nm. The presence of porphyrin observed on UV-vis spectroscopy is an indication that porphyrin **7** has been successfully conjugated/non-covalently bound onto CPMV, and hence may have resulted in the aggregation of **CPMV3**.

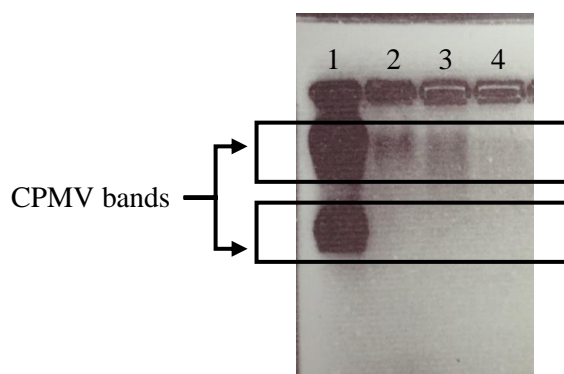


Figure 2.5 Native agarose gel electrophoresis of modified **CPMV3** under Coomassie blue stain. 1 = wtCPMV, 2 = unpurified **CPMV3**, 3 = 4 hr dialysis of **CPMV3**, 4 = 8 hr dialysis of **CPMV3**.

Native agarose gel electrophoresis (Figure 2.5) and TEM (Figure 2.6) were used to characterised **CPMV3**. Different aliquots of **CPMV3** were taken at several time intervals during dialysis up to 26 hours. However, dialysis beyond 8 hours resulted in excess dilution of **CPMV3** making observation by agarose gel electrophoresis impossible. Migration of **CPMV3** onto native agarose gel in Figure 2.5 shows no difference in migration distance and shows fainter bands in comparison to wtCPMV. The fainter bands can be due to the lower concentration of viral nanoparticles as

visible precipitates were observed in the loading wells. No difference in migration may be due to non-conjugated/non-aggregated CPMV successfully migrated onto the agarose gel, leaving conjugated aggregates in the loading wells, hence, showing similar migration with wtCPMV. Note that wtCPMV in Figure 2.5 shows more than one band on than Figure 2.3, this is due to different batches of CPMV varies, hence certain CPMV bands may appear fainter/brighter. TEM images (Figure 2.6) show intact viral nanoparticles, however, this was carried out at low concentration, and may not represent the bulk of CPMV3.

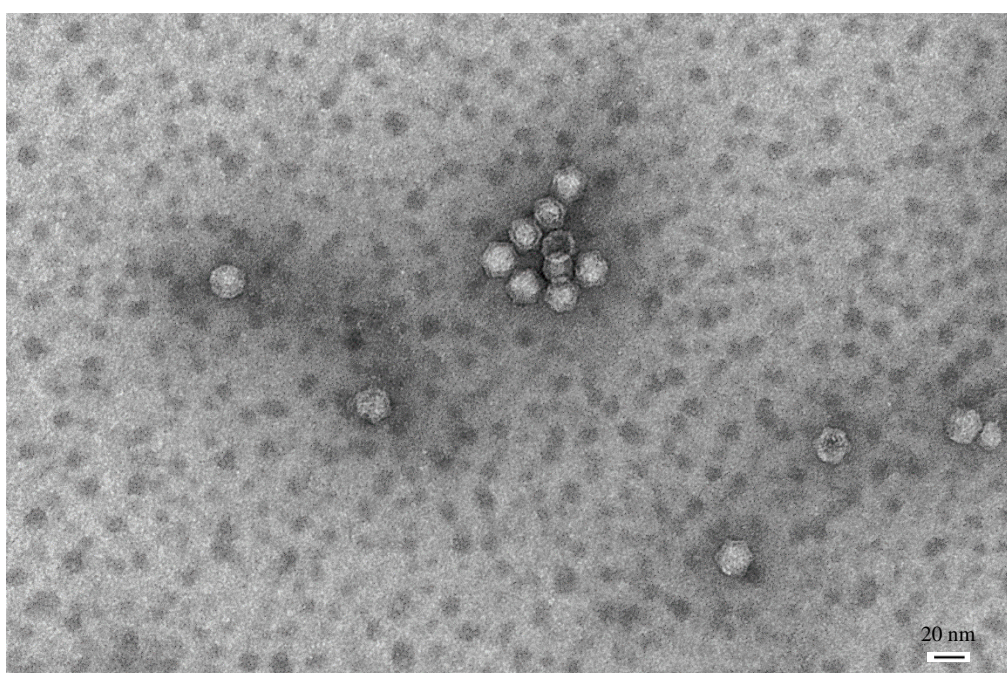
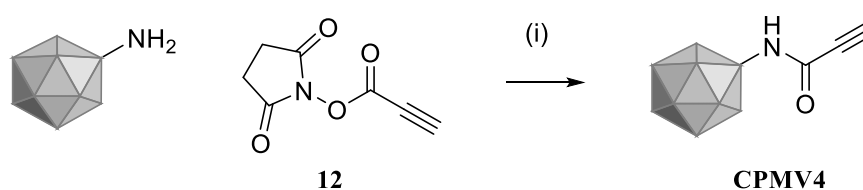


Figure 2.6 2% (w/v) uranyl acetate stained TEM images obtained for modified CPMV3.

2.2.3 Modification of CPMV for CuAAC



Scheme 2.6 Reaction scheme for the bioconjugation of propiolic NHS-ester onto lysine residues on wtCPMV. Reagents, conditions, and yields: (i) 0.1 M pH 7 sodium phosphate buffer, 20% DMSO, propiolic acid, EDC, NHS, room temperature, overnight, 46-60%.

Attempts to modify wtCPMV *via* CuAAC requires the pre-functionalisation of the viral nanoparticle with an alkyne moiety. Commercially available propiolic acid (Sigma Aldrich) was used as the bifunctional linker for conjugation (Figure 2.6). Propiolic acid was stirred with excess EDC and NHS to prepare the activated ester 2,5-dioxopyrrolidin-1-yl propiolate **12** and was used immediately without purification. Bioconjugation was carried out with varying linker concentration: 10,000, 20,000, 50,000, and 100,000 molar excess of propiolic acid linker relative to wtCPMV.

As expected at higher linker concentration, more linkers were conjugated onto wtCPMV, and this was shown using native agarose gel electrophoresis (Figure 2.7). Conjugation of linker onto lysine groups will result in the negation of positively charged amine groups, increasing the overall negative charge of the viral nanoparticles, resulting in an increased mobility towards the anode in electrophoresis.

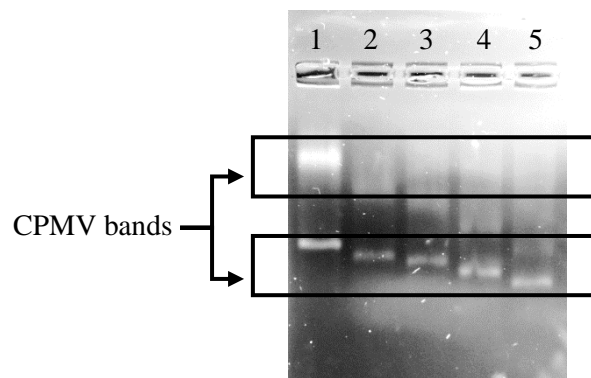
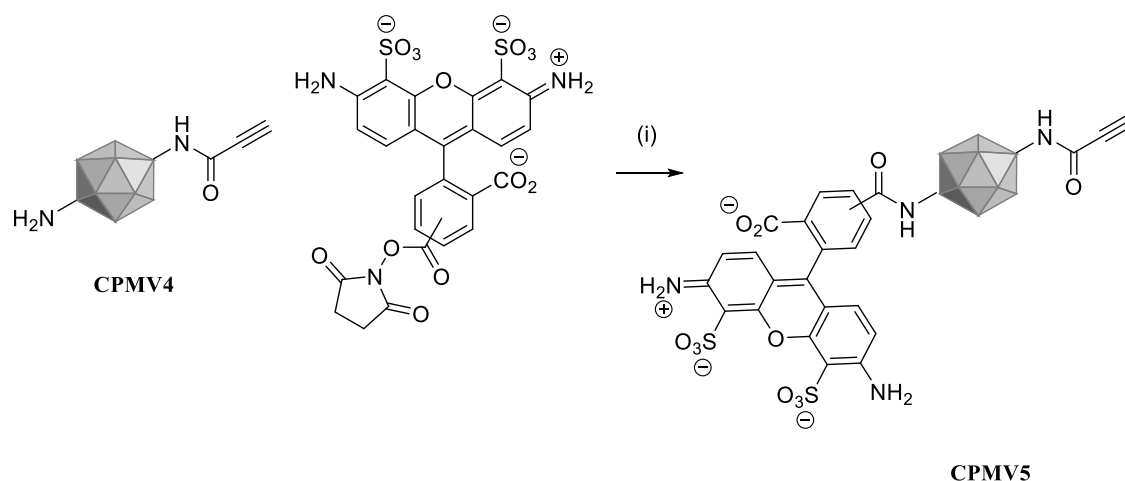


Figure 2.7 Native agarose gel electrophoresis of modified **CPMV4** under ethidium bromide stain. 1= wtCPMV, 2,3,4,5 = **CPMV4** with 10,000, 20,000, 50,000, and 100,000 molar excess of propiolic acid, respectively.



Scheme 2.7 Reaction scheme for bioconjugation of Alexafluor-488 NHS onto **CPMV4** to determine the presence of excess amine. Reagents, conditions, and yields: (i) 0.1 M pH 7 sodium phosphate buffer, 20% DMSO, Alexafluor-488 NHS, 4 °C, overnight, 38%.

To prove most/all conjugatable lysine groups had reacted, **CPMV4** prepared with 100,000 molar excess linker **12**, was conjugated with commercially available Alexafluor-488 NHS (Thermo Fisher Scientific), which is a typical fluorophore used to indicate the presence/absence of conjugatable amine post-modification on CPMV. Alexafluor-488 has a strong absorbance at 494 nm with an extinction coefficient of $73,000 \text{ cm}^{-1} \text{ M}^{-1}$ (value obtained from Thermo Fischer scientific). Excess Alexafluor-488 NHS (30,000 molar excess) was incubated with **CPMV4** to give **CPMV5** (Figure 2.7). Upon purification, UV-vis spectroscopy of the purified reaction product indicated low to negligible absorbance at 494 nm showed absence or negligible amounts of conjugatable amine on **CPMV4** (Figure 2.8). This subsequently prompted the attempt to conjugate porphyrin *via* CuAAC reaction.

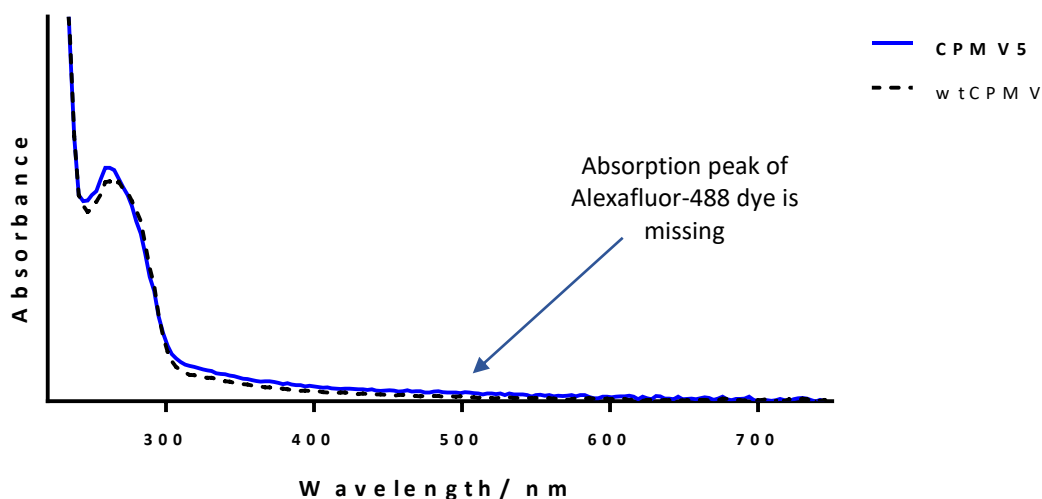
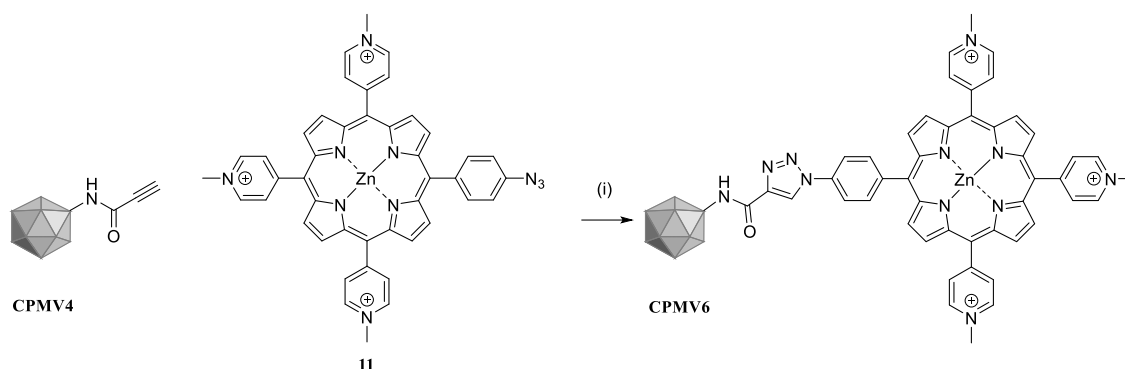


Figure 2.8 UV-vis absorption spectrum of purified modified **CPMV5** and wtCPMV. The absence of absorption at 494 nm indicates the absence or a negligible amount of conjugatable amine.



Scheme 2.8 Reaction scheme for bioconjugation of azide-porphyrin **11** onto alkyne modified CPMV 15 via CuAAC click reaction. Reagents, conditions, and yields: (i) 0.1 M pH 7 sodium phosphate buffer, 20% DMSO, porphyrin **11**, CuSO₄, sodium ascorbate, THPTA, 4 °C, overnight, 17%.

CuAAC was attempted using **CPMV4** and azido porphyrin **11** under Cu(I) catalysed conditions (Scheme 2.8). Cu(I) was generated *in situ* by reduction of Cu(II) using sodium ascorbate, in the presence of accelerating ligand, tris(3-hydroxypropyltriazolylmethyl)amine (THPTA). The use of accelerating ligand has been shown to enhance reaction rate and also prevents decomposition and aggregation of CPMV in the presence of CuSO₄ and sodium ascorbate.^{223,224} Similarly to the preparation of **CPMV3** *via* peptide coupling using porphyrin **7**, post-reaction of **CPMV6** showed aggregation. Purification using centrifugal filter resulted in the immediate loss of all viral nanoparticle. Hence, purification *via* dialysis was carried out instead. UV-vis spectroscopy of **CPMV6** showed presence of viral nanoparticles (as determined from wtCPMV absorption maxima at 260 nm) with the presence of the porphyrin Soret band (Figure 2.9), indicating conjugation of porphyrin onto viral nanoparticles. Figure 2.10 shows the native agarose gel electrophoresis of **CPMV6**. The extent of aggregation of **CPMV6** can be observed as the loading well showed intense absorption post-electrophoresis, with no migration of any viral bands onto the gel.

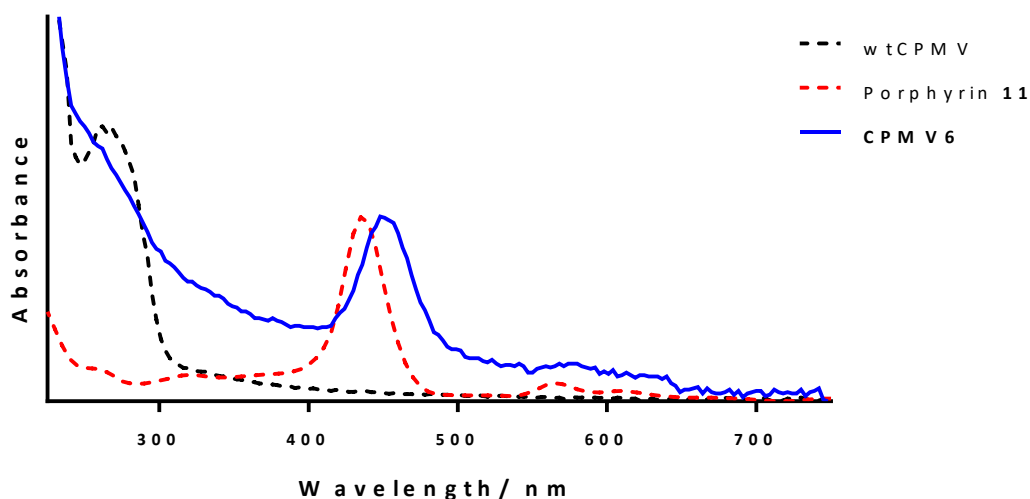


Figure 2.9 UV-vis spectra of wtCPMV, porphyrin **11**, and **CPMV6** after 6 hours dialysis. UV-vis spectrum of **CPMV6** shows clear indication of the presence of porphyrin after purification *via* dialysis.

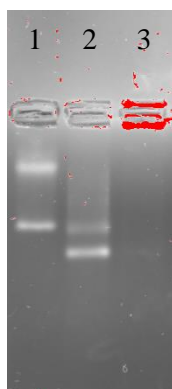


Figure 2.10 Native agarose gel electrophoresis with ethidium bromide stain for viral nanoparticles of 1 = wtCPMV, 2 = **CPMV4**, 3 = **CPMV6**. Lane 3 shows high absorption in loading well, indicating aggregation of viral particles.

2.3 Summary

A range of conjugatable cationic water-soluble porphyrins were successfully synthesised and characterised.

Bioconjugation of aryl-amine porphyrin **3** was unsuccessful as shown on agarose gel electrophoresis. This may be due to the unsuccessful synthesis of *O*-succinimide **CPMV1** and/or due to the poor reactivity of porphyrin **3**.

Bioconjugation of *O*-succinimide porphyrin **7** onto the amine groups on wtCPMV and azido porphyrin **11** onto alkyne-modified **CPMV5** resulted in the aggregation of viral nanoparticles, severe loss of sample, and rendered further analysis and studies impossible. Hence, this was not further pursued.

It was hypothesised that conjugating positively-charged cationic porphyrins onto the innately negatively charged wtCPMV caused these aggregations. Steinmetz research group published a literature that showed similar observation, for instance, covalent conjugation of tricationic

porphyrin onto a virus caused aggregation, hence, conjugation of positively-charged porphyrins was proceeded *via* electrostatic interaction.^{225,226}

To address these issues, instead of using cationic water-soluble porphyrin, anionic water-soluble porphyrin or neutral water-soluble porphyrin could be used. The synthesis of anionic and neutral water-soluble porphyrins are well documented^{227,228} and the subsequent conjugation of these porphyrins should prevent the negation of charges on wtCPMV and also prevents the non-covalent binding of porphyrin with wtCPMV.

Chapter 3 Polyacrylamide nanoparticles synthesis and conjugation

This chapter focusses on the use of multifunctional polyacrylamide nanoparticles and will describe the development of polyacrylamide nanoparticles for use in cancer treatment and cancer diagnosis. The aim is to develop and synthesize multifunctional polyacrylamide nanoparticles as PDT agents and as MRI contrast agents.

This chapter will first give a brief introduction to polyacrylamide nanoparticles and their synthesis *via* free radical polymerisation. This is followed by the synthesis of acrylamide monomers with suitable reactive functionality; for instance, amine, alkyne, or azide groups. Incorporation of porphyrins as photodynamic agents into the nanoparticles *via* covalent incorporation during nanoparticle polymerisation, or to pre-formed nanoparticles; subsequent conjugation of suitable metal-chelators allowing the complexation of metals such as Gd^{3+} for magnetic resonance imaging (MRI) is also described.

3.1 Polyacrylamide nanoparticle

Polyacrylamide nanoparticles are innately hydrophilic, naturally lending themselves to biological applications.²²⁹ They are highly versatile due to their chemical flexibility; synthesis of polyacrylamide nanoparticles and subsequent modification can alter their physical and chemical properties and can be tuned to improve *in vivo* performance, for instance, cell permeance, intracellular localisation, and pharmacokinetic profiles. Furthermore, drug and imaging molecules can be encapsulated and/or conjugated to the nanoparticle to enable co-delivery of molecules.

Polyacrylamide nanoparticles can be synthesised using the inverse microemulsion free radical polymerisation technique. The synthesis involves a water-in-oil (W/O) microemulsion system in which the emulsion is stabilised using surfactants (Figure 3.3). Primary monomers, acrylamide, along with cross-linking monomer, *N,N'*-methylenebisacrylamide (Figure 3.1) are dissolved in water and are dispersed in hexane (oil phase) stabilised with surfactants. The polymerisation of these monomers is initiated using a water-soluble chemical initiator, ammonium persulfate (APS) which readily decomposes into free radical species. The rate of this process is often increased using an accelerator, typically a reactive nucleophile (see chapter 3.1.1, Scheme 3.1).

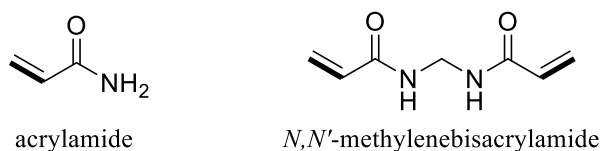


Figure 3.1 Structural formula of acrylamide and *N,N'*-methylenebisacrylamide. Carbon-carbon double bond in bold to highlight the site of attack for free radicals.

Upon reaction completion, purification of nanoparticle can be carried out by removing the oil phase and repeated washing with ethanol. This is possible due to precipitation of ethanol-insoluble

nanoparticles, allowing removal of residual organic solvent and surfactants, and collection of nanoparticles *via* filtration.

Alternatively, monomers bearing reactive moieties can also be introduced during the polymerisation reaction (Figure 3.2). This introduces reactive groups onto the nanoparticle allowing further modification of the nanoparticles.

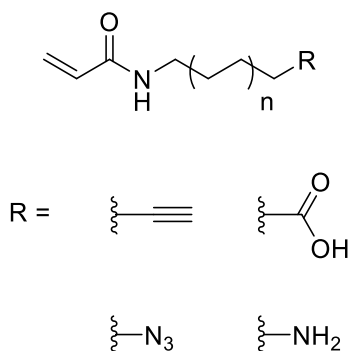


Figure 3.2 Acrylamide monomers bearing reactive functionality.

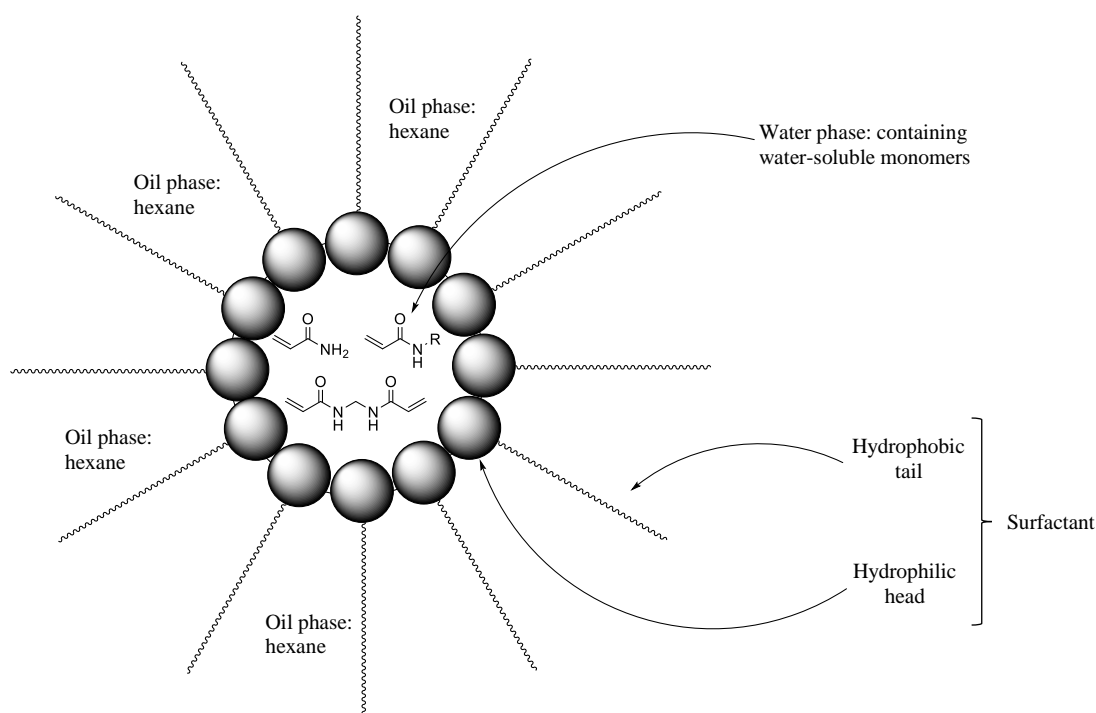


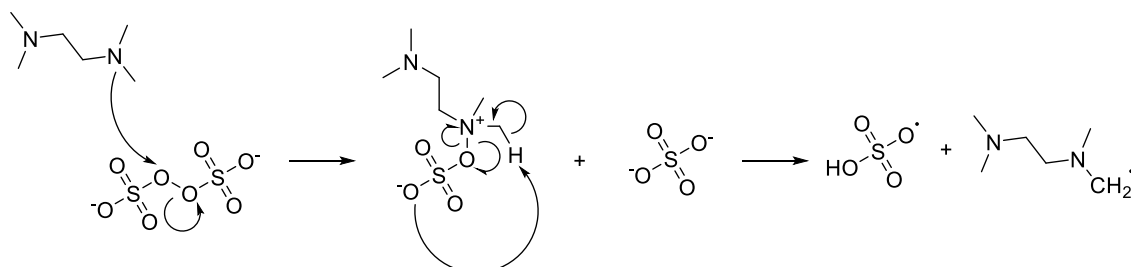
Figure 3.3 Schematic of a reverse micelle (water-in-oil micelle).

3.1.1 Free radical polymerisation

There are three main steps to free radical polymerisation: initiation, propagation, and termination.²³⁰

Radical polymerisation is typically started with the addition of an initiator.²³⁰ Examples of initiators are ammonium persulfate (water-soluble) and 2,2'-azobis(isobutyronitrile) (AIBN, oil-soluble). These initiators typically begin to dissociate almost immediately upon dissolution in

water/aqueous media, and this can be aided by a nucleophilic accelerator such as *N,N,N',N'*-tetramethylethylenediamine (TEMED) (Scheme 3.1). Upon dissociation, these initiators form two free radical species, capable of reacting with electron rich π -system, typically double bonds. The radical species will react with the π -system, forming a σ -bond and produces another radical (Scheme 3.2). This new radical species is then free to attack another molecule, causing a chain reaction.



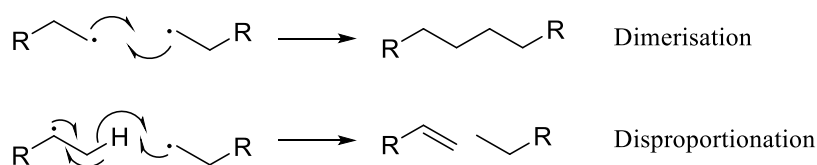
Scheme 3.1 Dissociation of persulfate with TEMED as an accelerator to generate free radicals.²³¹



Scheme 3.2 Initiation and propagation reaction scheme for free radical polymerisation.

This chain reaction allows the growth of the polymer chain, and is known as the propagation step in free radical polymerisation.²³⁰ This process will continue until monomers are exhausted. The depletion of monomers and/or radical species leads to the termination phase of the polymerisation.

The termination phase occurs when monomer concentrations begin to deplete. Upon depletion of monomers, polymer radicals can undergo two different reactions: dimerization or disproportionation (Scheme 3.3).²³⁰ Dimerization is the combination of two radical polymers forming a bigger polymer chain with no active reaction site (no radical). Disproportionation can also occur instead of dimerization, when a proton is transferred from one radical polymer chain to another radical polymer chain, while retaining an electron, resulting in two neutral polymers with no active reaction site. Disproportionation can also occur between radical polymer chains with impurities present in the reaction mixture, or with a radical scavenger such as molecular oxygen.



Scheme 3.3 Termination phase of free radical polymerisation, (Top) dimerization and (bottom) disproportionation.

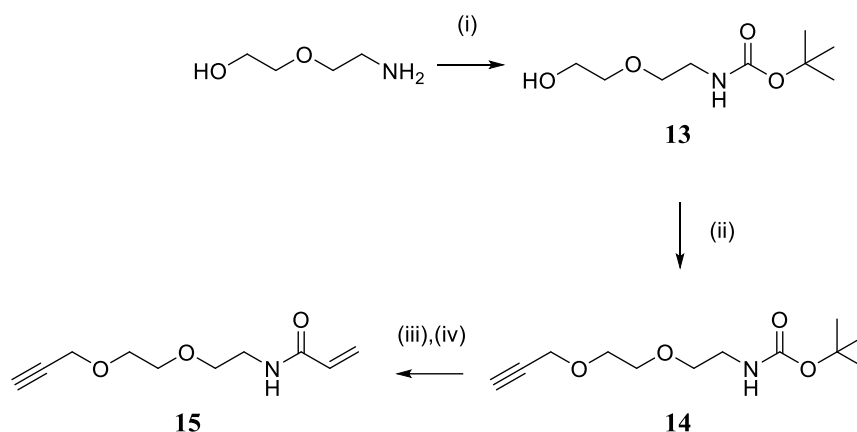
3.2 Synthesis of bifunctional acryloyl monomers and conjugatable molecules

Multifunctional polyacrylamide nanoparticles can be synthesised by incorporation of acryloyl monomers bearing reactive functionality. Incorporation of two or more types of reactive functionality allows the orthogonal conjugation of these reactive functional groups.

Amine functionalised acryloyl monomer is available as the commercially available *N*-(3-aminopropyl)methacrylamide (APMA). Unsurprisingly, several literature reports have shown their use in the synthesis of nanoparticles.^{203,229,232–238} However, there are no commercially available alkyne or azide functionalised acryloyl monomer, hence, in this sub-chapter, the synthesis of acrylamide monomers bearing alkyne and azide moieties are described.

These monomers incorporate ethylene glycol spacers as these chains are flexible and have little steric hindrance without increasing hydrophobicity. Subsequently, porphyrins bearing acryloyl group and azido groups are described. The former allows covalent incorporation of porphyrin into the nanoparticle during polymerisation, and the latter allows conjugation of porphyrin post nanoparticle synthesis.

3.2.1 Alkyne-bearing monomer



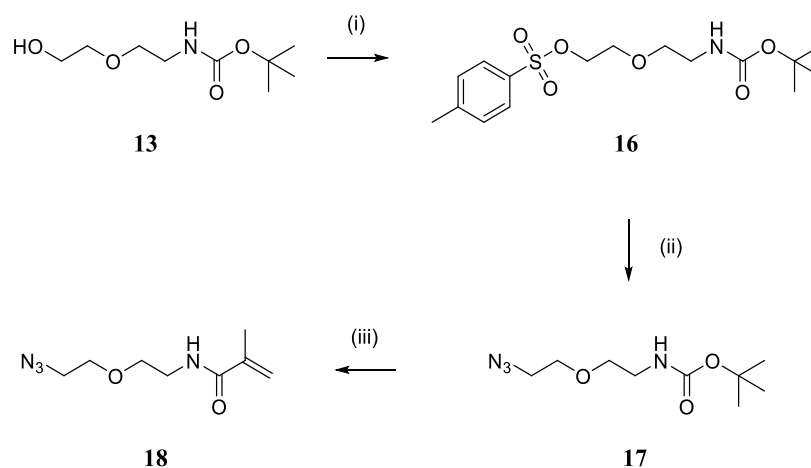
Scheme 3.4 Synthesis of *N*-(2-(2-(prop-2-yn-1-yloxy)ethoxy)ethyl)acrylamide from commercially available 2-(2-aminoethoxy)ethanol. Reagents, conditions, and yields; (i) DCM, di-*tert*-butyl dicarbonate, 40 °C, overnight, 93%, (ii) DMF, NaH, 30 mins, propargyl bromide, room temperature, overnight, 86%, (iii) 4 N HCl in dioxane, room temperature, 1 hour. (iv) dry DCM, Ar atmosphere, TEA, acryloyl chloride, 0 °C-room temperature, 4 hours, 21%.

Synthesis of the alkyne-acrylamide **15** was carried out using the commercially available 2-(2-aminoethoxy)ethanol (Scheme 3.4). Initially, boc-protection of the amine group was carried out using di-*tert*-butyl dicarbonate to give **13** in quantitative yield.²³⁹ Boc-protection is necessary to allow selective Williamson ether synthesis between propargyl bromide and the hydroxyl group on **13**, otherwise, the amine group can act as a nucleophile and participate in the substitution reaction. ¹H NMR clearly indicated the Boc-group with a chemical shift of 1.43 ppm which integrated to nine protons and matches literature values.²³⁹

Subsequent Williamson ether synthesis with propargyl bromide was carried out to afford **14** in 86% yield. ^1H NMR showed extra alkyl proton and the presence of the alkyne proton at δ 2.43 ppm. Electrospray ionization mass spectrometry showed a peak at m/z 244 $[\text{M}+\text{H}]^+$ confirming the identity of **14**.

Deprotection of the Boc-amine group on linker **14** was carried out in 4 N HCl solution in dioxane, and subsequent acetylation using acryloyl chloride afforded the acrylamide monomer with an alkyne functionality **15** in 21% yield, which is comparable to literature yields.²²⁹ ^1H NMR clearly indicates the characteristic resonance of the acryloyl group, with three double doublets at δ 5.63, 6.10, and 6.16 ppm. The successful synthesis of **15** afforded an alkyne functionalised acrylamide capable of introducing an alkyne moiety into polyacrylamide nanoparticles.

3.2.2 Azido-bearing monomer



Scheme 3.5 Synthesis of *N*-(2-(2-azidoethoxy)ethyl)methacrylamide from *tert*-butyl (2-(2-hydroxyethoxy)ethyl)carbamate, described earlier in chapter 3.2.1. Reagents, conditions, and yields: (i) dry DCM, *p*-toluenesulfonyl chloride, DIPEA, DMAP, inert atmosphere, 0 °C-room temperature, overnight, 89%, (ii) dry DMF, NaN_3 , 90 °C, 48 hours, 82%, (iii) 4 N HCl in dioxane, room temperature, 1 hour. (iv) DMF, methacrylic anhydride, DIPEA, inert atmosphere, overnight, 23%.

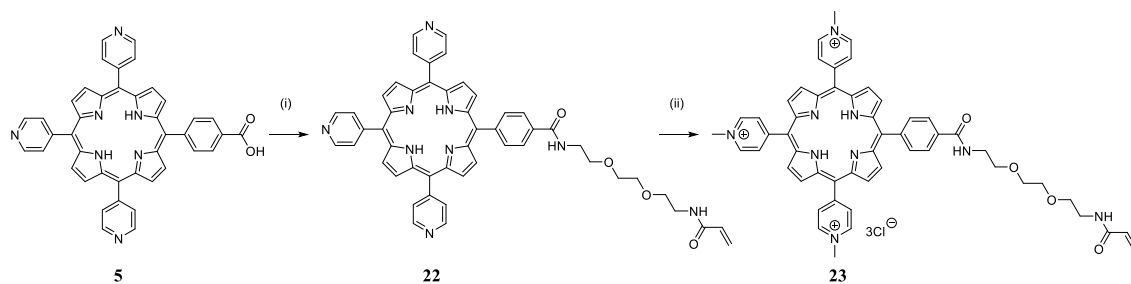
Synthesis of an azide-bearing acryloyl monomer **18** is shown in Scheme 3.5. Initially, reaction with *p*-toluenesulfonyl chloride to prepare **16** was carried out in inert and basic conditions to activate the hydroxyl group. This afforded **16** in 89% yield with an excellent tosyl leaving group, compared to the poor hydroxyl leaving group in **13**. The introduction of the tosyl group was identified using NMR, with clear indication of the presence of aromatic groups (δ 7.34-7.79) and additional singlet alkyl peak (δ 2.44).

Subsequent nucleophilic substitution with NaN_3 was carried out at elevated temperature (90 °C) and suggested quantitative conversion of **16** to **17** on TLC, however, the isolated yield was 82%. The lower isolated yield was suspected due to loss of product during liquid-liquid extraction workup, which is an essential step for the removal of toxic azide salts. Removal of the tosyl group is observed on NMR and mass spectrometry, indicating the successful synthesis of the product.

Boc-deprotection using HCl in dioxane afforded an amine group allowing further conjugation. Reaction with methacrylic anhydride under basic condition yielded **18** in 23% yield, with NMR spectroscopy confirming the identity of the product. The methacrylic group is capable of undergoing free radical polymerisation, as shown by the extensive use of the commercially available APMA in literature,^{203,229,232–238} which allows the introduction of reactive azide groups onto polymeric nanoparticles *via* **18**.

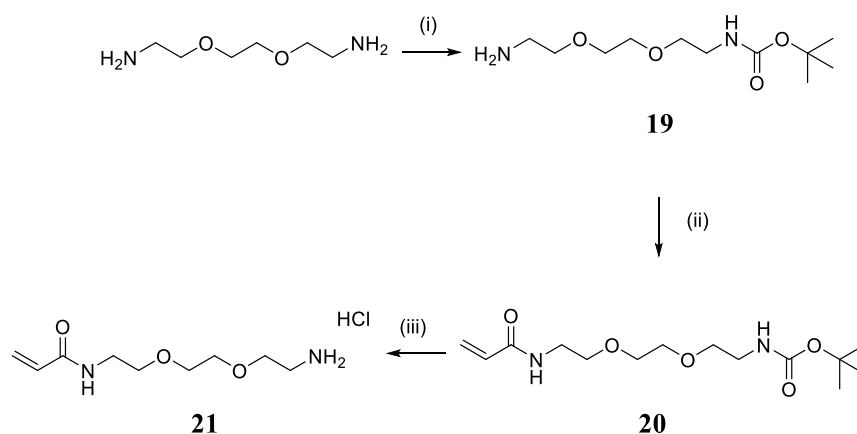
3.2.3 Porphyrin synthesis for covalent incorporation

An alternative strategy for the incorporation of drug molecules into polyacrylamide nanoparticles is through encapsulation or incorporation. There are numerous literature examples of inclusion of molecules in polymeric nanoparticles either *via* non-covalent encapsulation^{203,229,232,233,238,240–242} or covalent incorporation.^{243–246} In this subchapter, synthesis of porphyrin for covalent incorporation is described. Covalent incorporation is the incorporation of porphyrin together with the polymerisation/formation of nanoparticle and is not to be mistaken for covalent conjugation with pre-formed nanoparticles.



Scheme 3.6 Synthesis of water-soluble acryloyl-porphyrin. Reagents, conditions, and yields: (i) DMF, EDC, HOBT, DMAP, **21**, 40 °C, overnight, 48%, (ii) DMF, MeI, 40 °C, overnight, 97%.

Despite extensive research into polymeric nanoparticles, there are limited examples of covalent incorporation of porphyrins into polymeric nanoparticles. Thereby, the synthesis of a water-soluble porphyrin with an appended acryloyl group **23** was attempted (Scheme 3.6). Porphyrin **23** has been described in the literature for use in embedding into a polyacrylamide support for the use in photodynamic inactivation of microorganisms,²⁰² hence, porphyrin **23** was chosen to be translated for covalent incorporation into polyacrylamide nanoparticles for the use in photodynamic therapy.

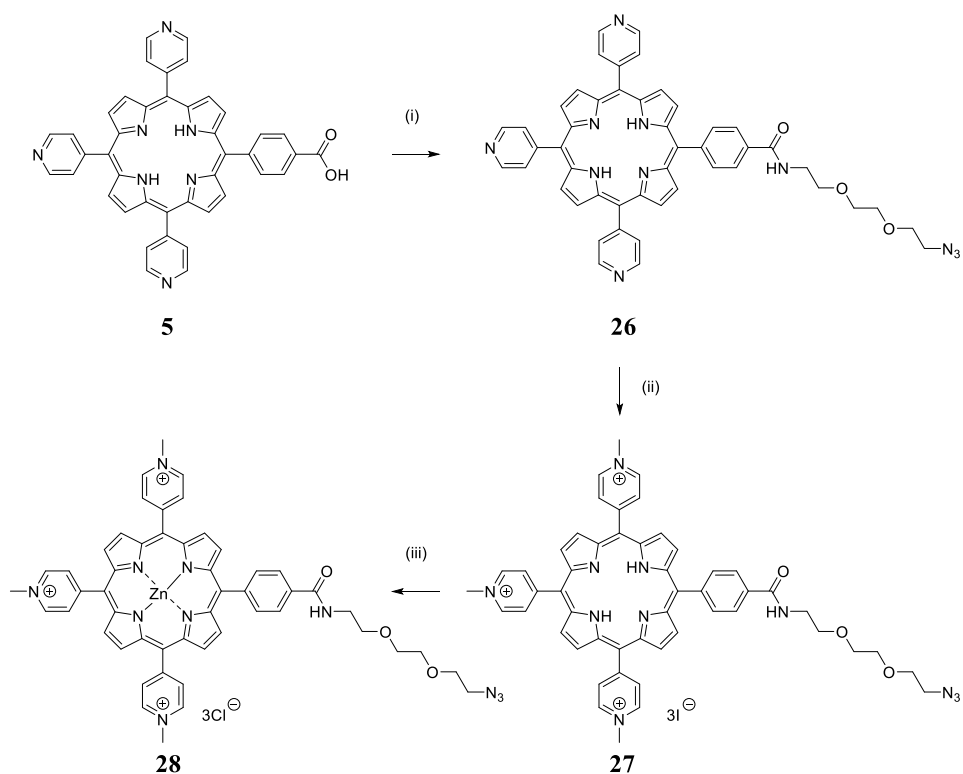


Scheme 3.7 Synthesis of acryloyl-functionalised linker **21**. Reagents, conditions, and yields: (i) dry DCM, di-tert-butyl decarbonate, inert atmosphere, 0 °C-room temperature, overnight, 76%. (ii) dry DCM, acryloyl chloride, 0 °C-room temperature, overnight, 40%. (iii) 4 N HCl in dioxane, room temperature, 1 hour, 98%.

Initially, synthesis of an acryloyl-functionalised linker **21** was carried out as shown in Scheme 3.7. Starting with commercially available 2,2'-(ethylenedioxy)diethylamine, it was selectively mono-Boc protected using a method described in the literature.²⁴⁷ This reaction gives a mixture of starting material, mono-boc, and di-boc protected diamine linkers. Purification by column chromatography afforded **19** in 76% yield and allows the selective peptide coupling of one amine group with acryloyl chloride. Using a literature method, reaction between **19** and acryloyl chloride afforded **20** in 40% yield with NMR spectroscopy matching literature values.²⁴⁸ Subsequent HCl-mediated Boc-deprotection afforded acryloyl-functionalised linker **21** in quantitative yield with a primary amine group allowing further conjugation with a porphyrin.

Synthesis of porphyrin **23** is shown in Scheme 3.6 and was carried out according to a literature method.²⁰² Briefly, porphyrin **5** described in chapter 2.1.2 was coupled with linker **21** using common coupling reagents, EDC and HOBt. The desired product, **22**, was isolated using column chromatography in 48% yield with NMR spectroscopy matching literature values, showing aromatic porphyrin protons (δ 8.15-9.05), alkyl protons from the linker (δ 3.58-3.84), and characteristic acryloyl protons (δ 5.59-6.26).²⁰² Quaternisation of pyridyl groups with methyl iodide afforded porphyrin **23** in quantitative yield, with the identity of the product confirmed using NMR spectroscopy, with the presence of *N*-methylated protons at δ 4.70. The successful synthesis of porphyrin **23** afforded a water-soluble porphyrin with an appended acryloyl group capable of covalent incorporation into polyacrylamide nanoparticles.

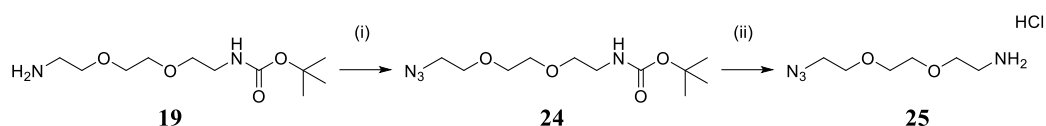
3.2.4 Porphyrin synthesis for covalent conjugation



Scheme 3.8 Synthesis of zinc complexed water-soluble azido porphyrin. Reagents, conditions, and yields: Reagents and conditions: (i) DMF, EDC, HOBT, DMAP, **25**, 40 °C, overnight, 73% (ii) DMF, MeI, 40 °C, overnight, 99%, (iii) water, zinc acetate, 40 °C, overnight, 93%.

Herein, a water-soluble porphyrin, complexed with zinc, and bearing an azido-appended group was synthesised according to a literature method.²⁴⁹ As mentioned before in chapter 2.1.3, the zinc complex of the porphyrin is a necessity for copper-catalysed azide-alkyne cycloaddition (CuAAC), as free-base porphyrins can readily complex copper, and this has been shown to have a detrimental effect on photodynamic activity.³ Instead of using azido-porphyrin **11** as described in chapter 2.1.3, an ethylene glycol spacer group was also introduced. It has been shown that photocytotoxicity of porphyrins conjugated to an antibody can be improved by introducing a hydrophilic spacer group.²⁰⁰ When conjugated porphyrins are in close proximity, this leads to excited state quenching, resulting in poorer singlet oxygen quantum yields, hence, the use of a spacer group has been shown to improve photocytotoxicity.²⁰⁰ Hereby, porphyrin **28** was devised to covalently conjugate onto nanoparticles (Scheme 3.8).

Using a similar synthetic strategy as for porphyrin **23**, an amine linker bearing an azido group **25** was initially synthesised, as shown in Scheme 3.9. Following a modified method from literature, mono-Boc protected diamine linker **19**, described earlier in chapter 3.2.3, was reacted with an azide transfer reagent, imidazole-1-sulfonyl azide hydrochloride to afford **24** in 71% yield with analysis matching literature values.²⁵⁰ Similar HCl-mediated Boc-deprotection utilised for linker **21** was carried out to afford **25**, an azide-functionalised linker with an amine group for conjugation onto the porphyrin.



Scheme 3.9 Synthesis of azido-functionalised linker. Reagents, conditions, and yields: (i) MeOH, $\text{CuSO}_4 \cdot 5\text{H}_2\text{O}$, K_2CO_3 , Imidazole-1-sulfonyl azide hydrochloride, room temperature, overnight, 71%, (ii) 4 N HCl in dioxane, room temperature, 1 hour, 91%.

Scheme 3.8 shows the synthesis of zinc complexed water-soluble azido porphyrin. Similar to the synthesis of porphyrin **23**, peptide coupling using EDC and HOBt was carried out between porphyrin **5** and linker **25** to afford porphyrin **26**. Subsequent quaternisation of *meso*-pyridyl groups on porphyrin **26** with methyl iodide afforded water-soluble porphyrin **27**. Porphyrin **27** readily complexes zinc in water to afford the desired clickable porphyrin **28** capable of covalent conjugation onto nanoparticles. The successful synthesis of porphyrin **26-28** were confirmed using NMR spectroscopy, showing aromatic porphyrin proton (δ 8.30-9.45), alkyl protons from the linker (δ 3.40-3.65), and *N*-methylated protons (δ 4.69). Accurate mass spectrometry and UV-vis spectroscopy are also in agreement with the identity of the compound which matches literature values.²⁵¹

3.2.5 Synthesis of conjugatable metal chelator

The acyclic metal-chelator, diethylenetriaminepentaacetic acid (DTPA) was chosen as the ligand of choice. This is due to the flexibility of DTPA to chelate various MRI, PET, or SPECT imaging metals such as Gd, ^{68}Ga , $^{99\text{m}}\text{Tc}$, ^{111}In , $^{86/90}\text{Y}$, and ^{89}Zr .⁸⁶ DTPA also has been FDA approved for pharmaceutical and radiopharmaceutical applications, such as Magnevist® for use as an MRI contrast agent and technetium-99m pentetate as a SPECT imaging agent (Figure 3.4).²⁵²

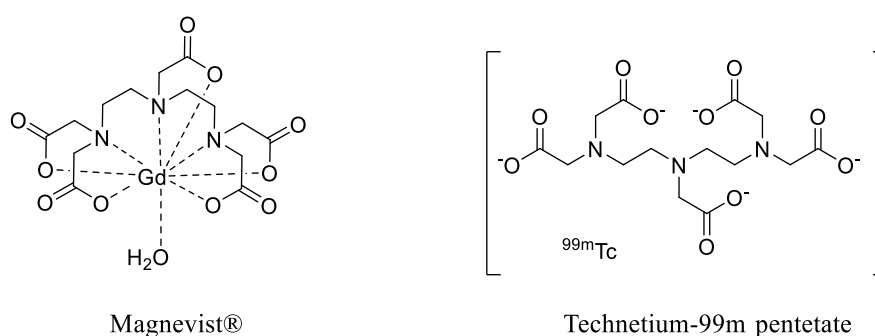
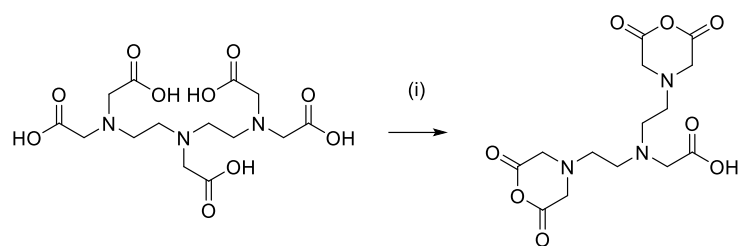


Figure 3.4 Magnevist® and technetium-99m pentetate.

The ease of conjugation with DTPA has also been shown in the literature, which describe conjugation of DTPA onto nanoparticles²⁵³ and biomolecules.^{254,255} The relatively low cost of DTPA, highly flexible metal chelate, and the extensive literature of DTPA, presented it as an excellent candidate for conjugation onto nanoparticles.



29

Scheme 3.10 Synthesis of DTPA-DA. Reagents, conditions, and yields: (i) acetic anhydride, pyridine, 65 °C, overnight, 93%.

Prior to nanoparticle conjugation, DTPA was activated to form the more reactive DTPA-dianhydride (DTPA-DA) **29** as shown in Scheme 3.10. Following a well-established literature method, DTPA-DA **29** was prepared by heating DTPA with acetic anhydride in the presence of pyridine.²⁵⁶ The formation of DTPA-DA **29** was followed using NMR, showing protons in the alkyl region (δ 2.55-3.68) which matches literature values.²⁵⁶ This afforded a metal chelate capable of conjugating onto amine groups on nanoparticles.

3.3 Synthesis of polyacrylamide nanoparticle (PAN)

Throughout this chapter, polyacrylamide nanoparticle will be referred to as PAN. Functional groups'/molecules' names following PAN denotes functional groups/molecules covalently incorporation into the nanoparticle during polymerisation. Molecules' name preceding PAN denotes molecules covalently conjugated onto the nanoparticle. Subscript following the names of functional groups/molecules denotes the molar percentage of the molecules, % added during synthesis/polymerisation of PAN. For example:



Where this PAN consists of 1.0% amine group covalently incorporated during polymerisation of PAN and these amine groups are available for further modification. This PAN also consists of porphyrin covalently conjugated onto a 1.0% functional group on the PAN. Molar percentage of functional groups/molecules was calculated using the following formula:

$$\text{molar percentage} = \frac{\text{number of moles of functional groups/molecules}}{\text{number of moles of (acrylamide + methylenebisacrylamide)}}$$

3.3.1 Synthesis of blank PAN

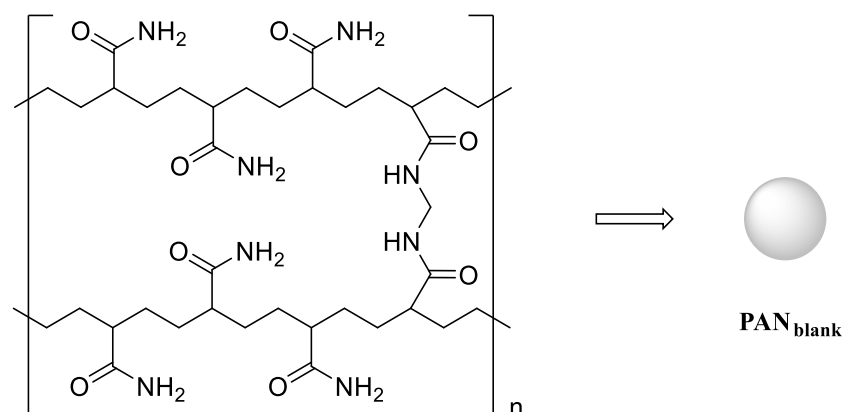


Figure 3.5 PAN_{blank} prepared by polymerisation of acrylamide, and *N,N'*-methylenebisacrylamide.

Using a modified literature method as mentioned earlier in chapter 3.1, blank polyacrylamide nanoparticles (PAN_{blank}) were synthesised using acrylamide and *N,N'*-methylenebisacrylamide as the monomers, without the addition of any other functional groups or drug/imaging molecules (Figure 3.5).^{203,257,258} PAN_{blank} acted as a control for subsequent PAN synthesis and was analysed using DLS and zeta potential. PAN_{blank} size measured by intensity dynamic light scattering (DLS), z_{ave} , is 41 nm (Figure 3.6), with a zeta potential of -8.3 mV.

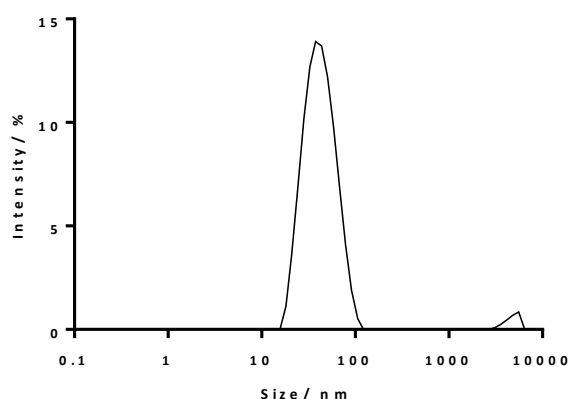


Figure 3.6 DLS size distribution by intensity of PAN_{blank}.

3.3.2 Synthesis of mono-functionalised PAN

3.3.2.1 Amine-functionalised PAN

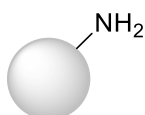


Figure 3.7 PAN-(amine) prepared by co-polymerisation of APMA, acrylamide, and *N,N'*-methylenebisacrylamide.

Numerous literature reports have shown amine groups can be introduced into PAN using APMA.^{203,229,232–238} Hereby, following similar literature methods, 0.5% APMA was added to the

aqueous monomer mixture, acrylamide and *N,N'*-methylenebisacrylamide.²²⁹ Resulting **PAN-(amine_{0.5})** (Figure 3.7) shows an increase in z_{ave} and zeta potential in comparison to **PAN_{blank}** from 41 nm, -8.3 mV to 69 nm, -1.6 mV.

3.3.2.2 Covalent-encapsulation of porphyrin into PAN

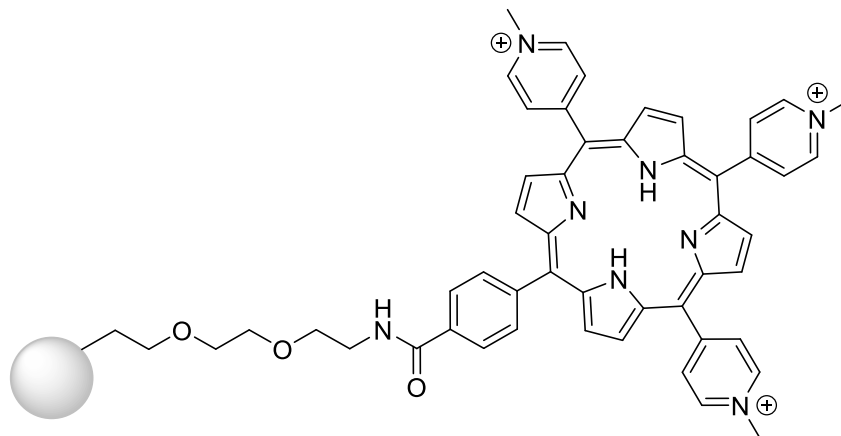


Figure 3.8 **PAN-(porphyrin)** prepared by co-polymerisation of porphyrin **23**, acrylamide, and *N,N'*-methylenebisacrylamide.

Incorporation of porphyrin *via* covalent encapsulation was carried out using porphyrin **23**. **PAN-(porphyrin)** was prepared by adding porphyrin **23** along with acrylamide and *N,N'*-methylenebisacrylamide for co-polymerisation (Figure 3.8).

Initially, 0.05% porphyrin was used to prepare **PAN-(porphyrin_{0.05})**. Repeated washing with ethanol removed excess porphyrin **23**, which is ethanol-soluble, yielding **PAN-(porphyrin_{0.05})** as a brown solid. UV-vis. spectroscopy confirmed the presence of porphyrin with a loading of 4.6 nmol per mg of PAN. By incorporating a cationically charged porphyrin into the PAN, an increase in zeta potential was observed from -8.3 mV (**PAN_{blank}**) to -4.3 mV **PAN-(porphyrin_{0.05})**, with a z_{ave} of 44 nm (Figure 3.9).

A higher concentration of porphyrin (0.5%) was also used to increase the loading of porphyrin, and prepare **PAN-(porphyrin_{0.5})**. As expected, a higher loading of porphyrin on the PAN (26 nmol per mg), higher zeta potential (+4.1 mV), and larger z_{ave} (83 nm) was observed (Figure 3.9).

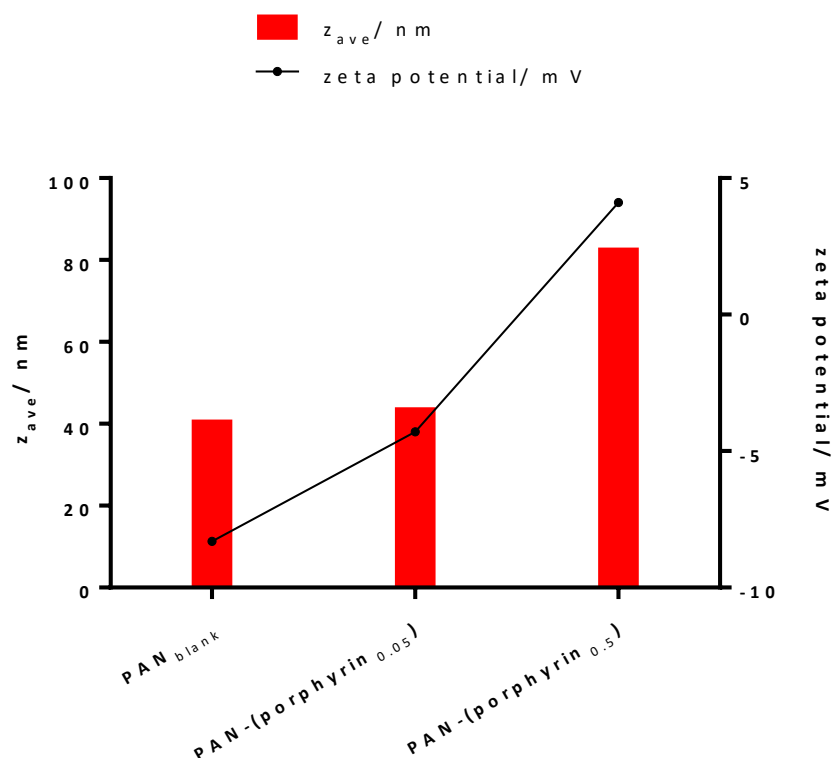


Figure 3.9 z_{ave} and zeta potential of PAN_{blank}, PAN-(porphyrin_{0.05}), and PAN-(porphyrin_{0.5}).

However, the incorporation of porphyrin **23** resulted in the formation of PAN with greater polydispersity and a severe loss in yield; 21% yield for PAN-(porphyrin_{0.5}). Polydispersity was observed in both PAN-(porphyrin_{0.5}) and PAN-(porphyrin_{0.05}) with a polydispersity index (PDI) of 0.55 and 0.38, respectively. Greater polydispersity observed in PAN-(porphyrin_{0.5}) is expected due to the high PDI and as observed in its DLS size distribution (Figure 3.10), which shows multiple and broad size population.

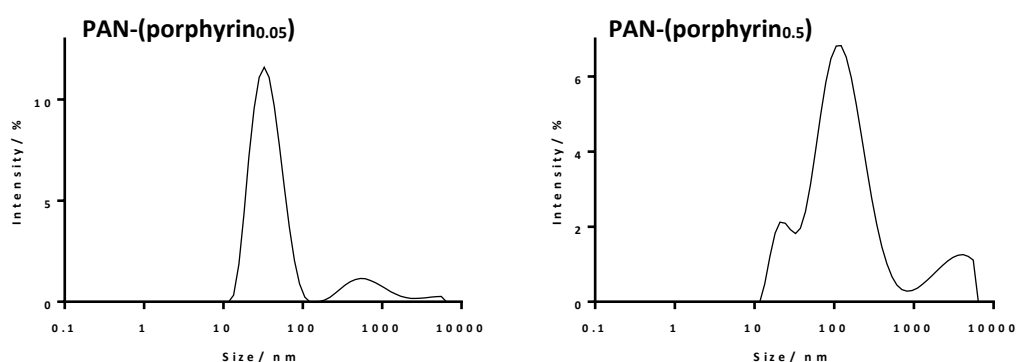


Figure 3.10 DLS size distribution by intensity of PAN-(porphyrin_{0.05}) (left) and PAN-(porphyrin_{0.5}) (right).

Nevertheless, incorporation of porphyrin was clearly observed on UV-vis. spectroscopy, with agreement from data obtained from DLS and zeta potential. Hence, attempts to introduce additional functionality for further modification onto PAN-(porphyrin) was carried out.

3.3.3 Synthesis of dual functional PAN *via* covalent-encapsulation of porphyrin

3.3.3.1 Covalent-encapsulation of porphyrin into PAN with amine functionality

In chapter 3.3.2, the introduction of amine groups using APMA was achieved efficiently by co-polymerised into PAN; however, polydispersity and multimodal populations were observed using DLS following the synthesis of PAN with covalently incorporated porphyrins **23**. Despite these results, attempts to covalently incorporate porphyrin **23** with an additional amine-functionality was carried out (Figure 3.11).

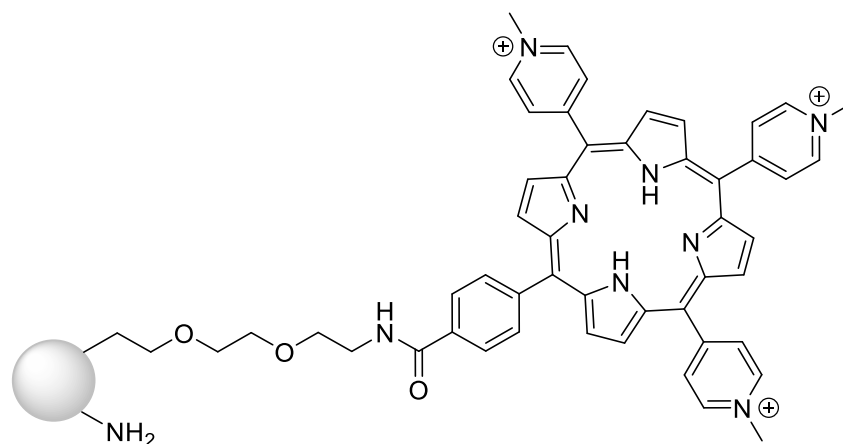


Figure 3.11 **PAN-(porphyrin-amine)** prepared by co-polymerisation of porphyrin **23**, APMA, acrylamide, and *N,N'*-methylenebisacrylamide.

Porphyrin 23 / %	APMA/ %	Zeta potential/ mV	Intensity DLS/ nm	Porphyrin loading/ nmol per mg of PAN	PDI	One size population	Yield / %
0.02	0.5	+5.5±2.6	61±23	2.3	0.32	✓	64
0.05	0.5	+6.2±4.3	33±5	4.2	0.22	✓	60
0.5	0.5	+5.8±2.0	128±60	27.0	0.34	×	28
0.05	1.0	+9.7	31	3.7	0.27	✓	70
0.05	2.0	+16	23	4.2	0.23	✓	82

Table 3.1 Varying molar percentage of porphyrin **23** and APMA used for the synthesis of **PAN-(porphyrin-amine)**.

Table 3.1 summarises results obtained from varying molar percentages of porphyrin **23** and APMA used for the synthesis of **PAN-(porphyrin-amine)**. Initially, molar percentages of porphyrin **23** used were 0.02%, 0.05% and 0.5% with 0.5% APMA. As expected, with higher molar percentages of porphyrin, more than one size population distribution with irreproducible z_{ave} was observed (Figure 3.12) for **PAN-(porphyrin_{0.5}-amine_{0.5})**; a decrease in PAN yield for **PAN-(porphyrin_{0.5}-amine_{0.5})** was also observed, with a yield of 28%. Zeta potential measurements showed positive potentials for all **PAN-(porphyrin-amine)** synthesised (Figure

3.13), indicating incorporation of both positively charged porphyrins and amine groups. Porphyrin loadings of 2.3, 4.2, and 27 nmol for **PAN-(porphyrin_{0.02}-amine_{0.5})**, **PAN-(porphyrin_{0.05}-amine_{0.5})**, and **PAN-(porphyrin_{0.5}-amine_{0.5})**, respectively, were obtained using UV-vis. spectroscopy. It was deduced that the highly charged and bulky porphyrin **23** was preventing a higher loading of porphyrin and was detrimentally affecting the synthesis of PAN, resulting in lower PAN yields.

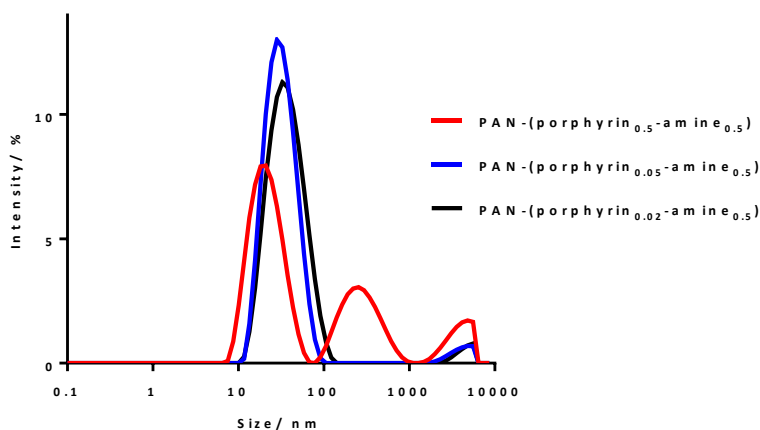


Figure 3.12 DLS Size distribution by intensity of PAN-(porphyrin_{0.02}-amine_{0.5}), PAN-(porphyrin_{0.05}-amine_{0.5}), and PAN-(porphyrin_{0.5}-amine_{0.5}).

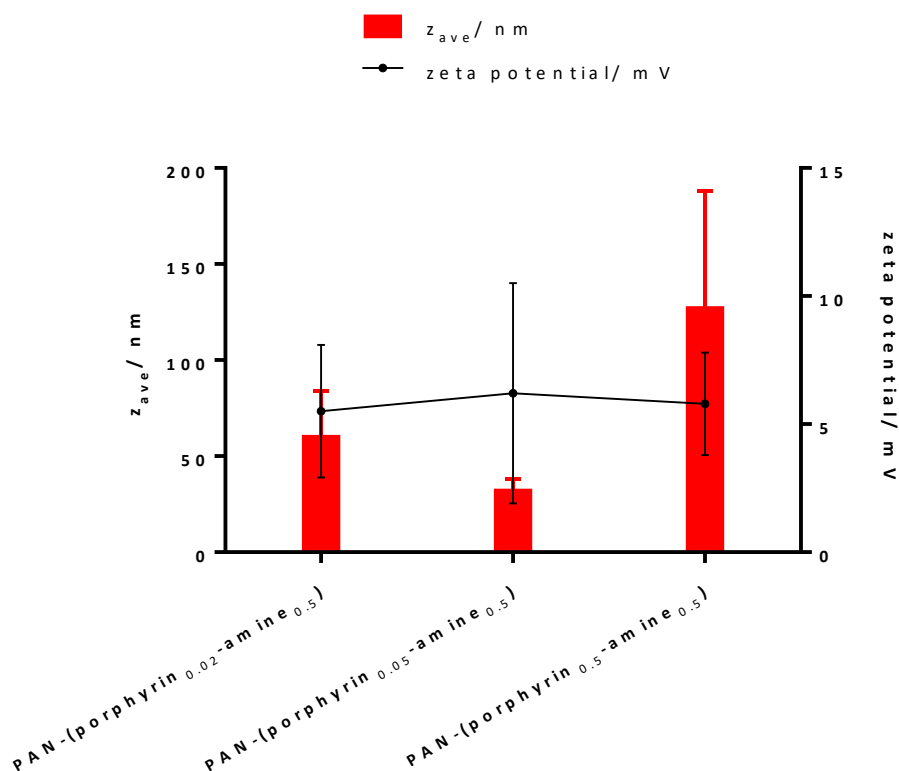


Figure 3.13 z_{ave} and zeta potential of PAN-(porphyrin_{0.02}-amine_{0.5}), PAN-(porphyrin_{0.05}-amine_{0.5}), and PAN-(porphyrin_{0.5}-amine_{0.5}). Error bars shown were obtained from triplicate measurements.

Introduction of higher molar percentages of amine groups was also attempted using 1.0% and 2.0% of APMA with 0.05% porphyrin **23**. Increasing the molar percentage of APMA resulted in an increase in zeta potential (Figure 3.15), indicating greater incorporation of amine groups. DLS measurement shows that using higher molar percentages of APMA does not detrimentally affect the polydispersity of PAN (Figure 3.14).

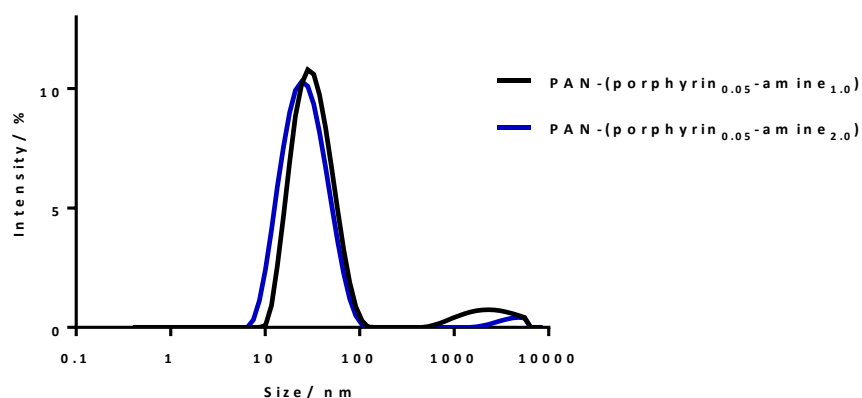


Figure 3.14 DLS Size distribution by intensity of PAN-(porphyrin_{0.05}-amine_{1.0}) and PAN-(porphyrin_{0.05}-amine_{2.0}).

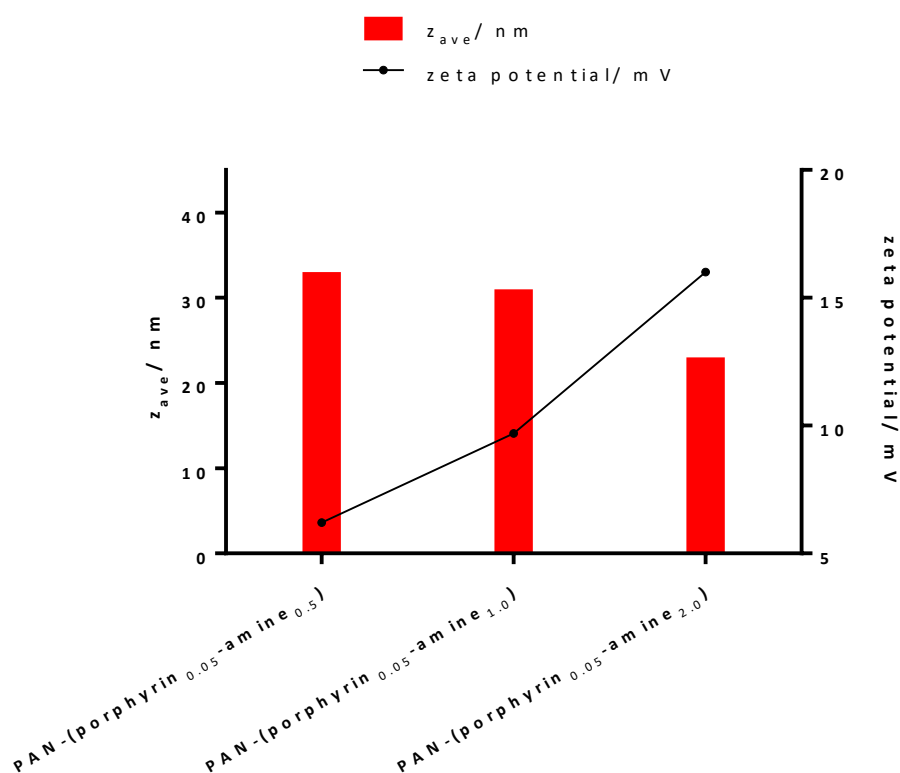
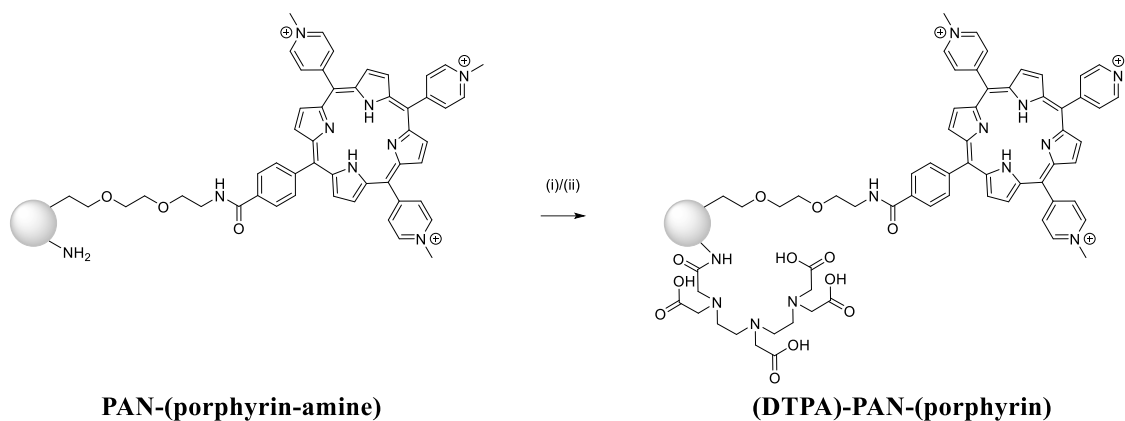


Figure 3.15 z_{ave} and zeta potential of PAN-(porphyrin_{0.05}-amine_{0.5}), PAN-(porphyrin_{0.05}-amine_{1.0}) and PAN-(porphyrin_{0.05}-amine_{2.0}).

3.3.3.2 Conjugation of DTPA onto PAN

Conjugation with DTPA was attempted with PAN-(porphyrin_{0.05}-amine_{0.5}), and PAN-(porphyrin_{0.5}-amine_{0.5}).



Scheme 3.11 Reaction scheme for the synthesis of **(DTPA)-PAN-(porphyrin)** from **PAN-(porphyrin-amine)**. Reagents and conditions: (i) DTPA-DA **29**, triethylamine, room temperature, overnight. (ii) DTPA-DA **29**, saturated NaHCO₃, room temperature, overnight.

Several methods were attempted to conjugate DTPA onto the amino groups incorporated into the PAN (Figure 3.11). It has been reported in the literature that the rate of reaction of DTPA-DA **29** in water is rapid, with reactions complete in 20 seconds, and the rate of reaction determined by the rate of dissolution of DTPA-DA **29**.²⁵⁵ Hence, **PAN-(porphyrin-amine)** was first dispersed in water with triethylamine or saturated aqueous NaHCO₃, and this was quickly added to DTPA-DA **29** with vigorous stirring.²⁵⁵ Purification using gel filtration chromatography and precipitation from ethanol, yielded PAN with negative zeta potentials, indicating conjugation of negatively charged DTPA onto PAN.

(DTPA_{0.5})-PAN-(porphyrin_{0.05}) prepared from **PAN-(porphyrin_{0.05}-amine_{0.5})** using triethylamine as a base, yielded PAN with zeta potential of -6.0 ± 8.0 mV and z_{ave} of 55 ± 17 nm. **(DTPA_{0.5})-PAN-(porphyrin_{0.5})** prepared from **PAN-(porphyrin_{0.5}-amine_{0.5})** with either triethylamine or aqueous NaHCO₃ as a base, yielded PAN with zeta potential of -5.4 mV and -1.8 mV, and z_{ave} of 54 nm and 220 nm, respectively (Figure 3.16).

Unsurprisingly, multiple size populations were observed in the size distribution of **PAN-(porphyrin_{0.5}-amine_{0.5})** as described earlier in chapter 3.3.3.1, and its polydispersity remained even after DTPA conjugation to prepare **(DTPA_{0.5})-PAN-(porphyrin_{0.5})**, with PDI of 0.47 and 0.57 for **(DTPA_{0.5})-PAN-(porphyrin_{0.5})** prepared with triethylamine and NaHCO₃, respectively (Figure 3.17).

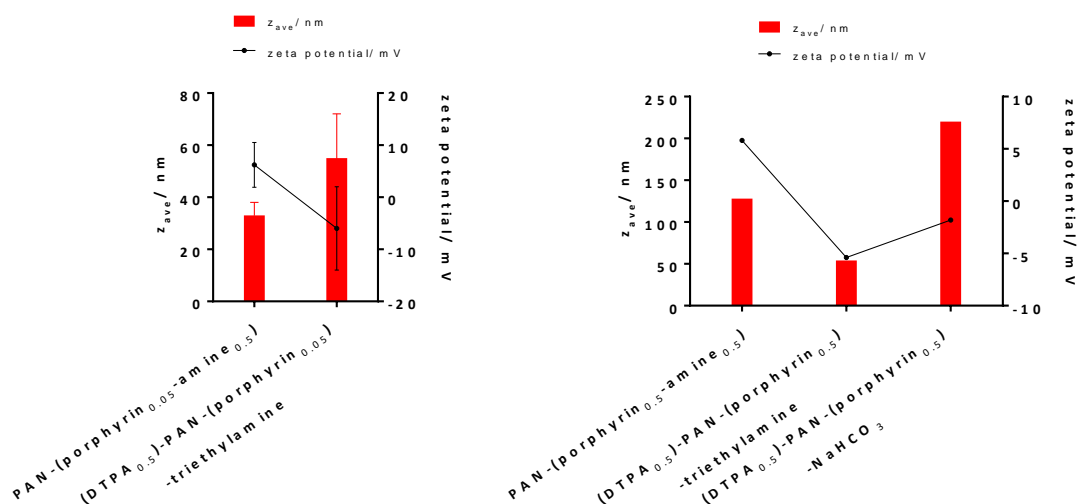


Figure 3.16 z_{ave} and zeta potential of PAN-(porphyrin_{0.05}-amine_{0.5}) and DTPA_{0.5}-PAN-(porphyrin_{0.05}) (left), and PAN-(porphyrin_{0.5}-amine_{0.5}), DTPA_{0.5}-PAN-(porphyrin_{0.5})-triethylamine, and DTPA_{0.5}-PAN-(porphyrin_{0.5})-NaHCO₃ (right). Error bars shown were obtained from triplicate measurements.

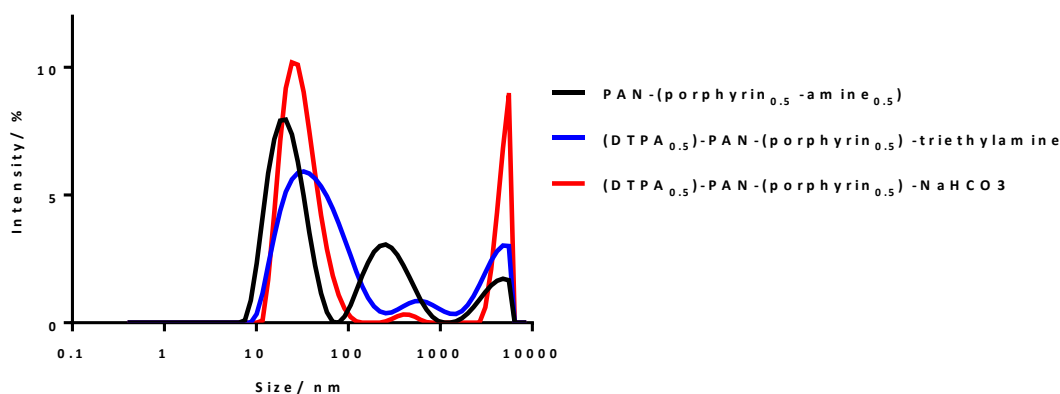


Figure 3.17 DLS Size distribution by intensity of PAN-(porphyrin_{0.5}-amine_{0.5}), (DTPA_{0.5})-PAN-(porphyrin_{0.5})-triethylamine, and (DTPA_{0.5})-PAN-(porphyrin_{0.5})-NaHCO₃.

3.3.3.3 Addressing polydispersity in covalent-encapsulation of porphyrin

Synthesis of PAN *via* covalent incorporation of porphyrin resulted in low yielding PAN with multiple size population measured using DLS, with higher degree of polydispersity observed with the incorporation of higher molar percentage of porphyrin **23**, as shown and described in chapter 3.3.2 and chapter 3.3.3.

It was deduced that the bulky and highly-charged porphyrin affects the efficiency of the synthesis of PAN. To further investigate this issue, certain reaction conditions were changed to optimise the reaction. Variables changed included varying the ratio of primary monomers, acrylamide and *N,N'*-methylenebisacrylamide.

Primary monomer ratios of 100:1 and 2:1 of acrylamide:*N,N'*-methylenebisacrylamide with 0.5% porphyrin **23**, with other variables kept constant, were attempted (Table 3.2 and Figure 3.18).

	Porphyrin 23	Acrylamide	<i>N,N'</i> - methylenebis- acrylamide	Yield/ %	PDI	Single size population
PAN- (porphyrin_{0.5}) Ratio 7.4:1	40 mg, 0.04 mmol	527 mg, 7.4 mmol	160 mg, 1.0 mmol	21	0.55	×
Ratio 100:1	40 mg, 0.04 mmol	576 mg, 8.1 mmol	12 mg, 0.08 mmol	20	0.14	✓
Ratio 2:1	20 mg, 0.02 mmol	201 mg, 2.8 mmol	216 mg, 1.4 mmol	19	0.45	×

Table 3.2 Effect of monomer ratio on PAN yield and PAN polydispersity.

With a higher ratio of acrylamide and a lower amount of cross-linking monomer, *N,N'*-methylenebisacrylamide, a single size population was observed on DLS, with a z_{ave} of 88 nm. This was justified as, with less cross-linker, a more porous PAN was formed, and hence the sterically bulky and charged porphyrin was capable of covalently incorporating into the PAN without detrimental effecting the polydispersity.

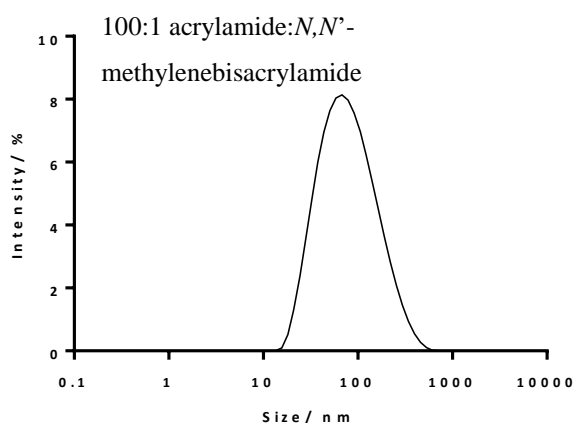


Figure 3.18 DLS Size distribution by intensity of PAN synthesised with primary monomer ratio of 100:1 acrylamide:*N,N'*-methylenebisacrylamide (left) and (right).

Nevertheless, the yields of PAN resulting from varying the monomer ratio remained low (20%) and this was not further pursued.

3.3.3.4 Dynamic light scattering (DLS) analysis: size distribution by intensity and by number

Dynamic light scattering (DLS) measures the hydrodynamic radius of nanoparticles. This is determined from the Brownian motion of nanoparticles, which decreases with increasing nanoparticle size. DLS does so by illuminating the nanoparticle sample with a laser and analysing the intensity fluctuations in the scattered light against a time period, hence the name dynamic light scattering. By using a correlation function, the size distribution of the nanoparticle can be calculated. The size distribution can then be expressed as size distribution by intensity, volume,

number, and sometimes in mass, which unfortunately gives quite different sizes. However, neither of these results are inherently ‘right’ or ‘correct’,²⁵⁹ and an explanation is given below.

In chapter 3.3.2 and chapter 3.3.3, PANs synthesised *via* covalent incorporation of porphyrin **23** resulted in multiple size populations as observed using DLS. This indicates the presence of two or more nanoparticle size populations in the sample. However, this may not be a true representation of the sample, as bigger particles scatter much more light than smaller particles, hence, there are only tiny amounts of nanoparticles in the bigger size population shown earlier in this chapter.

Figure 3.19 gives a visual representation for this explanation.²⁶⁰ Briefly, assuming a sample with two size distributions at 10 nm and 100 nm, each with equal number of nanoparticles. Size distribution by number will show equal amplitude at both sizes. Size distribution by volume will show nanoparticle size at 100 nm to be 1000 times larger in amplitude compared to the nanoparticle size at 10 nm. This is due to the volume of 100 nm nanoparticles being 1000 times larger than 10 nm (volume of sphere = $\frac{4}{3}\pi r^2$). Size distribution by intensity will show nanoparticle size at 100 nm to be 1,000,000 times larger in amplitude compared to the nanoparticle size at 10 nm. This is due to the intensity of scattering of a particle being proportional to the sixth power of its diameter (from Rayleigh’s approximation).

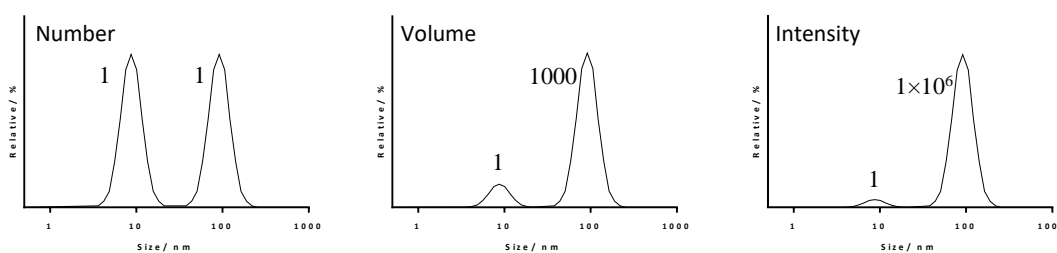


Figure 3.19 Difference between size distribution by number (left), volume (middle), and intensity (right). Figure was redrawn with reference from *Zetasizer Nano Series User manual*, Malvern Instrument, Series 1.1., 2013.²⁶⁰

If DLS analysis using size distribution by number was employed, the following results (Figure 3.20) can be obtained for PAN described in chapter 3.3.2 and chapter 3.3.3, giving a reproducible size, and a good representation of the nanoparticle size. Unsurprisingly, some literature chooses to show DLS analysis of polymeric nanoparticles by size distribution by volume^{235,261} and by number.²⁴³

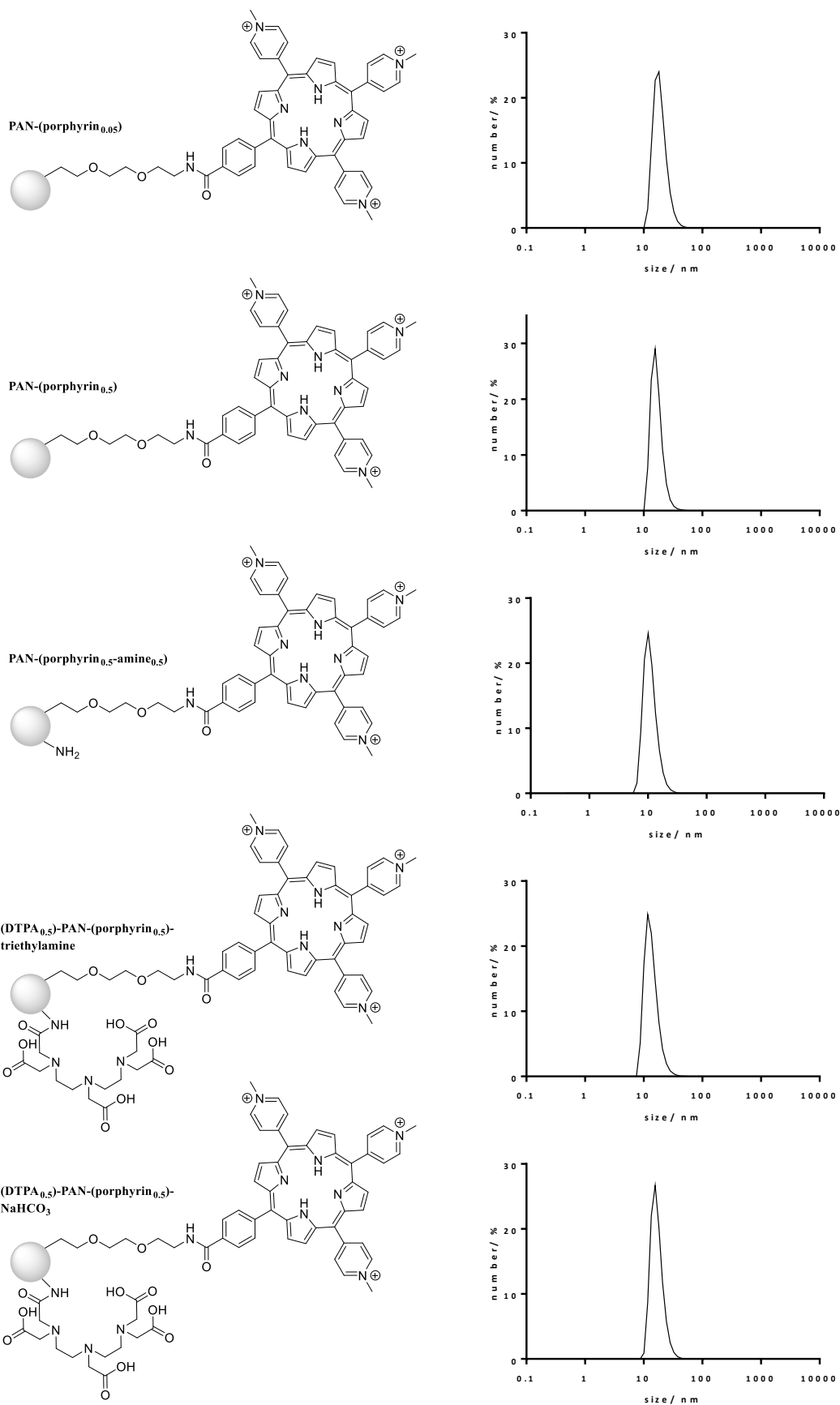


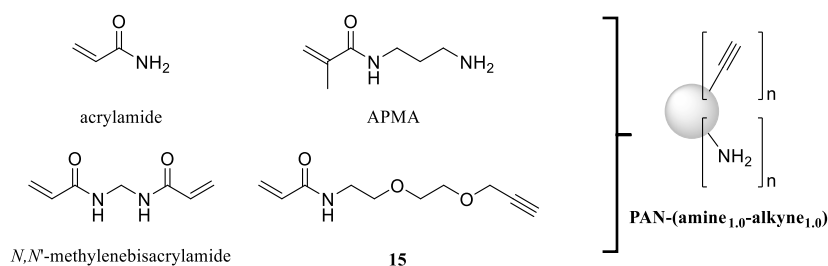
Figure 3.20 DLS size distribution by number of PAN-(porphyrin_{0.05}), PAN-(porphyrin_{0.5}), PAN-(porphyrin_{0.5}-amine_{0.5}), (DTPA_{0.5})-PAN-(porphyrin_{0.5})-triethylamine, and (DTPA_{0.5})-PAN-(porphyrin_{0.5})-NaHCO₃.

3.3.4 Synthesis of dual-functional PAN for orthogonal conjugation

The undesirable polydispersity and low yields of PAN encountered with the covalent incorporation of porphyrin into PAN prompted alternative synthesis of PAN suitable for post-conjugation of drug molecules. Orthogonal conjugation of PAN has been attempted and investigated in the literature.²²⁹ Hereby, a similar strategy was adopted for the synthesis of dual-functional PAN.

3.3.4.1 Synthesis of dual-functional alkyne and amine bearing PAN

Alkyne-functionalised monomer **15**, together with APMA, acrylamide, and *N,N'*-methylenebisacrylamide were co-polymerised for the synthesis of **PAN-(amine_{1.0}-alkyne_{1.0})** (Scheme 3.12). This yielded a nanoparticle with two types of reactive functionality on the nanoparticle, one capable of CuAAC, alkyne groups, and one capable of peptide conjugation, amino groups. The successful synthesis of **PAN-(amine_{1.0}-alkyne_{1.0})** afforded a nanoparticle with a z_{ave} of 36 ± 2 nm (Figure 3.21), a zeta potential of $+12.7 \pm 0.7$ mV, and PDI of 0.22 ± 0.01 .



Scheme 3.12 Scheme for the synthesis of **PAN-(amine_{1.0}-alkyne_{1.0})** via inverse microemulsion polymerisation of acrylamide, *N,N'*-methylenebisacrylamide, APMA, and **15**.

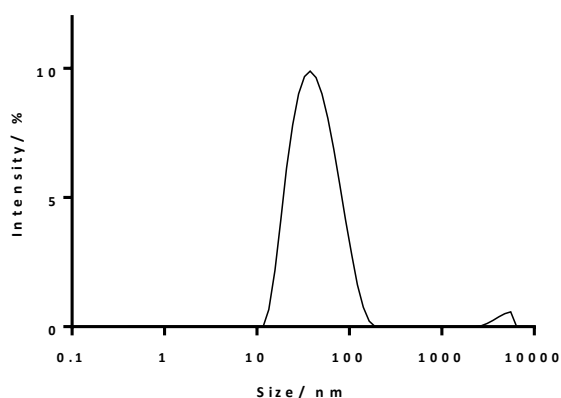
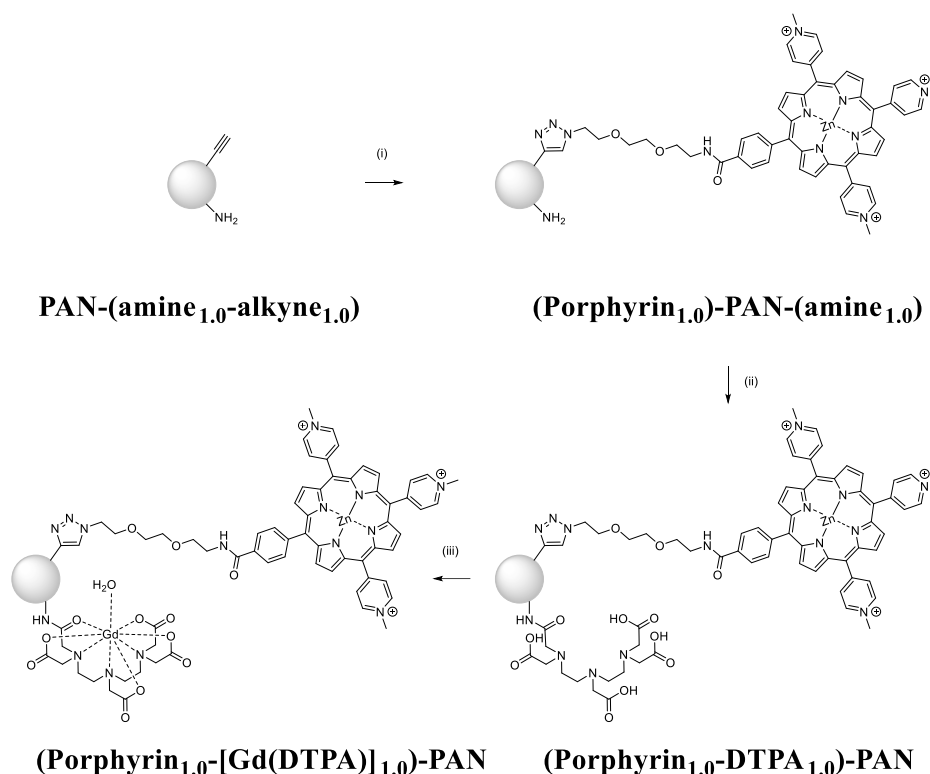


Figure 3.21 DLS size distribution by intensity of **PAN-(amine_{1.0}-alkyne_{1.0})**.

3.3.4.2 Orthogonal conjugation of PAN



Scheme 3.13 Reaction scheme for the orthogonal conjugation of PAN for the synthesis of **(porphyrin_{1.0}-[Gd(DTPA)]_{1.0})-PAN**. Reagents, conditions, and yields: (i) porphyrin **28**, CuSO₄, sodium ascorbate, microwave (50 °C, 4 hours, 75 W), 93%, (ii) DTPA-DA **29**, aq. NaHCO₃, room temperature, overnight, 83%, (iii) GdNO₃·6H₂O, pH 4.5 acetate buffer, room temperature, overnight, 84%.

The successful synthesis of **PAN-(amine_{1.0}-alkyne_{1.0})** prompted subsequent conjugation onto the PAN. A CuAAC “click” reaction was first carried out using porphyrin **28** (Scheme 3.13) prior to DTPA conjugation as DTPA is known to chelate various metals including copper, albeit with poor stability.^{262,263}

The CuAAC reaction was carried out at an elevated temperature (50 °C) for 4 hours in a microwave reactor to prepare **(porphyrin_{1.0})-PAN-(amine_{1.0})**. Purification of PAN was carried out *via* precipitation from ethanol and gel filtration through Sephadex G-25 to remove excess reagents and porphyrin. An average of 32±2 nmol of porphyrin per mg of PAN was obtained from three separate runs using these standardised synthetic conditions.

PAN has been shown to be capable of encapsulating and entrapping molecules without covalent conjugation.^{264,265} Hence, a control CuAAC porphyrin conjugation reaction with **PAN_{blank}** was carried out using similar reaction and purification conditions. UV-vis. spectroscopy indicated that blank polyacrylamide nanoparticles were capable of entrapping 0.73 nmol of porphyrin per mg of nanoparticles. This shows that the presence of the alkyne functionality on the porphyrin allows significantly (44 ×) greater loading via covalent conjugation.

Having successfully conjugated porphyrin onto the **PAN-(amine_{1.0}-alkyne_{1.0})** *via* CuAAC, conjugation of **(porphyrin_{1.0})-PAN-(amine_{1.0})** with DTPA to prepare **(porphyrin_{1.0}-DTPA_{1.0})-PAN** proceeded *via* peptide conjugation onto the amine groups. Using a similar method described for the synthesis of **(DTPA_{0.5})-PAN-(porphyrin_{0.5})** in chapter 3.3.3, conjugation with DTPA was carried out with DTPA-DA **29** in aqueous NaHCO₃. Toxic triethylamine was not used as a base for DTPA conjugation and the easy purification and removal of NaHCO₃ using gel filtration chromatography makes NaHCO₃ the reagent of choice.

As mention in chapter 3.2.5, DTPA is capable of chelating various metals, including Gd³⁺. [Gd(DTPA)]²⁻ is an FDA approved drug known as Magnevist®, which is routinely used in clinical settings as an MRI contrast agent. The non-radioactive gadolinium and the ease of purification using gel filtration chromatography allows the complexation of Gd³⁺ onto the conjugated DTPA. Complexation with Gd(NO₃)₃.6H₂O in acetate buffer at pH 4.5 yielded the desired **(porphyrin_{1.0}-[Gd(DTPA)]_{1.0})-PAN**. Using the Evans magnetic susceptibility method (detailed procedure in experimental section), a loading of 37±3 nmol of gadolinium per mg of nanoparticles was achieved.²⁶⁶ A control gadolinium complexation reaction was also carried out on the **(porphyrin_{1.0})-PAN-(amine_{1.0})** without the DTPA ligand, revealing that no gadolinium was complexed/entrapped in the absence of DTPA on the nanoparticle.

3.3.4.3 PAN characterisation

Conjugated PAN was analysed using DLS and zeta potential as shown in Figure 3.22. Upon conjugation, the nanoparticles showed a general trend of increasing hydrodynamic size, with the exception for **(porphyrin_{1.0}-DTPA_{1.0})-PAN**. Upon conjugation of tri-cationic porphyrin **28** the PAN size increased from 36±2 nm to 46±11 nm. This is attributed to the introduction of charged groups increasing the hydrodynamic radius of the PAN. Subsequent peptide conjugation of DTPA saw a significant increase in size from 46±11 nm to 95±29 nm. This effect can be explained by the introduction of negatively-charged carboxyl groups on to the positively charged nanoparticle, which reduces interparticle repulsion. Following complexation of Gd³⁺ cation, this aggregation effect was seen to diminish.

Zeta potential measurements provided further evidence and showed agreement with DLS measurements for the modification of the nanoparticle. **PAN-(amine_{1.0}-alkyne_{1.0})** has a slight positive potential of +12.7±0.7 mV due to the presence of amino groups. Porphyrin conjugation *via* CuAAC resulted in an increase in potential to +23.9±1.8 mV, which decreases to +11.9±3.4 mV upon DTPA conjugation, and finally, an increase to +31.4±3.2 mV was observed upon Gd³⁺ complexation.

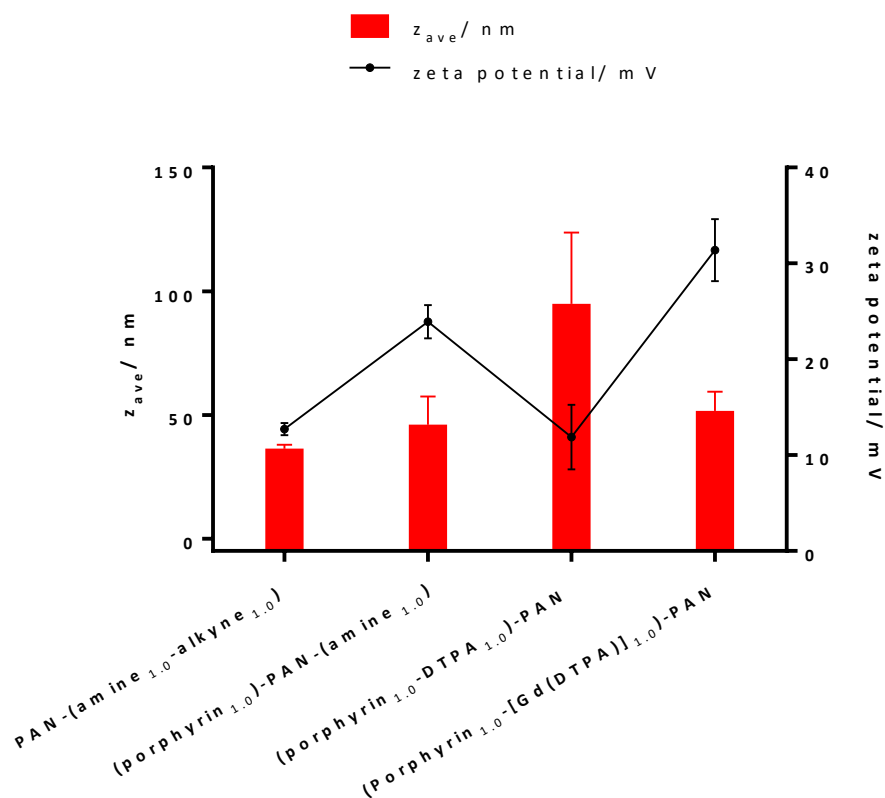


Figure 3.22 z_{ave} and zeta potential of PAN-(amine_{1.0}-alkyne_{1.0}), (porphyrin_{1.0})-PAN-(amine_{1.0}), (porphyrin_{1.0}-DTPA_{1.0})-PAN, and (Porphyrin_{1.0}-[Gd(DTPA)]_{1.0})-PAN. Error bars shown were obtained from triplicate measurements.

Transmission electron microscopy (TEM) images were also obtained for these nanoparticles. Uranyl acetate was used to negatively stain these polymeric nanoparticles as they lack sufficient density to attenuate or deflect electrons for TEM. The images, as shown in Figure 3.23, show a modest size range for the nanoparticles, as expected, and in agreement with DLS measurements. TEM images also indicated that the nanoparticle retains its size and shape throughout subsequent modifications.

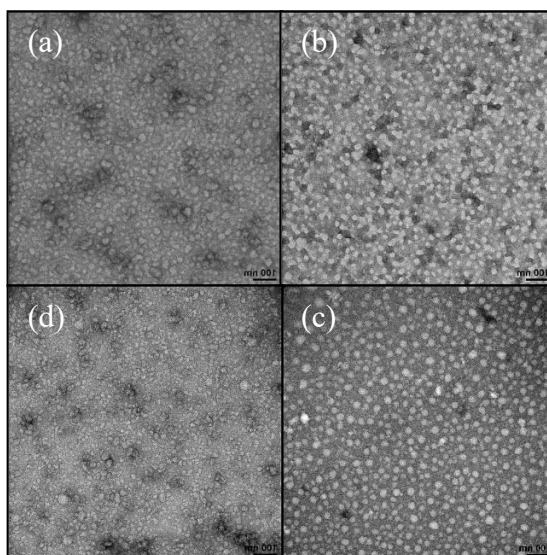


Figure 3.23 TEM images of nanoparticles negatively stained using 1% aqueous uranyl acetate. (a) PAN-(amine_{1.0}-alkyne_{1.0}), (b) (porphyrin_{1.0})-PAN-(amine_{1.0}), (c) (porphyrin_{1.0}-DTPA_{1.0})-PAN, (d) (porphyrin_{1.0}-[Gd(DTPA)]_{1.0})-PAN.

UV-vis. spectroscopy (Figure 3.24) was used to follow porphyrin conjugation; the modified nanoparticle showed the characteristic absorption spectrum for zinc-metalloporphyrin, and retained the same absorption spectrum with similar intensity after subsequent modification, indicating the porphyrin was intact and unaffected by further modification of the nanoparticle. A loading of 31 ± 7 nmol of porphyrin per mg of nanoparticle was determined using UV-vis. spectroscopy for **(porphyrin_{1.0}-[Gd(DTPA)]_{1.0})-PAN**. Gd^{3+} concentration was calculated using the Evans paramagnetic susceptibility measurement.²⁶⁶ This was measured at 9.4 T and showed that 37 ± 3 nmol of Gd^{3+} was loaded onto every mg of nanoparticle.

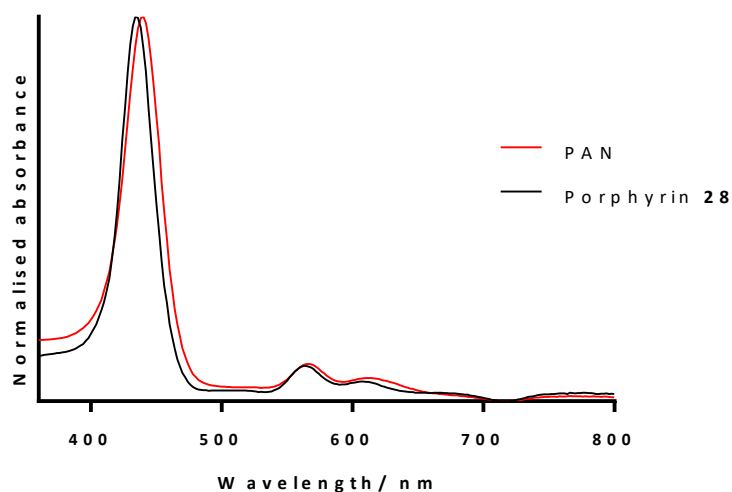


Figure 3.24 UV-vis absorbance spectrum of the porphyrin **28** and PAN after porphyrin conjugation.

The synthesis of dual-modal theranostic **(porphyrin_{1.0}-[Gd(DTPA)]_{1.0})-PAN** was characterised using DLS, zeta potential, TEM, UV-vis. spectroscopy, and Evans paramagnetic susceptibility measurement. These analysis gave evidence of the successful synthesis of the theranostic PAN.

This prompted the further investigation of **(porphyrin_{1.0}-[Gd(DTPA)]_{1.0})-PAN** efficacy as a photodynamic therapy (PDT) agent and as an MRI contrast agent.

3.4 *In vitro* cytotoxicity evaluation

With the successful synthesis and characterisation of the theranostic **(porphyrin_{1.0}-[Gd(DTPA)]_{1.0})-PAN**, cell cytotoxicity studies were carried out to evaluate the photodynamic efficacy on human colorectal adenocarcinoma (HT-29) cells. Cells were incubated with **(porphyrin_{1.0}-[Gd(DTPA)]_{1.0})-PAN** at varying concentrations and irradiation was carried out using a constant dose of visible light (20 J cm⁻²; 400-700 nm). The results were compared to a non-irradiated control. Although in a clinical setting, red light is more commonly used for PDT, the power of clinical lasers used in PDT are significantly higher compared to the quartz tungsten halogen light source used in this study.⁷ Hence, to compensate for the lower power, white light was used covering the whole porphyrin absorbance range, including the strong Soret band at 440 nm (Figure 3.24).

Figure 3.25 shows percentage cell survival of HT-29 cells incubated with varying concentration of **(porphyrin_{1.0}-[Gd(DTPA)]_{1.0})-PAN**. The concentration in Figure 3.25 is given in molar (M) and is based on the concentration of porphyrin calculated using the Beer-Lambert's equation (Eq. 7. 1) and the extinction coefficient, ϵ , of porphyrin **28**. Under the conditions mentioned above, **(porphyrin_{1.0}-[Gd(DTPA)]_{1.0})-PAN** showed excellent PDT effect as more than 90% cell death was observed at a low concentration of 0.62 μ M. Clinically approved Photofrin® was shown to inducing 90% cell death at a concentration of 40 ng mL⁻¹ (approximately 60 μ M porphyrin core as Photofrin® is a mixture of monomeric and oligomeric forms of porphyrin).²⁶⁷ **(porphyrin_{1.0}-[Gd(DTPA)]_{1.0})-PAN** also showed minimal dark toxicity (>93% cell survival) for all concentrations up to 100 μ M, indicating its non-toxicity in the dark. Furthermore, Gd toxicity was not observed within the time scale of the *in vitro* test, an indication of the stability of the complex.

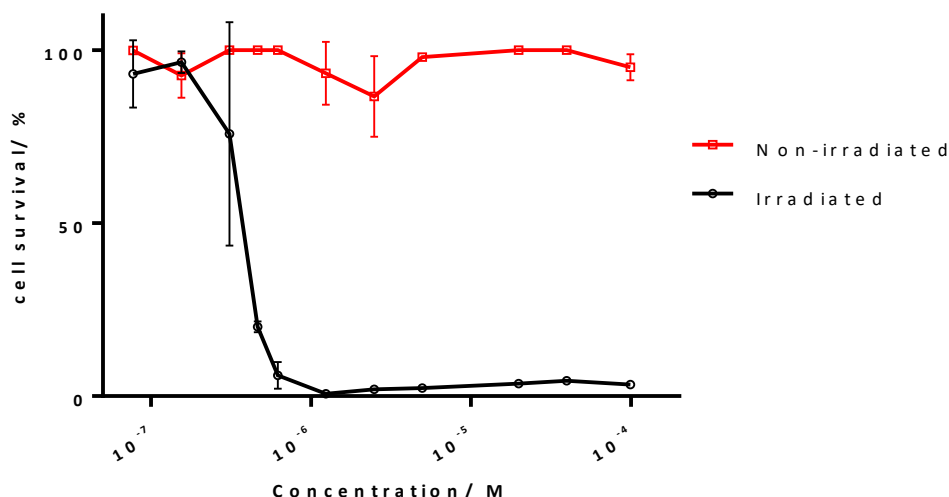


Figure 3.25 % cell survival after incubation with **(porphyrin_{1.0}-[Gd(DTPA)]_{1.0})-PAN** with and without light irradiation with varying porphyrin concentrations. Error bars shown were obtained from triplicate measurements.

These results further prove and agree with literature reporting that PAN is a non-toxic nanoparticle platform, ideal for biological applications.²³⁶ These results also show that **(porphyrin_{1.0}-[Gd(DTPA)]_{1.0})-PAN** is non-toxic after conjugation of drug molecules – porphyrin, DTPA, and Gd³⁺, and it also has the potential to be a viable and effective PDT agent.

3.5 Relaxivity studies and phantom MRI

With the successful evaluation of the PDT modality of **(porphyrin_{1.0}-[Gd(DTPA)]_{1.0})-PAN**, the imaging modality as an MRI contrast agent was investigated.

T1 measurements were carried out at a range of magnetic field strengths from 0.01 MHz up to 400 MHz. Relaxivity, r_1 was calculated from T1 relaxation time and Gd³⁺ concentration. At 60 MHz, r_1 of **(porphyrin_{1.0}-[Gd(DTPA)]_{1.0})-PAN** was calculated to be 14.7 mM⁻¹ s⁻¹ per gadolinium centre, higher than the clinical equivalent Magnevist® which has an r_1 value of 3.3 mM⁻¹ s⁻¹ in the same magnetic field (Figure 3.26). The fourfold higher relaxivity observed for **(porphyrin_{1.0}-[Gd(DTPA)]_{1.0})-PAN** can be explained by the fact that, when [Gd(DTPA)]²⁻ is bound to the nanoparticle, this increases its rotational correlation time, τ_R , hence increases the water exchange rate.²⁶⁸ As shown in the nuclear magnetic resonance dispersion (NMRD) profile (Figure 3.26), it can be observed that there is a small increase in relaxivity in **(porphyrin_{1.0}-[Gd(DTPA)]_{1.0})-PAN** at around 10-100 MHz. This can again be attributed to the characteristics of a slow tumbling nanoparticle T1 contrast agent.²⁶⁸⁻²⁷³ At 400 MHz, the decrease in r_1 to 5.37 mM⁻¹ s⁻¹ is expected, as r_1 relaxivity of paramagnetic contrast agents tends to decrease with increasing magnetic field strength.^{77,151,274,275}

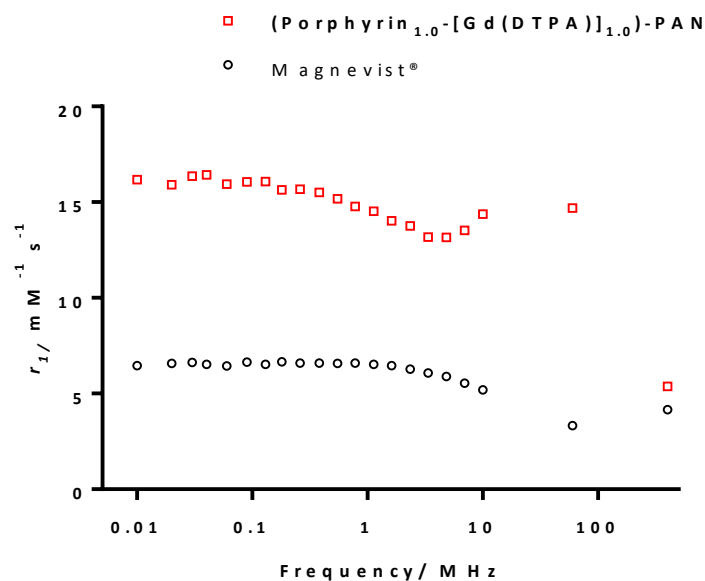


Figure 3.26 NMRD profile of **(porphyrin_{1.0}-[Gd(DTPA)]_{1.0})-PAN** and Magnevist® in varying magnetic field.

The T1 contrast of **(porphyrin_{1.0}-[Gd(DTPA)]_{1.0})-PAN** was further examined using a clinically relevant MRI machine. Measurements were carried out in a 3 T patient scanner, with Magnevist® and water as controls. Figure 3.27 shows an image of the phantom MRI obtained. The image was obtained in grey scale and was then colour-coded (ImageJ®) to highlight contrast. PAN concentration was adjusted based on Gd³⁺ concentration calculated using the Evans paramagnetic susceptibility measurement and compared with Magnevist® at similar concentrations. Brighter and more contrasted images were observed for **(porphyrin_{1.0}-[Gd(DTPA)]_{1.0})-PAN** than Magnevist® at all concentrations tested, and both were brighter than water.

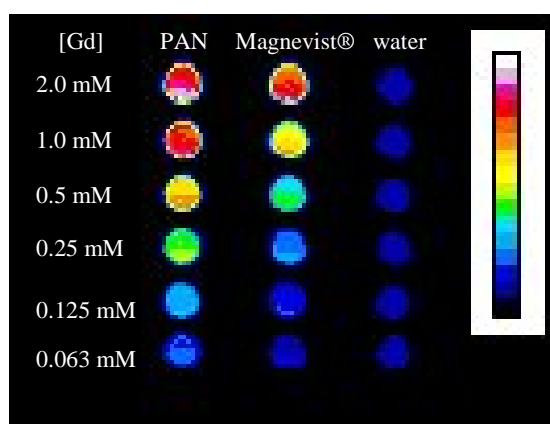
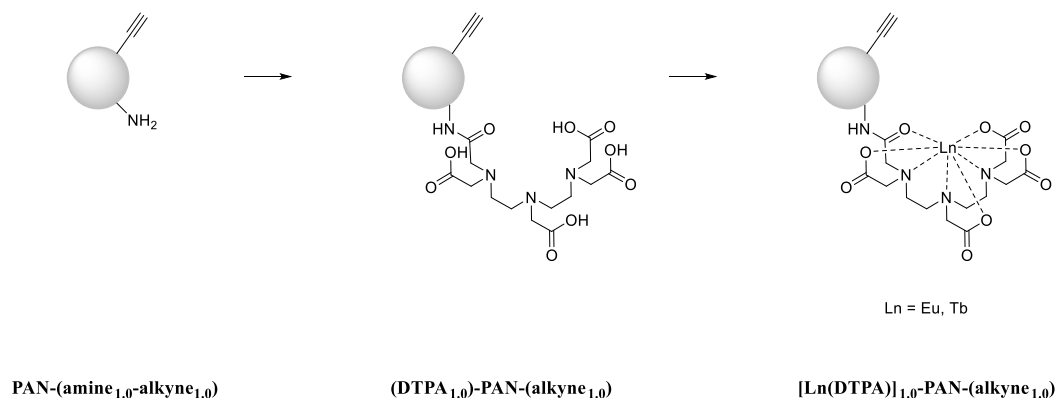


Figure 3.27 Phantom MRI obtained on 3 T MRI scanner of **(porphyrin_{1.0}-[Gd(DTPA)]_{1.0})-PAN** and Magnevist® at different concentrations, with water as a control.

The results obtained from phantom MRI is in good agreement with the relaxivity data previously obtained. This not only gives evidence that **(porphyrin_{1.0}-[Gd(DTPA)]_{1.0})-PAN** is a viable MRI contrast agent, but is also a better MRI contrast agent when compared to its clinical equivalent, Magnevist®.

3.6 Hydration state evaluation

The hydration state of Gd-based contrast agents is important as a higher hydration state should result in a higher relaxivity, hence a greater contrast in MRI.¹⁴⁴ Gadolinium belongs to the series of elements known as lanthanides. Lanthanides have interesting photophysical properties, with luminescence properties (excepting La^{3+} and Ln^{3+}). These trivalent ions luminesce in the visible and near-infrared regions with the exception of Gd^{3+} as it requires higher excitation energy and emits in the UV region. Due to the similarities of lanthanides across the series, Eu^{3+} and Tb^{3+} analogues are used to investigate hydration state of Gd^{3+} *via* luminescence measurements.²⁷⁶



Scheme 3.14 Synthesis of $([\text{Ln}(\text{DTPA})]_{1.0})\text{-PAN-(alkyne}_{1.0})$. Reagents and conditions: (i) DTPA-DA **29**, aq. NaHCO_3 , room temperature, overnight. (ii) $\text{EuCl}_3 \cdot 6\text{H}_2\text{O}$ / $\text{TbCl}_3 \cdot 6\text{H}_2\text{O}$, pH 4.5 acetate buffer, room temperature, overnight.

Porphyryns have absorption bands with high absorption extinction coefficients in the visible region ($\lambda_{\text{max}} = 400\text{-}450$ nm) and also luminesces in the visible part of the electromagnetic spectrum ($\lambda = 600\text{-}750$ nm). To prevent the absorption and luminescence properties of porphyrin from affecting the luminescence of Eu and Tb, a similar PAN with DTPA, but without porphyrin, was prepared, to provide insight to the hydration state of $[\text{Gd}(\text{DTPA})]$ on the PAN.

Scheme 3.14 shows the synthetic strategy adopted. Briefly, **PAN-(amine_{1.0}-alkyne_{1.0})** described earlier in chapter 3.3.4, without undergoing CuAAC with porphyrin **28**, was conjugated with DTPA-DA **29** in NaHCO_3 . This yielded **(DTPA_{1.0})-PAN-(alkyne_{1.0})** capable of complexation with Eu^{3+} and Tb^{3+} . Complexation with Eu^{3+} or Tb^{3+} was carried out in pH 4.5 acetate buffer yielded **([Eu(DTPA)]_{1.0})-PAN-(alkyne_{1.0})** and **([Tb(DTPA)]_{1.0})-PAN-(alkyne_{1.0})**, a similar method used for the complexation of Gd^{3+} to prepare **(Porphyrin_{1.0}-[Gd(DTPA)]_{1.0})-PAN**.

([Eu(DTPA)]_{1.0})-PAN-(alkyne_{1.0}) was excited at $\lambda_{\text{ex}} = 395$ nm to give the emission spectrum shown in Figure 3.28. Excited state lifetime measurements were carried out by exciting at the same wavelength, $\lambda_{\text{ex}} = 395$ nm, and monitoring the emission intensity at $\lambda_{\text{em}} = 615$ nm with time delay (Figure 3.29).

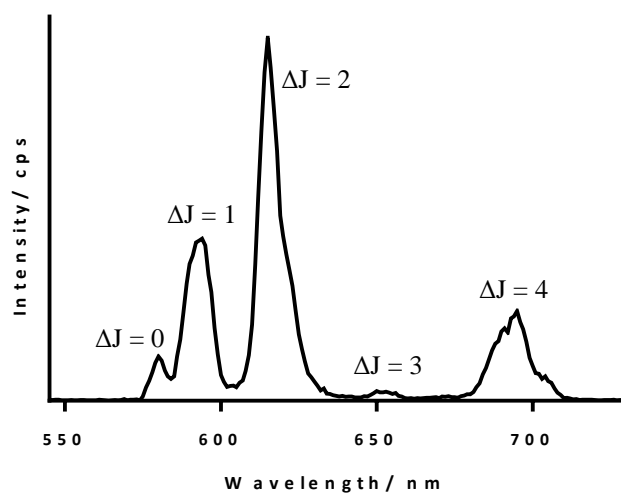


Figure 3.28 Luminescence emission spectrum of $([\text{Eu}(\text{DTPA})]_{1.0})\text{-PAN-(alkyne}_{1.0})$. ($\lambda_{\text{ex}} = 395 \text{ nm}$).

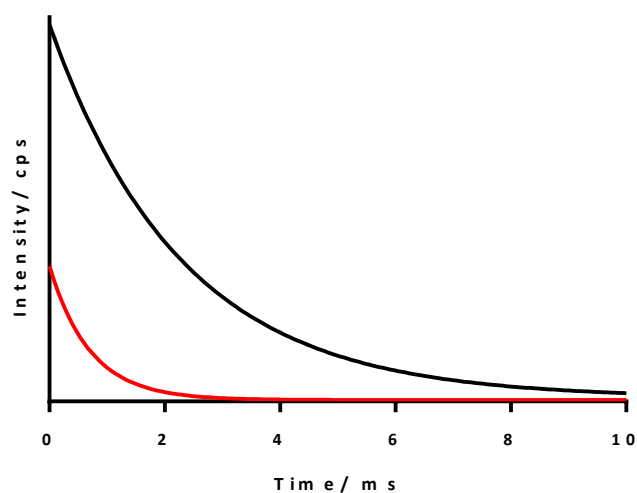


Figure 3.29 Excited state lifetime measurement of $([\text{Eu}(\text{DTPA})]_{1.0})\text{-PAN-(alkyne}_{1.0})$, $\lambda_{\text{ex}} = 395 \text{ nm}$, $\lambda_{\text{em}} = 615 \text{ nm}$. Red: H_2O , black: D_2O .

Similarly, $([\text{Tb}(\text{DTPA})]_{1.0})\text{-PAN-(alkyne}_{1.0})$ was excited at $\lambda_{\text{ex}} = 380 \text{ nm}$ to give the emission spectrum shown in Figure 3.30. Excited state lifetime measurements were carried out by exciting at $\lambda_{\text{ex}} = 380 \text{ nm}$ and monitoring the emission intensity at $\lambda_{\text{em}} = 545 \text{ nm}$ with time delay (Figure 3.31).

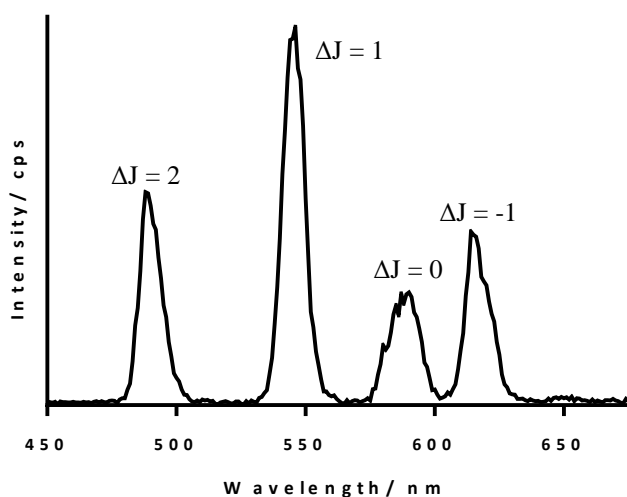


Figure 3.30 Luminescence emission spectrum of $([\text{Tb}(\text{DTPA})]_{1.0})\text{-PAN-(alkyne}_{1.0})$. ($\lambda_{\text{ex}} = 380 \text{ nm}$).

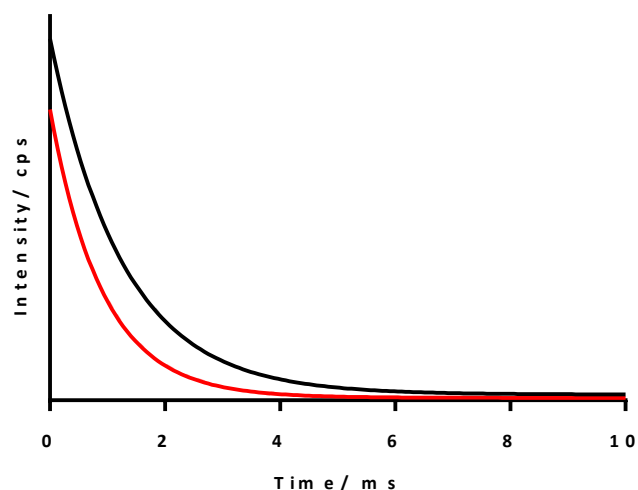


Figure 3.31 Excited state lifetime measurement of $([\text{Tb}(\text{DTPA})]_{1.0})\text{-PAN-(alkyne}_{1.0})$, $\lambda_{\text{ex}} = 380 \text{ nm}$, $\lambda_{\text{em}} = 545 \text{ nm}$. Red: H_2O , black: D_2O .

A one phase exponential decay was fitted onto the excited state lifetime measurement obtained for both $([\text{Eu}(\text{DTPA})]_{1.0})\text{-PAN-(alkyne}_{1.0})$ and $([\text{Tb}(\text{DTPA})]_{1.0})\text{-PAN-(alkyne}_{1.0})$ using GraphPad Prism (Figure 3.29 and Figure 3.31). The rate constant, $k_{\text{H}_2\text{O}/\text{D}_2\text{O}}$, for the excited state decay in H_2O and D_2O was calculated from the graph. The hydration state, q was derived from Eq. 3. 1 and Eq. 3. 2,²⁷⁶ and showed both $([\text{Eu}(\text{DTPA})]_{1.0})\text{-PAN-(alkyne}_{1.0})$ and $([\text{Tb}(\text{DTPA})]_{1.0})\text{-PAN-(alkyne}_{1.0})$ has a hydration state, $q = 1$ (Table 3.3).

$$q_{\text{Eu}} = 1.2[(k_{\text{H}_2\text{O}} - k_{\text{D}_2\text{O}}) - 0.25] \quad \text{Eq. 3. 1}$$

$$q_{\text{Tb}} = 5[(k_{\text{H}_2\text{O}} - k_{\text{D}_2\text{O}}) - 0.06] \quad \text{Eq. 3. 2}$$

Coordinationally unsaturated lanthanides, e.g. $q = 2$ are known to form ternary anion adducts (formation of two coordinative bonds) with biologically relevant anions, including hydrogencarbonates, carboxylates, dicarboxylates, citrates, lactates, and malates. Other anions are also known to displace metal coordination of water including acetates, hydroxides, phosphates,

and fluorides (Ln-F is the only halide interaction that can compete with $\text{Ln-H}_2\text{O}$) (Figure 3.32).²⁷⁷⁻

279

Complex	$\lambda_{\text{ex}}/\text{nm}$	$\lambda_{\text{em}}/\text{nm}$	$k_{\text{H}_2\text{O}}$	$k_{\text{D}_2\text{O}}$	q
([Eu(DTPA)]_{1.0})-PAN-(alkyne_{1.0})	395	615	1.5	0.44	0.98
([Tb(DTPA)]_{1.0})-PAN-(alkyne_{1.0})	380	545	1.1	0.79	1.23

Table 3.3 Rate constant, k , for the phosphorescence decay and the derived hydration state, q , for **([Eu(DTPA)]_{1.0})-PAN-(alkyne_{1.0})** and **([Tb(DTPA)]_{1.0})-PAN-(alkyne_{1.0})**.

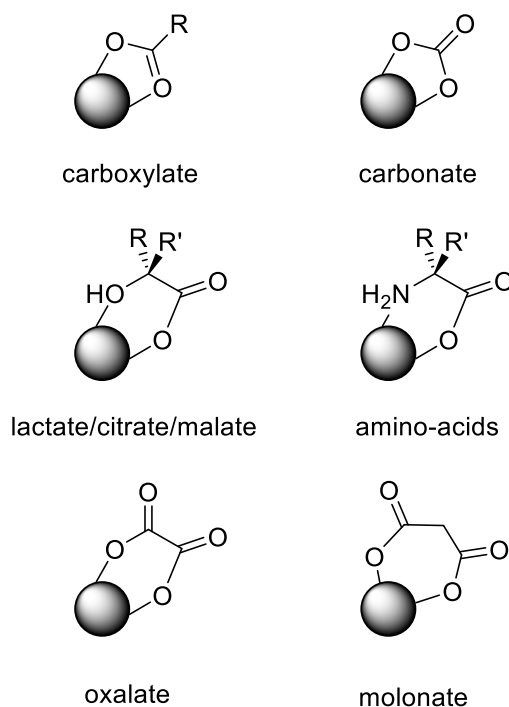


Figure 3.32 Ternary anion adducts formed at Ln^{3+} centres.

Concerns over the use of acetate buffer for the binding of acetate with Gd^{3+} , Eu^{3+} , and Tb^{3+} , prompted a control Eu^{3+} complexation without the use of acetate buffer to be carried out. Similarly, reaction pH was carried out at pH 4.5, however, adjusted using HCl and NaOH.

Under the same conditions, luminescence emission for **([Eu(DTPA)]_{1.0})-PAN-(alkyne_{1.0})** synthesised without the use of acetate buffer was comparable with the use of acetate buffer. Excited state lifetime measurements obtained gave similar rate constants, $k_{\text{H}_2\text{O}/\text{D}_2\text{O}}$, and hence similar q (Figure 3.33), indicating the use of acetate buffer do not affect the coordination of DTPA with lanthanides. It can also be deduced that the amide formed during DTPA conjugation is capable of coordinating Gd^{3+} , Eu^{3+} and Tb^{3+} , hence giving an 8-coordinated complex with a $q = 1$. This is to be expected as some clinically approved Gd-based DTPA derivatives, for example, Omniscan® and Optimark® have amides and still retain 8-coordination with gadolinium (Figure 3.34).²⁸⁰

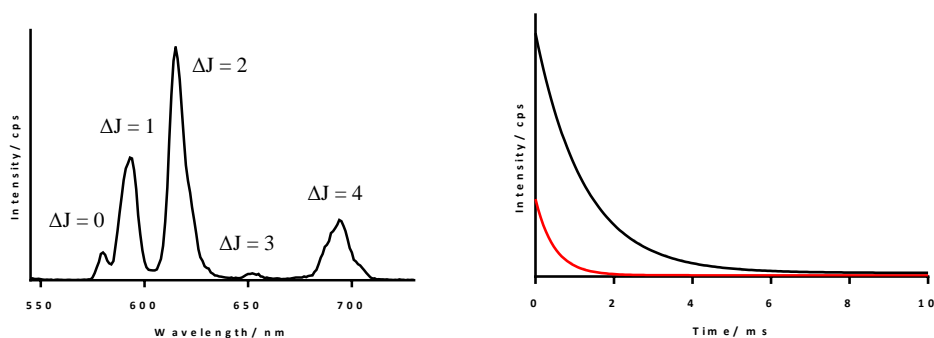


Figure 3.33 Luminescence emission spectrum (left, $\lambda_{\text{ex}} = 395 \text{ nm}$) and excited state lifetime measurement (right, Red: H_2O , black: D_2O , $\lambda_{\text{ex}} = 395 \text{ nm}$, $\lambda_{\text{em}} = 615 \text{ nm}$) of $([\text{Eu}(\text{DTPA})]_{1.0})\text{-PAN-(alkyne}_{1.0})$ prepared without the use of acetate buffer, showed similar spectra compared to Figure 3.28 and Figure 3.29.

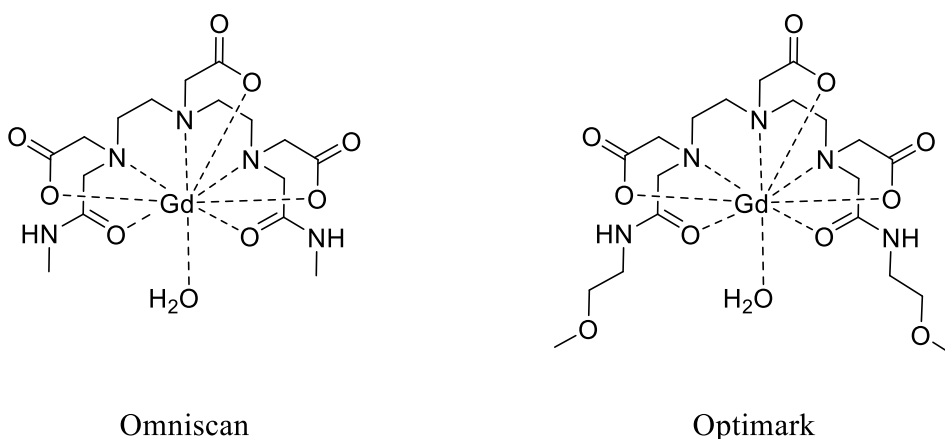


Figure 3.34 FDA approved DTPA derivative, Omniscan™ and Optimark®.

3.7 *In vivo* evaluation – PDT and MRI

In vitro evaluation showing that $(\text{porphyrin}_{1.0}\text{-}[\text{Gd}(\text{DTPA})]_{1.0})\text{-PAN}$ was a viable PDT agent and MRI contrast agent led to *in vivo* evaluation. Three mice bearing KB tumour (mouse 1, 3, and 5) were administered $(\text{porphyrin}_{1.0}\text{-}[\text{Gd}(\text{DTPA})]_{1.0})\text{-PAN}$ intravenously. Mouse 1 and 3 received 50 mg, and mouse 5 received 25 mg. Phosphate buffered saline (PBS) was administered to two mice bearing KB tumour as a control (mouse 2 and 4).

MRI T1 signal enhancement was carried out in a 7 T preclinical MRI system at pre-scan, 4-hour post injection, and 24-hour post injection. Unfortunately, no signal enhancement was observed (Figure 3.35).

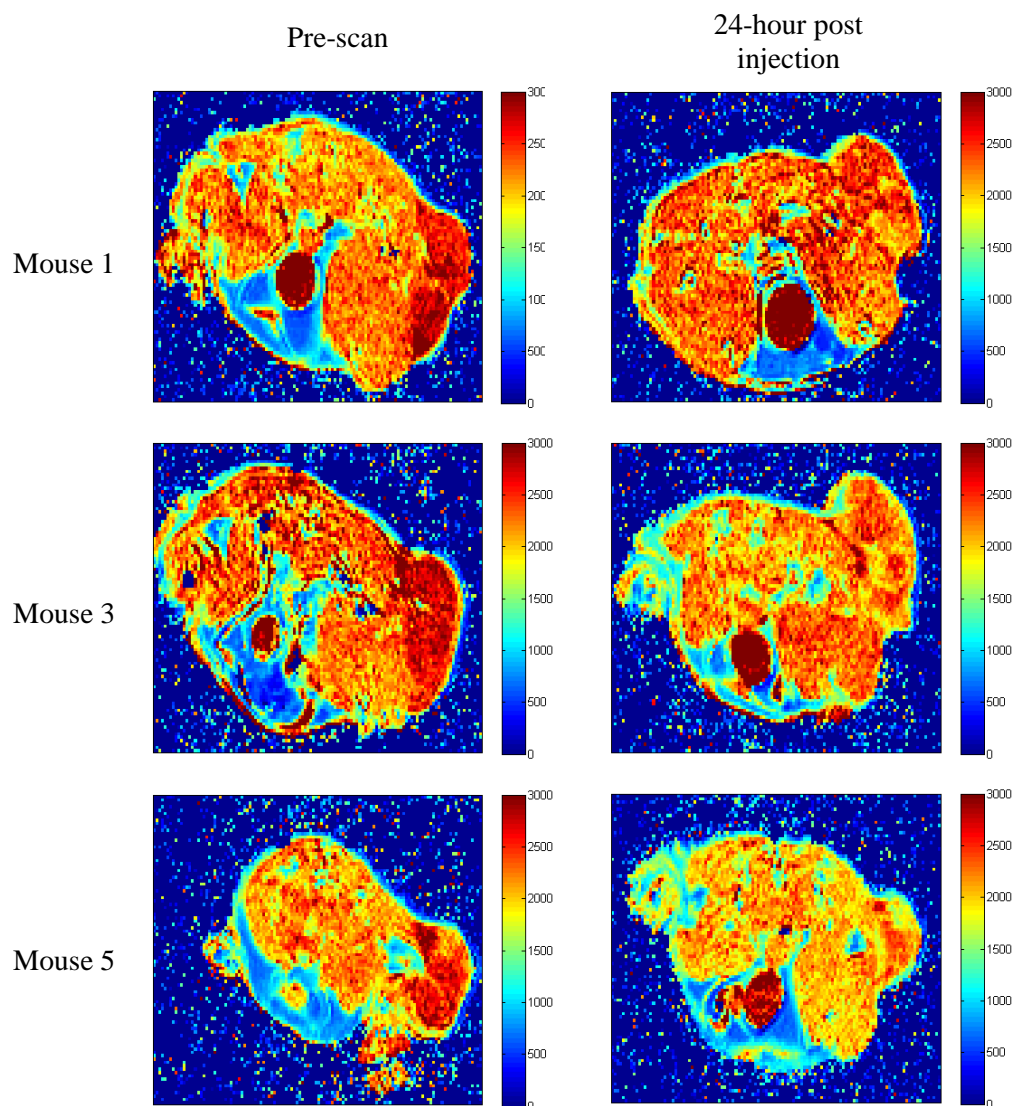


Figure 3.35 MRI images of mice pre-administered and 24-hour post administration with **(porphyrin_{1.0}-[Gd(DTPA)]_{1.0})-PAN**.

Fluorescent imaging, $\lambda_{em} = 600-750$ nm, at 24-hour post injection, however, showed clear indication of **(porphyrin_{1.0}-[Gd(DTPA)]_{1.0})-PAN** accumulation in the tumour in the right flank of the mice (Figure 3.36). Fluorescence was also observed in the main body of the mice indicating **(porphyrin_{1.0}-[Gd(DTPA)]_{1.0})-PAN** uptake in the liver, which has been shown previously to be a major site of deposition for PAN in mice without tumour.²³⁶

(Porphyrin_{1.0}-[Gd(DTPA)]_{1.0})-PAN

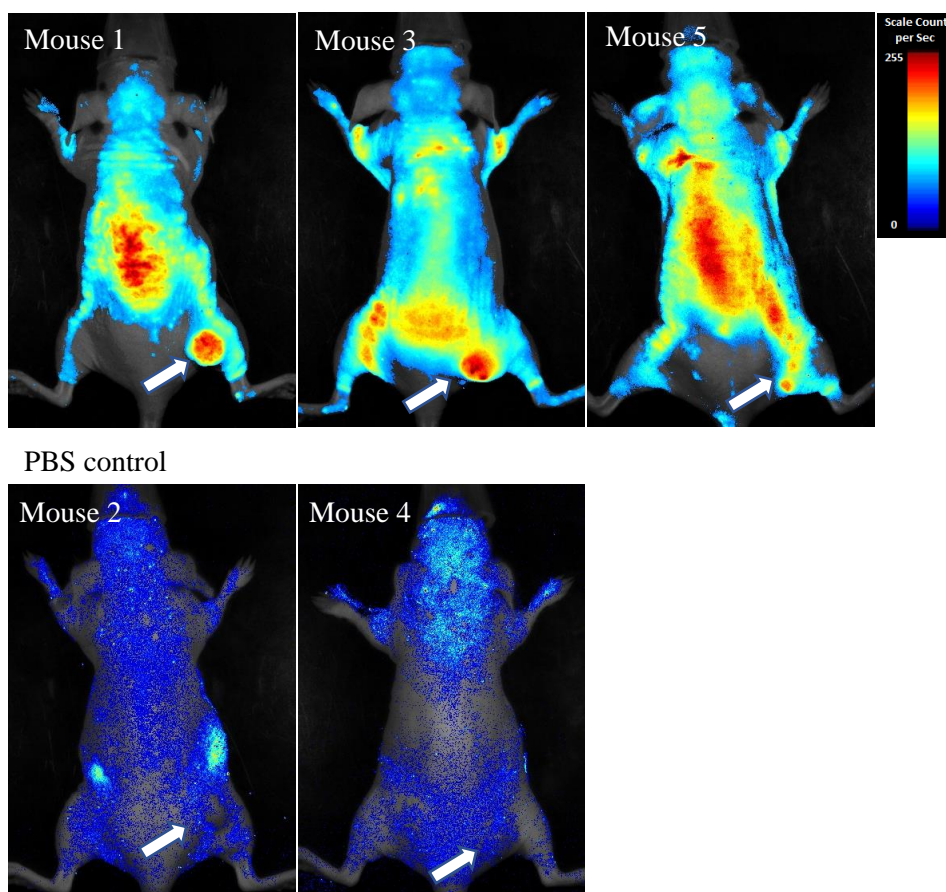


Figure 3.36 Fluorescence Maestro imaging of mice, 24-hour post administration with **(porphyrin_{1.0}-[Gd(DTPA)]_{1.0})-PAN** (top) and PBS (bottom).

Clear accumulation of **(porphyrin_{1.0}-[Gd(DTPA)]_{1.0})-PAN** in tumour as observed on fluorescence imaging prompted subsequent photodynamic treatment. Using a 671 nm laser with a power output of 78.8 mW, a dose of 125 J cm⁻² light was directly delivered to the tumour. 24 hours post PDT, the mice were sacrificed, and their organs and tumour were harvested for further histology studies, namely haematoxylin and eosin (H&E) staining and terminal deoxynucleotidyl transferase dUTP nick end labelling (TUNEL) staining. H&E staining post-PDT shows no acute toxicity or adverse side effects in organs, which included heart, liver, spleen, lung, and kidney (Figure 3.37). H&E and TUNEL staining were carried out on tumour tissues and showed a clear PDT effect when compared with the PBS control group (Figure 3.38 and Figure 3.39).

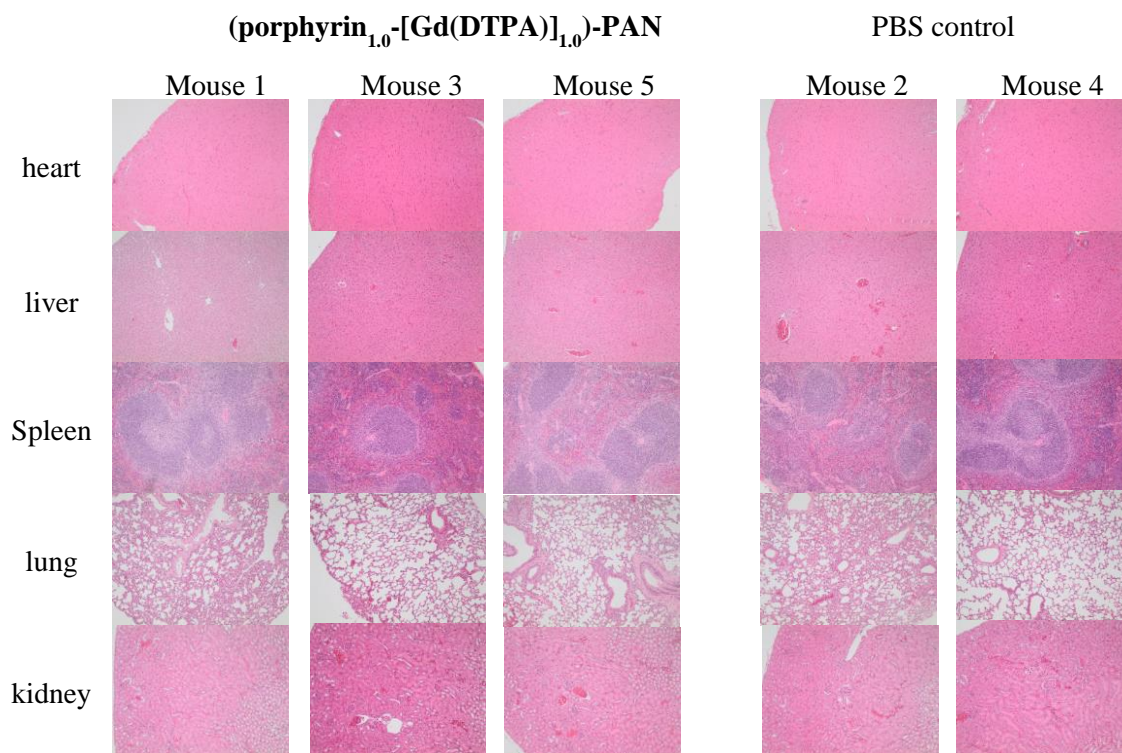


Figure 3.37 H&E evaluation of organ toxicity from each cohort. Organs include heart, liver, spleen, lung, and kidney. Histological slices do not show adverse effects on these tissues 24-hour post-PDT.

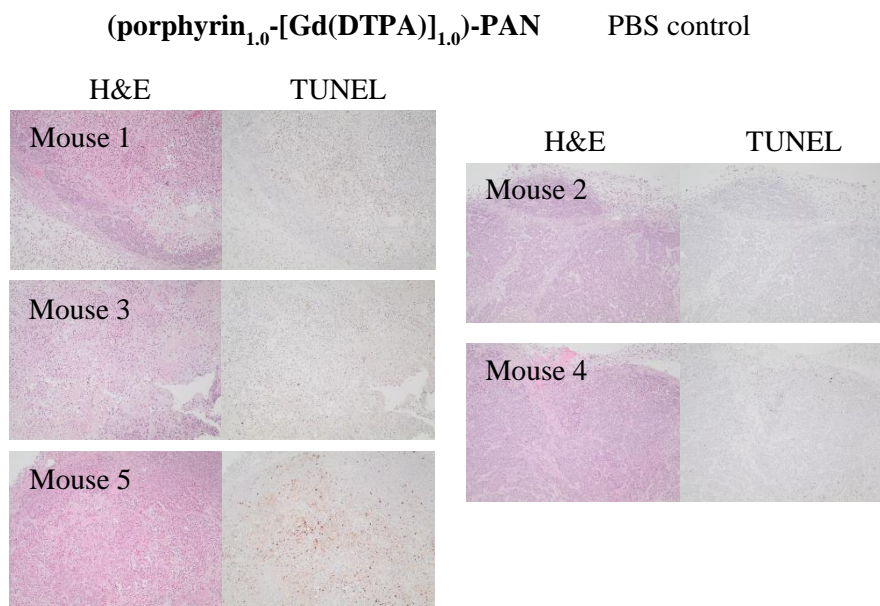


Figure 3.38 H&E and TUNEL staining on tumour cells, showed clear PDT effect on mice 1, 3, and 5 when compared to PBS control mice 2 and 4.

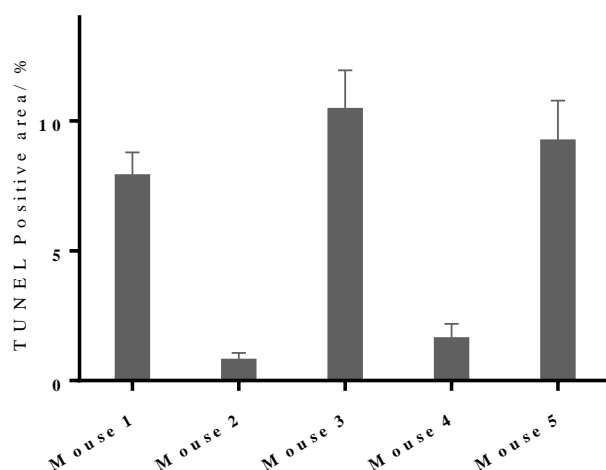


Figure 3.39 TUNEL quantification of tumour cells shown in Figure 3.38, shows clear PDT effect in mice 1, 3, and 5 when compared to PBS control mice 2 and 4.

Successful determination of accumulation of **(porphyrin_{1.0}-[Gd(DTPA)]_{1.0})-PAN** in tumour cells and successful photodynamic treatment led to further investigation into the lack of T1 enhancement. Organs and tumour cells harvested were subjected to ICP-MS biodistribution analysis to determine the amount of Gd³⁺. ICP-MS biodistribution analysis shows major uptake in the liver and spleen which is in accordance with fluorescence imaging, and also shows significant uptake of Gd³⁺ in tumour cells (3.3 mg kg⁻¹) as shown in Figure 3.40. These results confirm that the major clearance route for **(porphyrin_{1.0}-[Gd(DTPA)]_{1.0})-PAN** is *via* the liver and spleen (reticuloendothelial system), which was demonstrated for PAN and other micrometre to nanometre-scale materials and also further confirms the accumulation of **(porphyrin_{1.0}-[Gd(DTPA)]_{1.0})-PAN** in tumour tissues.^{236,281} The lack of significant T1 enhancement in the tumour tissues may be due to insufficient Gd loading on the PAN despite significant uptake of the nanoparticles, as shown by fluorescence imaging..

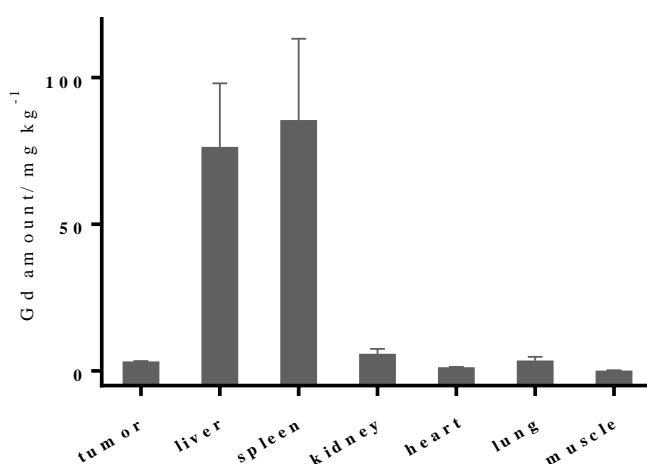


Figure 3.40 ICP-MS biodistribution analysis of mice 1, 3, and 5, shows major deposition of Gd in liver and spleen, and significant Gd uptake in tumour cells.

3.8 Summary

Several acryloyl-based monomers were synthesised, including an alkyne-functionalised monomer, an azide-functionalised monomer, and a water-soluble porphyrin bearing an acryloyl group. The successful synthesis of these monomers prompted the subsequent synthesis of mono- and dual-functional PANs. Initially, covalent incorporation of porphyrin bearing an acryloyl group was attempted. Successful incorporation of porphyrin into PAN was observed on UV-vis. spectroscopy, however, the PAN synthesised showed low yields and multiple size population on DLS. Attempts to vary monomers ratios successfully solved the polydispersity issue, albeit, still with low PAN yields. DLS analysis of size distribution by number greatly mitigates this polydispersity effect, which is an analysis some literature were shown to use.

Nevertheless, the problems encountered prompted the synthesis of conjugatable PAN. The PAN synthesised in this work is capable of multistep conjugation in aqueous media allowing orthogonal conjugation of drug and imaging molecules onto the nanoparticle. A dual-functional theranostic **(porphyrin_{1.0}-[Gd(DTPA)]_{1.0})-PAN** was successfully synthesised and characterised. *In vitro* cytotoxicity evaluation shows that **(porphyrin_{1.0}-[Gd(DTPA)]_{1.0})-PAN** at a porphyrin concentration of 0.62 μM was capable of inducing >90% cell death with minimal dark toxicity. Relaxivity studies indicate an r_1 of 14.7 $\text{mM}^{-1} \text{s}^{-1}$ at 60 MHz, a fourfold increase compared to the clinical equivalent Magnevist® (3.3 $\text{mM}^{-1} \text{s}^{-1}$). Phantom MRI images obtained were also in accordance with the relaxivity studies. Luminescence emission and excited state lifetime measurements of analogous **([Eu(DTPA)]_{1.0})-PAN-(alkyne_{1.0})** and **([Tb(DTPA)]_{1.0})-PAN-(alkyne_{1.0})** were also obtained, showing the complex has a hydration state, q , of 1, similar to some FDA-approved DTPA derivative. These promising results led to *in vivo* evaluation of **(porphyrin_{1.0}-[Gd(DTPA)]_{1.0})-PAN** as a theranostic platform. Accumulation of **(porphyrin_{1.0}-[Gd(DTPA)]_{1.0})-PAN** in tumour tissues was determined using fluorescence imaging and a PDT effect was clearly demonstrated *in vivo via* histology studies. However, no T1 enhancement was observed in tumour tissues, indicating insufficient Gd^{3+} concentration despite significant accumulation of **(porphyrin_{1.0}-[Gd(DTPA)]_{1.0})-PAN** in tumours.

Chapter 4 Radiolabelling of porphyrin conjugates with ^{68}Ga , a route towards a PDT/PET theranostic agent

Previous chapters showed the use of nanoparticles, viral and polymeric, as a platform to combine therapeutic drug and diagnostic molecules for the development of theranostic agents. The use of polyacrylamide nanoparticle in orthogonal conjugation of porphyrin as a photodynamic therapy (PDT) agent and diethylenetriaminepentaacetic acid (DTPA) complexed with gadolinium as a magnetic resonance imaging (MRI) agent, clearly shows porphyrins' capability as an excellent conjugatable molecule as well as a potent PDT agent.

In this chapter, a porphyrin conjugate capable of PDT and positron emission tomography (PET) imaging was investigated. As discussed in Chapter 1, PET has notable advantages as a medical imaging technique. One of PET most notable radiotracer is [^{18}F]-flurodeoxyglucose ([^{18}F]-FDG), which is routinely used in cancer diagnosis.⁸³ Incorporation of many PET isotopes (^{11}C , ^{13}N , ^{15}O , ^{18}F) requires the formation of covalent bonds in a rapid, specific manner following the production of the radioisotope in a cyclotron. However, this procedure must be performed rapidly to ensure delivery of a radiotracer with sufficient activity for imaging. This limits the application of PET using these tracers to sites with ready access to cyclotron produced isotopes and specialised synthesis units.

There has been significant growth in the use of ^{68}Ga as a PET radioisotope,^{81,282,283} culminating in the recent FDA approval of the [^{68}Ga]-DOTATATE in July 2016 (Figure 1.24).⁹⁵ This interest is often attributed to the development of the $^{68}\text{Ge}/^{68}\text{Ga}$ generator, allowing facile on-site generation of the desired radionuclide.²⁸³ ^{68}Ga can be readily incorporated into a radiotracer through the conjugation of a chelate to the targeting unit; this simplifies the synthesis that must be performed following production of the radionuclide.⁸¹

Porphyrins are known to be able to complex a host of metals.¹³⁶ Not surprisingly, there are several reports showing the complexation of ^{68}Ga with porphyrins as theranostic agents.^{153,155,157,159,160} However, the complexation of ^{68}Ga within the porphyrin core often requires harsh conditions; with reaction temperatures in excess of 100 °C. These conditions would be unsuitable for temperature-sensitive moieties, especially peptide-based targeting motifs and other biomolecules.⁸¹

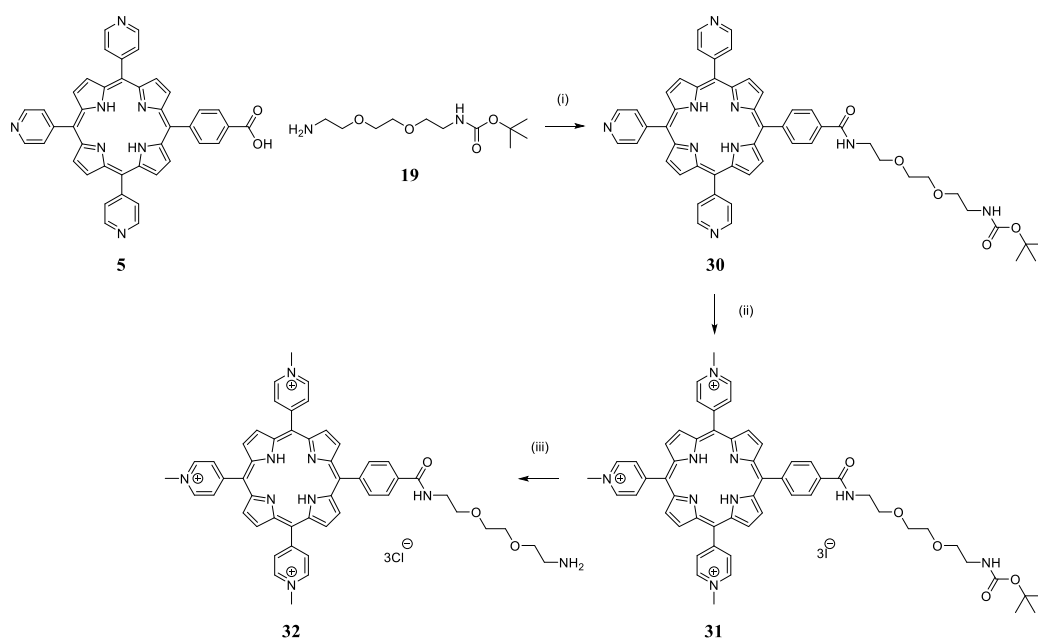
Traditional macrocyclic chelators for ^{68}Ga are 1,4,7,10-tetraazacyclododecane-1,4,7,10-tetraacetic acid (DOTA) and 1,4,7-triazacyclononane-1,4,7-triacetic acid (NOTA); however, these chelators also require harsh conditions for complexation which involves in excess of 80 °C (required for DOTA) and acidic conditions (pH 4, required for both DOTA and NOTA).⁸¹ Recent developments in the design of chelates for ^{68}Ga have resulted in a number of chelates that are capable of radiolabelling under less acidic conditions.^{108,111,284}

Our group has recently reported a series of picolinic acid-amino acid based chelators (Dpaa), capable of chelating ^{68}Ga at ambient temperature under physiological pH (pH 7.4) with excellent radiochemical yield (RCY).¹¹³ In this chapter, the use of a bifunctional chelator, *N,N*-bis[(6-carboxypyridin-2-yl)methyl]glutamic acid ($\text{H}_4\text{Dpaa.ga}$) was employed for the synthesis and evaluation of a novel porphyrin- H_3Dpaa conjugate.

4.1 Synthesis and evaluation of porphyrin- H_3Dpaa conjugate

$\text{H}_4\text{Dpaa.ga}$ was supplied by Thomas Price and was synthesised using a published literature method.¹¹³ A peptide coupling strategy was employed to conjugate porphyrin with $\text{H}_4\text{Dpaa.ga}$. Bifunctional chelator, $\text{H}_4\text{Dpaa.ga}$ has a carboxylic moiety available for conjugation (Scheme 4.2), hence, the synthesis of an amine-appended porphyrin was carried out.

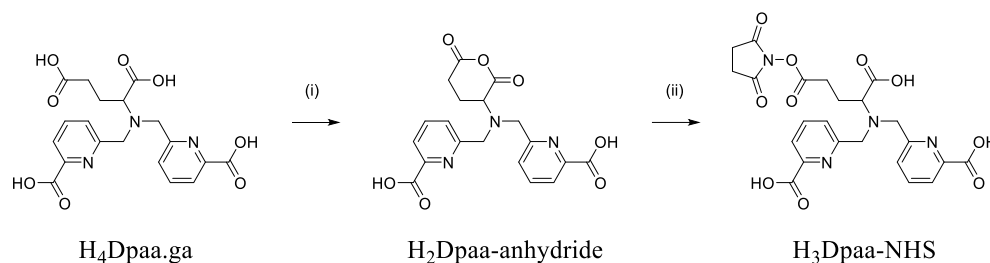
Scheme 4.1 shows the synthesis of amine-appended porphyrin **32**. Initially, carbodiimide and acylazole mediated peptide coupling strategy was employed; porphyrin **5** and mono-Boc diamine chain **19** described previously in chapter 2 and chapter 3, respectively, were conjugated together using a method from literature to afford porphyrin **30** in 89% yield.¹⁷¹ The identity of porphyrin **30** was confirmed using NMR spectroscopy and matches values in literature. Quaternisation of pyridyl groups was carried out with methyl iodide using a similar method described in previous chapters to yield water-soluble porphyrin **31** in good yield (82%). Subsequent HCl mediated Boc-deprotection using a modified method from the literature yielded porphyrin **32** in quantitative yield.^{170,171}



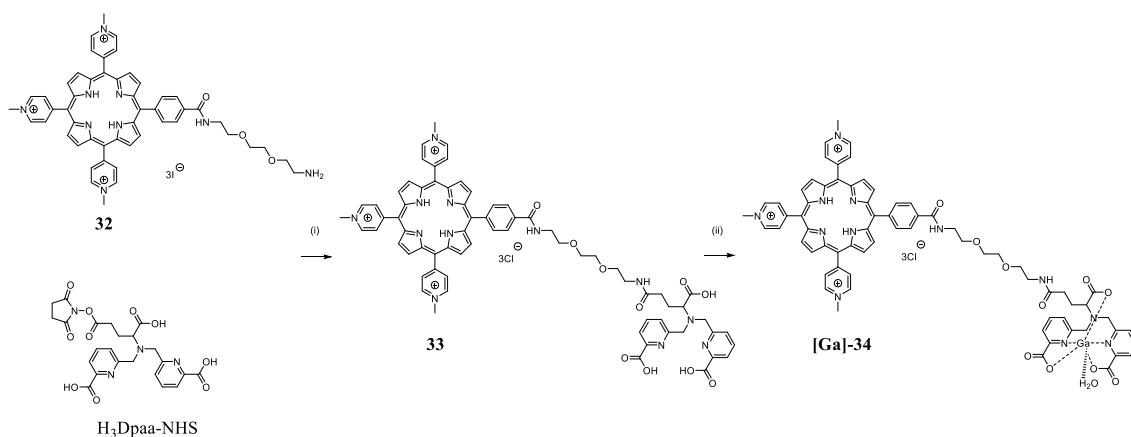
Scheme 4.1 Reaction scheme for the synthesis of amine-appended porphyrin **32**. Reagents, conditions, and yields: (i) DMF, EDC, HOBt, DMAP, room temperature, overnight, 89%, (ii) DMF, MeI, 40 °C, overnight, 82%, (iii) DCM, TFA, room temperature, 3 hours, 98%.

The porphyrin-chelate conjugate **33** was prepared in a 3-step process; activation of $\text{H}_4\text{Dpaa.ga}$, *via* an anhydride ring closing, formation of the activated *N*-hydroxysuccinimide (NHS)-ester, and

conjugation to the amine functionalised porphyrin **32** (Scheme 4.2 and Scheme 4.3). During the ring closing step, the formation of product was monitored using electrospray ionization (ESI) mass spectrometry. Excess acetic anhydride was removed by precipitation of the H₂Dpaa-anhydride using diethyl ether. H₃Dpaa-NHS was formed by addition of NHS in *N,N*-dimethylformamide (DMF) and was used without further purification.



Scheme 4.2 NHS esterification of H₄Dpaa.ga. (i) MeCN, Ac₂O, pyridine, r.t. 30 mins. (ii) DMF, NHS, TEA, r.t. 2 hrs.



Scheme 4.3 Peptide conjugation and subsequent Ga complexation of porphyrin-H₃Dpaa conjugate **33**. Reagents, conditions, and yields: (i) DMF, TEA, room temperature, overnight, 82%, (ii) 0.1 M pH 4.5 acetate buffer, GaCl₃, room temperature, overnight, 71%.

Scheme 4.3 shows the peptide conjugation between porphyrin **32** and H₃Dpaa-NHS to prepare conjugate **33** and the subsequent Ga complexation to prepare [Ga]-**34**. Addition of excess H₃Dpaa-NHS and triethylamine to **32** yielded **33** with quantitative conversion as observed on TLC and HPLC (Figure 4.1). Purification was achieved by exchanging the anionic counter-ions of the porphyrin, which alters the solubility of the porphyrin. Exchange of the iodide anions with hexafluorophosphate rendered the conjugate insoluble in water. This allowed filtration and removal by washing of excess starting materials and reagents. Subsequent anionic conversion to chloride yielded the water-soluble conjugate **33**. ¹H NMR spectroscopy indicated the characteristic aromatic signals of a porphyrin (δ 8.26-9.52), methylated pyridinium protons (δ 4.72), and pegylated protons (δ 3.50) from the linker. The spectrum also indicated picolinic acid protons and amino acid protons from Dpaa both in the aromatic (δ 7.44-7.63) and in the alkyl regions (δ 1.86-3.83). Analytical-HPLC also confirmed the purity of the reaction product (Figure 4.1).

Complexation with non-radioactive $^{nat}\text{GaCl}_3$ was carried out under acidic conditions (pH 4.5) to produce the gallium complex ^{nat}Ga -**34** as the HPLC standard and for use in biological evaluation. Purification of the complex by exchanging the anionic counter-ions was successful in removing excess Ga^{3+} , as confirmed by xylenol orange test. HPLC analysis confirmed the formation of the resulting complex (Figure 4.1). The identity of the product was also confirmed by high resolution mass spectrometry; indicating the formation of a Ga^{3+} complex and the stability of the conjugate to the acidic reaction condition used.

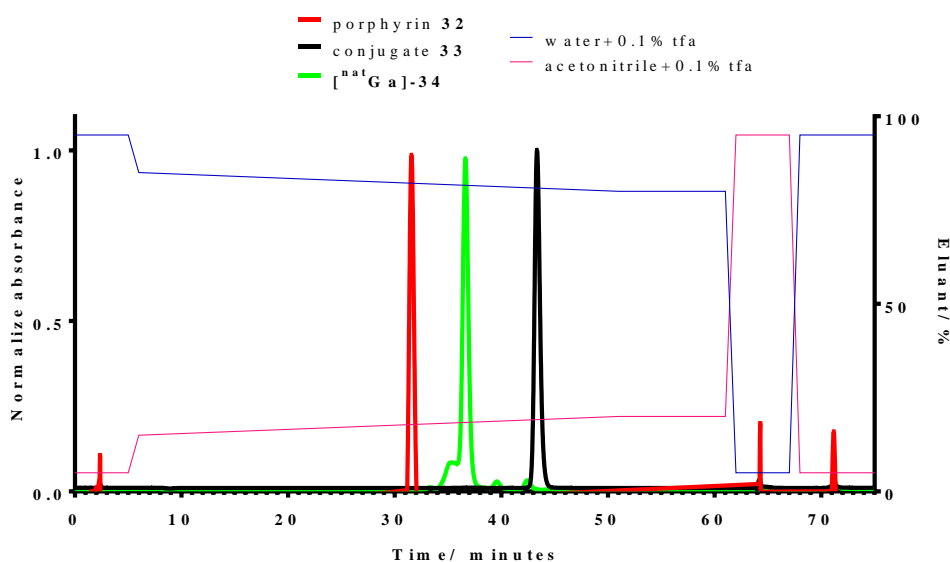


Figure 4.1 UV-vis HPLC chromatograms of porphyrin **32**, conjugate **33**, and complex ^{nat}Ga -**34**.

4.2 ^{68}Ga radiolabelling

According to literature, radiochemical yield (RCY) of H_3Dpaa for complexing ^{68}Ga is pH dependant; with a high RCY (>95%) in acidic conditions of pH 4.¹¹³ Nevertheless, H_3Dpaa is capable of complexing ^{68}Ga at physiological conditions with high RCY, a desired trait for radionuclide chelators and radio-pharmaceuticals for ease of clinical-translation.

Ligand	$\text{H}_4\text{Dpaa.g}$ ^a	Conjugate 33 ^a	Porphyrin 32 ^b
pH 4.5 ^c	99%	93%	0%
pH 7.4 ^d	96%	80%	0%

Table 4.1 Radiochemical yields of ^{68}Ga labelling reactions. Reaction conditions: ^{a,b}[L] = 100 μM . ^at = 15 mins, T = 25 $^\circ\text{C}$. ^bt = 45 mins, T = 99 $^\circ\text{C}$. ^cI = 0.1 M acetate buffer. ^dI = 0.1 M phosphate buffer.

Herein, the radiolabelling efficiency of the conjugate **33** with ^{68}Ga to form ^{68}Ga -**34** was assessed at two different pHs - pH 4.5 and pH 7.4 using radio-HPLC. Table 4.1 shows RCY of ^{68}Ga labelling reactions. At pH 4.5 and 25 $^\circ\text{C}$, $\text{H}_4\text{Dpaa.g}$ and conjugate **33** complexed ^{68}Ga with RCY of >99% (Figure 4.2) and 93% (Figure 4.3), respectively in 15 minutes. At pH 7.4 and 25 $^\circ\text{C}$,

H₄Dpaa.ga and conjugate **33** complexed ⁶⁸Ga with RCY of 96% (Figure 4.2) and 80% (Figure 4.3), respectively in 15 minutes.

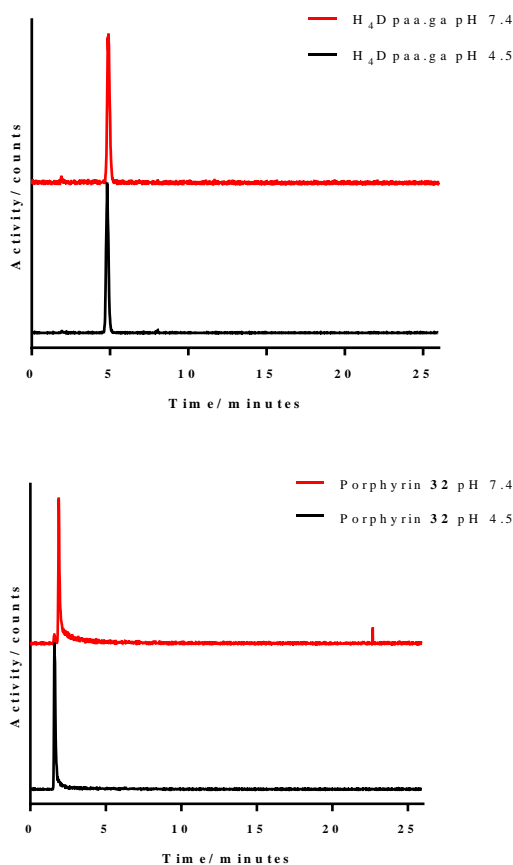


Figure 4.2 Radio-HPLC chromatograms of radiolabelling mixtures of [⁶⁸Ga(Dpaa.ga)] (left) and porphyrin **32** (right). Red line indicates radiolabelling at pH 7.4 and black line indicates radiolabelling at pH 4.5. Reaction conditions: [H₄Dpaa.ga] = 100 μM, T = 25 °C, t = 15 mins. [**32**] = 100 μM, T = 99 °C, t = 45 mins.

Porphyrins are capable of complexing ⁶⁸Ga as mentioned previously, albeit, only under harsh conditions. Hence, radiolabelling of ⁶⁸Ga was also attempted with **32**, with conventional heating at 99 °C. At both pH 4.5 and pH 7.4, radio-HPLC only indicated free-⁶⁸Ga and no radiolabelling was observed (Table 4.1 and Figure 4.2). This shows that, even with heating, the porphyrin moiety did not take part in gallium complexation.

Figure 4.4 shows radio-TLC data obtained for all the radiolabelling reaction mentioned above and agree with radio-HPLC data. These radio-TLC were carried out on aluminium-backed silica TLC plates with 0.1 M aqueous 1:1 trisodium citrate: citric acid as the mobile phase. This solvent system gives definitive separation between labelled complex ($R_f = 0$) and free ⁶⁸Ga ($R_f = 1$) (Figure 4.4).

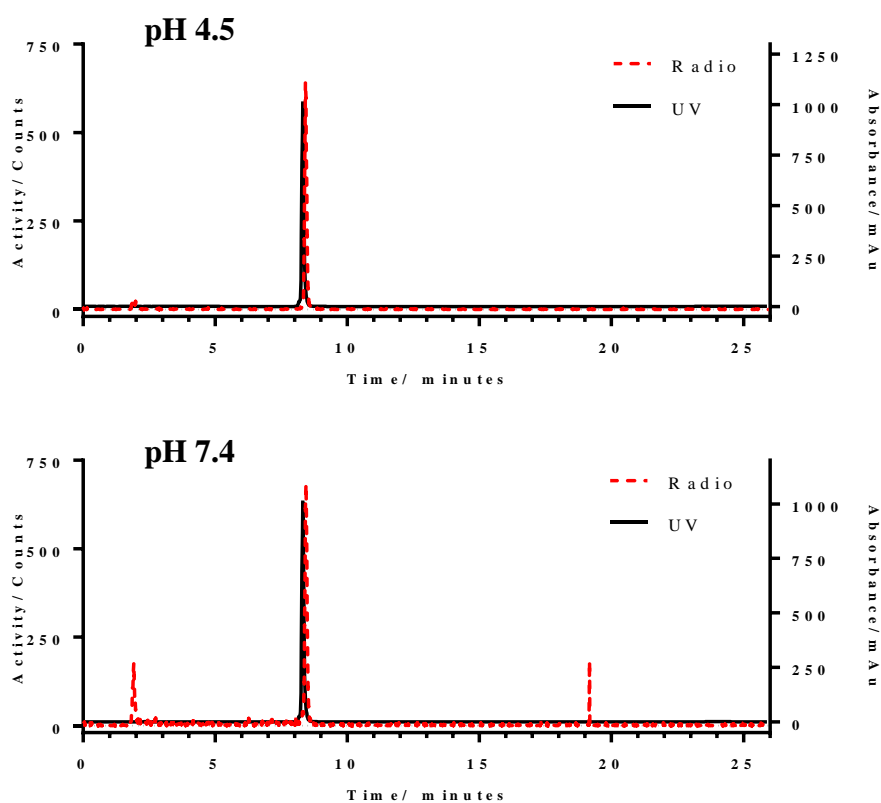


Figure 4.3 Radio-HPLC chromatograms of radiolabelling mixture [^{68}Ga]-**34** and UV-vis HPLC chromatograms of [$^{\text{nat}}\text{Ga}$]-**34**. (top) pH 4.5, 0.1 M acetate buffer, (bottom) pH 7.4, 0.1 M phosphate buffer. Red dashed line indicates radio-HPLC of [^{68}Ga]-**34**. Black solid line indicates UV-HPLC of [$^{\text{nat}}\text{Ga}$]-**34**. Reaction conditions: [**33**] = 100 μM , T = 25 $^{\circ}\text{C}$, t = 15 mins.

Guleria *et al.* has also employed a similar strategy for ^{68}Ga radiolabelling of porphyrins.¹⁶⁰ Whereby, a porphyrin-chelate conjugate was described and evaluated; the chelate used was either DOTA or NOTA. As expected with these traditional macrocycle, radiolabelling reactions were carried out at pH 4 at 100 $^{\circ}\text{C}$, and an RCY of 80% was obtained. Results obtained and described in this chapter showed that conjugate **33** could produce similar RCY for ^{68}Ga radiolabelling under physiological conditions, demonstrating a distinct advantage over this recent literature.¹⁶⁰

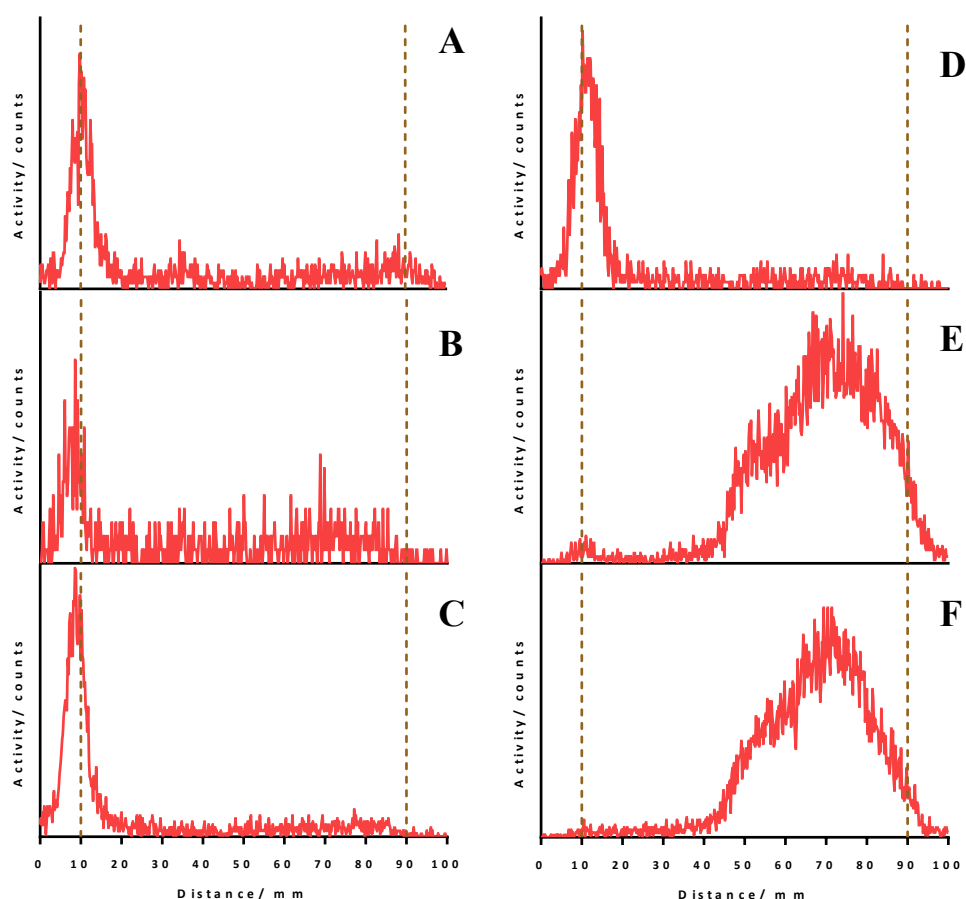


Figure 4.4 Radio-TLC of radiolabelling mixture [^{68}Ga]-**34** at pH 4.5 (A) and pH 7.4 (B), [$^{68}\text{Ga}(\text{Dpaa.ga})$] at pH 4.5 (C) and pH 7.4 (D), and porphyrin **32** at pH 4.5 (E) and pH 7.4 (F). Dotted lines indicate baseline (left, $R_f = 0$) and solvent front (right, $R_f = 1$). Radio-TLC were carried out on aluminium-backed silica TLC plates with 0.1 M aqueous 1:1 trisodium citrate: citric acid as the mobile phase. Reaction conditions: (A-D) $[\text{L}] = 100 \mu\text{M}$, $t = 15 \text{ mins}$, $T = 25 \text{ }^\circ\text{C}$. (E,F) $[\text{L}] = 100 \mu\text{M}$, $t = 45 \text{ min}$, $T = 99 \text{ }^\circ\text{C}$.

4.3 *In vitro* phototoxicity evaluation

The phototoxicity of **33** and [^{nat}Ga]-**34** was assessed in human adenocarcinoma (HT-29) cells (Figure 4.6) using MTT assay. Cells were incubated with either **33** or [^{nat}Ga]-**34** at varying concentrations and irradiation was carried out using a constant dose of visible light (20 J cm^{-2} ; 400 – 700 nm). The results were compared to a non-irradiated control. Similar to the *in vitro* phototoxicity evaluation carried out in chapter 3, irradiation with visible light was used instead of red light. Red light is more commonly used for PDT in a clinical setting, however, the strength and power of clinical lasers used in PDT are significantly higher compared to the quartz tungsten halogen light source used in this study. Hence, to compensate for the lower power, white light was used, covering the whole porphyrin absorbance range (Figure 4.5).

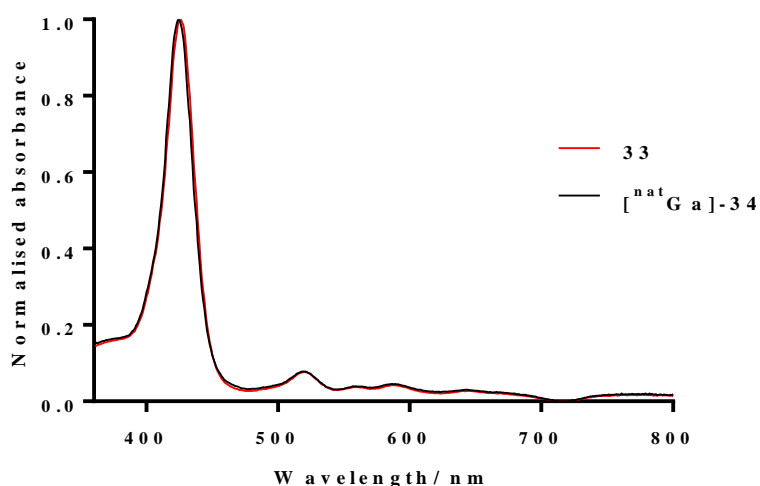


Figure 4.5 UV-vis absorbance spectrum of **33** and $[\text{natGa}]\text{-34}$.

Under these conditions, >50% cell death was observed at 50 μM , and >90% cell death was observed at a concentration of 160 μM for both **33** and $[\text{natGa}]\text{-34}$ when irradiated. Minimal dark toxicity was observed in the non-irradiated controls with more than 95% cell survival at all concentrations tested (Figure 4.6). These results shows that **33** and $[\text{natGa}]\text{-34}$ have lower photodynamic activity and requires a higher concentration to induce cell death. This is apparent when compared to an FDA approved porphyrin PDT agent, Photofrin®, in HT-29 cells, which requires concentration of 40 ng mL^{-1} (approximately 60 μM porphyrin core as Photofrin® is a mixture of monomeric and oligomeric forms of porphyrin) to induced 90% cell death.²⁶⁷ These results also show complexation of gallium do not affect the PDT efficacy of the porphyrin.

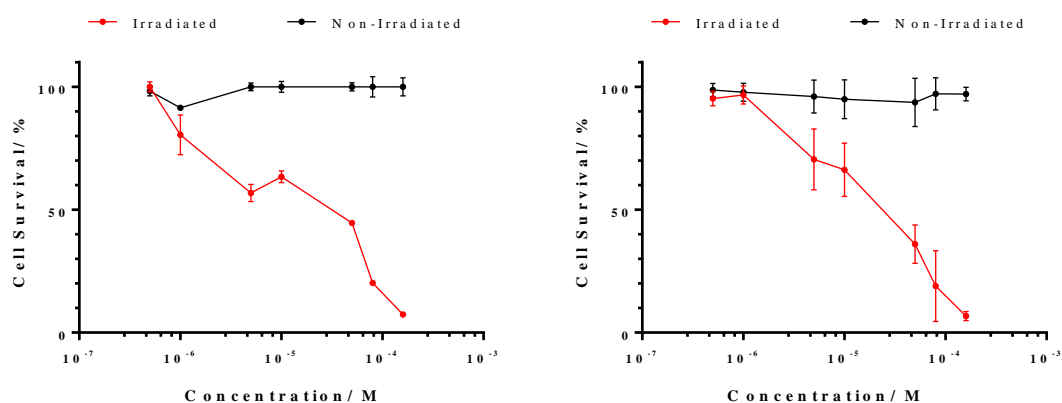


Figure 4.6 % cell survival of HT-29, irradiated cell and non-irradiated cells (control), determined using MTT assay. Cells were incubated with varying concentration of conjugate **33** (left) and $[\text{natGa}]\text{-34}$ (right) for 1 hour and irradiated cells received 20 J cm^{-1} white light. Error bars shown were obtained from triplicate measurements.

4.4 Summary

In summary, porphyrin- H_3Dpaa conjugate **33** was successfully prepared from an amine-appended porphyrin **32** and picolinic acid-amino acid-based chelator ($\text{H}_4\text{Dpaa.g}$) and was successfully characterised. Complexation with natGa yielded non-radioactive $[\text{natGa}]\text{-34}$ as an HPLC standard

and for use in biological evaluation. Radiolabelling reactions showed conjugate **33** is capable of ^{68}Ga complexation at physiological conditions (15 minutes, pH 7.4, room temperature) to produce [^{68}Ga]-**34** with a radiochemical yield of 80%, which is a trait introduced by the H₃Dpaa moiety (H₄Dpaa.ga is capable of ^{68}Ga complexation at physiological conditions with radiochemical yield of 93%). To further show the H₃Dpaa moiety is responsible for ^{68}Ga complexation, a control ^{68}Ga radiolabelling with porphyrin **32** was carried out, and no radiolabelling was observed.

Phototoxicity and toxicity of **33** and [^{nat}Ga]-**34** was evaluated on human adenocarcinoma (HT-29) cells with and without irradiation with visible light, respectively; >50% cell death was induced upon light irradiation at a concentration of 50 μM , with minimal toxicity observed on cells without light irradiation (>95% cell survival at all concentrations tested).

Porphyrin-H₃Dpaa conjugate **33** has demonstrated its capability as both a PDT agent and can be selectively radiolabelled under mild conditions with ^{68}Ga for PET imaging. These results have also been published in literature.²⁴⁷

Chapter 5 Porphyrins and amino acids “clicked” conjugates for ^{99m}Tc radiolabelling as PDT/SPECT theranostic agent

Porphyrin- H_3Dpaa conjugate, as is described in chapter 4, has shown potential as a PET/PDT theranostic agent. Incorporation of ^{68}Ga with Dpaa moiety on the conjugate, allows PET imaging. Despite the ease of generation of ^{68}Ga using $^{68}\text{Ge}/^{68}\text{Ga}$ generator, ^{68}Ga is still a relatively new radioisotope in radiopharmaceutics, with only one FDA approved ^{68}Ga radiotracer to date, [^{68}Ga]-DOTATATE.⁹⁵

This chapter will focus on porphyrin conjugates capable of PDT and single-photon emission computed tomography (SPECT) imaging. As discussed earlier in Chapter 1, SPECT is also a highly-sensitive radioimaging technique. It relies on the administration of a radiotracer, which will biodistribute/accumulate in the body. SPECT imaging will then generate a 3D image showing the distribution of the radiotracer in the body. ^{99m}Tc is SPECT most notable radioisotope with more than 15 food and drug administration (FDA) approved radiopharmaceutics.¹¹⁵ Its well-established chemistry, availability of $^{99}\text{Mo}/^{99m}\text{Tc}$ generator, and its relative low cost, made ^{99m}Tc the radioisotope of choice.

Hereby, SPECT presented itself as a well-established radioimaging method, to be incorporated onto porphyrins as a combined PDT/SPECT theranostic agents. Unsurprisingly, literature, though quite limited, has presented the combination of porphyrin with ^{99m}Tc .^{166,167,169–171} In this chapter, the investigation on the incorporation of SPECT imaging onto porphyrins is described.

Histidine has been shown to form stable complex with [$^{99m}\text{Tc}(\text{CO})_3(\text{H}_2\text{O})_3$]⁺, and has been used to incorporate ^{99m}Tc biomolecules and peptides as targeted radiopharmaceutics.^{168,285} Schibli's research group has further shown that alkyne/azide-modified amino acids “click” via copper-catalyse azide alkyne cycloaddition (CuAAC) with other azide/alkyne-functionalised molecules, can produce efficient [$^{99m}\text{Tc}(\text{CO})_3(\text{H}_2\text{O})_3$]⁺ chelates. The formation 1,4-disubstituted 1,2,3-triazole during CuAAC has similar structural and electronic features as a 1,4-disubstituted imidazole, creating a histidine-like structure capable of complexing [$^{99m}\text{Tc}(\text{CO})_3(\text{H}_2\text{O})_3$]⁺.²⁸⁶ The utilisation of “click” chemistry unlocks the possibility to use a high yielding, high purity “click” reaction to combine two moieties together, paving the way towards molecular theranostic medicine.

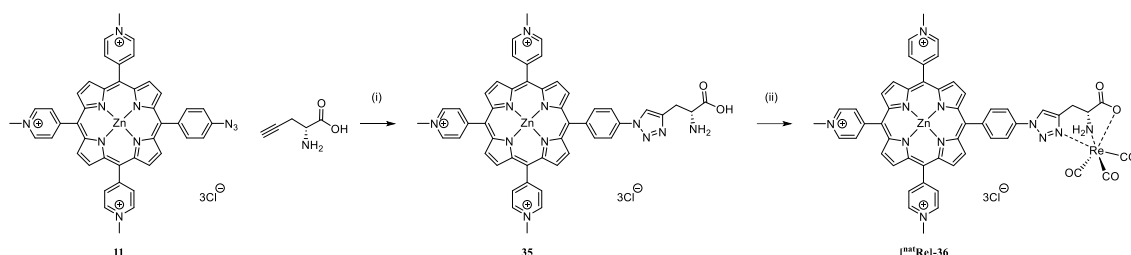
Naturally, this provides an excellent route towards combining a chelate capable of complexing ^{99m}Tc with porphyrins. Despite the ease and potential of these “clickable” histidine-like amino acids, no literature has reported the usage of these “clickable” amino acids with porphyrins, and there is only one example on the usage of a porphyrin-histidine conjugate as a ^{99m}Tc chelate.¹⁶⁹

Herein, a similar strategy to Schibli's research group was utilised. “Clickable” alkyne-functionalised amino acids were conjugated with water-soluble azido porphyrin to form

porphyrin-amino acid conjugates capable of $[^{99m}\text{Tc}(\text{CO})_3]^+$ complexation, affording a PDT/SPECT theranostic agent. This chapter will describe the synthesis and evaluation of, firstly, a bifunctional theranostic porphyrin-Gly conjugate, and subsequently, a trifunctional targeted theranostic porphyrin-Lys-TM (TM = targeting molecule) conjugate.

5.1 Synthesis of bifunctional and trifunctional porphyrin-amino acid conjugates

5.1.1 Synthesis and characterisation of porphyrin-Gly conjugate and porphyrin- $[\text{natRe}(\text{Gly})]$ complex



Scheme 5.1 Synthesis of porphyrin-Gly conjugate **35** and porphyrin- $[\text{natRe}(\text{Gly})]$ complex $[\text{natRe}]\text{-36}$. Reagents, conditions, and yields: (i) 1:1 t-butanol:water, CuSO_4 , sodium ascorbate, TBTA, microwave (20 mins, 75 W, 50 °C), 84%, (ii) phosphate buffer (pH 7), $[\text{Re}(\text{CO})_3\text{Br}_3][\text{NEt}_4]_2$ **37**, 65 °C, 2 hours, 76%.

Scheme 5.1 shows the synthesis of porphyrin-Gly conjugate **35** and porphyrin- $[\text{natRe}(\text{Gly})]$ complex $[\text{natRe}]\text{-36}$. Water-soluble azido porphyrin **11** described in chapter 2.1.3 was utilised and conjugated using the commercially available D-propargylglycine *via* CuAAC “click” reaction. Although CuAAC are known to proceed to completion at ambient temperature and pressure, similar to the CuAAC conjugation of porphyrin onto polyacrylamide nanoparticles described in chapter 3.3.4.2, reaction times can be accelerated through microwave synthesis,²⁸⁷ and with complete regioselectivity.²⁸⁸ With excess D-propargylglycine, quantitative conversion of porphyrin **11** to conjugate **35** was shown using TLC and HPLC analysis, with a clear shift in HPLC retention time from 10.8 mins to 7.5 mins (Figure 5.1). Purification of conjugate **35** was carried out by exchanging the anionic counter-ions of the porphyrin, similar to the purification method described in chapter 4.1. The changing of the anionic counter-ion to hexafluorophosphate, render the conjugate **35** water insoluble and allowed the collection of the product by filtration and the washing of starting material and catalyst. Subsequent anionic conversion to chloride yielded the water-soluble conjugate **35**. The identity of **35** was confirmed using HPLC, NMR, and mass spectrometry.

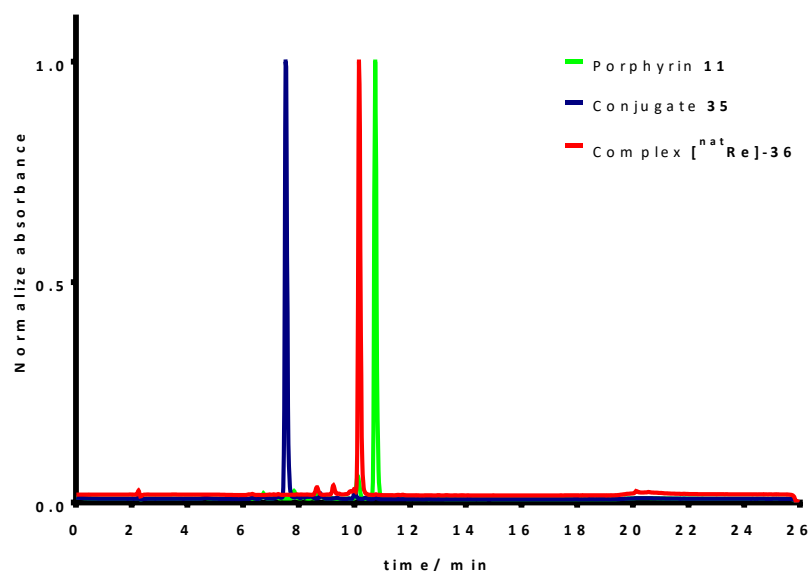


Figure 5.1 UV-vis HPLC chromatograms of porphyrin **11**, conjugate **35**, and complex **36**.

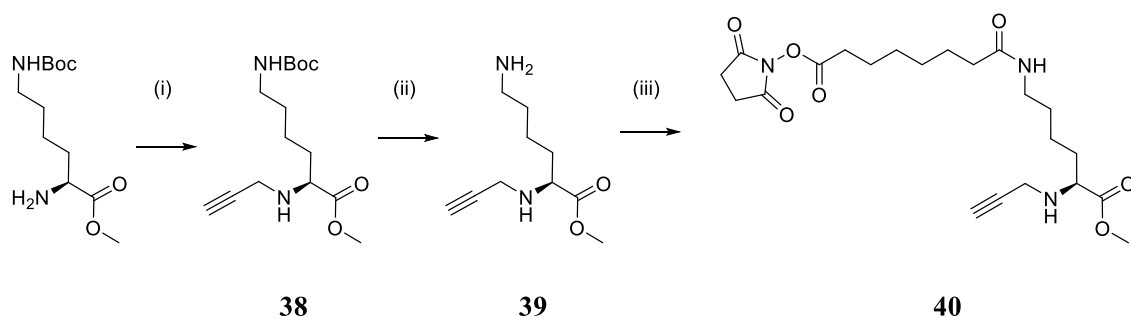
Complexation of conjugate **35** with chemically and physically similar rhenium was carried out prior to radiolabelling with ^{99m}Tc .^{289–291} The histidine-like chelate on conjugate **35** has been shown in literature to stably chelate $[\text{Tc}(\text{CO})_3]^+$, hence, the rhenium equivalent, $[\text{natRe}(\text{CO})_3\text{Br}_3][\text{NEt}_4]_2$ was first prepared using a literature method.²⁹² Complexation of conjugate **35** was carried out with excess $[\text{natRe}(\text{CO})_3]^+$ at 65 °C for 2 hours to produce a non-radioactive complex $[\text{natRe}]\text{-36}$ for use as an HPLC standard and for use in biological cytotoxic evaluation. TLC and HPLC analysis of the reaction mixture showed quantitative conversion to $[\text{natRe}]\text{-36}$, and purification by exchanging anionic counter-ions was carried out. Analytical HPLC indicated a shift in retention time from 7.5 min to 10.2 min (Figure 5.1). NMR spectroscopy clearly confirmed the formation of the product. The aromatic region in ^1H NMR showed characteristic aromatic protons for the porphyrin, which included pyridyl protons, phenyl protons, β -protons, and also the triazole proton which comes to resonance at δ 9.28. The alkyl region in ^1H NMR also showed methylated pyridinium protons, and protons responsible for the glycine moiety, with clear observation of amine protons on the amino acid in ^1H NMR at δ 5.54 and 6.14. The huge splitting and clear observation of these amine protons is due to the rigid conformation of the amino acid which is fixed in place upon chelation of $^{\text{nat}}\text{Re}$. The resulting ^1H - ^1H COSY spectrum agrees with this observation; clearly showing coupling between the two amine protons, coupling of the amine at δ 6.14 with alkyl glycine α -proton at δ 3.99, and coupling between triazole proton at δ 9.28 with alkyl glycine proton at δ 3.42. Coupling is only observed between the amine proton at δ 6.14 and not the amine proton at δ 5.54 with glycine α -proton at δ 3.99, this can be explained using the Karplus rule, where the magnitude of coupling is determined by the angle between protons.²⁹³ ^{13}C NMR shows addition of three carbonyl carbon peaks between δ 197–199, showing the successful chelation of rhenium. This subchapter shows the successful synthesis of a porphyrin-Gly conjugate capable of $^{\text{nat}}\text{Re}$ complexation.

5.1.2 Synthesis and characterisation of porphyrin-Lys-TM conjugate and porphyrin-[^{nat}Re(Lys)]-TM complex

In the early 1990s, Nobel Laureate Paul Ehrlich described the idea of a “magic bullet”, a drug molecule that precisely and selectively targets diseased cells. Since then, scientists have used this notion, and combined drug molecules with targeting molecules, including, sugars, monoclonal antibodies, peptides, and other biomolecules.

As mentioned above, SPECT imaging relies on the biodistribution and accumulation of radiotracer inside the body. Hence, there is a need for a SPECT imaging agent to be able to accumulate or target a specific region of interest in the body could not be more important.

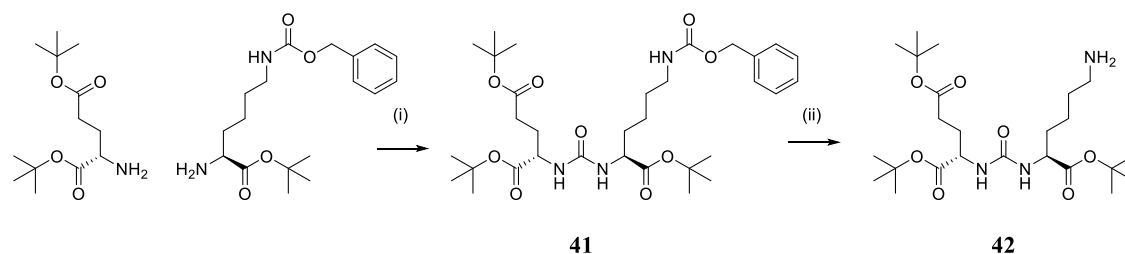
Herein, as an extension to the bifunctional theranostic porphyrin-Gly conjugate **35** described above (Chapter 5.1.1), a trifunctional targeted theranostic porphyrin-Lys-TM conjugate **47** is described. A small molecule dipeptide, which acts as an inhibitor for the prostate specific membrane antigen (PSMA, also known as glutamate carboxypeptidase II (GCPII)), was selected as the targeting molecule (TM). PSMA is a type 2 integral membrane glycoprotein that is overexpressed on the surface of prostate carcinomas and on the neovasculature of most other solid tumours.²⁹⁴ The targeting molecule has the structure: lysine-urea-glutamate, with the glutamate moiety responsible for targeting and binding to the pharmacophore pocket of PSMA.^{295,296} The aim was to incorporate the aforementioned small molecule PSMA inhibitor onto porphyrin-amino acid conjugate, to allow targeted delivery of the conjugate to prostate cancer.



Scheme 5.2 Synthesis of “clickable” and conjugatable alkyne-functionalised lysine. Reagents, conditions, and yields: (i) DMF, K₂CO₃, propargyl bromide, room temperature, 48 hours, 72%, (ii) DCM, TFA, room temperature, 2 hours, 95%, (iii) DMF, disuccinimidyl suberate, TEA, room temperature, overnight, 88%.

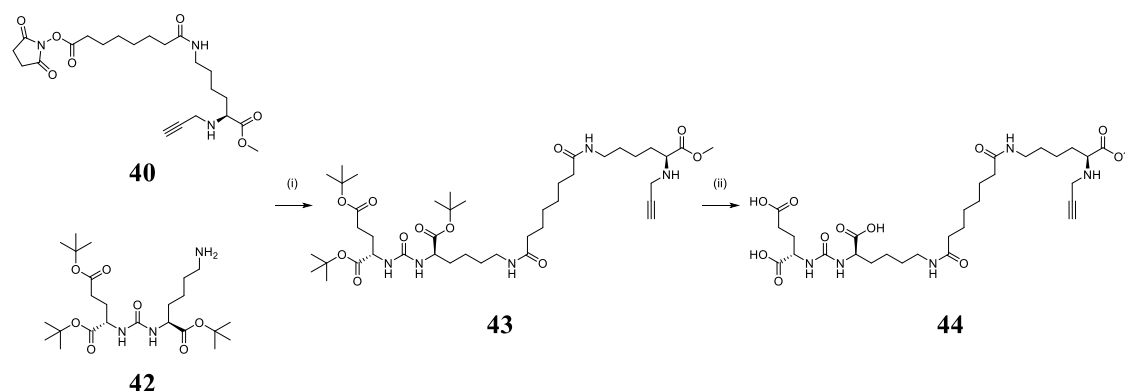
To incorporate a third functionality, the use of a “clickable” alkyne-functionalised lysine was investigated. Lysine has an extra amine group compared to glycine, which can be used for further conjugation, hence, allowing the third functionality to be introduced. However, there is no commercially available propargyl lysine, hence, modification of commercially available *N*(ε)-Boc-Lys(OMe) was required. Scheme 5.2 shows the modification of *N*(ε)-Boc-Lys(OMe) to introduce an alkyne-functionality and also a conjugatable linker. According to a modified literature method, reaction between *N*(ε)-Boc-Lys(OMe) and propargyl bromide afforded **38** in 72% yield. Subsequent, Boc-deprotection using trifluoroacetic acid (TFA) afforded **39** in

quantitative yield with an amine group for further conjugation. A suitable linker, disuccinimidyl suberate, was introduced onto **39** to give **40** in 88% yield. The introduction of a suberate linker is essential as this not only allows conjugation onto the PSMA inhibitor **42** (described below), which also has an amine group for conjugation, it also acts as a spacer group to ensure the PSMA binding affinity of inhibitor **42** is unaffected.²⁹⁷ The identity of **38-40** was confirmed using NMR spectroscopy and mass spectrometry.



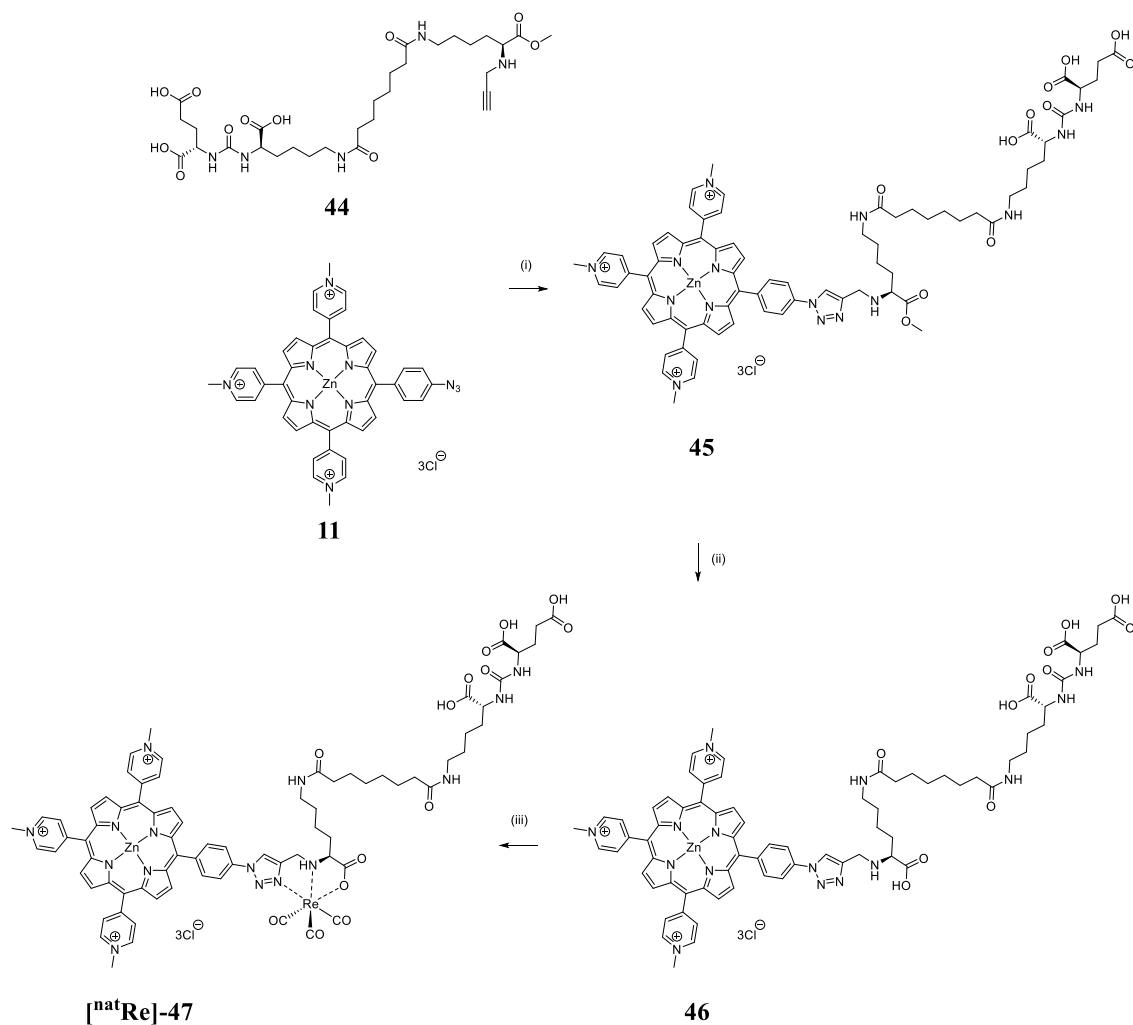
Scheme 5.3 Synthesis of small molecule dipeptide precursor **39** for the targeting molecule for PSMA. Reagents, conditions, and yields: (i) dry DCM, triphosgene, TEA, 0 °C-room temperature, 3 hours, 34%. (ii) MeOH, Pd on C, hydrazine, room temperature, overnight, 89%.

Scheme 5.3 shows the synthesis of the precursor **42** as the targeting molecule. Using a method adapted from the literature, **38** was synthesised using protected amino acids, L-glutamic acid di-*tert*-butyl ester and *N*(ϵ)-benzyloxycarbonyl-L-lysine-*tert*-butyl ester.²⁹⁸ Formation of a urea bond between the amino acids was mediated using triphosgene, and the product was confirmed using NMR spectroscopy, with NMR peaks in agreement with literature values. Subsequent deprotection of the benzyloxycarbonyl group *via* hydrogenation afforded **39** with an amine group for further conjugation.



Scheme 5.4 Conjugation of **40** and **42** and subsequent *tert*-butyl deprotection. Reagents, conditions, and yields: (i) DMF, TEA, room temperature, overnight, 62%, (ii) DCM, TFA, room temperature, 3 hours, 96%.

Scheme 5.4 shows the conjugation of “clickable” lysine **40** with **42**. Peptide coupling was carried out under basic conditions in DMF to afford **43** in 62% yield. The *tert*-butyl protecting group was removed using TFA. Repeated trituration and evaporation using dichloromethane afforded the “clickable” lysine with attached targeting molecule **44** in quantitative yield.



Scheme 5.5 “Click” conjugation of **44** with porphyrin **11**, methyl deprotection, and $^{\text{nat}}\text{Re}$ complexation. Reagents, conditions, and yields: (i) 1:1 *t*-butanol:water, CuSO_4 , sodium ascorbate, TBTA, microwave (3 hours, 75 W, 70 °C), 77%, (ii) water, LiOH, room temperature 3 hours, 90%, (iii) phosphate buffer (pH 7), $[\text{Re}(\text{CO})_3\text{Br}_3][\text{NET}_4]_2$ **37**, 65 °C, 30 mins, 75%.

The successful synthesis of **44** prompted the “click” conjugation with porphyrin **11** as shown in Scheme 5.5. Using similar “click” conditions as for the synthesis of conjugate **35**, excess **44** was used and quantitative conversion of porphyrin **11** to conjugate **45** was observed on TLC and HPLC, with an isolate yield of 77%. A clear shift in retention time in analytical HPLC was observed, from 10.8 min for porphyrin **11** to 8.6 min for conjugate **45** (Figure 5.2). Using an anionic exchange method, excess reagents and starting materials were efficiently removed *via* filtration. NMR spectroscopy confirmed the identity of **45**; clearly showing characteristic aromatic signals of porphyrin and along with the alkyl protons of lysine, suberic linker, and targeting molecule. The formation of the triazole ring was also confirmed using ^1H NMR with the triazole proton peak overlapping with the β -protons and ortho-pyridyl proton at δ 8.91.

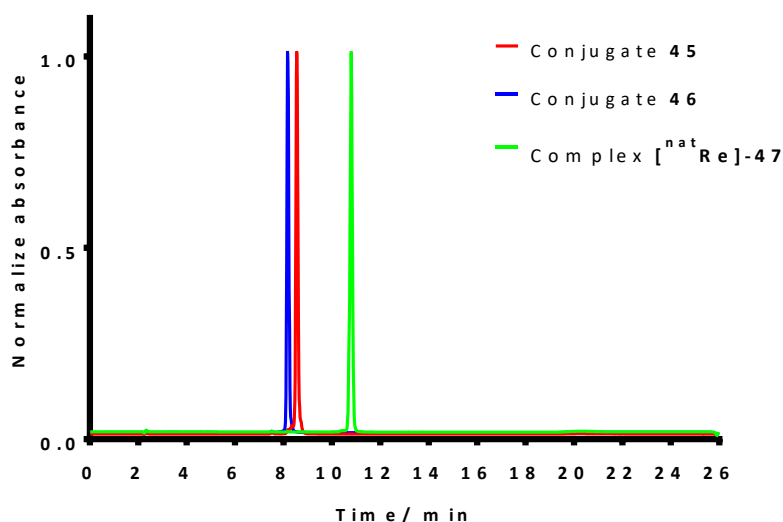


Figure 5.2 UV-vis HPLC chromatograms of conjugate **45**, conjugate **46**, and complex $[\text{natRe}]\text{-47}$.

Subsequent, deprotection of the methyl ester on **45** was carried out in aqueous LiOH to prepare the desired porphyrin-Lys-TM conjugate **46**. Quantitative conversion of **45** to **46** and completion of the reaction was followed using TLC and HPLC. An anion exchange method was used to remove water soluble lithium salts. However, careful manipulation of pH was required for the anion exchange method to work efficiently. This is due to the presence of several carboxylate groups; hexafluorophosphate anion exchange and protonation of carboxylate groups under mild acidic conditions were required to render **46** water-insoluble for the filtration and washing of lithium salts. Subsequently, anion exchange back to a chloride counter ion afforded water-soluble conjugate **46** in 90% yield. A shift in retention time from 8.6 min to 8.2 min for **45** to **46** was observed in analytical HPLC (Figure 5.2). NMR spectroscopy showed clearly the removal of the methyl ester peak at δ 3.67.

Successful synthesis of conjugate **46** prompted the complexation with rhenium to form the analogous, non-radioactive porphyrin- $[\text{natRe}(\text{Lys})]\text{-TM}$ $[\text{natRe}]\text{-47}$. Similarly to complexation of rhenium with conjugate **35**, $[\text{Re}(\text{CO})_3\text{Br}_3][\text{NEt}_4]_2$ **37** was added to conjugate **46** at pH 7 and heated at 65 °C. Quantitative conversion of **46** to $[\text{natRe}]\text{-47}$ was observed on analytical HPLC, with a shift in retention time from 8.2 min to 10.8 min (Figure 5.2). Similarly to the anion exchange method used for conjugate **46**, acidification of reaction mixture to protonate carboxylate group was required. ^{13}C NMR spectroscopy showed the presence of three extra carbonyl peaks between δ 197-198, indicating rhenium tricarbonyl peaks, and hence confirming the identity of $[\text{natRe}]\text{-47}$.

The successful synthesis of both porphyrin-Gly conjugate **35** and porphyrin-Lys-TM conjugate **46**, and their non-radioactive complex, $[\text{natRe}]\text{-36}$ and $[\text{natRe}]\text{-47}$, respectively, prompted subsequent $^{99\text{m}}\text{Tc}$ complexation to form a theranostic PDT/SPECT agent.

5.2 ^{99m}Tc radiolabelling

As described in the previous subchapter, these porphyrin amino-acid conjugates, **35** and **46**, were shown to have histidine-like structures that efficiently complex $[\text{Re}(\text{CO})_3]^+$. To impart SPECT imaging modality on these conjugates, ^{99m}Tc radiolabelling was carried out.

^{99m}Tc can be easily obtained from a $^{99}\text{Mo}/^{99m}\text{Tc}$ generator. Elution of the generator was carried out using 0.9% saline solution to afford $\text{Na}[^{99m}\text{TcO}_4]$. Reduction of $^{99m}\text{Tc}(\text{VII})$ to $^{99m}\text{Tc}(\text{I})$ is required prior to labelling. Several literature methods have shown the production of $[\text{Tc}(\text{CO})_3]^+$; Waibel *et al.* reported the usage of NaCO_3 , NaBH_4 , and carbon monoxide gas to react with $[\text{TcO}_4]^-$ to produce $[\text{Tc}(\text{CO})_3]^+$.¹⁶⁸ The usage of a highly toxic gas, carbon monoxide, in a radioactive environment may introduce complications and can increase risk of chemical and radioactivity contamination. Another method reported by Alberto *et al.* involved the synthesis and isolation of a boranocarborane, namely, $\text{K}_2[\text{H}_3\text{BCO}_2]$, which acts as both a carbon monoxide source and a reducing agent, capable of *in situ* preparation of $[\text{Tc}(\text{CO})_3]^+$.²⁹⁹ However, the synthesis of $\text{K}_2[\text{H}_3\text{BCO}_2]$ still involved the use of carbon monoxide and also a pyrophoric gas H_3BCO . To avoid this, commercially available $\text{Na}_2[\text{H}_3\text{BCO}_2]$ was selected as a carbon monoxide source and reducing agent for the preparation of $[\text{Tc}(\text{CO})_3]^+$. Using a method reported by Alberto *et al.*, $[\text{Tc}(\text{CO})_3]^+$ was prepared and analysed using radio-HPLC (Figure 5.3) and radio-TLC (Figure 5.4). Radio-HPLC shows a radiochemical yield (RCY) of 97% for the conversion of $[\text{TcO}_4]^-$ to $[\text{Tc}(\text{CO})_3]^+$, a similar yield reported in the literature.²⁹⁹ Radio-TLC was carried out with 1% HCl in methanol as the mobile phase according to a literature method.³⁰⁰ With this mobile phase, $[\text{TcO}_4]^-$ elutes at the solvent front ($R_f = 1$) and $[\text{Tc}(\text{CO})_3]^+$ elutes as a smear on the TLC ($R_f = 0.2\text{-}0.8$).

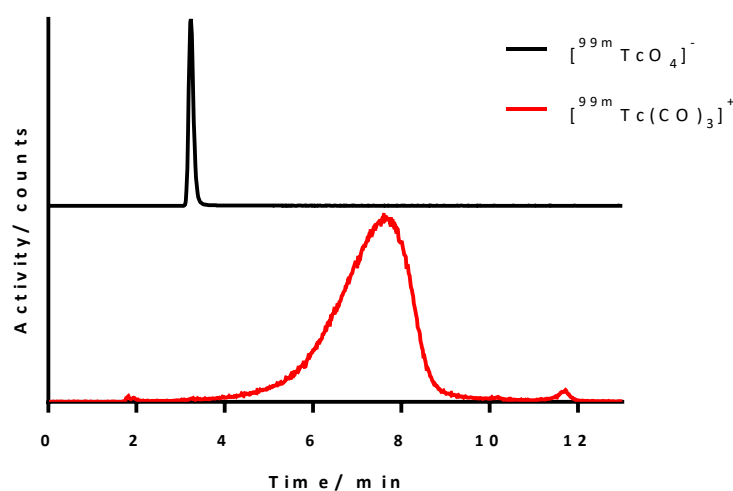


Figure 5.3 Radio-HPLC chromatogram of $[\text{TcO}_4]^-$ and $[\text{Tc}(\text{CO})_3]^+$.

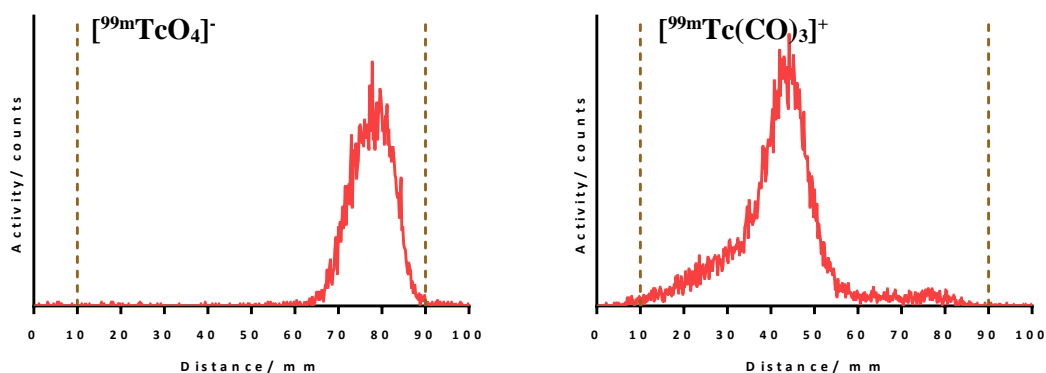
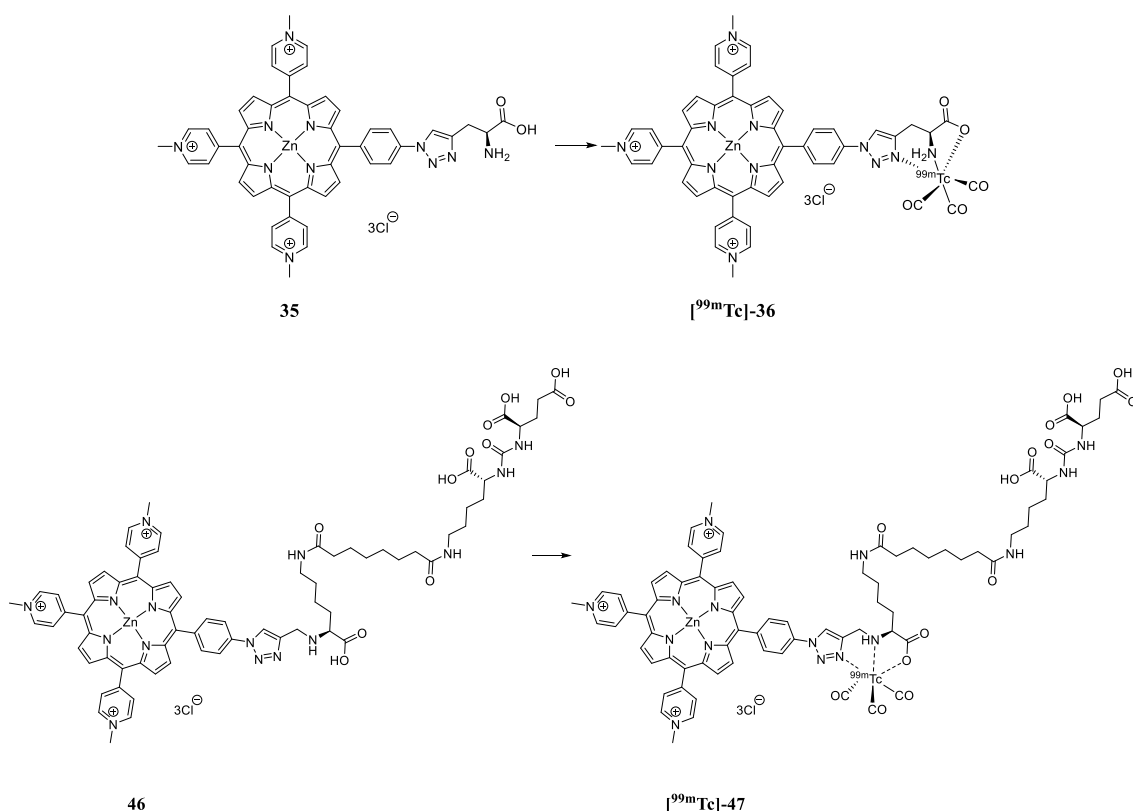


Figure 5.4 Radio-TLC chromatograms of reduction of $[^{99m}\text{TcO}_4]^-$ to $[^{99m}\text{Tc}(\text{CO})_3]^+$. Dotted lines indicate baseline (10 cm, $R_f = 0$) and solvent front (90 cm, $R_f = 1$). Radio-TLC were carried out on aluminium-backed silica TLC plates with 1% HCl in methanol as the mobile phase.



Scheme 5.6 Radiolabelling of conjugate **35** and conjugate **46** to prepare complex $[^{99m}\text{Tc}]\text{-36}$ and $[^{99m}\text{Tc}]\text{-47}$. Reaction conditions: $t = 30$ mins, $T = 99$ °C, pH 7.4 or pH 11.

Following the successful preparation of $[^{99m}\text{Tc}(\text{CO})_3]^+$, radiolabelling of conjugate **35** and conjugate **46** to prepare $[^{99m}\text{Tc}]\text{-36}$ and $[^{99m}\text{Tc}]\text{-47}$ was carried out (Scheme 5.6). Radiolabelling efficiency was evaluated at 99 °C for 30 mins with varying concentrations of conjugates (0.5 – 150 μM) and at two different pHs, pH 7.4 and pH 11. pH 11 was initially evaluated as preparation of $[^{99m}\text{Tc}(\text{CO})_3]^+$ is carried out under basic conditions, and radiolabelling was carried out without any post-processing of $[^{99m}\text{Tc}(\text{CO})_3]^+$. Physiological pH 7.4 was also evaluated as radiolabelling at pH 7.4 will minimise post-radiolabelling processing, simplifying the production of radiotracer for use in preclinical or clinical imaging.

Radiolabelling reaction mixtures were characterised using radio-HPLC and radio-TLC. Formation of the desired ^{99m}Tc complexes, $[^{99m}\text{Tc}]\text{-36}$ and $[^{99m}\text{Tc}]\text{-47}$ were followed using radio-HPLC and compared with UV-vis HPLC of the corresponding rhenium complexes, $[\text{natRe}]\text{-36}$ and $[\text{natRe}]\text{-47}$, respectively (Figure 5.5).

At pH 11, RCY of $>80\%$ were achieved for both conjugates, **35** and **46**, at $150\ \mu\text{M}$ with an EC_{50} of $20\ \mu\text{M}$ and $44\ \mu\text{M}$, respectively (Figure 5.6), showing that conjugate **35** is more efficient at radiolabelling ^{99m}Tc . This may be due to **35** being a simpler and smaller molecule, with less non-coordinating carboxylate groups interfering with ^{99m}Tc radiolabelling.

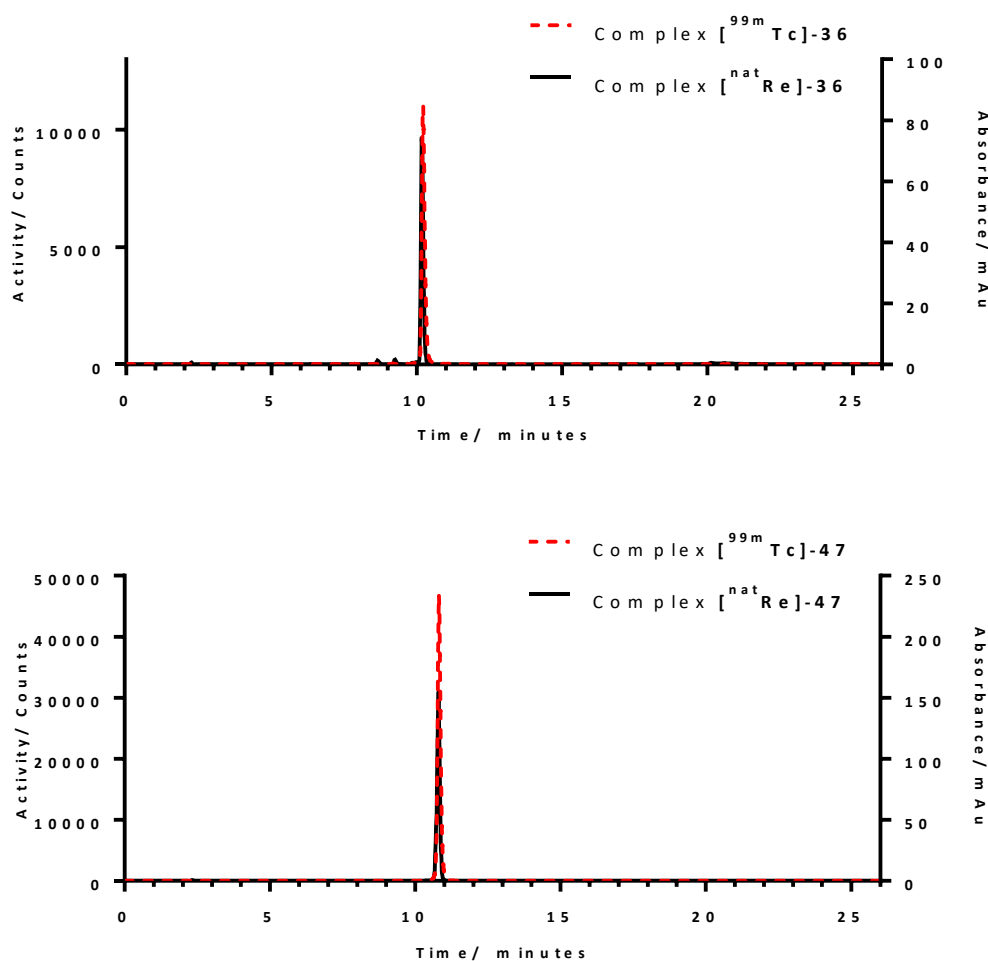


Figure 5.5 Overlays of radio-HPLC of $[^{99m}\text{Tc}]\text{-36}$ and $[^{99m}\text{Tc}]\text{-47}$ and UV-vis HPLC chromatograms $[\text{natRe}]\text{-36}$ and $[\text{natRe}]\text{-47}$. Reaction conditions: $[\text{L}] = 150\ \mu\text{M}$, $t = 30\ \text{mins}$, $T = 99\ ^\circ\text{C}$, $\text{pH } 7.4$.

Nevertheless, the relatively poor RCY prompted a change in reaction conditions. Radiolabelling reaction conditions was carried out at pH 7.4, while keeping other variables constant. At pH 7.4, $>95\%$ RCY was achieved for both conjugates, **35** and **46**, at $150\ \mu\text{M}$ with an EC_{50} of $6.8\ \mu\text{M}$ and $6.2\ \mu\text{M}$, respectively (Figure 5.7). Radiolabelling efficiency is fairly similar for both conjugates at pH 7.4 with very similar EC_{50} . It was deduced that at pH 7.4, protonation of carboxylate groups may have occurred and the interference of non-coordinating carboxylate groups from the targeting molecule was seen to diminish, hence, both conjugates **35** and **46**

radiolabelled ^{99m}Tc with similar efficiency. Radio-TLC were also carried out, with citrate buffer as the mobile phase according to the literature.³⁰⁰ With this mobile phase, definitive separation between $[\text{}^{99m}\text{Tc}(\text{CO})_3]^+$ – elutes to solvent front ($R_f = 1$) and radiolabelled conjugates $[\text{}^{99m}\text{Tc}]\text{-36}$ and $[\text{}^{99m}\text{Tc}]\text{-47}$ – stays at baseline ($R_f = 0$) were achieved (Figure 5.8). The large separation allows the TLC plates to be cut in half and both baseline and solvent front analysed using a gamma counter, with the radio-TLC data in agreement with data obtained from radio-HPLC. With this optimise radiolabelling conditions, specific activities of $76 \text{ GBq } \mu\text{mol}^{-1}$ and $96 \text{ GBq } \mu\text{mol}^{-1}$ were achieved for conjugates **35** and **46**, respectively.

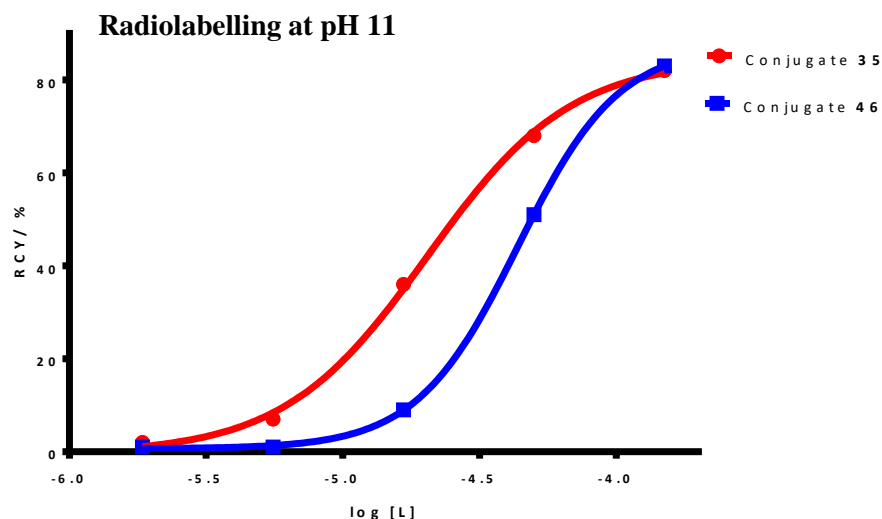


Figure 5.6 RCY for the $[\text{}^{99m}\text{Tc}(\text{CO})_3]^+$ radiolabelling of conjugate **35** and conjugate **46** with varying concentration. Reaction conditions: $t = 30 \text{ mins}$, $T = 99 \text{ }^\circ\text{C}$, $\text{pH } 11$.

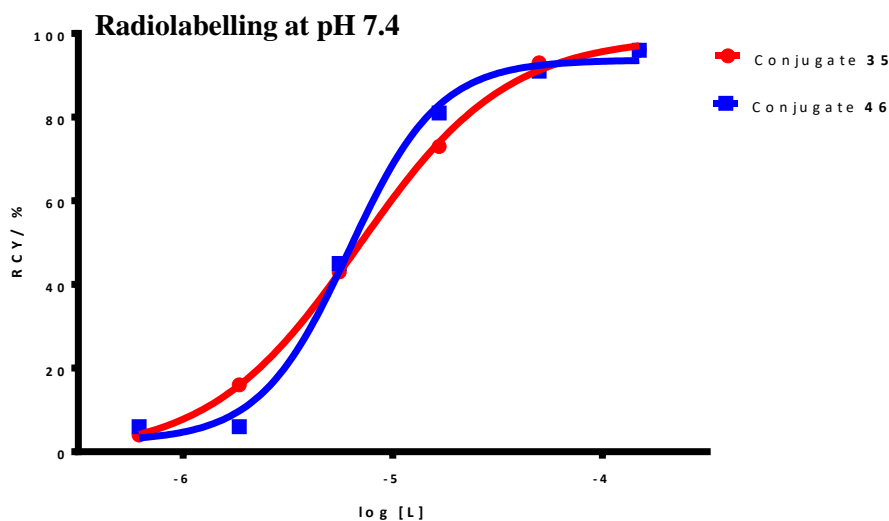


Figure 5.7 RCY for the $[\text{}^{99m}\text{Tc}(\text{CO})_3]^+$ radiolabelling of conjugate **35** and conjugate **46** with varying concentration. Reaction conditions: $t = 30 \text{ mins}$, $T = 99 \text{ }^\circ\text{C}$, $\text{pH } 7.4$.

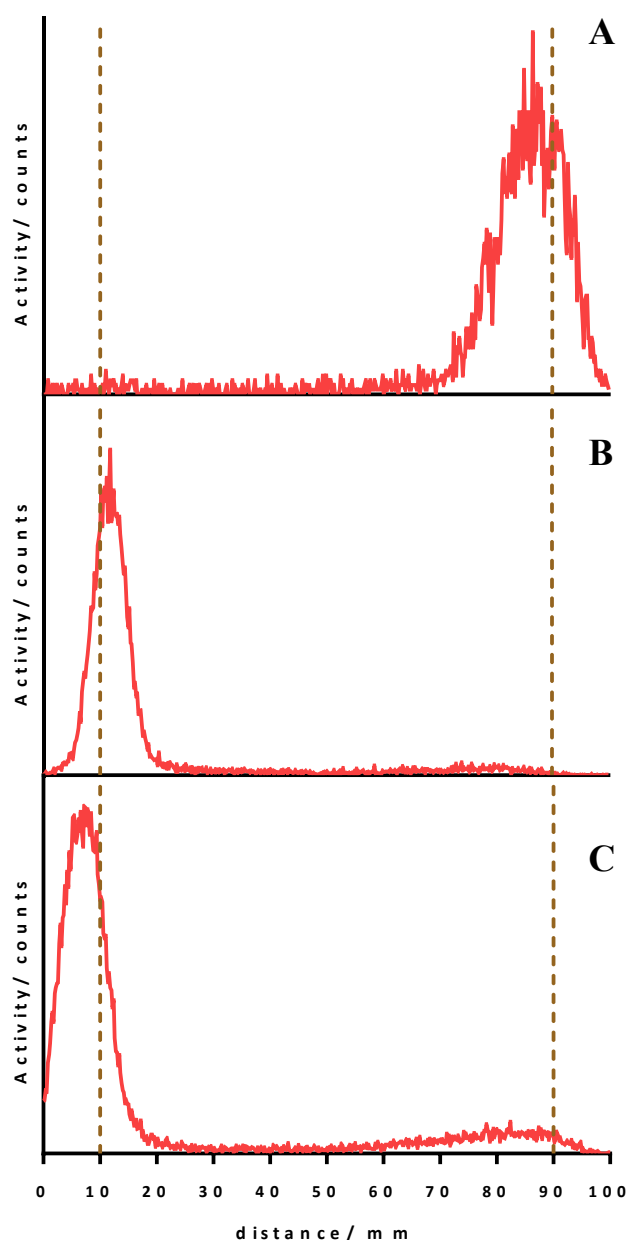


Figure 5.8 Radio-TLC of radiolabelling mixture of $[^{99m}\text{Tc}(\text{CO})_3]^+$ (A), $[^{99m}\text{Tc}]\text{-36}$ (B), and $[^{99m}\text{Tc}]\text{-47}$ (C). Dotted lines indicate baseline (left, $R_f = 0$) and solvent front (right, $R_f = 1$). Radio-TLC were carried out on aluminium-backed silica TLC plates with 0.1 M 1:1 citric acid:trisodium citrate as the mobile phase. Reaction conditions: (A) $t = 30$ mins, $T = 99$ °C. (B,C) $[\text{L}] = 150$ μM , $t = 30$ mins, $T = 99$ °C, pH 7.4.

The stability of the radiolabelled conjugates, $[^{99m}\text{Tc}]\text{-36}$ and $[^{99m}\text{Tc}]\text{-47}$, were tested against 50% foetal bovine serum (FBS). The radiolabelled conjugates were purified using semi-preparative HPLC, formulated in 1:1 ethanol:phosphate buffered saline (PBS), and subsequently incubated with 50% FBS at 37 °C for up to 6 hours. Analysis of stability of $[^{99m}\text{Tc}]\text{-36}$ and $[^{99m}\text{Tc}]\text{-47}$ was carried out *via* precipitation of serum proteins with methanol prior to analytical radio-HPLC.

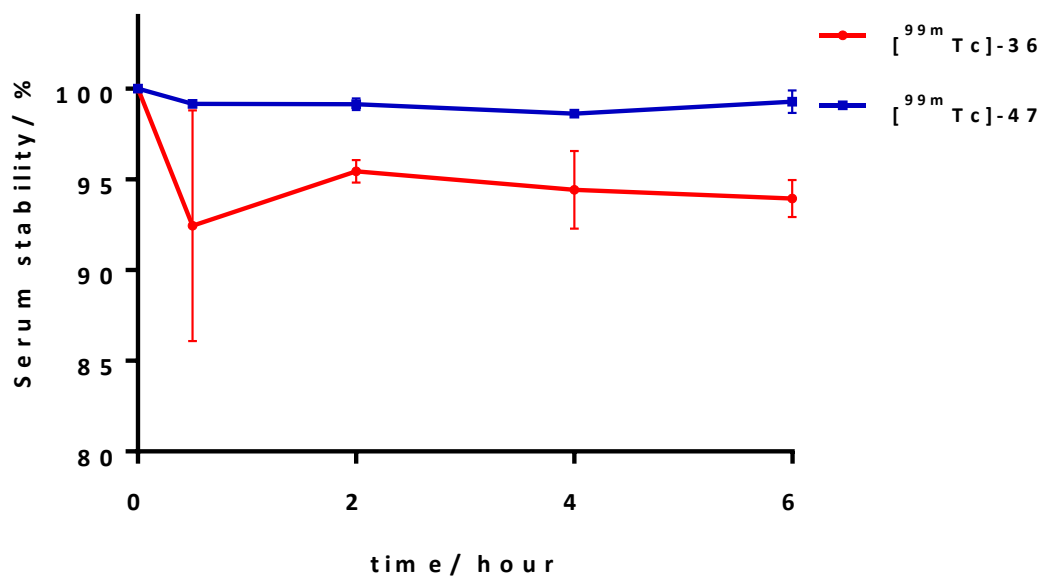


Figure 5.9 Serum stability of radiolabelled conjugates, [^{99m}Tc]-36 and [^{99m}Tc]-47.

Figure 5.9 shows the stability of [^{99m}Tc]-36 and [^{99m}Tc]-47 in 50% FBS. [^{99m}Tc]-36 shows slight and gradual dissociation of ^{99m}Tc with 94% ^{99m}Tc still associated after 6 hours. [^{99m}Tc]-47 shows remarkable stability against 50% FBS with >99% ^{99m}Tc still associated after incubation for 6 hours. The high serum stability of these ^{99m}Tc conjugates was expected as literature has shown the stability of histidine and histidine-like complex against serum.^{286,301,302}

5.3 *In vitro* phototoxicity evaluation

Initially, phototoxicity of conjugate **35** and complex [^{nat}Re]-36 was evaluated on human colon adenocarcinoma (HT-29) cells. Cells were incubated with **35** and complex [^{nat}Re]-36 at varying concentrations (1-18 μM) for 1 hour, using a protocol similar to that for previous *in vitro* phototoxicity studies in earlier chapters. The results were compared with a non-irradiated control. Under these conditions, both conjugate **35** and complex [^{nat}Re]-36 were capable of inducing >50% cell death at 4.5 μM as shown in Figure 5.10 and with minimal dark toxicity observed in the non-irradiated controls. This *in vitro* study also showed that [^{nat}Re]-36 is slightly more “dark” toxic and phototoxic than conjugate **35** at higher concentrations. [^{nat}Re]-36 is capable of inducing >90% cell death at a concentration of 13 μM, while conjugate **35** failed to achieve this at the same concentration.

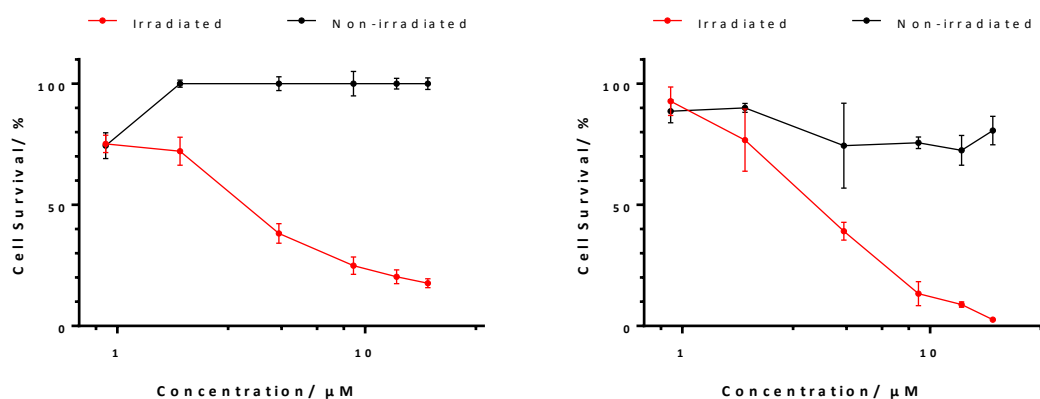


Figure 5.10 Percentage cell survival of HT-29, irradiated cell and non-irradiated cells (control), determined using MTT assay. Cells were incubated with varying concentration of conjugate **35** (left) and [^{nat}Re]-**36** (right) for 1 hour and irradiated cells received 20 J cm⁻¹ white light.

These results show conjugate **35** and the subsequent complex [^{nat}Re]-**36** are viable PDT agents with minimal dark toxicity. These promising results prompted the *in vitro* studies of the trifunctional conjugate **46** and complex [^{nat}Re]-**47**. As conjugate **46** and complex [^{nat}Re]-**47** both have a targeting molecule which binds to PSMA, two different human prostate cell lines were used to evaluate the toxicity and phototoxicity of conjugate **46** and complex [^{nat}Re]-**47**, namely DU145, which does not express PSMA, and DU145-PSMA, a PSMA-expressing variant.³⁰³ DU145 and DU145-PSMA cells were incubated with varying concentrations (1.5 – 24 μM) of conjugate **46** and complex [^{nat}Re]-**47** for 30 mins, prior to irradiation with visible light. Similarly, the results obtained were compared with a non-irradiated control.

Figure 5.11 shows the results of cytotoxicity and photocytotoxicity of conjugate **46** and complex [^{nat}Re]-**47** on DU145 and DU145-PSMA. Without irradiation, both conjugate **46** and complex [^{nat}Re]-**47** show minimal toxicity at these concentration with more than 86% cell survival in both DU145 and DU145-PSMA.

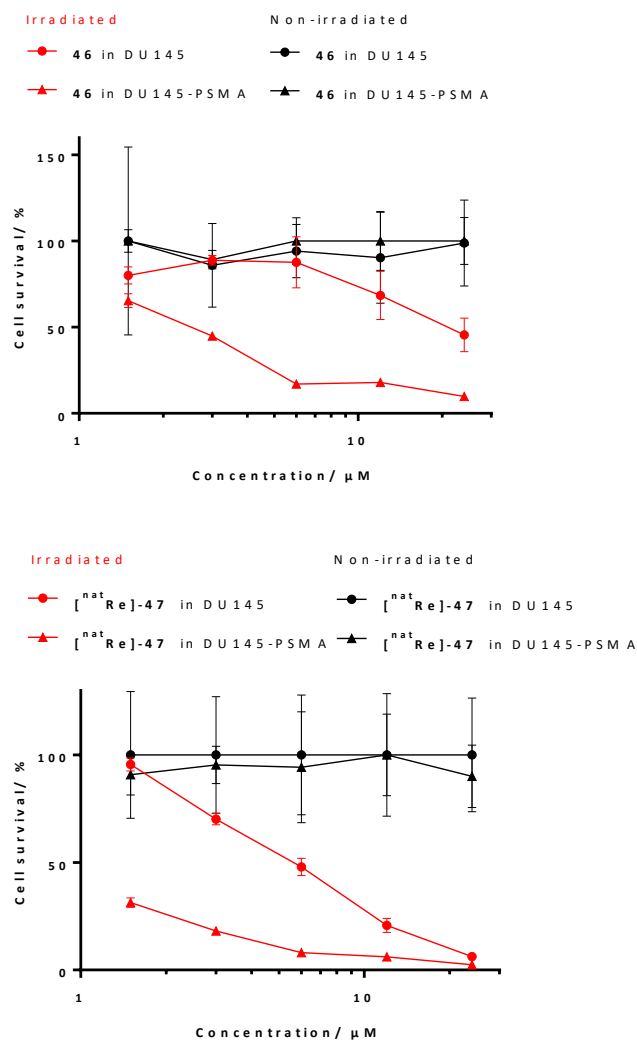


Figure 5.11 Percentage cell survival of DU145 (circle) and DU145-PSMA (triangle) cells, irradiated (red) and non-irradiated (black) cells. Cells were incubated with varying concentration of conjugate **46** (top) and $[\text{natRe}]\text{-47}$ (bottom) for 30 mins and irradiated cells received 20 J cm^{-1} white light.

Under irradiation with visible light (20 J cm^{-2} ; 400 – 700 nm), conjugate **46** and complex $[\text{natRe}]\text{-47}$ were capable of inducing death in both DU145 and DU145-PSMA cells, with more potent phototoxicity towards DU145-PSMA. At a conjugate **46** concentration of $6 \mu\text{M}$, 85% cell survival was observed in DU145 cells with light irradiation, while only 17% cell survival was observed in DU145-PSMA cells under similar conditions. Complex $[\text{natRe}]\text{-47}$ showed minimal phototoxicity towards DU145 cells at a concentration of $1.5 \mu\text{M}$ with $>90\%$ cell survival, but was capable of inducing near 70% cell death towards DU145-PSMA under similar conditions. These results show, conjugate **46** and complex $[\text{natRe}]\text{-47}$ are capable of inducing greater cell death in DU145-PSMA cells compared to DU145 cells under similar conditions. This is due to the overexpression of PSMA on DU145-PSMA, resulting in the higher binding and uptake of conjugate **46** and complex $[\text{natRe}]\text{-47}$ into DU145-PSMA.

Nevertheless, phototoxicity of conjugate **46** and complex [^{nat}Re]-**47** towards native DU145 increases with concentration (Figure 5.11). This could be due to native expression of PSMA on DU145 and non-specific uptake/binding of conjugate **46** and complex [^{nat}Re]-**47**.

It can also be noted that complex [^{nat}Re]-**47** is more phototoxic than conjugate **46** in these cell lines. Figure 5.11 shows that complex [^{nat}Re]-**47** induced more cell death than conjugate **46** upon visible light irradiation towards DU145-PSMA at all concentration tested. This suggest that the complexation of [Re(CO)₃]⁺, causes a slight change in the molecule and in the overall charge of complex [^{nat}Re]-**47**, and may have a minor effect on the binding/uptake of complex [^{nat}Re]-**47**. This effect has been observed in literature, whereby, two porphyrin conjugates upon complexation of [Re(CO)₃]⁺ resulted in the increase/decrease of phototoxicity of porphyrin complex.¹⁷⁰

5.4 Summary

In summary, two porphyrin-amino acid conjugates, porphyrin-Gly **35** and porphyrin-Lys-TM conjugate **46** were successfully synthesised and characterised. Complexation of these conjugates with chemically and physically similar [^{nat}Re(CO)₃]⁺ was carried out to prepare a non-radioactive controls, [^{nat}Re]-**36** and [^{nat}Re]-**47**, which were used as HPLC standards and for *in vitro* evaluation. ^{99m}Tc radiolabelling showed both **35** and **46** are both capable of [^{99m}Tc(CO)₃]⁺ complexation to produce [^{99m}Tc]-**36** and [^{99m}Tc]-**47**, with an EC₅₀ of 6.8 μM and 6.2 μM, respectively. [^{99m}Tc]-**36** and [^{99m}Tc]-**47** also showed good stability against serum, with 94% and >99% ^{99m}Tc associated after 6 hours, respectively. Phototoxicity and toxicity of **35** and [^{nat}Re]-**36** were evaluated on human colorectal adenocarcinoma (HT-29) cells with and without visible light irradiation respectively. >50% cell death was induced by both **35** and [^{nat}Re]-**36** upon light irradiation at a concentration of 4.5 μM. Minimum dark toxicity was observed with >70% cell survival at all concentrations tested for **35** and [^{nat}Re]-**36**. To investigate the specificity towards PSMA, phototoxicity, and toxicity of **46** and [^{nat}Re]-**47**, *in vitro* cytotoxicity was tested on two prostate carcinoma cell lines, DU145 and DU145-PSMA. Similarly, both **46** and [^{nat}Re]-**47**, showed minimal toxicity in the dark, with >84% cell survival in all concentrations tested in both cell lines. When irradiated with visible light, both **46** and [^{nat}Re]-**47** are able to induce cell death in both cell lines. Specificity of **46** and [^{nat}Re]-**47** towards PSMA was confirmed as more cell death was induced in DU145-PSMA when compared to the DU145 under similar conditions. This is most likely due to higher binding and higher uptake of **46** and [^{nat}Re]-**47** towards the DU145-PSMA which overexpress PSMA, compared to the native expressing DU145.

Chapter 6 Conclusion and Future Outlook

Research into photosensitisers for photodynamic therapy (PDT) has seen the development of fourth-generation multimodal photosensitisers. The development of fourth-generation photosensitiser involves the combination of an additional modality onto photosensitisers to complement its PDT capability for, but not limited to, cancer treatment. This additional modality can be a diagnostic modality for the combined diagnosis and treatment of disease. This will allow the careful monitoring and accumulation of the fourth-generation photosensitisers in the patient, allowing optimisation of treatment, paving a way towards personalised medicines. In this thesis, porphyrin-based photosensitisers were investigated to develop fourth-generation nano- and molecular-theranostic agents. These strategies include the utilisation of a cowpea mosaic virus (CPMV) as a multifunctional virus nanoscaffold and synthetic polyacrylamide nanoparticles (PAN) for the conjugation of porphyrin and diagnostic agents. For the development of molecular-theranostic, conjugation of porphyrin with metal chelates to allow complexation of diagnostic metals or radio-metals were carried out. The synthesis, chemical and physical characterisation, *in vitro* photodynamic activities, *in vitro* diagnostic efficacy, and *in vivo* studies are discussed and evaluated. Successful evaluation and some promising results obtained show the potential of these nano- and molecular-theranostic agents for the combined use of cancer PDT and cancer diagnostic. It is hoped that these promising results discussed and showed in this thesis can provide further insight and pave a way towards development of fourth-generation nano- and molecular-theranostic porphyrin.

Chapter 7 Experimental Section

7.1 Materials and methods

NMR spectra were recorded on a JEOL ECZ 400S spectrometer at 400 MHz for ^1H NMR and 100.6 MHz for ^{13}C NMR, with residual protic solvent as the internal reference. Chemical shifts are given in ppm (δ) and coupling constants (J) are given in Hertz (Hz). Mass spectrometry data were obtained from the EPSRC National Mass Spectrometry Facility at Swansea University. UV-vis spectroscopy was carried out on a Varian Cary 50 Bio UV-vis spectrophotometer or NanoDrop 1000 Spectrophotometer. All commercially available starting material used in synthesis were obtained from Sigma Aldrich, Fluorochem, and Alfa Aesar and were used without further purification. Deionised water was obtained from a Millipore Milli-Q reagent water system. All solvents were obtained from Fisher Scientific, Honeywell, and VWR. Solvents were dried according to the procedure by William *et al.*³⁰⁴ Bioconjugation of wtCPMV particles were all carried out in 0.1 M sodium phosphate buffer pH 7.0. Sodium phosphate buffer was made using the following protocol: 1 L of 0.2 M sodium phosphate dibasic, Na_2HPO_4 (27.0 g) and 1 L of 0.2 M sodium phosphate monobasic, NaH_2PO_4 (28.39 g) were prepared in Milli-Q water and autoclaved before mixing. To prepare 0.1 M buffer solution; 305 ml of Na_2HPO_4 solution and 195 ml of NaH_2PO_4 solution was added to 500 ml Milli-Q water that gave a pH of 7.0.

7.2 HPLC conditions

HPLC analysis were performed on Agilent HPLC system. The separations were performed on a Gemini® 5 μm C18 110 Å, LC column 150×4.6 mm (Phenomenex) at a flow rate of 1 mL min⁻¹, with a mobile phase consisting of 0.1% TFA in water (solvent A) and 0.1% TFA in acetonitrile (solvent B). Gradient 1 [time/min](solvent A:solvent B): [0-2](95:5). [2-17](95:5-5:95). [17-19](5:95). [19-21](5:95-95:5). [21-23](95:5). Gradient 2 [time/min](solvent A:solvent B): [0-5](95:5). [5-6](95:5-85:15).[6-51](85:15-80:20). [51-61](80:20). [61-62](80:20-5:95). [62-67](5:95). [67-68](5:95-95:5). [68-75](95:5). Gradient 3 [time/min](solvent A:solvent B): [0-2](95:5). [2-17](95:5-60:40). [17-18](60:40-5:95). [18-23](5:95). [23-24](5:95-95:5). [24-26](95:5). Gradient 4 [time/min](solvent A:solvent B): [0-2](85:15). [2-17](85:15-40:60). [17-18](40:60-5:95). [18-23](5:95). [23-24](5:95-85:15). [24-26](85:15).

Semi-preparative HPLC was carried out on Luna® 5 μm C18(2) 100 Å LC column 250×10 mm (Phenomenex) and Pursuit 200Å C18 10×250 mm 10 μm HPLC column (Agilent) at a flow rate of 5 mL min⁻¹, with a mobile phase consisting of 0.1% TFA in water (solvent A) and 0.1% TFA in acetonitrile (solvent B). Semi-preparative gradient time/min](solvent A:solvent B): [0-2](95:5). [2-22](95:5-50:50). [22-23](50:50-5:95). [23-28](5:95). [28-29](5:95-95:5). [29-33](95:5).

7.3 ⁶⁸Ga radiochemistry

The IGG100 generator was eluted with 0.6 M aq. HCl (4 mL). This eluate (300–200 MBq) was diluted with H₂O (20 mL) and passed through a Strata-X-C 33 μM Cation Mixed-mode polymeric support. The activity was liberated from the column using 98:2 acetone:0.1 M aq. HCl (1 mL). Aliquots (~30 MBq) of this solution were dried at 90 °C and allowed to cool before use.

1 mL of porphyrin-H₃Dpaa conjugate **33** (0.1 mM) in buffered solution was added to the cool and dried ⁶⁸Ga and shaken. 5 μL aliquots were taken for analysis by TLC and 20 μL aliquots for analysis by HPLC. TLC analysis was performed on Kieselgel 60 F254 plates (Merck) with an eluate of 0.1 M aqueous 1:1 trisodium citrate: citric acid. Radiochemical yield (RCY) was determined using radio-HPLC via integration on the intensity of the peak with reference to free gallium which eluted at solvent front.

7.4 ^{99m}Tc radiochemistry

7.4.1 Synthesis of [^{99m}Tc(CO)₃(H₂O)₃]⁺

[^{99m}Tc(CO)₃(H₂O)₃]⁺ was prepared as described previously.¹ Briefly, sodium tetraborate decahydrate (2.9 mg, 7.6 μmol), sodium carbonate (7.8 mg, 73.6 μmol), potassium sodium tartrate tetrahydrate (9.0 mg, 31.9 μmol) and disodium boranocarbonate (4.5 mg, 43.3 μmol) was purged with argon for 10 minutes, after which Na[^{99m}Tc]TcO₄ in saline (1 mL, 407-658 MBq) was added and heated at 99 °C for 20 minutes. [^{99m}Tc(CO)₃]⁺ was analysed using radio-HPLC and radio-TLC. Radio-TLC was carried out on Kieselgel 60 F₂₅₄ plates (1×10 cm, Merck) with mobile phase of 1% HCl in methanol (R_f = 0.2-0.8). For reactions at pH 7.4, [^{99m}Tc(CO)₃]⁺ was neutralised with 1 M HCl (160 μL) and was buffered with PBS 1× (pH 7.4, 100 μL). pH was measured using universal indicator paper.

7.4.2 ^{99m}Tc radiolabelling

Porphyrin-conjugate (100 μL, 3×10⁻⁶-3×10⁻⁴ M) in saline (pH 11) or PBS (pH 7.4) was degassed for 10 minutes using argon. Previously reduced [^{99m}Tc(CO)₃(H₂O)₃]⁺ (25-95 MBq, 100 μL) was added to the degassed ligand solution and heated at 90 °C for 30 minutes. After cooling (10 mins), radio-HPLC and radio-TLC analysis were carried out to determine radiochemical yield. Radio-TLC was carried out on Kieselgel 60 F₂₅₄ plates (1×10 cm, Merck) with mobile phase of 0.1 M aqueous 1:1 trisodium citrate: citric acid. This mobile phase give definitive separation between labelled-complex (R_f = 0) and unreduced [^{99m}TcO₄]⁻ and unreacted [^{99m}Tc(CO)₃]⁺ (both with R_f = 1). The TLC plates to be cut in half and both baseline and solvent front analysed using a PerkinElmer Wallac Wizard 3'' 1480 Automatic Gamma counter.

7.5 *In vitro* cytotoxicity evaluation (MTT assay)

7.5.1 General procedure for phototoxicity and toxicity assay

A stock solution of drug/compound was made in 1-2 mL McCoy's 5A medium (Lonza™). The stock was sterilized by filtration through 0.22 μm PES syringe filter unit (Millex-GP). The concentration of the stock was recalculated by UV-vis spectroscopy. The stock was diluted further with medium to give the desired concentration range. 800 μl of cells, adjusted to a concentration of 1×10^6 cells ml⁻¹ in medium with L-glutamine, was added to 200 μL stock solution in a 12×75 mm polystyrene FACS tube (Falcon). The cells were allowed to incubate in the dark at 37 °C and 5% CO₂, after which they were centrifuged with 3 × excess of medium to remove unbound drugs/compounds. The pellet of cells was resuspended in 1 ml medium and 4×100 μl of each concentration was put in two 96 wells plates. One plate was irradiated with light (400-700 nm) to a dose of 20 J cm⁻² while the other served as a “no light” control. After irradiation, 5 μl of foetal bovine serum (FBS) was added to each well and the plates are returned to the incubator overnight. After 24 hours, the cell viability was determined using 3-[4,5-dimethylthiazol-2-yl]-2, 5 diphenyltetrazolium bromide (MTT) colorimetric assay. 10 μL of 12 mM MTT solution was added to each well and incubated between 1 and 4 hours at 37 °C to allow MTT metabolism. The crystals formed were dissolved by adding 150 μL of acid-alcohol mixture (0.04 M HCl in absolute 2-propanol). The absorbance at 570 nm was measured on a Biotek ELX800 Universal Microplate Reader. The results were expressed with respect to control values.

7.5.2 Phototoxicity and toxicity evaluation of PAN described in Chapter 3

(Porphyrin_{1.0}-[Gd(DTPA)]_{1.0})-PAN (40 mg) was dispersed in 2 mL McCoy's 5A medium (Lonza™) through sonication. The concentration of nanoparticles was determined using the extinction coefficient of porphyrin **28** (ϵ (434nm) = 200767 M cm⁻¹) and were further diluted with culture medium to appropriate concentration. Phototoxicity and toxicity was evaluated on human colorectal adenocarcinoma (HT-29) cells, by incubation of varying concentration of nanoparticles for 1 hour. The remaining steps are the same as described in sub-chapter 6.5.1.

7.5.3 Phototoxicity and toxicity evaluation of porphyrin conjugate described in Chapter 4

Porphyrin-H₃Dpaa conjugate **33** and porphyrin-[^{nat}Ga(H₃Dpaa)] complex [^{nat}Ga]-**34** were dissolved in 2 mL McCoy's 5A medium (Lonza™) separately. Phototoxicity and toxicity was evaluated on human colorectal adenocarcinoma (HT-29) cells, by incubation of varying concentration of nanoparticles for 1 hour. The remaining steps are the same as described in sub-chapter 6.5.1.

7.5.4 Phototoxicity and toxicity evaluation of porphyrin conjugate described in Chapter 5

Porphyrin-Gly conjugate **35**, porphyrin-[^{nat}Re(Gly)] complex [^{nat}Re]-**36**, porphyrin-Lys-TM complex **46**, and porphyrin-[Re(Lys)]-TM complex [^{nat}Re]-**47** were dissolved in 1-2 mL McCoy's 5A medium (Lonza™) separately. Phototoxicity and toxicity of **35** and [^{nat}Re]-**36** was evaluated on human colorectal adenocarcinoma (HT-29) cells, by incubation of varying concentration of nanoparticles for 1 hour. Phototoxicity and toxicity of **46** and [^{nat}Re]-**47** was evaluated on native and transfected prostate carcinoma cells, DU145 and DU145-PSMA, by incubation of varying concentration for 30 mins. The remaining steps are the same as described in sub-chapter 6.5.1.

7.6 CPMV purification and characterisation

7.6.1 Ultrafiltration

Ultrafiltration was used as a method for purification and concentration of virus particles. Samples were applied to centrifugal filter units of various volumes (500 µL to 15 mL) with 100 kDa molecular weight (Amicon Millipore and Sartorius Stedim) and centrifuged at 14,000 rpm for 5-15 min depending on the volume. The particles were retained on the filter of these tubes while the buffer and small impurities passed through.

7.6.2 Dialysis

This method was used for CPMV purification and for buffer solution exchange. Slide-A-Lyzer mini dialysis device, 10 kDa molecular weight cutoff (MWCO) (Thermo Fisher Scientific) were used for dialysis in 0.1 M sodium phosphate buffer pH7. The membrane allows small molecules, to pass through the semi-permeable membrane into the buffer reservoir.

7.6.3 Agarose gel electrophoresis

Tris-borate EDTA-Buffer (TBE) buffer (50 ml) is added to a glass bottle, agarose powder (0.6 g) was added into the liquid to give a 1.2 % (w/v) solution of agarose. The solution was heated until all the agarose has dissolved. The mixture was cooled to 50 – 55 °C before casting into plates. For nucleic acid staining, ethidium bromide (10 µl, 0.1 mg/ml) in milliQ water was added to the gel before setting.

30-50 µg/mL of CPMV particles in 0.1 M sodium phosphate buffer pH 7.0 (17 µL) with 3 µL of 6× DNA loading dye were loaded onto the gel prepared. An electric current of constant 60 V was applied to the gel for 1 – 2 hours. The gel was then visualised on ChemiDoc XRS+. For visualisation of protein bands, unstained agarose gel was stained with Coomassie solution after electrophoresis overnight prior to imaging.

7.6.4 UV-vis analysis of CPMV

CPMV concentration was determined using UV-vis spectroscopy on a NanoDrop 1000 Spectrophotometer at room temperature. CPMV has an absorption maximum at a wavelength, λ of 260 nm with an extinction coefficient, ϵ of $8.1 \text{ mL mg}^{-1} \text{ cm}^{-1}$ (derived from the encapsidated RNA).

The particle concentration was calculated using the Beer-Lambert's law:

$$A = \epsilon cl \quad \text{Eq. 7. 1}$$

Where A is the absorbance, ϵ is the absorption extinction coefficient in $\text{mL mg}^{-1} \text{ cm}^{-1}$, c is the concentration in mg mL^{-1} , and l is the path length of light in cm.

7.6.5 TEM sample preparation and imaging

A sample of CPMV (0.01 mg mL^{-1} , $3 \mu\text{L}$) was pipetted onto carbon-coated copper TEM grid and left for 30 s. Excess sample was wicked off using filter paper. 2% uranyl acetate ($3 \mu\text{L}$) was pipetted onto the grid and left for 30s, excess uranyl acetate was wicked off using filter paper. The grids were allowed to air dry for 1 min and were kept in desiccator overnight prior to imaging. Images were obtained using a FEI Tecnai 20 TEM, FEI UK Ltd, Cambridge.

7.7 PAN characterisation and evaluation

7.7.1 Dynamic light scattering and zeta potential measurements

A Malvern Zetasizer Nano ZS equipped with He-Ne, 4.0 mW laser operating at 633 nm wavelength at an angle of 173° backscatter detection was used for DLS and zeta potential measurements. Measurements were performed at 25°C at a concentration of 5.0 mg mL^{-1} and 2.5 mg mL^{-1} of nanoparticles for DLS and zeta potential measurements, respectively. Data reported with errors represent an average of triplicate measurements on three separate sets of nanoparticle batches and the error calculated is sample standard deviation.

7.7.2 TEM sample preparation and imaging

A stock solution of the nanoparticles of 1 mg mL^{-1} was placed in an ultrasonic bath for 15 minutes, filtered through a $0.22 \mu\text{m}$ filter, and sonicated for a further 15 minutes. A drop of the sample was placed on Parafilm and a carbon-coated copper TEM grid floated face-down on the droplet for 2 minutes. Excess sample was wicked off using filter paper. This process was repeated on ultrapure water for a few seconds, and on 1% aqueous uranyl acetate for 1 minute. The grids were allowed to air dry prior to imaging. Images were obtained using a Gatan Ultrascan 4000 digital camera attached to a JEOL 2010 Transmission Electron Microscope running at 200 kV.

7.7.3 Phantom MRI

(Porphyrin_{1.0}-[Gd(DTPA)]_{1.0})-PAN and diethylenetriaminepentaacetic acid gadolinium (III) dihydrogen salt hydrate was dispersed/dissolved in deionized water at concentration (calculated based on Gd) 0.0625, 0.125, 0.25, 0.50, 1.0, and 2.0 mM. 900 μ L of each concentration were loaded into Eppendorf tubes. Samples and water controls were scanned using a Discovery MR750 3.0 T MRI scanner (GE Medical Systems, Milwaukee, WI, USA) and eight-channel phased-array head coil. A clinical T₁-weighted 3D fast-spoiled gradient echo sequence was modified to image the samples, Repetition Time / Echo Time = 7.3 / 2.8 ms, Field of View = 160 x 160 mm², Matrix = 192 x 192, Slice Thickness = 1 mm, Flip Angle = 12°.

7.7.4 T1 measurements and Evans magnetic susceptibility measurement

Relaxivity at 9.4 T (400 MHz) was measured on a Jeol ECZ 400S spectrometer and at 1.4 T (59.7 MHz) was measured on Pulsar™ NMR spectrometer. For measurements at 9.4 T, 100 μ L of 50 mg mL⁻¹ (approximately 2 mM gadolinium concentration) nanoparticles were loaded in a capillary tube surrounded by deuterated water in a standard NMR tube. D₂O acted as the reference and the difference in chemical shift between relaxed water and deuterated water allowed the measurement of gadolinium concentration using the Evans magnetic susceptibility method. The T₁ relaxation time of the nanoparticles was obtained by applying a non-linear inversion single phase decay fit onto the water peak. NMR measurement at 1.4 T was measured without the D₂O reference, with the same non-linear fit applied to calculate T₁ relaxation time. NMRD profiles from 0.01 MHz to 10 MHz were obtained at 25 °C on a benchtop fast field cycling relaxometer fitted with a VTC90 temperature control unit (SMARtracer™, Stelar) at 2 mM of Gd(III). The following parameters were used during acquisition: observe offset: 6000-9000 Hz, RF attenuation: 39 dB, recycle delay: 0.5 s, delay tau: 0.1 s, switching time: 0.003 s, polarisation field: 7 MHz and acquisition field: 7.2 MHz.

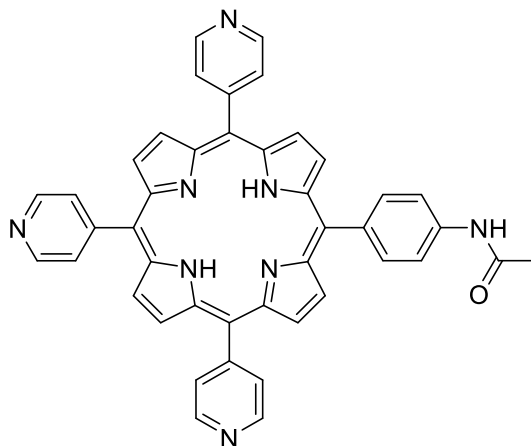
7.7.5 Luminescence measurements and hydration states calculation

Luminescence measurements of Eu and Tb were made with Horiba Fluoromax-4P spectrofluorometer in 10 mm quartz cuvette. All spectra were obtained in either H₂O or D₂O. Phosphorescence measurement obtained using following parameters: Flash delay: 0.05 s, sample window: 0.2 nm, time per flash: 41, flash count: 50, λ_{ex} : 395 nm for (**[Eu(DTPA)]_{1.0})-PAN-(alkyne_{1.0})**), and λ_{ex} : 380 nm for (**[Tb(DTPA)]_{1.0})-PAN-(alkyne_{1.0})**). Excited state lifetime measurements obtained using following parameters: sample window: 10 nm, time per flash: 41, flash count: 50, λ_{ex} : 395 nm, λ_{em} : 615 nm for (**[Eu(DTPA)]_{1.0})-PAN-(alkyne_{1.0})**), and λ_{ex} : 380 nm, λ_{em} : 545 nm for (**[Tb(DTPA)]_{1.0})-PAN-(alkyne_{1.0})**).

One phase exponential decay was fitted onto the excited state lifetime measurement and the rate constant, k_{H_2O/D_2O} , for the phosphorescence decay in H₂O and D₂O measured using GraphPad Prism. Hydration state, q , was derived from Eq. 3. 1 and Eq. 3. 2.

7.8 Synthesis and bioconjugation described in chapter 2

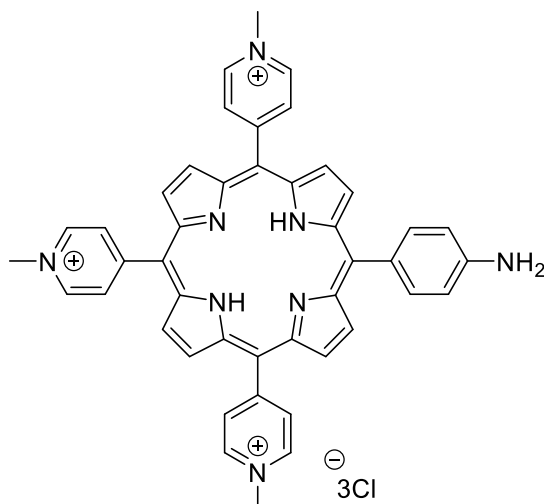
5-[4-acetamidophenyl]-10,15,20-tri-(4-pyridyl)porphyrin **1**¹⁹⁷



To a stirred solution of 4-acetamidobenzaldehyde (2.95 g, 18 mmol) and 4-pyridinecarboxaldehyde (5.08 mL, 54 mmol) in propionic acid (500 mL) were added pyrrole (5 mL, 72 mmol) dropwise. The reaction mixture was refluxed at 170 °C for 1 hour. Propionic acid was removed under reduced pressure. The crude was purified using column chromatography (silica, 6-7% MeOH:DCM) and recrystallizes from methanol over DCM to yield a purple solid (764 mg, 1.13 mmol, 6.3%).

¹H NMR (400 MHz, CDCl₃) δ 2.39 (s, 3H, -CH₃), 7.95 (d, 2H, m-Ph), 8.16 (m, 8H, βH), 8.83 (m, 6H, o-Py), 8.94 (d, 2H, o-Ph), 9.05 (m, 6H, m-Py). ¹³C NMR (100 MHz, CDCl₃) δ 24.98 (CH₃-C=O), 117.15, 117.54, 118.22, 121.20, 129.45 (β-C), 135.23, 137.44, 138.14, 148.47 (β-C), 150.09, 168.75 (C=O). UV-vis [CH₂Cl₂, nm] 418, 513, 550, 590, 645. ε (418 nm) = 416925 M⁻¹ cm⁻¹. MS: (ESI) m/z 675 [M+H]⁺, HRMS: calcd. for C₄₃H₃₁N₈O₁ 675.2615 found 675.2605.

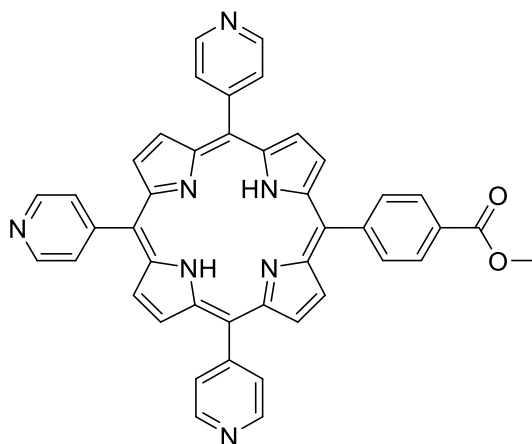
5-[4-aminophenyl]-10,15,20-tri-(*N*-methyl-4-pyridinium)porphyrin trichloride 3¹⁹⁸



5-[4-acetamidophenyl]-10,15,20-tri-(*N*-methyl-4-pyridinium)porphyrin trichloride (300 mg, 0.364 mmol) was dissolved in HCl (18%, 30 mL) and stirred at reflux for 3 hours. The solvent was removed under reduced pressure and the residue redissolved in water. Porphyrin was neutralised with 1 M NaOH and NH_4PF_6 was added. The resulting solution was filtered and the precipitate redissolved in acetone. Tetrabutylammonium chloride was added, and the resulting solution filtered. The product was precipitated from diethyl ether over methanol to yield the product (224 mg, 0.286 mmol, 79%).

^1H NMR (400 MHz, $\text{DMSO}-d_6$) δ 4.73 (s, 9H, N- CH_3), 5.78 (bs, 2H, NH_2), 7.06 (d, 2H, m-Ph), 7.89 (d, 2H, o-Ph), 9.06 (m, 14H, o-Py and βH), 9.51 (d, 6H, m-Py). ^{13}C NMR (100 MHz, $\text{DMSO}-d_6$) δ 48.31 (N- CH_3), 113.26, 114.39, 115.69, 123.21, 131.44, 132.63 (βC), 136.54, 144.72 (βC), 157.20. UV-vis (H_2O , nm): 424, 522, 547, 584, 642. ϵ (424 nm) = $137817 \text{ M}^{-1} \text{ cm}^{-1}$. MS: (ESI) m/z 225 $[\text{M}-3\text{Cl}]^{3+}$, HRMS: calcd. for $\text{C}_{44}\text{H}_{37}\text{N}_8$ 225.7708 found 225.7709.

5-[4-methoxycarbonylphenyl]-10,15,20-tri-(4-pyridyl)porphyrin 4²⁰²

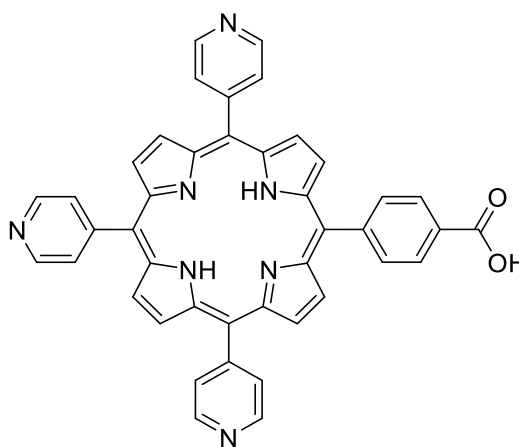


To a stirred solution of methyl 4-formylbenzoate (5.90 g, 36 mmol) and 4-pyridinecarboxaldehyde (10.16 mL, 108 mmol) in propionic acid (500 mL) were added pyrrole

(10 mL, 144 mmol) dropwise. The reaction mixture was refluxed at 170 °C for 1 hour. Propionic acid was removed under reduced pressure. The crude was purified by column chromatography (silica, 5% MeOH:DCM) and recrystallizes from methanol over DCM to yield a purple solid (2.029g, 3.0 mmol, 8.3%).

^1H NMR (400 MHz, CDCl_3): δ 4.12 (s, 3H, O- CH_3), 8.16 (d, 6H, o-Py), 8.29 (d, 2H, o-Ph), 8.46 (d, 2H, m-Ph), 8.86 (m, 8H, βH), 9.05 (m, 6H, m-Py). ^{13}C NMR (100 MHz, CDCl_3): δ 52.62 (O- CH_3), 117.52, 117.71, 120.22, 128.17, 129.44 ($\beta\text{-C}$), 130.08, 134.60, 146.30, 148.44 ($\beta\text{-C}$), 150.03, 167.24 (C=O). UV-vis (CH_2Cl_2 , nm) 416, 513, 547, 588, 644. ϵ (416 nm) = 485574 $\text{M}^{-1} \text{cm}^{-1}$. MS: (ESI) m/z 676 $[\text{M}+\text{H}]^+$, HRMS: calcd. for $\text{C}_{43}\text{H}_{30}\text{N}_7\text{O}_2$ 676.2455 found 676.2450.

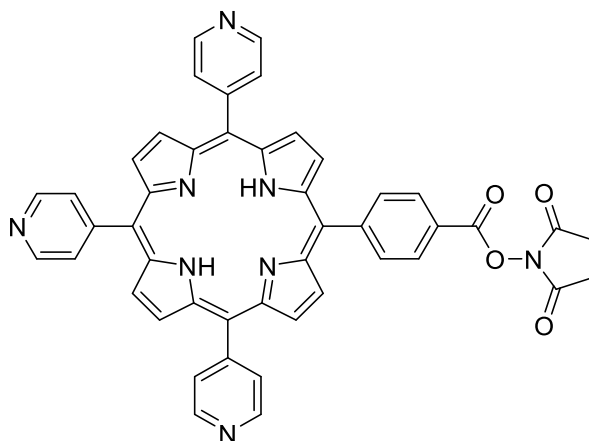
5-[4-carboxyphenyl]-10,15,20-tri-(4-pyridyl)porphyrin **5**²⁰²



To a stirred solution of 5-[4-methoxycarboxyphenyl]-10,15,20-tripyridylporphyrin (1 g, 1.48 mmol) in ethanol (100 ml) was added a solution of potassium hydroxide (4.0 g, 78 mmol) in water (10 ml) and the mixture stirred at 40 °C overnight. The solvent was removed under reduced pressure, and the residue neutralised with 1 M HCl. The mixture was filtered, and the crude precipitated from MeOH over DCM to yield the product as a purple solid (957 mg, 1.45 mmol, 97%).

^1H NMR (400 MHz, 9:1, CDCl_3 : CD_3OH): δ 8.11 (m, 6H, o-Py), 8.17 (d, 2H, o-Ph), 8.36 (d, 2H, m-Ph), 8.75 (bs, 8H, βH), 8.88 (m, 6H, m-Py). ^{13}C NMR (100 MHz, 9:1, CDCl_3 : CD_3OH): δ 117, 117.27, 120.52, 128.29, 129.68 ($\beta\text{-C}$), 130.47, 134.45, 145.98, 147.62 ($\beta\text{-C}$), 150.74, 168.83 (C=O). UV-vis (CH_3OH , nm) 413, 510, 546, 591, 641. ϵ (413 nm) = 82876 $\text{M}^{-1} \text{cm}^{-1}$. MS: (ESI) m/z 660 $[\text{M}-\text{H}]^-$, HRMS: calcd. for $\text{C}_{42}\text{H}_{26}\text{N}_7\text{O}_2$ 660.2153 found 660.2139.

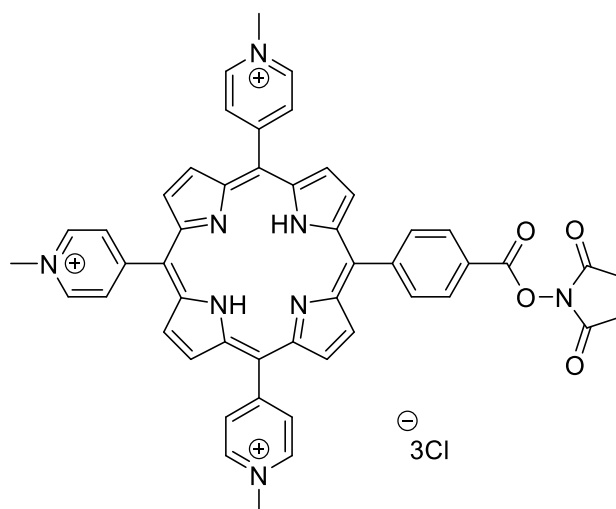
5-[4-(succinimide-*N*-oxycarbonyl)phenyl]-10,15,20-tri-(4-pyridyl)porphyrin **6**²⁰³



To a stirred solution of 5-[4-carboxyphenyl]-10,15,20-tri-(4-pyridyl)porphyrin (100 mg, 0.151 mmol), in dry pyridine (10 ml) was slowly added thionyl chloride (0.20 ml, 2.72 mmol). The reaction was then stirred at 50 °C, protected from light and moisture for 30 minutes. After this period, *N*-hydroxysuccinimide (400 mg, 3.48 mmol) was added and the mixture maintained under the previous conditions for 3 hours. The solvent was removed under reduced pressure and the crude dissolved in DCM. The organic layer was washed with saturated sodium hydrogen carbonate solution and water, dried (MgSO₄), and the solvent removed under reduced pressure. The crude was purified by flash column chromatography (silica, 7% MeOH:DCM). The crude was recrystallized from methanol over DCM to yield a brick red solid (76 mg, 0.10 mmol, 66%).

¹H NMR (400 MHz, CDCl₃): δ 3.01 (bs, 4H, N(COCH₂)₂), 8.16 (m, 6H, o-Py), 8.36 (d, 2H, o-Ph), 8.56 (d, 2H, m-Ph), 8.87 (m, 8H, βH), 9.06 (m, 6H, m-Py). ¹³C NMR (100 MHz, CDCl₃): δ 25.89 (-CH₂), 117.86, 119.27, 124.99, 129.20, 129.44 (β-C), 131.28, 134.90, 148.45 (β-C), 149.97, 162.06 (N-C=O), 169.45 (O-C=O). UV-vis (CH₂Cl₂, nm): 417, 513, 547, 590, 643. ε (417 nm) = 446621 M⁻¹ cm⁻¹. MS: (ESI) m/z 759 [M+H]⁺, HRMS: calcd. for C₄₆H₃₁N₈O₄ 759.2463 found 759.2460.

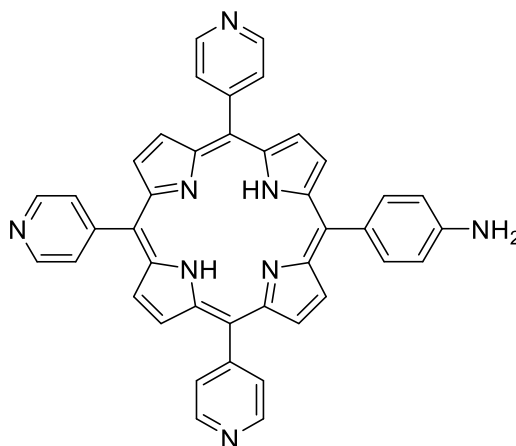
5-[4-(succinimide-*N*-oxycarbonyl)phenyl]-10,15,20-tri-(*N*-methyl-4-pyridinium)porphyrin trichloride 7²⁰³



To a stirred solution of 5-[4-(succinimide-*N*-oxycarbonyl)phenyl]-10,15,20-tri-(4-pyridyl)porphyrin (195 mg, 0.256 mmol) in DMF (10ml) was added methyl iodide (3 ml, 0.0482 mol) *via* syringe. The reaction mixture was allowed to proceed at 40 °C overnight. The mixture was cooled to room temperature and cold diethyl ether (100 ml) was added. The reaction mixture was filtered through cotton wool, and the residue redissolved in water. NH₄PF₆ was added, filtered, and the residue redissolved in acetone. Tetrabutylammonium chloride was added and filtered. The crude was precipitated from diethyl ether over methanol to yield the product as a purple solid (129 mg, 0.142 mmol, 55%).

¹H NMR (400 MHz, DMSO- *d*₆): δ 3.03 (s, 4H, O=C-CH₂), 4.77 (d, 9H, N-CH₃), 8.53 (d, 2H, *o*-Ph), 8.61 (d, 2H, *m*-Ph), 9.11 (m, 14H, βH and *o*-Py), 9.58 (m, 6H, *m*-Py). ¹³C NMR (100 MHz, DMSO- *d*₆): δ 26.28 (O=C-CH₂), 38.38 (N-CH₃), 115.62, 116.12, 121.24, 125.15, 129.48, 132.68 (βH), 135.72, 144.85 (βH), 147.92, 156.99, 162.59 (N-C=O), 171.11(O-C=O). UV-vis (CH₃OH, nm) 424, 516, 554, 592, 650. ε (424 nm) = 216898 M⁻¹ cm⁻¹. MS: (ESI) *m/z* 267 [M-3Cl]³⁺, HRMS: calcd. for C₄₉H₃₉N₈O₄ 267.7693 found 267.7696.

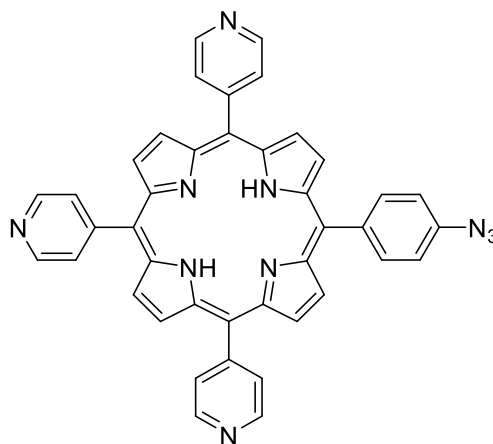
5-[4-aminophenyl]-10,15,20-tri-(4-pyridyl)porphyrin **8**³⁰⁵



5-[4-acetamidophenyl]-10,15,20-tripyridylporphyrin (400 mg, 0.593 mmol) was dissolved in HCl (5M, 100 ml) and stirred at reflux (80 °C) for 3 hours. The reaction was cooled to room temperature and concentrated under reduced pressure. The residue was dissolved in DCM:TEA (9:1, 200 ml) and stirred for 10 minutes at room temperature. The solution was washed with water (3x200 ml) and the organic layer dried (Na₂SO₄). The solvent was removed under reduced pressure and the residue recrystallizes from MeOH over DCM to yield the product as purple solid (345 mg, 0.545 mmol, 92%).

¹H NMR (400 MHz, CDCl₃): δ 4.08 (s, 2H, NH₂), 7.08 (d, 2H, o-Ph), 7.98 (d, 2H, m-Ph), 8.15 (m, 6H, o-Py), 8.82 (m, 6H, m-Py), 9.03 (m, 8H, βH). ¹³C NMR (100 MHz, CDCl₃): δ 113.65, 116.74, 117.38, 122.66, 129.47 (βH), 131.68, 135.92, 146.54, 148.46 (βH), 148.51, 150.11, 150.21. UV-vis (CH₂Cl₂, nm) 420, 515, 555, 590, 650, ε (420 nm) = 661835 M⁻¹cm⁻¹. MS: (ESI) m/z 633 [M-H]⁺, HRMS: calculated for C₄₁H₂₈N₈ 633.2510, found: 633.2512.

5-[4-Azidophenyl]-10,15,20-tri-(4-pyridyl)porphyrin **9**³⁰⁶

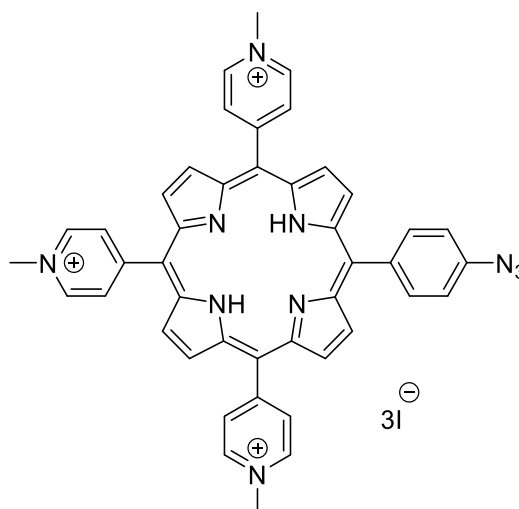


To a stirred solution of YY144 (580 mg, 0.917 mmol) in TFA (6 mL) at 0 °C was added a solution of sodium nitrite (132 mg, 1.91 mmol) in water. The reaction mixture was allowed to proceed for 15 mins at 0 °C. A solution of sodium azide (249 mg, 3.83 mmol) in water. The reaction mixture

was allowed to proceed for 1 hour at 0 °C. The reaction mixture was diluted with water and neutralised using saturated sodium hydrogen carbonate solution. The solution was extracted using DCM (3×50 mL), the organic layer dried and removed under reduced pressure. The crude was purified using column chromatography (silica, 3% MeOH:DCM). The crude was recrystallized from MeOH over DCM to yield the product as a purple solid (438 mg, 0.665 mmol, 73%).

¹H NMR (400 MHz, CDCl₃) δ -2.90 (s, 2H, NH), 7.44 (d, *J* = 8.3 Hz, 2H, o-Ph), 8.16 (d, *J* = 5.9 Hz, 6H, o-Py), 8.18 (d, *J* = 8.3 Hz, 2H, m-Ph), 8.87 (m, 8H, βH), 9.05 (d, *J* = 5.8 Hz, 6H, m-Py). ¹³C NMR (100 MHz, CDCl₃) δ 117.32, 117.64, 117.74, 120.56, 129.46, 135.81, 138.25, 140.43, 148.53, 149.98, 150.02. UV-vis (CH₂Cl₂, nm): 418, 514, 550, 590, 644. ε (418 nm) = 483927 M⁻¹ cm⁻¹. MS: (ESI) *m/z* 659 [M+H]⁺, HRMS: calcd. for C₄₁H₂₇N₁₀ 659.2415 found 659.2408.

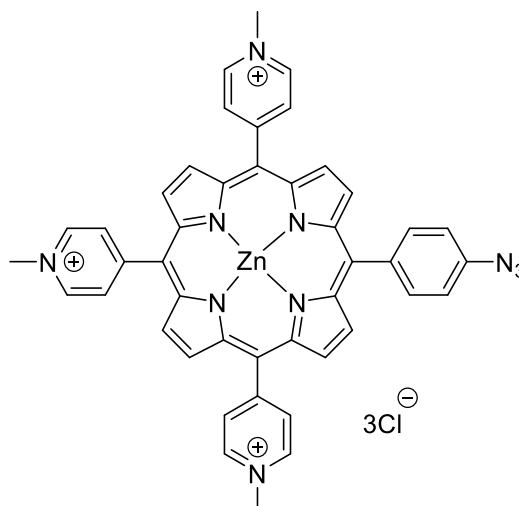
5-[4-azidophenyl]-10,15,20-tri-(*N*-methyl-4-pyridinium)porphyrin triiodide 10³⁰⁶



To a stirred solution of 5-[4-Azidophenyl]-10,15,20-tri-(4-pyridyl)porphyrin (588 mg, 0.893 mmol) in DMF (60 mL) was added methyl iodide (6 mL, 0.096 mol) dropwise via a syringe. The reaction mixture was heated to 40 °C and was allowed to proceed overnight. The reaction mixture was allowed to cool to room temperature and diethyl ether added to promote precipitation the precipitate was filtered through cotton wool. The residue was redissolved in MeOH and diethyl ether was added. Precipitate formed was filtered and collected to yield a purple solid (941 mg, 0.868 mmol, 97%).

¹H NMR (400 MHz, DMSO-*d*₆) δ -3.06 (s, 2H, NH), 4.68 (s, 9H, N-CH₃), 7.61 (d, *J* = 8.2 Hz, 2H, o-Ph), 8.23 (d, *J* = 8.0 Hz, 2H, m-Ph), 8.97 (d, *J* = 5.4 Hz, 6H, o-Py), 9.06 (m, 8H, βH), 9.44 (d, *J* = 5.8 Hz, 6H, m-Py). ¹³C NMR (100 MHz, DMSO-*d*₆) δ 48.42 (N-CH₃), 115.14, 115.88, 118.67, 122.46, 132.64 (C-β), 136.26, 137.56, 140.57, 144.71 (C-β), 157.07. UV-vis (H₂O, nm): 424, 520, 562, 584, 646, ε (424 nm) = 184756 M⁻¹ cm⁻¹. MS: (ESI) *m/z* 234 [M-3I]³⁺, HRMS: calcd. for C₄₄H₃₃N₁₀I₃ found 234.4343.

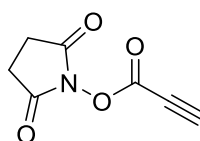
Zinc 5-[4-azidophenyl]-10,15,20-tri-(*N*-methyl-4-pyridinium)porphyrin trichloride **11**³⁰⁶



To a stirred solution of 5-[4-azidophenyl]-10,15,20-tri-(*N*-methyl-4-pyridinium)porphyrin triiodide (300 mg, 0.277 mmol) in water (30 mL) was added zinc (II) acetate (300 mg, 1.64 mmol). The reaction mixture was allowed to proceed at 40 °C overnight. The reaction mixture was diluted with water. NH_4PF_6 was added, filtered, and the residue redissolved in acetone. Tetrabutylammonium chloride was added, and filtered. The residue was precipitated from diethyl ether over methanol to yield a green solid (235 mg, 0.270 mmol, 98%).

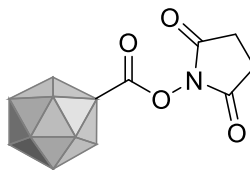
HPLC: gradient 3 $R_f = 14.6$ min, gradient 4 $R_f = 10.8$ min. ^1H NMR (400 MHz, $\text{DMSO-}d_6$) δ 4.67 (s, 9H, N- CH_3), 7.56 (d, $J = 7.5$ Hz, 2H, o-Ph), 8.16 (d, $J = 7.9$ Hz, 2H, m-Ph), 8.88 (m, 14H, o-Py, βH), 9.38 (m, 6H, m-Py). ^{13}C NMR (100 MHz, $\text{DMSO-}d_6$) δ 48.25 (N- CH_3), 115.25, 116.02, 118.20, 132.65 (C β), 136.06, 139.23, 139.87, 144.14 (C β), 148.39, 148.68, 148.86, 150.74, 158.91. UV-vis (H_2O , nm): 435, 564, 612, ϵ (435 nm) = $170651 \text{ M}^{-1} \text{ cm}^{-1}$. MS: (ESI) m/z 255 [$\text{M}-3\text{Cl}]^{3+}$, HRMS calcd. for $\text{C}_{44}\text{H}_{33}\text{N}_{10}\text{Zn}$ 255.0722 found 255.0725.

2,5-dioxopyrrolidin-1-yl propiolate **12**



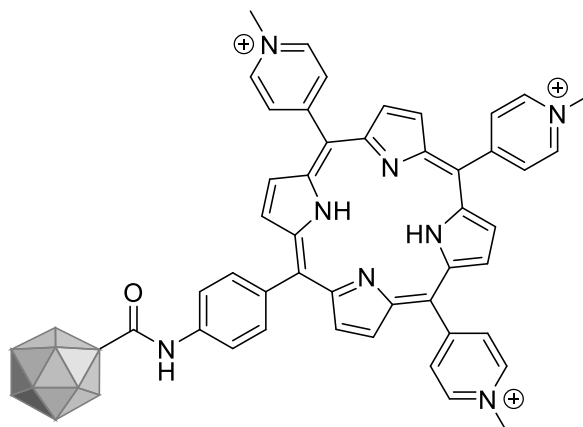
Propiolic acid (10 μL , 0.16 mmol) was added to a solution of EDC (60 mg, 0.313 mmol) in 600 μL DMSO and stirred at room temperature for 10 minutes. A solution of NHS (40 mg, 0.348 mmol) in 100 μL DMSO was added to the reaction mixture and was allowed to stir at room temperature for 3 hours. The product formed was used immediately without purification.

CPMV1



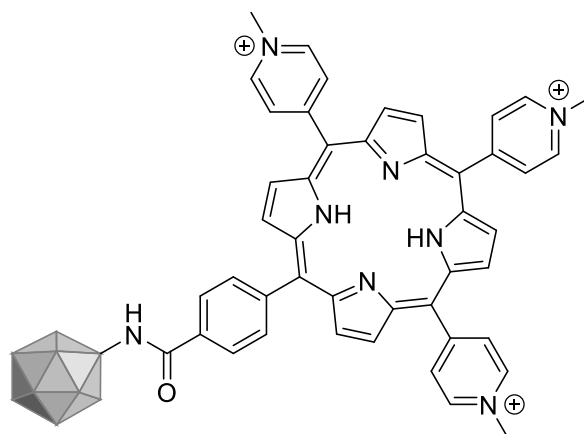
100 μL of 0.1 mg mL^{-1} wtCPMV in phosphate buffer (0.1 M, pH 7) was incubated with a freshly prepared Milli-Q water solution of EDC (2000 molar excess) for 10 minutes followed by the addition of a freshly prepared DMSO solution of NHS (8000 molar excess). DMSO concentration of reaction mixture was adjusted to 20%. The reaction was allowed to proceed for 2 hours at RT with gentle stirring. The *O*-succinimide esterified wtCPMV particles were purified using centrifugal filter (Sartorius Stedium 100 kDa). Native agarose gel electrophoresis was carried out. Viral nanoparticle recovery was 73% as determined using UV-vis spectroscopy.

CPMV2



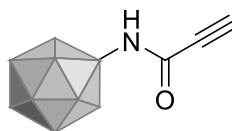
CPMV1 was incubated with porphyrin **1** (5000 molar excess) in phosphate buffer (0.1 M, pH 7) adjusted to 20% DMSO. The reaction mixture was stirred overnight at RT. The porphyrin-wtCPMV conjugate was purified using centrifugal filter (Sartorius Stedium 100 kDa). Native agarose gel electrophoresis was carried out. Viral nanoparticle recovery was 64% as determined using UV-vis spectroscopy.

CPMV3



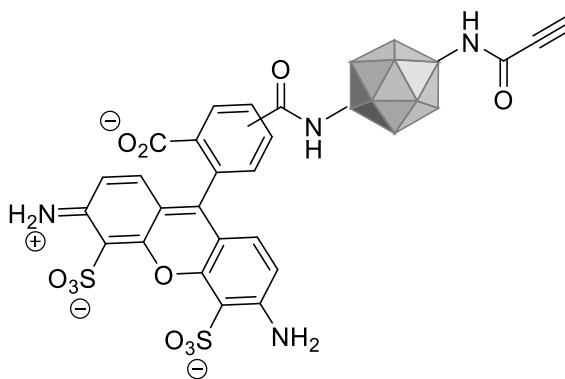
150 μL 0.2 mg mL^{-1} wtCPMV in phosphate buffer (0.1 M, pH 7) adjusted to 20% DMSO was incubated with porphyrin **7** (2000 molar excess) and was stirred at room temperature overnight. Precipitate formed were resuspended through pipetting, and 100 μL of the reaction mixture were purified using dialysis (Slide-A-Lyzer Mini dialysis device, 10K MWCO) against phosphate buffer (0.1 M, pH7). Aliquots of dialysis was taken at regular time intervals and analysed using UV-vis spectroscopy, native agarose gel electrophoresis, and TEM. Viral nanoparticle recovery was 19% as determined using UV-vis spectroscopy.

CPMV4



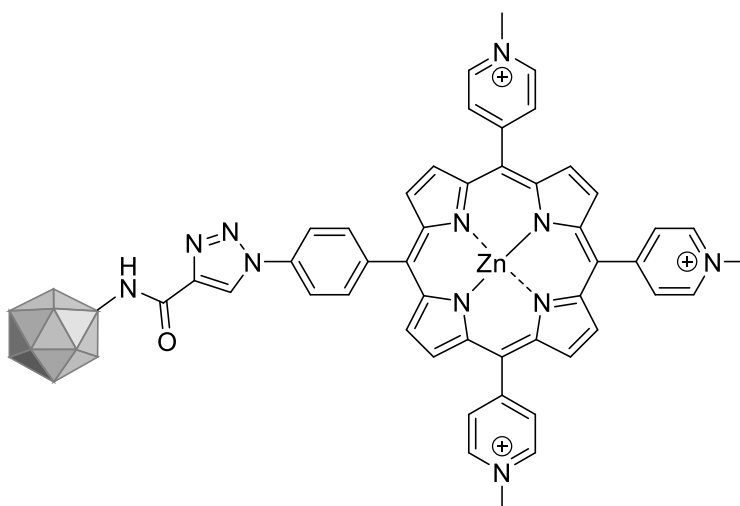
100 μL 0.2 mg mL^{-1} wtCPMV in 80% 0.1 M pH7 sodium phosphate buffer 20% DMSO was incubated with varying amount of **12** at 10,000 molar excess, 20,000 molar excess, 50,000, and 100,000 molar excess. The reaction mixture was allowed to proceed on a rolling shaker overnight. The modified CPMV was not purified using centrifugal filter (Amicon® ultra centrifugal filter, 100 kDa NMWL). Native gel electrophoresis was carried out. Viral nanoparticle recovery was in the range of 46-60% as determined using UV-vis spectroscopy.

CPMV5



100 μL 0.2 mg mL^{-1} **CPMV4** in 4:1 phosphate buffer (0.1 M, pH 7):DMSO was incubated with Alexafluor-488 NHS (ThermoFisher, 30,000 molar excess). The reaction mixture was allowed to proceed on a shaker at room temperature for 1 hour and then 4 °C overnight. The reaction mixture was purified using centrifugal filter (Amicon® ultra centrifugal filter, 100 kDa NMWL). Viral nanoparticle recovery was 38% as determined using UV-vis spectroscopy.

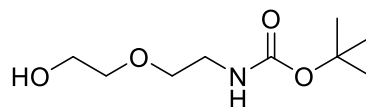
CPMV6



100 μL 0.2 mg mL^{-1} **CPMV4** was added porphyrin **11** (5000 molar excess), THPTA (5000 molar excess), aq. CuSO₄ (5000 molar excess), aq. sodium ascorbate (50,000 molar excess). DMSO level were adjusted to 20% (v/v) of the reaction volume, giving 132 μL as the final volume. The reaction mixture was allowed to proceed in a rolling shaker overnight at 4 °C. The reaction mixture was purified using dialysis device (Slide-A-Lyzer, 10 kDa) against pH 7 0.1 M sodium phosphate buffer. Viral nanoparticle recovery was 17% as determined using UV-vis spectroscopy.

7.9 Synthesis and PAN functionalisation described in chapter 3

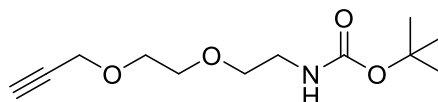
Tert-butyl (2-(2-hydroxyethoxy)ethyl)carbamate **13**



To a solution di-*tert*-butyl carbonate (10.8 g, 49.4 mmol) in 80 mL DCM was added 2-(2-aminoethoxy)ethanol (4.4 mL, 40 mmol). The reaction mixture was allowed to proceed at 40 °C overnight. The reaction mixture was concentrated under reduced pressure and purified by column chromatography (silica, 1:1 hexane:ethyl acetate) to yield the product as a transparent oil (7.6 g, 37 mmol, 93%).

^1H NMR (400 MHz, CDCl_3) δ 1.43 (s, 9H), 3.31 (t, $J = 5.2$ Hz, 2H), 3.54 (m, 4H), 3.72 (m, 2H). ^{13}C NMR (100 MHz, CDCl_3) δ 28.48, 60.49, 61.83, 70.39, 72.25, 100.00, 156.18. MS: (ESI) m/z 206 $[\text{M}+\text{H}]^+$, HRMS: calcd. for $\text{C}_9\text{H}_{20}\text{N}_1\text{O}_4$: 206.1387 found 206.1388.

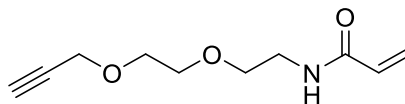
Tert-butyl (2-(2-(prop-2-yn-1-yloxy)ethoxy)ethyl)carbamate **14**



To a stirred solution of *tert*-butyl (2-(2-hydroxyethoxy)ethyl)carbamate **13** (1.0 g, 4.88 mmol) in 25 mL dry DMF at 0 °C was added sodium hydride (60% dispersion in mineral oil, 880 mg, 22.0 mmol). The reaction mixture was allowed to warm up to room temperature and proceed for 30 minutes. The reaction mixture was then cooled to 0 °C and propargyl bromide (1.63 mL, 14.61 mmol) was added dropwise. The reaction mixture was allowed to warm up to room temperature and proceed overnight. The reaction mixture was quenched with brine and extracted with ethyl acetate (2×50 mL). The organic layer was washed with brine (5×50 mL) and dried over anhydrous magnesium sulphate. The solvent was removed under reduced pressure at low temperature, 30 °C, and dried under vacuum overnight, the product was used without further purification (1.02 g, 4.2 mmol, 86%).

^1H NMR (400 MHz, CDCl_3) δ 1.43 (s, 9H, C- CH_3), 2.43 (m, 1H, $\text{C}\equiv\text{CH}$), 3.30 (m, 2H), 3.53 (m, 2H), 3.65 (m, 4H), 4.19 (m, 2H). ^{13}C NMR (100 MHz, CDCl_3) δ 28.49 (C- $\underline{\text{C}}\text{H}_3$), 58.52, 69.11, 70.20, 70.40, 74.75, 79.60, 156.05. MS (ESI) m/z 244 $[\text{M}+\text{H}]^+$, HRMS: calcd. for $\text{C}_{12}\text{H}_{22}\text{N}_1\text{O}_4$: 244.1543 found 244.1546

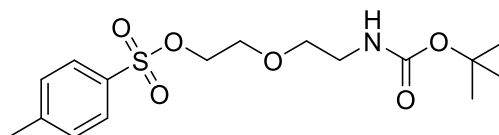
***N*-2-(2-(prop-2-yn-1-yloxy)ethoxy)ethylacrylamide **15**²²⁹**



Tert-butyl (2-(2-(prop-2-yn-1-yloxy)ethoxy)ethyl)carbamate **14** (500 mg, 2.06 mmol) was treated with 4 N HCl in 1,4-dioxane (3 mL). The resulting solution was stirred at room temperature for 1 h, and the solvent was evaporated. The residue was triturated with diethyl ether and thoroughly dried in vacuo. The solid residue was taken in dry DCM (5 mL) and the resulting solution was maintained in an Ar atmosphere and cooled at 0 °C. Triethylamine (630 μ L, 4.52 mmol) was added to the solution, followed by dropwise addition of acryloyl chloride (250 μ L, 3.084 mmol). The mixture was stirred for 4 h, while being allowed to reach room temperature. The reaction mixture was diluted with DCM (45 mL) and washed with 0.1 M aqueous HCl (50 mL), and with brine (2 \times 50 mL). The crude was purified using column chromatography (silica, 1:1, diethyl ether:DCM) to yield the product as a yellow oil (83 mg, 0.42 mmol, 21%).

¹H NMR (400 MHz, CDCl₃) δ 6.28 (dd, *J* = 17.0, 1.0 Hz, 1H, CH₂CHCO), 6.15 (bs, 1H, NH), 6.10 (dd, *J* = 17.0, 10.2 Hz, 1H, CH₂CHCO), 5.63 (dd, *J* = 10.2, 1.0 Hz, 1H, CH₂CHCO), 4.20 (dd, *J* = 2.4, 0.6 Hz, 2H, CHCCH₂O), 3.63 (m, 8H, CH₂), 2.44 (td, *J* = 2.4, 0.6 Hz, 1H, CHCCH₂O). ¹³C NMR (100 MHz, CDCl₃) δ 165.61, 130.92, 126.55, 79.51, 74.88, 70.15, 69.84, 69.13, 58.53, 39.29. MS: (ESI) *m/z* 198 [M+H]⁺, HRMS: calcd. for C₁₀H₁₆N₁O₃: 198.1125 found 198.1125.

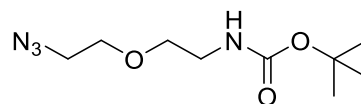
2-(2-((*tert*-butoxycarbonyl)amino)ethoxy)ethyl 4-methylbenzenesulfonate **16**



To a stirred solution of *tert*-butyl (2-(2-hydroxyethoxy)ethyl)carbamate **13** (1.00 g, 4.88 mmol) in dry DCM (6 mL) was added *p*-toluenesulfonyl chloride (1.85 g, 9.74 mmol), DIPEA (2.5 mL, 14.6 mmol) and DMAP (356 mg, 2.92 mmol) at 0 °C under Ar atmosphere. After 30 mins, the reaction mixture was allowed to proceed at room temperature to stir overnight. The solution was concentrated under reduced pressure. The crude was purified using column chromatography (silica, 99:1 DCM:MeOH) to yield the product as an oil. (1.57 g, 4.37 mmol, 89%).

¹H NMR (400 MHz, CDCl₃) δ 1.43 (s, 9H, C-(CH₃)₃), 2.44 (s, 3H, Ph-CH₃), 3.22 (m, 2H, CH₂), 3.43 (m, 2H, CH₂), 3.61 (m, 2H, CH₂), 4.15 (m, 2H, CH₂), 7.34 (d, *J* = 7.9 Hz, 2H, *m*-Ph), 7.79 (d, *J* = 8.3 Hz, 2H, *o*-Ph). ¹³C NMR (100 MHz, CDCl₃) δ 21.75 (Ph-CH₃), 28.49 (C(CH₃)₃), 40.30 (C(CH₃)₃), 68.44 (CH₂), 69.16 (CH₂), 70.45 (CH₂), 79.45 (CH₂), 128.07 (Ph-C), 129.92 (Ph-C), 133.07 (Ph-C), 145.00 (Ph-C), 155.97 (C=O). MS: (ESI) *m/z* 360 [M+H]⁺, HRMS: calcd. for C₁₆H₂₆N₁O₆S₁: 360.1475 found 360.1472.

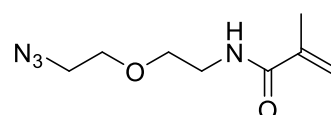
Tert*-butyl (2-(2-azidoethoxy)ethyl)carbamate **17*



To a stirred solution of 2-(2-((*tert*-butoxycarbonyl)amino)ethoxy)ethyl 4-methylbenzenesulfonate **16** (500 mg, 1.39 mmol) in dry DMF (5 mL) was added sodium azide (540 mg, 8.35 mmol). The reaction mixture was allowed to proceed at 90 °C for 48 hours. The reaction mixture was diluted with water (50 mL) and extracted with DCM (3×50 mL). The organic layer was dried (MgSO₄), and the solvent removed under reduced pressure to yield the product as a yellow oil (261 mg, 1.1 mmol, 82%).

¹H NMR (400 MHz, CDCl₃) δ 1.44 (s, 9H, C(CH₃)₃), 3.35 (m, 4H, CH₂), 3.54 (t, *J* = 5.2 Hz, 2H, CH₂), 3.64 (t, *J* = 5.0 Hz, 2H, CH₂), 4.90 (bs, 1H, NH). ¹³C NMR (101 MHz, CDCl₃) δ 28.48 (C(CH₃)₃), 38.05 (CH₂), 50.75 (CH₂), 70.01 (CH₂), 70.43 (CH₂). MS: (ESI) *m/z* 231 [M+H]⁺, HRMS calcd. for C₉H₁₉N₄O₃ 231.1453 found 231.1452.

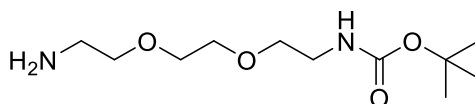
N*-(2-(2-azidoethoxy)ethyl)methacrylamide **18*



Tert-butyl (2-(2-azidoethoxy)ethyl)carbamate **17** (250 mg, 1.09 mmol) was taken up in 4 N HCl in dioxane (1 mL) and was allowed to proceed at room temperature for 1 hour. The solvent was removed under reduced pressure and the crude was taken up in DMF (10 mL) and was added methacrylic anhydride (336 mg, 324 μL, 2.18 mmol) and DIPEA (282 mg, 380 μL, 2.18 mmol). The reaction mixture was allowed to proceed at room temperature under inert atmosphere overnight. Solvent was removed under reduced pressure. The crude was purified using column chromatography (silica, 1:1 hexane:ethyl acetate) to yield the product as an oil (50 mg, 0.25 mmol, 23%).

¹H NMR (400 MHz, CDCl₃) δ 1.94 (s, 3H, CH₃), 3.36 (t, *J* = 4.8 Hz, 2H, CH₂), 3.52 (q, *J* = 5.4 Hz, 2H, CH₂NH), 3.58 (t, *J* = 5.0 Hz, 2H, CH₂), 3.66 (t, *J* = 4.8 Hz, 2H, CH₂), 5.31 (m, 1H, C=CH₂), 5.70 (m, 1H, C=CH₂), 6.26 (s, 1H, NH). ¹³C NMR (100 MHz, CDCl₃) δ 18.67 (CH₃), 39.44 (CH₂), 50.71 (CH₂), 69.95 (CH₂), 70.21 (CH₂), 119.90 (C=CH₂), 139.84 (C=CH₂), 168.52 (C=O). MS (ESI): *m/z* (%): 198.5 (72) [M+H]⁺, 220.5 (100) [M+Na]⁺.

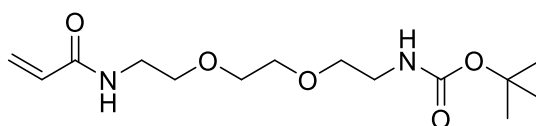
***N*-Boc-2,2'-(ethylenedioxy)-diethylamine **19**²⁴⁷**



2,2'-(ethane-1,2-diylbis(oxy))diethaneamine (20 mL, 20.3 g, 137 mmol) was dissolved in dry DCM (20 mL) and cool to 0 °C under nitrogen. Di-*tert*-butyl dicarbonate (9.97 g, 45 mmol) was dissolved in dry DCM (30 mL) was added dropwise over a period of 1 hour. The reaction mixture was allowed to warm up to room temperature and stirred overnight under nitrogen. The solution was diluted with DCM (50 mL) and washed with water (3×100 mL). The organic layer dried (MgSO₄) and removed under reduced pressure. The crude was purified using column chromatography (95:5-75:25 DCM:MeOH) to yield the product as a colourless oil (8.4 g, 34 mmol, 76%).

¹H NMR (400 MHz, CDCl₃): δ 1.43 (s, 9H, C-(CH₃)₃), 1.51 (bs, 2H, NH₂), 2.87 (t, 2H, CH₂), 3.31 (m, 2H, CH₂), 3.52 (m, 4H, CH₂), 3.61 (s, 4H, CH₂), 5.13 (s, 1H, NH). ¹³C NMR (100 MHz, CDCl₃): δ 28.50 (C-(CH₃)₃), 40.41, 41.84, 70.30, 73.57. MS: (ESI) m/z 248 (M+H)⁺, HRMS: calcd. for C₁₁H₂₅N₂O₄ 249.1809 found 249.1808.

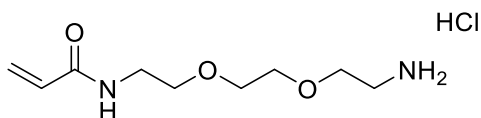
***N*-{2-[2-(2-*tert*-Butoxycarbonylaminoethoxy)ethoxy]ethyl}acrylamide **20**²⁰²**



N-Boc-2,2'-(ethylenedioxy)-diethylamine **19** (500 mg, 2.01 mmol) and diisopropylethylamine (1.0 mL, 2.01 mmol) were dissolved in dry dichloromethane (10 mL) in an argon atmosphere. Acryloyl chloride (327 μl, 4.03 mmol) was added dropwise at 0 °C. The reaction mixture was allowed to stirred overnight, while being allowed to reach room temperature, then it was diluted with dichloromethane, and washed with 5% aqueous solution of citric acid (2×50 mL) and brine (3×50 mL). The organic fraction was dried, concentrated under reduced pressure and the crude was purified by column chromatography oil (silica, 95:5 DCM:MeOH) to yield the product as a yellow (245 mg, 0.81 mmol, 40%).

¹H NMR (400 MHz, CDCl₃) δ 1.43 (s, 9H, C-(CH₃)₃), 3.32 (d, *J* = 5.1 Hz, 2H, CH₂O), 3.58 (m, 10H, CH₂O), 5.63 (d, *J* = 10.2 Hz, 1H, CH₂CHCO), 6.12 (dd, *J* = 17.0, 10.2 Hz, 1H CH₂CHCO) 6.29 (dd, *J* = 17.0, 1.7 Hz, 1H, CH₂CHCO). ¹³C NMR (100 MHz, CDCl₃) δ 28.44 (C(CH₃)₃), 39.34, 40.34, 69.11, 69.81, 70.17, 70.31, 79.43, 126.45 (C=C), 130.90 (C=C), 156.14 (C=O), 165.83 (C=O). MS: (ESI) m/z 303 [M+H]⁺, HRMS: calcd. for C₁₄H₂₇N₂O₅ 303.1914, found 303.1917.

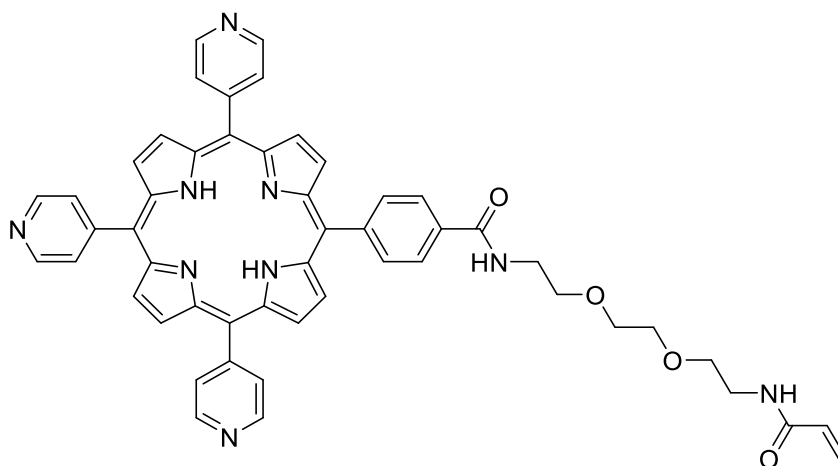
***N*-(2-(2-(2-aminoethoxy)ethoxy)ethyl)acrylamide hydrochloride 21**²⁰²



N-{2-[2-(2-*tert*-Butoxycarbonylaminoethoxy)ethoxy]ethyl}acrylamide **20** (1.67 g, 5.53 mmol) was dissolved in 4 N HCl in dioxane (3.45 mL, 113.8 mmol). The resulting solution was stirred at room temperature for 1 h, and the solvent was evaporated. The residue was triturated with diethyl ether and thoroughly dried *in vacuo* to yield the product as a highly viscous yellow oil (1.3g, 5.46 mmol, 98%).

¹H NMR (400 MHz, DMSO-*d*₆) δ 2.88 (m, 2H, CH₂), 3.24 (m, 2H, CH₂), 3.48 (m, 8H, CH₂), 5.52 (m, 2H, CH₂CHCO, O=CNH), 6.03 (m, 1H, CH₂CHCO), 6.24 (m, 1H, CH₂CHCO). ¹³C NMR (100 MHz, DMSO-*d*₆) δ 38.95, 39.09, 67.10, 69.52, 69.97, 70.16, 125.55, 132.31, 165.26. MS: (ESI) *m/z* 203 [M+H]⁺, HRMS calcd. for C₉H₁₈N₂O₃ 203.1390 found 203.1390.

(5-4-(*N*-(2-(2-(acrylamidoethoxy)ethoxy)ethyl)aminocarbonyl)phenyl)-10,15,20-tri-(4-pyridyl)porphyrin 22²⁰²

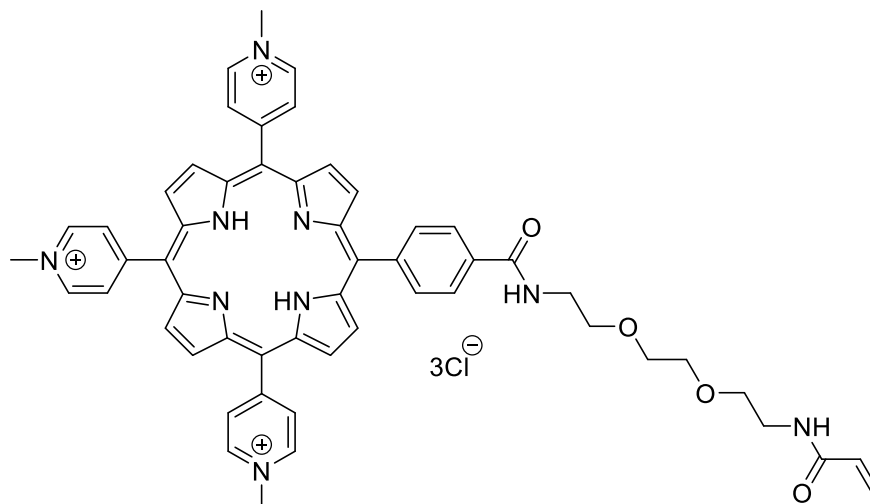


To a stirred solution of porphyrin **5** (1.0 g, 1.51 mmol) in DMF (100 mL) was added EDC (440 mg, 2.3 mmol), HOBT (310 mg, 2.3 mmol), *N*-(2-(2-(2-aminoethoxy)ethoxy)ethyl)acrylamide (470 mg, 2.3 mmol), and DMAP (310 mg, 2.53 mmol). The mixture was stirred for overnight at 40 °C. The solvent was removed under reduced pressure and the crude purified using column chromatography (silica, 92:8 DCM:MeOH). The crude was precipitated from hexane over DCM to yield the product as a brick red solid (677 mg, 0.801 mmol, 48%).

¹H NMR (400 MHz, CDCl₃) δ -2.91 (s, 2H, NH), 3.58 (m, 2H, CH₂), 3.65 (m, 4H, CH₂), 3.74 (m, 4H, CH₂), 3.84 (m, 4H, CH₂), 5.59 (dd, *J*_{cis} = 10.0, *J*_{gem} = 1.6 Hz, 1H, CHHCHCO), 6.13 (dd, *J*_{trans} = 17.0, *J*_{cis} = 10.2 Hz, 1H, CHHCHCO), 6.19 (s, 1H, NH), 6.26 (dd, *J*_{trans} = 16.9, *J*_{gem} = 1.6 Hz, 1H, CHHCHCO), 8.15 (m, 6H, *o*-Py), 8.21 (d, *J* = 8.2 Hz, 2H, *o*-Ph), 8.28 (d, *J* = 8.1 Hz, 2H, *m*-Ph), 8.84 (m, 8H, βH), 9.05 (m, 6H, *m*-Py). ¹³C NMR (100 MHz, CDCl₃) δ 14.22, 22.75, 29.80,

31.68, 39.38, 40.14, 69.94, 70.08, 70.45, 117.49, 117.71, 120.21, 125.68, 126.75, 129.43 (β C), 130.83, 134.31, 134.73, 144.95, 148.49 (β C), 149.97, 165.69 (C=O), 167.60 (C=O). UV-vis [CH_2Cl_2 , nm]: 417, 512, 546, 588, 644. ϵ (417 nm) = $426942 \text{ M}^{-1} \text{ cm}^{-1}$. MS: (ESI) m/z 846 [$\text{M}+\text{H}$] $^+$, HRMS calcd. for $\text{C}_{51}\text{H}_{44}\text{N}_9\text{O}_4$ 846.3511 found 846.3535.

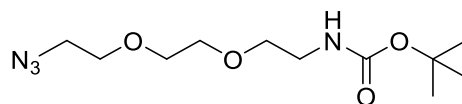
(5-4-(*N*-(2-(2-(acrylamidoethoxy)ethoxy)ethyl)aminocarbonyl)phenyl)-10,15,20-tri-(*N*-methyl-4-pyridinium)porphyrin trichloride **23²⁰²**



To a stirred solution of porphyrin **22** (170 mg, 0.201 mmol) in DMF (17 mL) was added methyl iodide (3 mL, 48 mmol) via a syringe. The reaction mixture was allowed to proceed at 40 °C overnight. The reaction mixture was allowed to cool to room temperature, and diethyl ether was added. The mixture was filtered through cotton wool, and the residue redissolved in water. NH_4PF_6 was added, filtered, and the residue redissolved in acetone. Tetrabutylammonium chloride was added and filtered to yield a purple solid (194 mg, 0.195 mmol, 97%).

^1H NMR (400 MHz, $\text{DMSO-}d_6$) δ -3.08 (s, 2H, NH), 3.13 (m, 2H, CH_2), 3.47 (m, 2H, CH_2), 3.62 (m, 8H, CH_2), 4.70 (s, 9H, N- CH_3), 5.52 (d, $J = 10.2$ Hz, 1H, $\text{CH}_2=\text{CHCO}$), 6.03 (d, $J = 17.0$ Hz, 1H, $\text{CH}_2=\text{CHCO}$), 6.25 (dd, $J = 17.0, 10.2$ Hz, 1H, $\text{CH}_2=\text{CHCO}$), 8.29 (d, $J = 7.5$ Hz, 2H, o-Ph), 8.35 (d, $J = 7.8$ Hz, 2H, m-Ph), 9.03 (m, 14H, β H, o-Py), 9.50 (m, 6H, m-Py). ^{13}C NMR (100 MHz, $\text{DMSO-}d_6$) δ 14.06, 48.34 (N- CH_3), 69.53, 69.61, 70.18, 115.29, 115.94, 122.42, 125.63, 126.64, 132.28, 132.64, 134.71, 143.56, 144.75, 157.02, 165.25, 166.59. UV-vis [water, nm] 422, 518, 560, 584, 638. ϵ (422 nm) = $185207 \text{ M}^{-1} \text{ cm}^{-1}$. MS: (ESI) m/z 296 [$\text{M}-3\text{Cl}$] $^{3+}$, HRMS calcd. for $\text{C}_{54}\text{H}_{52}\text{N}_9\text{O}_4$ 296.8042 found 296.8048.

Tert*-butyl (2-(2-(2-azidoethoxy)ethoxy)ethyl)carbamate **24*

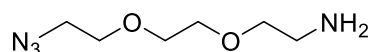


To a stirred solution of *N*-Boc-2,2'-(ethylenedioxy)-diethylamine **19** (500 mg, 2.01 mmol) in methanol (10 mL) was added copper (II) sulphate pentahydrate (1 mg), potassium carbonate (0.55 g, 4.0 mmol). Imidazole-1-sulfonyl azide hydrochloride (500 mg, 2.4 mmol) was added, and the mixture allowed to proceed at room temperature overnight. The solvent was removed under reduced pressure and the product purified by column chromatography (silica, 99:1 DCM:MeOH) to the product as a yellow oil (390 mg, 1.42 mmol, 71%).

^1H NMR (400 MHz, CDCl_3) δ 1.43 (s, 9H, C-(CH_3) $_3$), 3.31 (q, $J = 5.2$ Hz, 2H, NH- CH_2), 3.40 (m, 2H), 3.54 (t, $J = 5.1$ Hz, 2H), 3.65 (m, 6H). ^{13}C NMR (100 MHz, CDCl_3) δ 28.50 (C($\underline{\text{C}}\text{H}_3$) $_3$), 40.40, 50.73, 70.17, 70.31, 70.40, 70.66, 79.38, 156.10. MS: (ASAP) m/z 275 [$\text{M}+\text{H}$] $^+$, HRMS: calcd. for $\text{C}_6\text{H}_{15}\text{N}_4\text{O}_2$ 275.1720 found 275.1719.

2-(2-(2-azidoethoxy)ethoxy)ethan-1-amine hydrochloride **25**

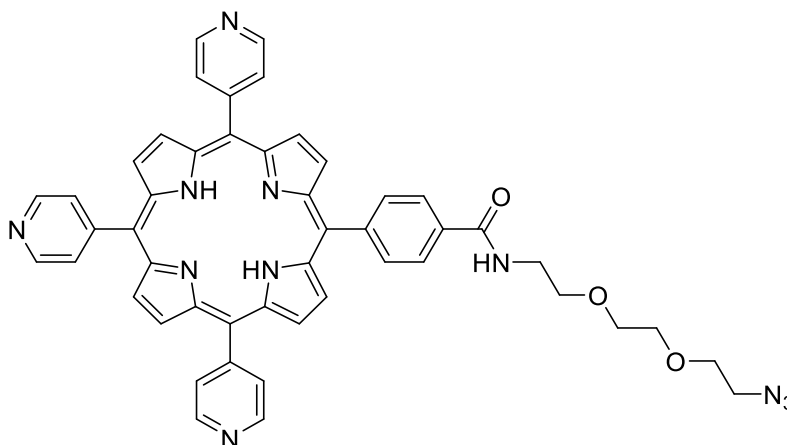
HCl



Tert-butyl (2-(2-(2-azidoethoxy)ethoxy)ethyl)carbamate **20** (389 mg, 1.42 mmol) was dissolved in 4 N HCl in dioxane (1 mL). The reaction mixture was allowed to proceed at room temperature for 2 hours. The solvent was removed under reduced pressure and the crude triturated with diethyl ether. The crude was dried under reduced pressure to yield the product as a yellow oil (272 mg, 1.29 mmol, 91%).

^1H NMR (400 MHz, CDCl_3) δ 3.26 (m, 2H, $\underline{\text{C}}\text{H}_2\text{-NH}_2$), 3.44 (m, 2H, $\text{CH}_2\text{-N}_3$), 3.69 (m, 6H, CH_2), 3.82 (m, 2H, CH_2). ^{13}C NMR (100 MHz, CDCl_3) δ 39.79, 50.71, 66.75, 69.97, 70.32, 70.46. MS: (ESI) m/z 175 [$\text{M}+\text{H}$] $^+$, HRMS: calcd. for $\text{C}_6\text{H}_{15}\text{N}_4\text{O}_2$ 175.1190 found 175.1188.

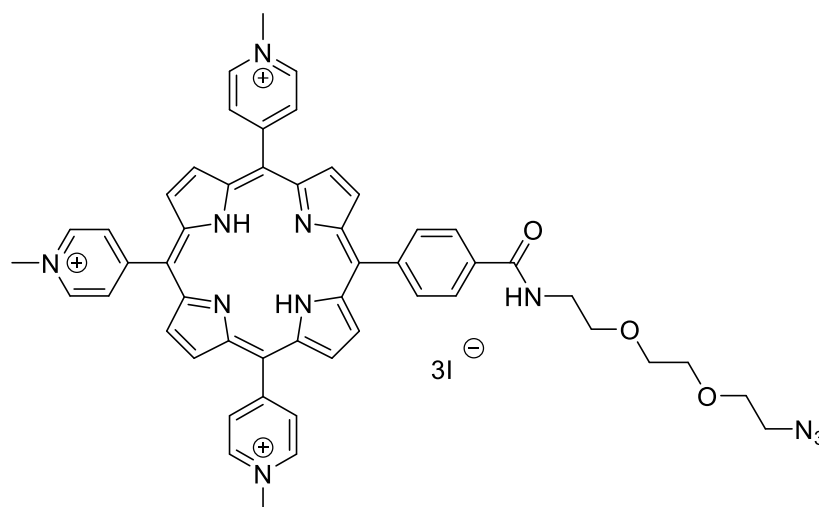
(5-4-(*N*-(2-(2-(azidoethoxy)ethoxy)ethyl)aminocarbonyl)phenyl)-10,15,20-tri-(4-pyridyl)porphyrin 26²⁵¹



To a stirred solution of porphyrin **5** (400 mg, 0.604 mmol) in DMF (30 mL) was added EDC (232 mg, 1.20 mmol), HOBT (164 mg, 1.20 mmol), 2-(2-(2-azidoethoxy)ethoxy)ethan-1-amine hydrochloride (200 mg, 0.95 mmol), and DMAP (146 mg, 1.20 mmol). The reaction mixture was allowed to stir for 48 hours at room temperature. Solvent was co-evaporated with toluene under reduced pressure. The crude was redissolved in DCM and washed with water (3×50 mL). The organic layer removed under reduced pressure. The crude was purified using column chromatography (silica, 94:6-93:7 DCM:MeOH). The crude was precipitated from hexane over DCM to yield a purple solid (359 mg, 0.439 mmol, 73%).

¹H NMR (400 MHz, CDCl₃) δ -2.91 (s, 2H, NH), 3.42 (t, *J* = 4.4 Hz, 2H, CH₂), 3.79 (m, 10H, CH₂), 8.15 (m, 6H, o-Py), 8.21 (d, *J* = 8.0 Hz, 2H, o-Ph), 8.28 (d, *J* = 7.8 Hz, 2H, m-Ph), 8.86 (m, 8H, βH), 9.04 (m, 6H, m-Py). ¹³C NMR (100 MHz, CDCl₃) δ 40.11, 50.74, 70.16, 70.24, 70.44, 70.71, 117.46, 117.70, 120.36, 125.74, 129.45 (Cβ), 134.47, 134.69, 144.80, 148.50 (Cβ), 149.98, 167.63 (C=O). UV-vis [CH₂Cl₂, nm] 416, 512, 546, 588, 644. MS: (ESI) *m/z* 818 [M+H]⁺, HRMS: calcd. for C₄₈H₄₀N₁₁O₃ 818.3310 found 818.3306.

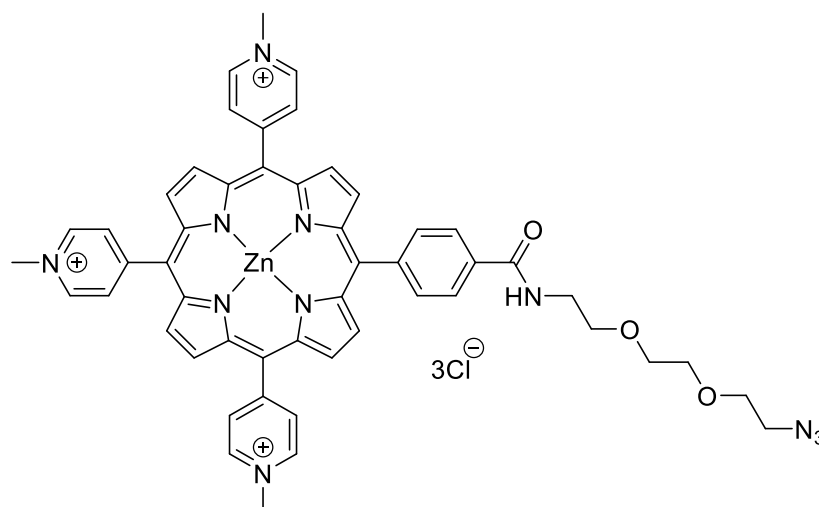
(5-4-(*N*-(2-(2-(azidoethoxy)ethoxy)ethyl)aminocarbonyl)phenyl)-10,15,20-tri-(*N*-methyl-4-pyridinium)porphyrin triiodide 27²⁵¹



To a stirred solution of porphyrin **26** (400 mg, 0.489 mmol) in DMF (40 mL) was added methyl iodide (4 mL, 0.064 mol) dropwise via a syringe. The reaction mixture was heated to 40 °C and was allowed to proceed overnight. The reaction mixture was allowed to cool to room temperature and diethyl ether added to promote precipitation the precipitate was filtered through cotton wool. The residue was redissolved in MeOH and diethyl ether was added. Precipitate formed was filtered and collected to yield a purple solid (604 mg, 0.486 mmol, 99%).

¹H NMR (400 MHz, DMSO-*d*₆) δ -3.07 (s, 2H, NH), 3.40 (m, 2H, CH₂-N₃), 3.65 (m, 10H, CH₂), 4.69 (s, 9H, N-CH₃), 8.30 (d, *J* = 8.2 Hz, 2H, o-Ph), 8.33 (d, *J* = 8.3 Hz, 2H, m-Ph), 9.03 (m, 14H, βH, o-Py), 9.45 (d, *J* = 6.2 Hz, 6H, m-Py). ¹³C NMR (100 MHz, DMSO-*d*₆) δ 48.46 (N-CH₃), 50.59 (CH₂), 69.58 (CH₂), 69.86 (CH₂), 70.25 (CH₂), 115.28, 115.93, 122.41, 126.61, 132.64 (βC), 134.72, 134.83, 143.58, 144.73 (βC), 157.05, 166.61 (C=O). UV-vis [water, nm] 422, 519, 560, 585, 640. ε (434 nm) = 154630 M cm⁻¹. MS: (ESI) *m/z* 287 [M-3I]³⁺, HRMS: calcd. for C₅₁H₄₈N₁₁O₃ 287.4642 found 287.4643.

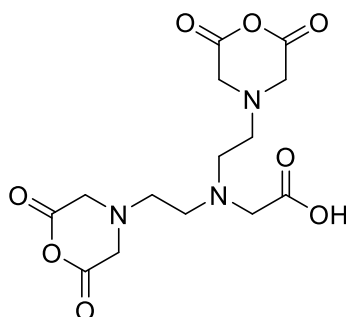
Zinc (5-4-(*N*-(2-(2-(azidoethoxy)ethoxy)ethyl)aminocarbonyl)phenyl)-10,15,20-tri-(*N*-methyl-4-pyridinium)porphyrin trichloride **28²⁵¹**



To a stirred solution of porphyrin **27** (300 mg, 0.241 mmol) in water (30 mL) was added zinc (II) acetate (300 mg, 1.6 mmol). The reaction mixture was allowed to proceed at 40 °C overnight. The reaction mixture was diluted with water, NH_4PF_6 was added, filtered, and the residue redissolved in acetone. Tetrabutylammonium chloride was added and filtered. The residue was precipitated from diethyl ether over methanol to yield a purple solid (230 mg, 0.223 mmol, 93%).

^1H NMR (400 MHz, $\text{DMSO-}d_6$) δ 3.40 (m, 2H, CH_2PEG), 3.65 (m, 10H, CH_2PEG), 4.68 (s, 9H, N- CH_3), 8.21 (d, $J = 8.1$ Hz, 2H, o-Ph), 8.30 (d, $J = 8.2$ Hz, 2H, m-Ph), 8.86 (m, 10H, βH , o-Py), 8.96 (d, $J = 4.8$ Hz, 4H, βH), 9.41 (m, 6H, m-Py). ^{13}C NMR (100 MHz, $\text{DMSO-}d_6$) δ 48.20 (N- CH_3), 50.56, 69.56, 69.86, 70.23, 115.31, 116.02, 122.76, 126.20, 132.13, 132.64 ($\text{C}\beta$), 132.82, 133.58, 134.21, 134.53, 144.14 ($\text{C}\beta$), 145.38, 148.43, 148.70, 148.85, 150.40, 158.99, 166.79 ($\text{C}=\text{O}$). UV-vis [water, nm] 434, 563, 607. ϵ (434 nm) = 200767 M cm^{-1} . MS: (ESI) m/z 479 [$\text{M}-2\text{Cl}]^{2+}$, HRMS: calcd. for $\text{C}_{51}\text{H}_{46}\text{N}_{11}\text{O}_3\text{ZnCl}$ 479.4377, found 479.6372.

Diethylenetriaminepentaacetic dianhydride (DTPA-DA) **29²⁵⁶**



A slurry of 1.60 g (4.1 mmol) of diethylenetriaminepentaacetic acid (DTPA), dry pyridine (2 mL), and acetic anhydride (2.24 g, 2.42 mL, 21.9 mmol) was prepared. The reaction mixture was stirred at 65 °C overnight. The reaction mixture was filtered whilst hot, and the solid residue was washed

with acetic anhydride, and then with diethyl ether to yield the product as an off-white solid (1.36 g, 3.81 mmol, 93%).

^1H NMR (400 MHz, $\text{DMSO-}d_6$) δ 2.55 (t, $J = 5.4$ Hz, 4H, $\text{NCH}_2\text{CH}_2\text{N}$), 2.70 (t, $J = 5.0$ Hz, 4H, $\text{NCH}_2\text{CH}_2\text{N}$), 3.26 (s, 2H, NCH_2COOH), 3.68 (m, 8H, $\text{O}(\text{O}=\text{CCH}_2)_2\text{N}$). ^{13}C NMR (100 MHz, $\text{DMSO-}D_6$) δ 51.19, 52.25, 53.12, 55.05, 166.39 ($\text{N}(\text{CH}_2\text{CO})_2\text{O}$), 172.49 (COOH).

Synthesis of blank polyacrylamide nanoparticle ($\text{PAN}_{\text{blank}}$)²²⁹

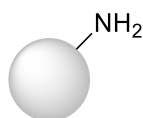
To stirred degassed hexane (42 mL) was added Brij L4 (3.08 g) and dioctyl sulfosuccinate sodium salt (1.59 g, 3.6 mmol). The mixture was allowed to stir under argon until complete dissolution of the surfactants. A solution of acrylamide (527 mg, 7.4 mmol) and N,N' -methylenebisacrylamide (160 mg, 1.04 mmol) in water (2 mL). 10% aqueous ice-cold ammonium persulfate (30 μL) was added to the reaction vessel, followed by N,N,N',N' -tetramethylethylenediamine (15 μL), and the reaction mixture allowed to stir at room temperature under argon for two hours. Excess hexane was evaporated in vacuo, and the resulting white viscous liquid was washed with ethanol and centrifuged (7 x 50 ml, 10 min, 4000 rpm). The solid was taken in ethanol and isolated by filtration through membrane (484 mg, 70%).

Zeta potential (mV): -8.3, PCS z_{ave} (nm): 41.

General procedure for the synthesis of mono-/dual-functionalised polyacrylamide nanoparticle (PAN)²²⁹

To stirred degassed hexane (42 mL) was added Brij L4 (3.08 g) and dioctyl sulfosuccinate sodium salt (1.59 g, 3.6 mmol). The mixture was allowed to stir under argon until complete dissolution of the surfactants. A solution of acrylamide (527 mg, 7.4 mmol), N,N' -methylenebisacrylamide (160 mg, 1.04 mmol), monomer 1 (and monomer 2) in water (2 mL). 10% aqueous ice-cold ammonium persulfate (30 μL) was added to the reaction vessel, followed by N,N,N',N' -tetramethylethylenediamine (15 μL), and the reaction mixture allowed to stir at room temperature under argon for two hours. Excess hexane was evaporated in vacuo, and the resulting white viscous liquid was washed with ethanol and centrifuged (7 x 50 ml, 5 min, 8000 rpm). The solid was taken in ethanol and isolated by filtration through membrane.

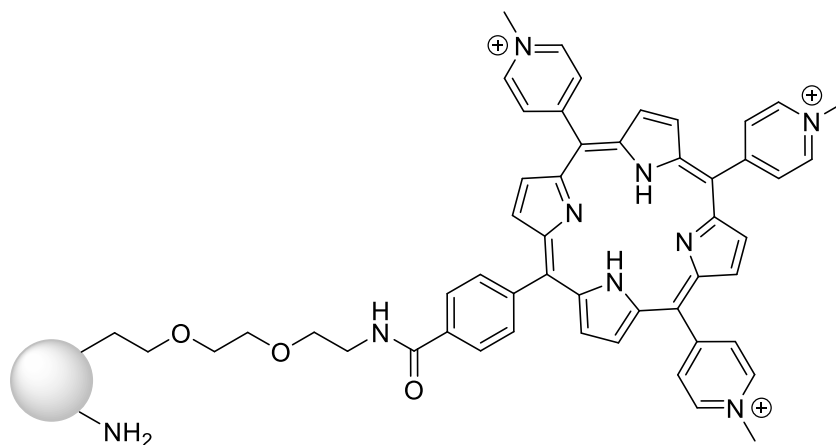
$\text{PAN-(amine}_{0.5})$



General procedure for PAN synthesis. Monomer 1: N -(3-Aminopropyl)methacrylamide hydrochloride (7 mg, 3.9×10^{-5} mol). White solid (435 mg).

Zeta potential (mV): -1.61. Intensity PCS z_{ave} (nm): 69.

PAN-(porphyrin_{monomer 1}-amine_{monomer 2})

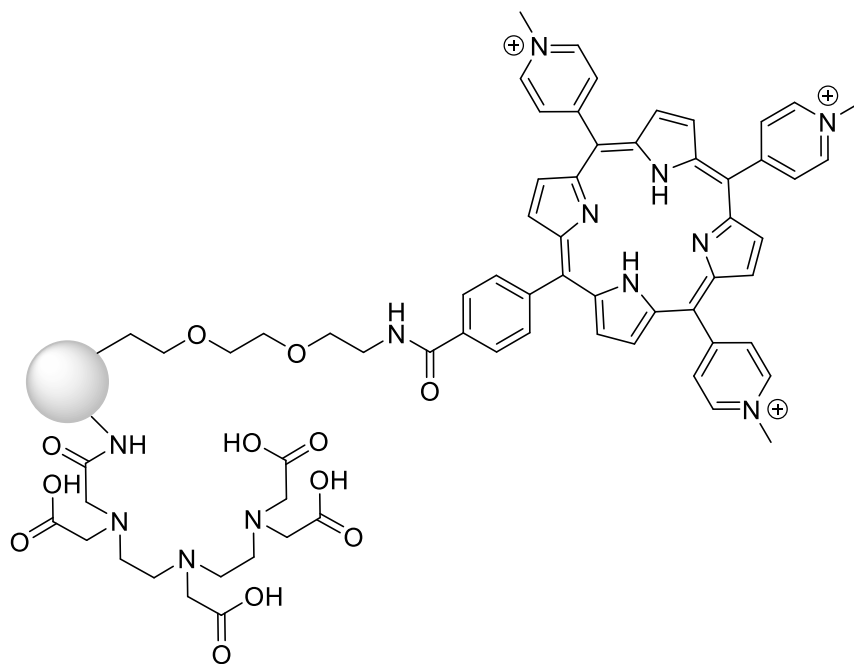


General procedure for PAN synthesis. Monomer 1: porphyrin **23**, monomer 2: APMA. Brown solid.

UV-vis [water, nm]: 428, 520, 556, 598, 660.

Monomer 1: Porphyrin 23	Monomer 2: APMA	Zeta potential/ mV	Intensity PCS/ nm	Number PCS/ nm	PDI	Porphyrin loading/ nmol per mg of PAN	Yield
1.6 mg, 1.6×10^{-6} mol, 0.02%	7 mg, 3.9×10^{-5} mol, 0.5%	+5.5±2.6	61±23	18±6	0.32±0.10	2.3	448 mg, 64%
4 mg, 4.0×10^{-6} mol, 0.05%	7 mg, 3.9×10^{-5} mol, 0.5%	+6.2±4.3	33±5	16±2	0.22±0.01	4.2	417 mg, 60%
4 mg, 4.0×10^{-6} mol, 0.05%	14 mg, 7.8×10^{-5} mol, 1%	+9.7	31	15.7	0.27	3.7	494 mg, 70%
4 mg, 4.0×10^{-6} mol, 0.05%	28 mg, 1.6×10^{-4} mol, 2%	+16	23	10.4	0.23	4.2	587 mg, 82%
40 mg, 4.0×10^{-5} mol, 0.5%	7 mg, 3.9×10^{-5} mol, 0.5%	+5.8±2.0	128±60	14±2	0.34±0.07	27	204 mg, 28%

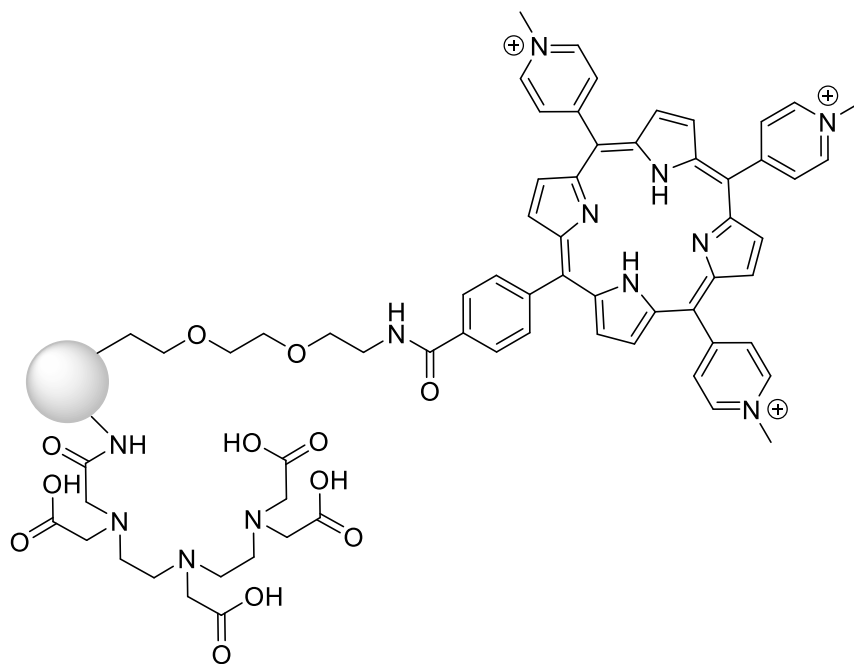
(DTPA_{0.5})-PAN-(porphyrin_{0.05})



PAN-(Porphyrin_{0.05}-amine_{0.5}) (50 mg) was dispersed in water (10 mL) and was added triethylamine (0.2 mL, 1.4 mmol) and DTPA-DA (150 mg, 0.42 mmol) at room temperature overnight. Ethanol was added to the reaction mixture and reaction mixture was acidified using 1 M HCl to promote precipitation. The product was isolated using filtration through membrane (47 mg, 94%).

Zeta potential (mV): -6.0 ± 8.0 . Intensity PCS z_{ave} (nm): 55 ± 17 , number PCS (nm): 14 ± 7 . PDI: 0.50 ± 0.07 . Porphyrin loading: 5.0 nmol per PAN mg.

(DTPA_{0.5})-PAN-(porphyrin_{0.5})

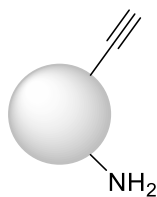


Method 1: **PAN-(Porphyrin_{0.5}-amine_{0.5})** (50 mg) was dispersed in water (10 mL) and was added triethylamine (0.2 mL). This solution was added quickly into a flask containing DTPA-DA **29** (150 mg, 0.42 mmol) at room temperature and stirred vigorously and left overnight. The reaction mixture was purified using gel filtration chromatography. Ethanol was added to promote precipitation, the precipitate centrifuged, and product isolated via microfiltration through membrane to yield a brown solid.

Method 2: **PAN-(Porphyrin_{0.5}-amine_{0.5})** (50 mg) was dispersed in saturated NaHCO₃. This solution was added quickly into a flask containing DTPA-DA **29** (150 mg, 0.42 mmol) at room temperature and stirred vigorously and left overnight. The reaction mixture was purified using gel filtration chromatography. Ethanol was added to promote precipitation, the precipitate centrifuged, and product isolated via microfiltration through membrane to yield a brown solid.

Method	Zeta potential (mV)	Intensity PCS (nm)	Number PCS (nm)	PDI	Porphyrin loading/ mol per mg of PAN	Yield
1	-5.4	54	14	0.47	49 nmol	41 mg, 82%
2	-1.8	220	19	0.57	21 nmol	36 mg, 72%

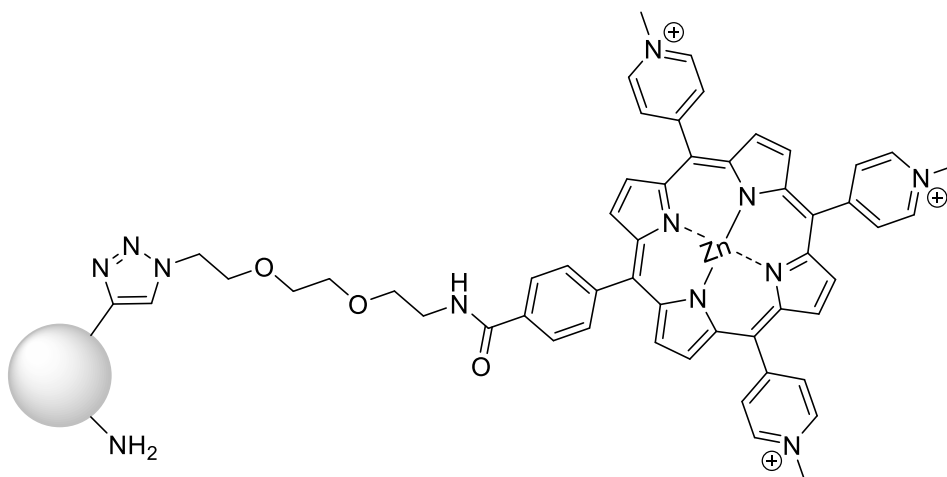
PAN-(amine_{1.0}-alkyne_{1.0})



General procedure for PAN synthesis. Monomer 1: *N*-(2-(2-(2-propynyloxy)ethoxy)ethyl)acrylamide (17 mg, 8.6×10^{-5} mol), monomer 2: *N*-(3-aminopropyl)methacrylamidex hydrochloride (14 mg, 8.6×10^{-5} mol). White solid (600 mg, 84%).

Zeta potential (mV): $+11 \pm 3$. Intensity PCS z_{ave} (nm): 36 ± 2 , number PCS (nm): 18 ± 1 . PDI: 0.22 ± 0.01 .

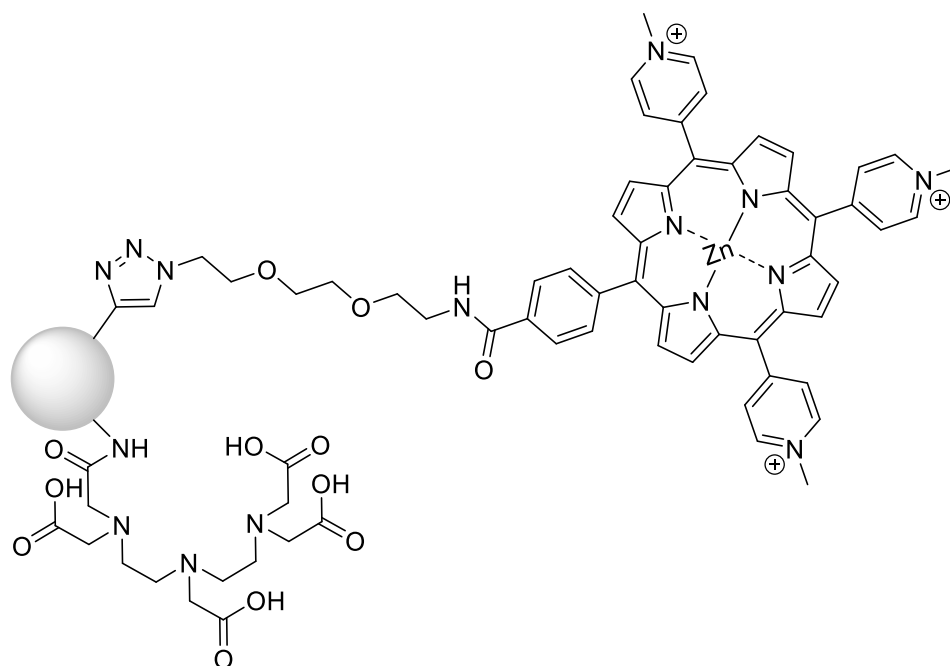
(Porphyrin_{1.0})-PAN-(amine_{1.0})



PAN-(amine_{1.0}-alkyne_{1.0}) (600 mg) was dispersed in water (30 mL) and was added porphyrin **28** (36 mg, 17.4×10^{-3} mmol), 10 mM aqueous CuSO_4 (1.5 mL, 15 mmol), and 100 mM aqueous sodium ascorbate (1.5 mL, 150 mmol). The resulting mixture was heated in a microwave reactor (50 °C, 4 hours, 75 W). The reaction mixture was precipitated from ethanol, centrifuged and the residue redissolved in water (10 mL). The reaction mixture was purified by gel filtration chromatography (Sephadex g-25 medium). The relevant fractions were combined and were precipitated with ethanol. The residue was collected via centrifugation and filtration to yield the product as a green solid (560 mg, 93%).

Zeta potential (mV): $+24 \pm 2$. Intensity PCS z_{ave} (nm): 46 ± 11 , number PCS (nm): 5 ± 1 . PDI: 0.43 ± 0.07 . UV-vis [water, nm]: 438, 564, 612. Porphyrin loading: 32 ± 2 nmol per PAN mg.

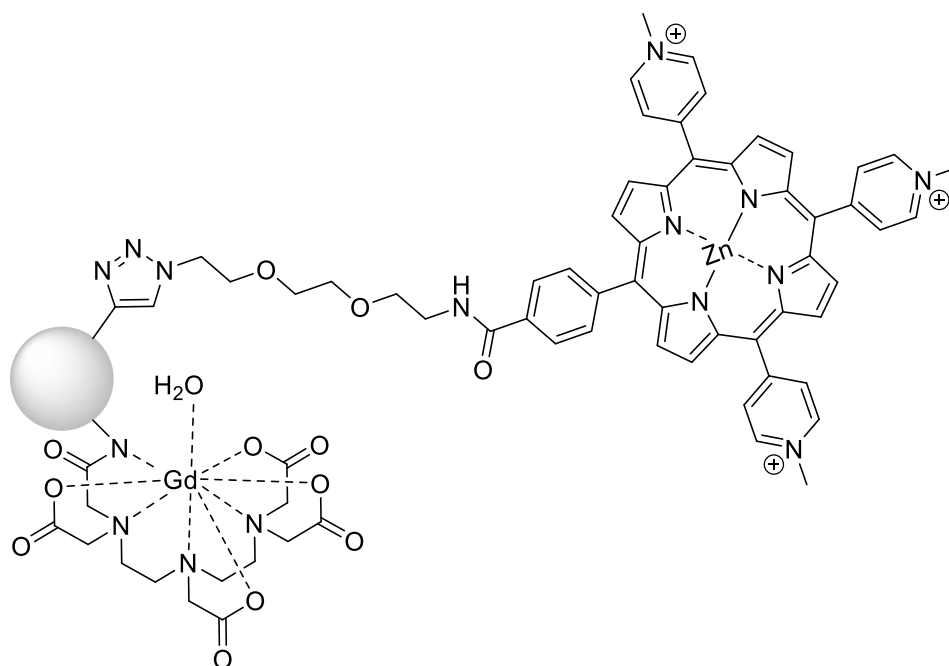
(Porphyrin_{1.0}-DTPA_{1.0})-PAN



(Porphyrin_{1.0})-PAN-(amine_{1.0}) (50 mg) was dispersed in saturated sodium bicarbonate (5 mL) and was quickly added into a flask containing DTPA-DA **29** (150 mg, 0.42 mmol). The reaction mixture was stirred vigorously and was allowed to proceed at room temperature overnight. The reaction mixture was purified by gel filtration chromatography (Sephadex g-25 medium). The filtrate was combined and precipitated with ethanol. The residue was collected via centrifugation and filtration to yield the product as a green solid (43 mg, 86%).

Zeta potential (mV): +12±3. Intensity PCS z_{ave} (nm): 95±29, number PCS (nm): 50±36. PDI: 0.21±0.05. UV-vis [water, nm]: 440, 566, 614. Porphyrin loading: 30±7 nmol per PAN mg.

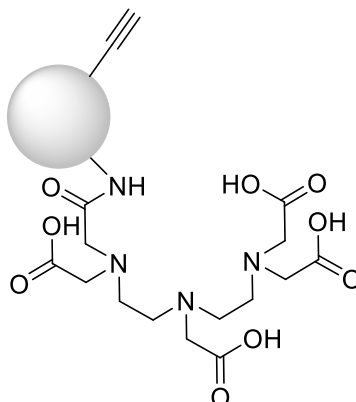
(Porphyrin_{1.0}-[Gd(DTPA)]_{1.0})-PAN



(Porphyrin_{1.0}-DTPA_{1.0})-PAN (200 mg) was dispersed in sodium acetate buffer (20 mL, pH 4.5, 0.1 M) and Gd (III) nitrate hexahydrate (40 mg, 0.088 mmol) was added. The reaction mixture was allowed to proceed at room temperature overnight. The reaction mixture was purified using gel filtration chromatography (Sephadex g-25 medium). The filtrate was co-evaporated with ethanol under reduced pressure. The residue was redispersed in ethanol (5 mL) and isolated via microfiltration through a membrane to yield the product as a green solid (168 mg, 84%).

Zeta potential (mV): +31±3. Intensity PCS z_{ave} (nm): 52±8, number PCS (nm): 5±1. PDI: 0.48±0.07 UV-vis [water, nm]: 440, 565, 610. Porphyrin loading: 31±7 nmol per PAN mg. Gd³⁺ loading: 37±3 nmol per PAN mg.

(DTPA_{1.0})-PAN-(alkyne_{1.0})

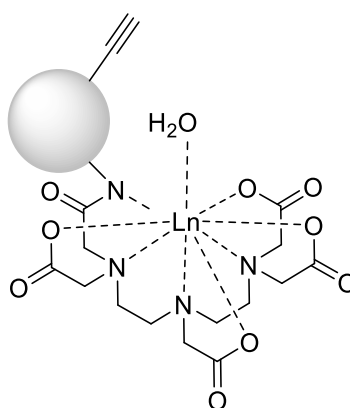


PAN-(amine_{1.0}-alkyne_{1.0}) (50 mg×6) was dispersed in 5 mL sat. sodium bicarbonate and was added quickly into a flask containing DTPA-DA (150 mg, 0.42 mmol) and stirred vigorously.

The reaction mixture was allowed to proceed at room temperature overnight. The reaction mixture was purified by gel filtration chromatography (sephadex g-25 medium). The filtrate is combined, co-evaporated with ethanol and precipitated with more ethanol and isolated via microfiltration through membrane to yield a white solid (298 mg, 99%).

Zeta potential (mV): -29. Intensity PCS z_{ave} (nm): 41, number PCS (nm): 24. PDI: 0.14.

[Ln(DTPA)]_{1.0}-PAN-(alkyne_{1.0})



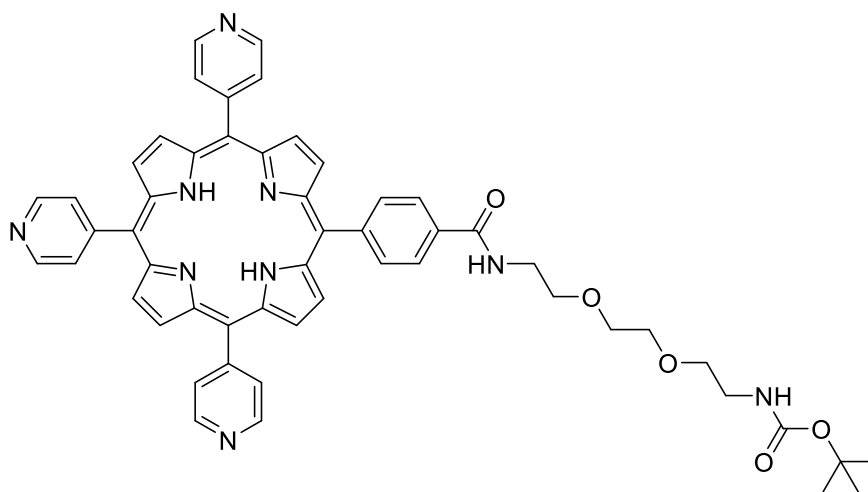
Ln = Eu, Tb

Method 1: **(DTPA_{1.0})-PAN-(alkyne_{1.0})** (50 mg) was dispersed in acetate buffer (pH 4.5, 0.1 M, 5 mL) and was added EuCl₃.6H₂O/ TbCl₃.6H₂O (50 mg, 0.14/0.13 mmol). The reaction mixture was allowed to proceed at room temperature overnight. The reaction mixture was purified by gel filtration chromatography (sephadex g-25 medium). The filtrate is combined, co-evaporated with ethanol and precipitated with more ethanol, centrifuged, and dried under vacuum at 40 °C.

Method 2: **(DTPA_{1.0})-PAN-(alkyne_{1.0})** (50 mg) was dispersed in water (4 mL) and was added EuCl₃.6H₂O (50 mg, 0.14 mmol). The reaction mixture was adjusted to pH 4-5 using 1 M HCl and 1 M NaOH. The reaction mixture was allowed to proceed at room temperature overnight. The reaction mixture was purified by gel filtration chromatography (sephadex g-25 medium). The filtrate is combined, co-evaporated with ethanol and precipitated with more ethanol, centrifuged, and dried under vacuum at 40 °C.

7.10 Synthesis described in Chapter 4

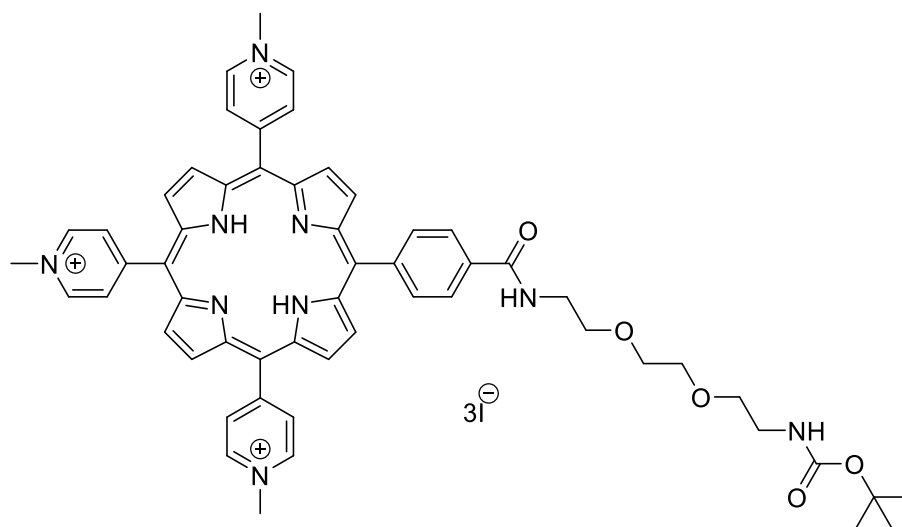
5-[4-(2-(2-(2-*N*-Boc-aminoethoxy)ethoxy)ethaneaminocarbonyl)phenyl]-10,15,20-tris-(4-pyridyl)porphyrin **30**²⁴⁷



To a stirred solution of porphyrin **5** (300 mg, 0.454 mmol) in DMF (30 mL) was added EDC (174 mg, 0.907 mmol), HOBt (123 mg, 0.907 mmol), *N*-Boc-2,2'-(ethylenedioxy)-diethylamine **19** (225 mg, 0.907 mmol), and DMAP (111 mg, 0.907 mmol). The reaction mixture was allowed to stirred overnight at room temperature. Solvent was co-evaporated with toluene under reduced pressure. The crude was redissolved in DCM and washed with brine (3×50 mL). The organic layer was dried (MgSO₄), and the solvent removed under reduced pressure. The crude was purified using column chromatography (silica, 95:5 DCM:MeOH). The crude was precipitated from hexane over DCM to yield the product as a purple solid (361 mg, 0.405 mmol, 89%).

¹H NMR (400 MHz, CDCl₃) δ -2.91 (s, 2H, NH), 1.39 (s, 9H, C(CH₃)₃), 3.35 (m, 2H, CH₂ peg), 3.61 (m, 2H, CH₂ peg), 3.74 (m, 4H, CH₂ peg), 3.85 (m, 4H, CH₂ peg), 8.15 (m, 6H, o-Py), 8.22 (d, J = 7.9 Hz, 2H, o-Ph), 8.28 (d, J = 7.7 Hz, 2H, m-Ph), 8.85 (q, J = 4.7 Hz, 8H, βH), 9.04 (m, 6H, m-Py). ¹³C NMR (100 MHz, CDCl₃) δ 28.49 (C(CH₃)₃), 40.14, 40.44, 70.41, 117.68, 125.74, 129.44 (C-β), 131.23, 134.70, 148.49 (C-β), 149.98. MS: (ESI) m/z 892 [M+H]⁺, HRMS: calcd. for C₅₃H₅₀N₉O₅ 892.3929 found 892.3933. UV-vis (CH₂Cl₂, nm): 417, 513, 549, 588, 643.

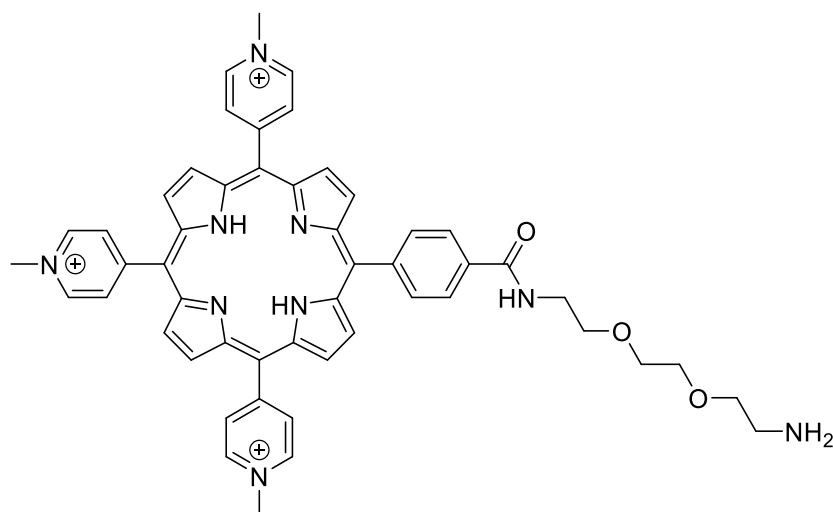
5-[4-(2-(2-(2-*N*-Boc-aminoethoxy)ethoxy)ethaneaminocarbonyl)phenyl]-10,15,20-tris-(*N*-methyl-4-pyridinium)porphyrin triiodide **31²⁴⁷**



To a stirred solution of porphyrin **30** (350 mg, 0.393 mmol) in DMF (35 mL) was added methyl iodide (4 mL, 0.064 mol) *via* a syringe. The reaction mixture was heated to 40 °C and was allowed to proceed overnight. The reaction mixture was allowed to cool to room temperature, diethyl ether added to promote precipitation, and the precipitate was filtered through cotton wool. The residue was redissolved in MeOH and diethyl ether was added. Precipitate formed was filtered and collected to yield the product as a purple solid (426 mg, 0.323 mmol, 82%).

¹H NMR (400 MHz, DMSO-*d*₆) δ -3.07 (s, 2H, NH), 3.07 (m, 2H, CH₂ peg), 3.40 (m, 2H, CH₂ peg), 3.60 (m, 8H, CH₂ peg), 4.69 (s, 9H, N-CH₃), 8.32 (m, 4H, o,m-Ph), 9.01 (m, 14H, βH, o-Py), 9.45 (m, 6H, m-Py). ¹³C NMR (100 MHz, DMSO-*d*₆) δ 28.77 (C(CH₃)₃), 48.45 (N-CH₃), 69.57, 69.76, 70.10, 70.18, 78.16, 115.29, 115.93, 122.39, 126.62, 132.64 (C-β), 134.74, 143.59, 144.72 (C-β), 156.16, 157.04, 166.61. MS: (ESI) *m/z* 312 [M-3I]³⁺, HRMS: calcd. for C₅₆H₅₈N₉O₅ 312.1515 found 312.1518. UV-vis (H₂O, nm): 422, 519, 560, 585, 656. ε (422 nm) = 207367 M cm⁻¹.

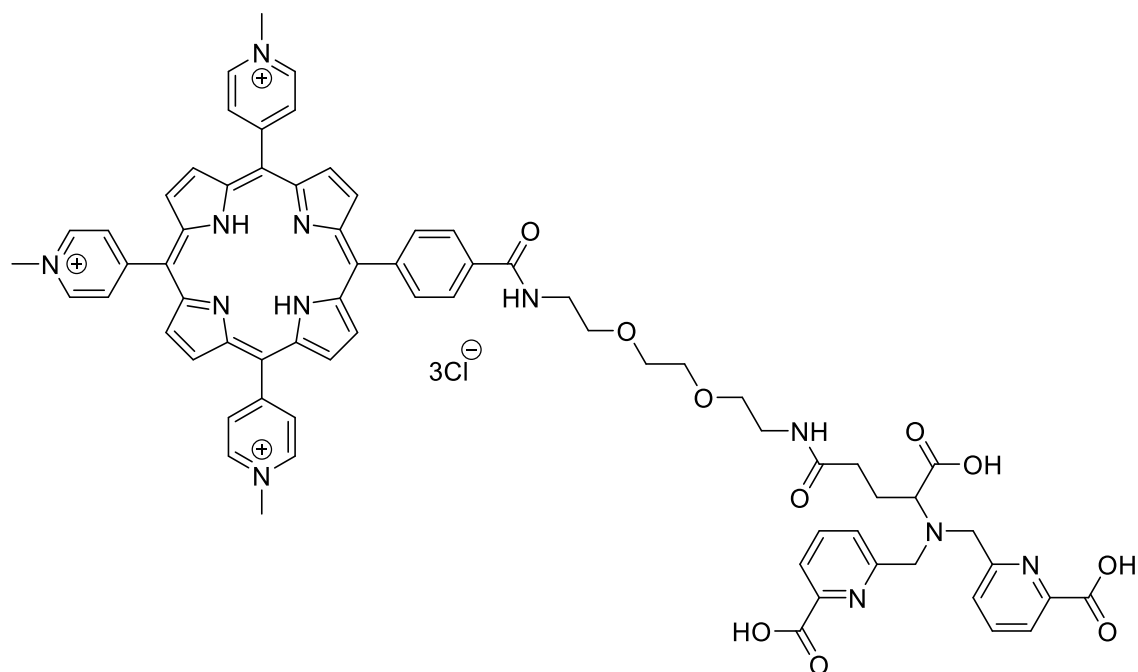
5-[4-(2-(2-(2-aminoethoxy)ethoxy)ethaneaminocarbonyl)phenyl]-10,15,20-tris-(*N*-methyl-4-pyridinium)porphyrin **32²⁴⁷**



Porphyrin **31** (100 mg, 0.076 mmol) was added dry DCM (5 mL) and TFA (190 μ L, 283 mg, 2.48 mmol). The reaction mixture was allowed to stir at room temperature for 3 hours. The solvent was removed under reduced pressure to give the product as a purple solid. The product formed was immediately redissolved in dry DMF and was used for subsequent reaction (70 mg, 0.074 mmol, 98%).

HPLC: gradient 1 R_f = 8.12 min, gradient 2 R_f = 31.6 min. ^1H NMR (400 MHz, $\text{DMSO-}d_6$) δ - 3.07 (s, 2H, NH), 2.95 (t, J = 5.3 Hz, 2H, CH_2 peg), 3.63 (m, 10H, CH_2 peg), 4.72 (s, 9H, N- CH_3), 8.29 (d, J = 8.2 Hz, 2H, o-Ph), 8.38 (d, J = 8.2 Hz, 2H, m-Ph), 9.02 (m, 14H, β H, m-Py), 9.53 (m, 6H, o-Py). ^{13}C NMR (100 MHz, $\text{DMSO-}d_6$) δ 38.98, 48.33 (N- CH_3), 67.19, 69.51, 70.06, 70.29, 115.32, 115.96, 122.39, 126.70, 131.56, 132.64 (C- β), 134.72, 143.58, 144.78 (C- β), 146.07, 156.93, 157.00, 166.61. MS: (ESI) m/z 278 [M-3Cl] $^{3+}$, HRMS: calcd. for $\text{C}_{51}\text{H}_{50}\text{N}_9\text{O}_3$ 278.8007 found 278.8008. UV-vis (H_2O , nm): 422, 518, 558, 585, 656. ϵ (422 nm) = 200671 M cm^{-1} .

Porphyrin-H₃Dpaa conjugate **33**²⁴⁷



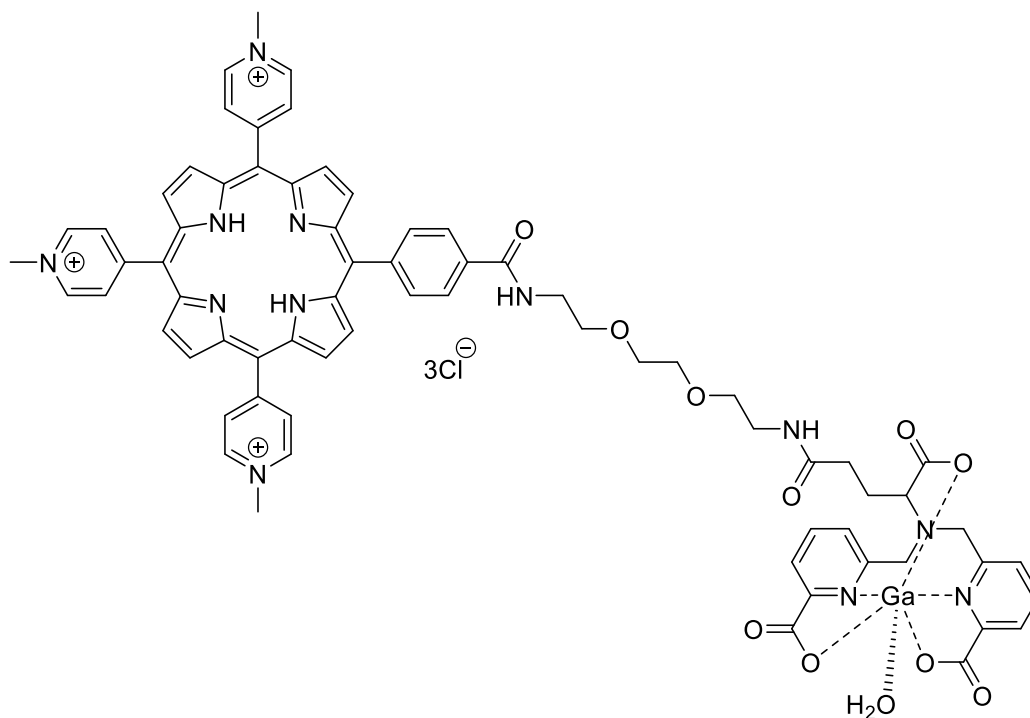
To H₄Dpaa.ga (79 mg, 0.19 mmol) was added acetic anhydride (29 mg, 27 μ L, 0.29 mmol), dry pyridine (45 mg, 46 μ L, 0.57 mmol), and dry acetonitrile (500 μ L). The reaction mixture was allowed to proceed at room temperature for 30 mins. Dry diethyl ether (1 mL) was added dropwise to promote precipitation. The resulting suspension was filtered through celite and washed with dry diethyl ether (1 mL). H₂Dpaa-anhydride was eluted from celite using dry DMF (1 mL) and was collected in the reaction flask. To this solution was added dry TEA (57 mg, 79 μ L, 0.57 mmol) and *N*-hydroxysuccinimide (75 mg, 0.65 mmol). The reaction mixture was allowed to proceed at room temperature for 2 hours to give H₃Dpaa-NHS. The product was not isolated, and the reaction mixture was used immediately for subsequent reaction.

To a stirred solution of porphyrin **32** (32 mg, 0.038 mmol) in dry DMF (2 mL) was added TEA (57 mg, 79 μ L, 0.57 mmol) and H₃Dpaa-NHS reaction mixture above. The reaction mixture was allowed to proceed at room temperature overnight. The solvent was co-evaporated with toluene under reduced pressure. The crude was redissolved in water, was added ammonium hexafluorophosphate, and the precipitate isolated via filtration. The residue collected was redissolved in acetone, was added tetrabutylammonium chloride, and the precipitate isolated via filtration. The residue was precipitate from diethyl ether over MeOH to yield the product as a clay red solid (42 mg, 0.031 mmol, 82%).

HPLC: gradient 1 R_f = 8.57 min, gradient 2 R_f = 43.3 min. ¹H NMR (400 MHz, DMSO-*d*₆) δ - 3.10 (s, 2H, NH), 1.86 (m, 2H, O=C-CH₂CH₂ α CH), 2.28 (m, 2H, O=C-CH₂CH₂ α CH), 3.50 (m, 13H, CH₂_{peg}, α C-H), 3.83 (m, 4H, Py-CH₂-N), 4.72 (s, 9H, N-CH₃), 7.44 (d, J = 7.1 Hz, 2H, dpaa-Py), 7.63 (dq, J = 17.6, 7.7 Hz, 4H, dpaa-Py), 8.26 (d, J = 7.8 Hz, 2H, o-Ph), 8.36 (d, J = 7.8 Hz, 2H, m-Ph), 9.05 (m, 14H, β H, porphyrin-o-Py), 9.52 (s, 6H, porphyrin-m-Py). ¹³C NMR (100

MHz, DMSO-*d*₆) δ 1.44, 15.71, 23.81, 25.77, 32.41, 48.32, 56.62, 57.07, 63.02, 65.45, 69.50, 69.65, 69.99, 70.11, 70.22, 123.12, 125.68, 126.67, 132.66, 134.83, 137.81, 144.81, 149.23, 157.01, 159.98, 166.58, 166.93, 167.10, 172.20, 172.37, 174.50, 174.83. MS: (ESI) *m/z* 411 [M-3Cl]³⁺, HRMS: calcd. for C₇₀H₆₇N₁₂O₁₀ 411.8362 found 411.8362. UV-vis (H₂O, nm): 426, 520, 561, 589, 643. ε (424 nm) = 216288 M cm⁻¹.

Porphyrin-[^{nat}Ga(Dpaa)] complex [^{nat}Ga]-34²⁴⁷

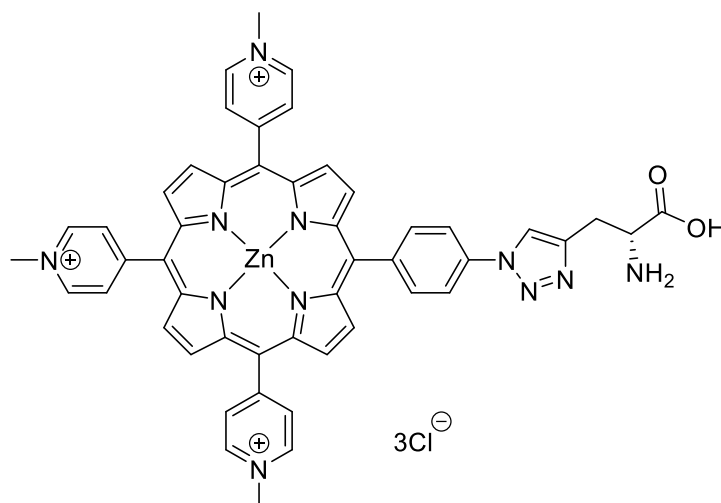


To porphyrin-H₃Dpaa conjugate **33** (25 mg, 18.7 μmol) was added a solution of GaCl₃ (550 μL, 51 mM, 28.1 μmol) in acetate buffer (1 mL, 0.1 M, pH 4.5). The reaction was allowed to proceed at room temperature overnight. NH₄PF₆ was added to the reaction mixture, and the precipitate isolated via filtration. The residue collected was redissolved in acetone, was added tetrabutylammonium chloride, and the precipitate isolated via filtration. The residue was precipitate from diethyl ether over MeOH to yield the product as a purple solid (19 mg, 13.3 μmol, 71%).

HPLC: gradient 1 *R_f* = 8.4 min, gradient 2 *R_f* = 36.6 min. ¹H NMR (400 MHz, DMSO-*d*₆) δ -3.09 (s, 2H, NH), 1.96 (m, 4H, O=C-CH₂CH₂αCH), 3.07 (m, 3H, CH₂PEG, αC-H), 3.60 (m, 12H, CH₂PEG, Py-CH₂-N), 4.71 (s, 9H, N-CH₃), 7.86 (m, 6H, Dpaa-Py), 8.30 (m, 4H, o,m-Ph), 9.04 (m, 14H, βH, porphyrin-o-Py), 9.50 (s, 6H, porphyrin-m-Py). ¹³C NMR (100 MHz, DMSO-*d*₆) δ 15.71, 48.42, 65.46, 69.50, 69.67, 70.13, 70.23, 115.23, 115.98, 122.32, 126.58, 132.65 (βC), 134.69, 144.78 (βC), 144.91, 151.80, 156.84, 157.03, 166.61, 172.34. MS: (ESI) *m/z* 650 [M-3Cl-H]²⁺, HRMS calcd. for C₇₀H₆₃GaN₁₂O₁₀ 650.2017 found 650.2013. UV-vis (H₂O, nm): 424, 519, 557, 588, 642. ε (424 nm) = 195424 M cm⁻¹.

7.11 Synthesis described in Chapter 5

Porphyrin-Gly conjugate 35



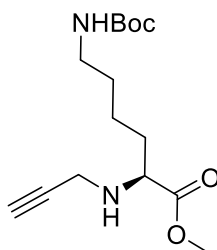
Porphyrin **11** (30 mg, 34 μmol) and D-propargylglycine (7 mg, 62 μmol) were dissolved in a mixture of t-butanol:water (1:1, 20 mL) and was added a solution of copper(II) sulphate (500 μL , 10 mM), followed by a solution of sodium ascorbate (500 μL , 100 mM). To the resulting solution was added tris[(1-benzyl-1H-1,2,3-triazol-4-yl)methyl]amine (TBTA) (1 mg). The reaction mixture was heated in a microwave reactor (20 mins, 75 W, 50 $^{\circ}\text{C}$). The reaction was concentrated under reduced pressure, was diluted with water, was added ammonium hexafluorophosphate, and the precipitate isolated via filtration. The residue collected was redissolved in acetone, was added tetrabutylammonium chloride, and the precipitate isolated via filtration. The crude was precipitated from diethyl ether over MeOH to yield the product as a purple-green solid (32 mg, 32 μmol , 84%).

HPLC: gradient 4 $R_f = 7.5$ min. ^1H NMR (400 MHz, $\text{DMSO-}d_6$) δ 3.12 (s, 2H, $\alpha\text{-CH}_2$), 4.68 (s, 9H, N- CH_3), 7.85 (m, 4H, Ph), 8.33 (s, 1H), 8.90 (m, 14H, βH , o-Py), 9.42 (s, 6H, m-Py). ^{13}C NMR (100 MHz, $\text{DMSO-}d_6$) δ 48.16 (N- CH_3), 115.19, 115.96, 118.17, 122.68, 132.01, 132.50, 132.65 (βC), 132.77, 133.60, 136.05, 139.41, 144.14 (βC), 148.38, 148.66, 148.85, 150.71, 159.05. MS: (ESI) m/z 293 $[\text{M}-3\text{Cl}]^{3+}$, HRMS: calcd. for $\text{C}_{49}\text{H}_{40}\text{N}_{11}\text{O}_2\text{Zn}$ 292.7547, found 292.7547. UV-vis (DMSO , nm): 436, 564, 610, ϵ (436 nm) = 189665 $\text{M}^{-1} \text{cm}^{-1}$.

white powder was then slurried in ethanol (3 mL) to remove unreacted NEt₃. Filtration and drying in vacuo yielded the product as a white powder (315 mg, 0.410 mmol, 84%).

Elemental analysis calcd. (%) for C₁₉H₄₀Br₃N₂O₃Re C, 29.62; H, 5.23; N, 3.64 found (%) C, 29.86; H, 5.17; N, 3.66.

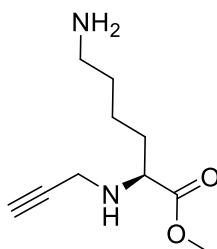
***N*(α)-propargyl-*N*(ϵ)-Boc-Lys(OMe) **38**³⁰²**



To a stir solution of *N*(ϵ)-Boc-Lys(OMe).HCl (1 g, 3.36 mmol) in DMF (30 mL) was added with potassium carbonate (953 mg, 6.89 mmol). The mixture was stirred under argon for 5 minutes. To the resulting solution was added propargyl bromide in toluene (80% wt., 599 μ L, 5.38 mmol). The reaction mixture was stirred for 48 h at room temperature. The solution was filtered, and excess solvent was removed under reduced pressure. The crude was purified using column chromatography (silica, 99:1 DCM:MeOH) to yield the product as a yellow oil (724 mg, 2.43 mmol, 72%).

¹H NMR (400 MHz, CDCl₃) δ 1.42 (m, 13H, C(CH₃)₃, CH₂CH₂), 1.75 (m, 2H, CH₂), 2.25 (m, 1H, CCH), 3.10 (m, 2H, CH₂), 3.52 (m, 2H, CH₂), 3.74 (s, 3H, CH₃), 4.57 (s, 1H, α -CH). ¹³C NMR (100 MHz, CDCl₃) δ 22.85, 28.50 (C(CH₃)₃), 29.84, 32.63, 36.90, 40.33, 52.06, 59.76, 72.34, 79.18, 156.03 (C=O). MS: (ESI) *m/z* 299.2 [M+H]⁺, HRMS: calcd. for C₁₅H₂₇N₂O₄ 299.1965 found 299.1969.

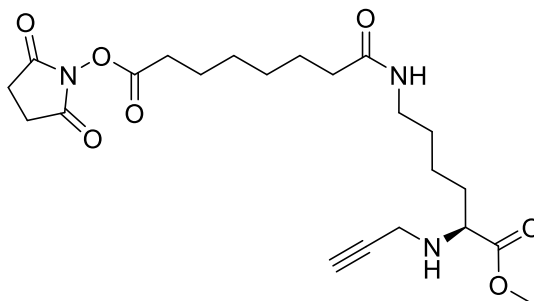
N*(α)-propargyl-Lys(OMe) **39*



38 (120 mg, 0.402 mmol) was taken up in 1 mL DCM and was added 1 mL TFA. The reaction mixture was allowed to proceed for 2 hours and solvent was removed under reduced pressure, triturated with diethyl ether and was dried further under reduced pressure to yield the product as a yellow oil (75 mg, 0.379 mmol, 95%).

^1H NMR (400 MHz, $\text{DMSO-}d_6$) δ 1.52 (m, 6H, CH_2), 2.73 (m, 2H, CH_2), 3.69 (s, 1H, $\alpha\text{-CH}$), 3.73 (s, 3H, CH_3), 3.89 (s, 2H, CH_2), 3.97 (m, 1H, CCH). ^{13}C NMR (100 MHz, $\text{DMSO-}d_6$) δ 15.70, 21.83, 27.04, 28.99, 35.45, 38.91, 53.53, 58.47, 65.45, 158.88. MS: (ESI) m/z 199.4 $[\text{M}+\text{H}]^+$.

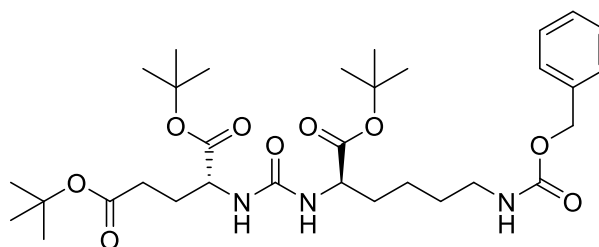
***N*(α)-propargyl-*N*(ϵ)-NHS-SA-Lys(OMe) 40**



Disuccinimidyl suberate (500 mg, 1.36 mmol) was taken up in dry DMF (3 mL), was added TEA (191 μL , 1.36 mmol) and a solution of **39** (128 mg, 0.65 mmol) in DMF (3 mL) dropwise. The reaction mixture was allowed to proceed at room temperature under inert atmosphere overnight. Solvent was removed under reduced pressure. The crude was purified using column chromatography (silica, 96:4 DCM:MeOH) to yield the product as a yellow oil (258 mg, 0.57 mmol, 88%).

^1H NMR (400 MHz, CDCl_3) δ 1.34 (m, 6H, CH_2), 1.46 (m, 2H, CH_2), 1.58 (m, 2H, CH_2), 1.69 (m, 4H, CH_2), 2.14 (t, $J = 7.5$ Hz, 2H, O=CCH_2), 2.25 (t, $J = 2.4$ Hz, 1H, $\text{C}\equiv\text{CH}$), 2.55 (t, $J = 7.3$ Hz, 2H, O=CCH_2), 2.80 (s, 4H, $\text{O=CCH}_2\text{CH}_2\text{C=O}$), 3.18 (m, 2H, $\epsilon\text{-CH}_2\text{NH}$), 3.47 (m, 3H, $\text{HC}\equiv\text{CCH}_2$, $\alpha\text{-CH}$), 3.69 (s, 3H, O-CH_3). ^{13}C NMR (100 MHz, CDCl_3) δ 22.52, 24.43, 25.39, 25.69 ($\text{O=CCH}_2\text{CH}_2\text{C=O}$), 28.13, 28.40, 28.93, 30.95, 31.78, 36.22, 36.52, 39.04 ($\epsilon\text{-CH}_2\text{NH}$), 52.35 (O-CH_3), 59.16 (αCH), 73.37 ($\text{C}\equiv\text{CH}$), 79.42 ($\text{C}\equiv\text{CH}$), 168.76 (C=O), 169.59 (C=O), 173.07 (C=O), 173.73 (C=O), 174.06 (C=O). MS: (ESI) m/z 452.2 $[\text{M}+\text{H}]^+$, HRMS: calcd. for $\text{C}_{22}\text{H}_{34}\text{N}_3\text{O}_7$ 452.2391 found 452.2389.

***Glu*(OtBu)₂-urea-*N*(ϵ)-Cbz-(OtBu)Lys **41**²⁹⁸**

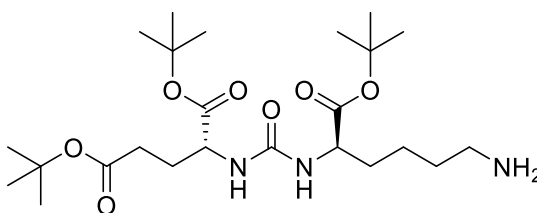


Triphosgene (0.83 g, 2.8 mmol) was dissolved in anhydrous dichloromethane (10 mL) and cooled to 0 °C. A mixture of L-glutamic acid di-*tert*-butyl ester hydrochloride (2.24 g, 7.6 mmol), triethylamine (2.1 mL, 15.2 mmol) and anhydrous dichloromethane (30 mL) was added dropwise during 1 hours at 0 °C, and was allowed to stir for a further 1 hour. A solution of *N*(ϵ)-

benzyloxycarbonyl-L-lysine-*tert*-butyl ester hydrochloride (2.82 g, 7.6 mmol), triethylamine (2.1 mL, 15.2 mmol), and anhydrous dichloromethane (25 mL) was added in one portion and the reaction mixture was allowed to stir at room temperature for 1 hour. The solution was evaporated under reduced pressure and ethyl acetate (50 mL) was added. The organic phase was washed with 2 M NaHSO₄ (2 x 50 mL), brine (40 mL), and dried over magnesium sulphate. The solvent was removed under reduced pressure to give a colourless oil. The crude was purified using column chromatography (silica, 7:3 hexane:ethyl acetate) to yield the product as a waxy white solid (1.6 g, 2.6 mmol, 34%).

¹H NMR (400 MHz, CDCl₃) δ 1.24 (m, 3H), 1.39 (m, 27H, C(CH₃)₃), 1.65 (m, 4H), 1.99 (m, 1H), 2.21 (m, 2H), 3.11 (m, 2H, Lys-εCH₂), 4.31 (d, *J* = 25.0 Hz, 2H, αCH-NH-CO-NH-αCH), 5.05 (q, *J* = 12.4 Hz, 2H, Ph-CH₂), 7.28 (m, 5H, C₆H₅). ¹³C NMR (100 MHz, CDCl₃) δ 22.48, 28.06 (C(CH₃)₃), 28.12 (C(CH₃)₃), 28.38, 29.40, 31.63, 32.67, 40.78 (Lys-εCH₂), 52.88 (αCH-NH-CO-NH-αCH), 53.34 (αCH-NH-CO-NH-αCH), 66.50 (Ph-CH₂), 80.51, 81.61, 82.23, 128.01 (Ph-C), 128.07 (Ph-C), 128.49 (Ph-C), 136.83 (Ph-C), 156.77 (C=O), 157.28 (C=O), 172.40 (C=O), 172.67 (C=O), 173.07 (C=O). MS: (ESI) *m/z* 623.3 [M+H]⁺.

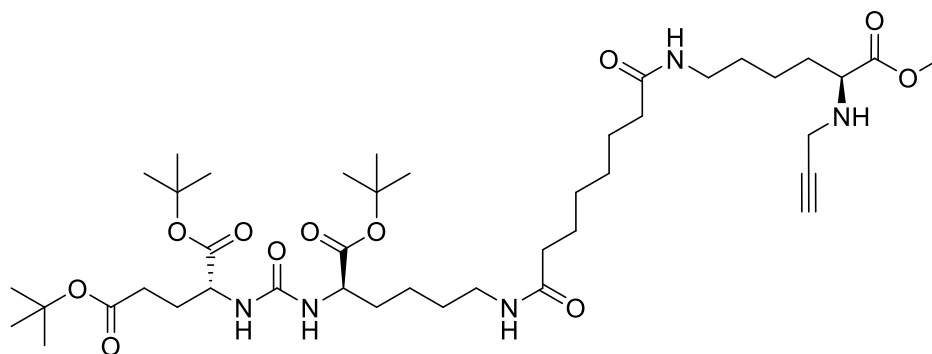
Glu(OtBu)₂-urea-(OtBu)Lys 42



41 (610 mg, 0.98 mmol) was dissolved in MeOH (10 mL) and was added Pd on C (50 mg), and hydrazine monohydrate (500 μL, 10 mmol). The reaction mixture was allowed to proceed at room temperature for overnight under argon. Reaction was analysed using mass spectrometry. The reaction mixture was filtered through celite and washed with MeOH. The volatile part was removed under reduced pressure, with co-evaporation with DCM (3x50 mL) and diethyl ether (3x50 mL). The crude was dried under high vacuum to yield the product as a transparent oil (425 mg, 0.87 mmol, 89%).

¹H NMR (400 MHz, CDCl₃) δ 1.05 (m, 3H), 1.24 (d, *J* = 11.3 Hz, 27H, C(CH₃)₃), 1.54 (m, 4H), 1.86 (m, 1H), 2.11 (m, 2H), 2.50 (t, *J* = 6.6 Hz, 2H), 4.17 (m, 2H, αCH-NH-CO-NH-αCH), 5.75 (s, 2H, αCH-NH-CO-NH-αCH). ¹³C NMR (100 MHz, CDCl₃) δ 22.37, 27.93 (C(CH₃)₃), 27.97 (C(CH₃)₃), 28.39, 31.54, 32.60, 32.71, 41.42 (Lys-εCH₂), 52.74 (αCH-NH-CO-NH-αCH), 53.31 (αCH-NH-CO-NH-αCH), 80.19, 81.22, 81.58, 157.36 (C=O), 172.27 (C=O), 172.51 (C=O), 172.77 (C=O). MS: (ESI) *m/z* 488.7 [M+H]⁺.

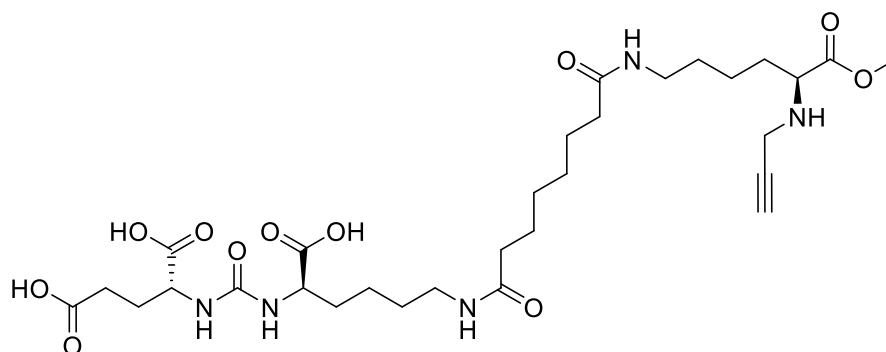
Glu(OtBu)₂-urea-(OtBu)Lys-SA-N(α)-propargyl-Lys(OMe) **43**



To a solution of **42** (158 mg, 0.35 mmol) in DMF (1 mL) was added TEA (115 μ L, 0.8 mmol) and **40** (85 mg, 0.175 mmol) in DMF (4 mL). The reaction mixture was allowed to proceed at room temperature overnight. Solvent was removed under reduced pressure. The crude was purified using column chromatography (97:3-95:5 DCM:MeOH), to yield the product as a transparent oil (90 mg, 0.109 mmol, 62%).

¹H NMR (400 MHz, CDCl₃) δ 1.26 (m, 8H), 1.37 (m, 27H, C(CH₃)₃), 1.55 (m, 13H), 2.16 (m, 8H, C \equiv CH), 3.14 (m, 4H, Glu-urea-Lys- ϵ -CH₂, Lys- ϵ -CH₂), 3.38 (m, 3H, Lys- α CH, HC \equiv CCH₂), 3.66 (s, 3H, O-CH₃), 4.21 (m, 2H, α CH-NH-CO-NH- α CH), 5.76 (d, J = 8.0 Hz, 1H, α CH-NH-CO-NH- α CH), 5.87 (d, J = 8.2 Hz, 1H, α CH-NH-CO-NH- α CH), 6.33 (t, J = 5.6 Hz, 1H, NH-linker-NH), 6.70 (t, J = 5.5 Hz, 1H, NH-linker-NH). ¹³C NMR (100 MHz, CDCl₃) δ 22.65, 22.79, 25.54, 25.62, 28.05 (C(CH₃)₃), 28.11 (C(CH₃)₃), 28.24, 28.64, 28.72, 28.84, 29.16, 29.73, 31.70, 32.39, 32.48, 36.35, 36.48, 36.76, 39.02, 39.11, 52.12 (O-CH₃), 53.00 (α CH-NH-CO-NH- α CH), 53.39 (α CH-NH-CO-NH- α CH), 59.53 (Lys- α CH), 72.50 (C \equiv CH), 80.61 (C \equiv CH), 81.52, 82.07, 157.60, 172.40 (C=O), 172.59 (C=O), 172.80 (C=O), 172.91 (C=O), 173.74 (C=O), 173.99 (C=O), 174.71 (C=O). MS: (ESI) m/z 825.2 [M+H]⁺.

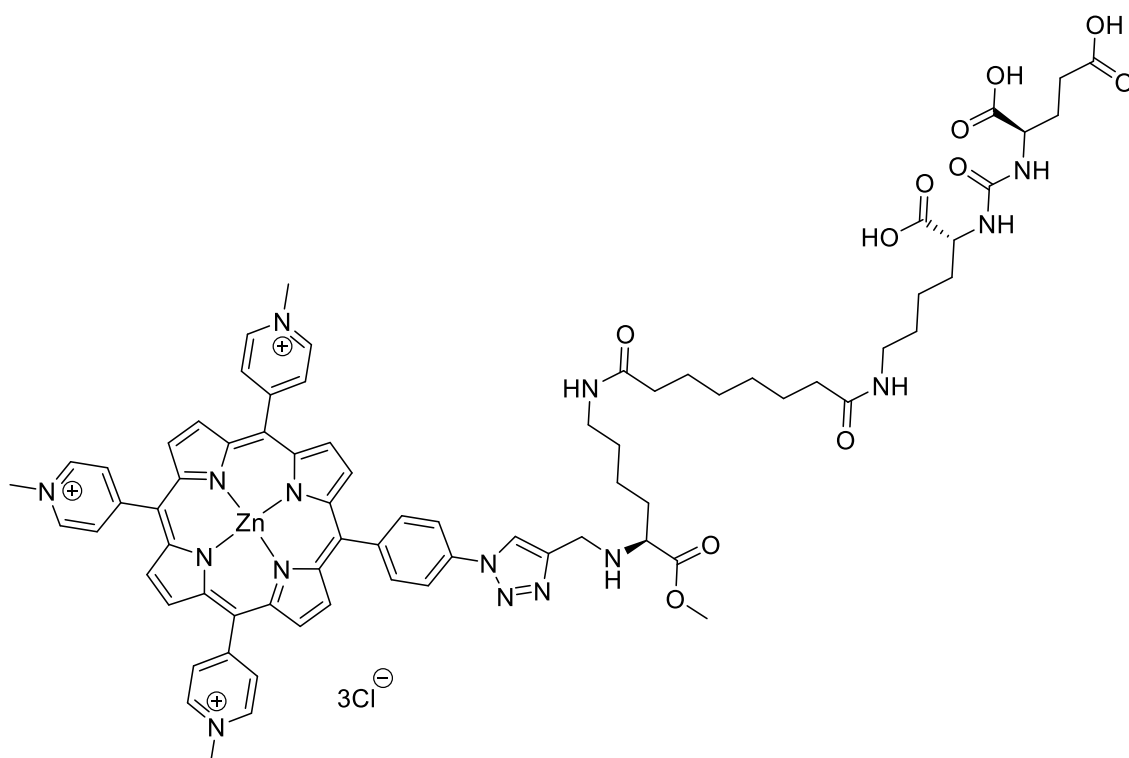
Glu-urea-Lys-SA-N(α)-propargyl-Lys(OMe) **44**



43 (150 mg, 0.182 mmol) was dissolved in DCM (2 mL) and was added TFA (2 mL). The reaction mixture was allowed to stir at room temperature for 3 hours. Solvent was removed under reduced pressure. The crude was washed with DCM (3 \times 50 mL) and evaporated, followed by diethyl ether (3 \times 50 mL) and evaporated, to yield the product as a yellow oil (115 mg, 0.175 mmol, 96%).

^1H NMR (400 MHz, D_2O) δ 1.22 (m, 17H), 1.53 (m, 2H), 1.87 (m, 8H), 2.29 (m, 2H), 2.81 (m, 1H), 2.95 (d, $J = 6.5$ Hz, 4H), 3.63 (m, 3H, O- CH_3), 3.78 (m, 2H, $\text{HC}\equiv\text{CCH}_2$), 3.97 (m, 1H, Lys- αCH), 4.05 (m, 2H, $\alpha\text{CH-NH-CO-NH-}\alpha\text{CH}$). ^{13}C NMR (100 MHz, D_2O) δ 21.28, 22.30, 25.10, 25.23, 26.30, 27.76, 27.80, 28.19, 29.95, 30.63, 35.39, 35.60, 38.58, 38.95, 52.44 (O- CH_3), 53.11 ($\alpha\text{CH-NH-CO-NH-}\alpha\text{CH}$), 53.61 ($\alpha\text{CH-NH-CO-NH-}\alpha\text{CH}$), 58.54 (Lys- αCH), 72.40 ($\text{C}\equiv\text{CH}$), 78.69 ($\text{C}\equiv\text{CH}$), 114.70, 117.58, 159.13 (C=O), 162.29 (C=O), 162.65 (C=O), 169.53 (C=O), 175.99 (C=O), 176.85 (C=O), 177.00 (C=O). MS: (ESI) m/z 656.3 [$\text{M}+\text{H}$] $^+$, HRMS: calcd. for $\text{C}_{30}\text{H}_{50}\text{N}_5\text{O}_{11}$ 656.3501 found 656.3498.

Porphyrin-Lys(OMe)-SA-Lys-urea-Glu 45

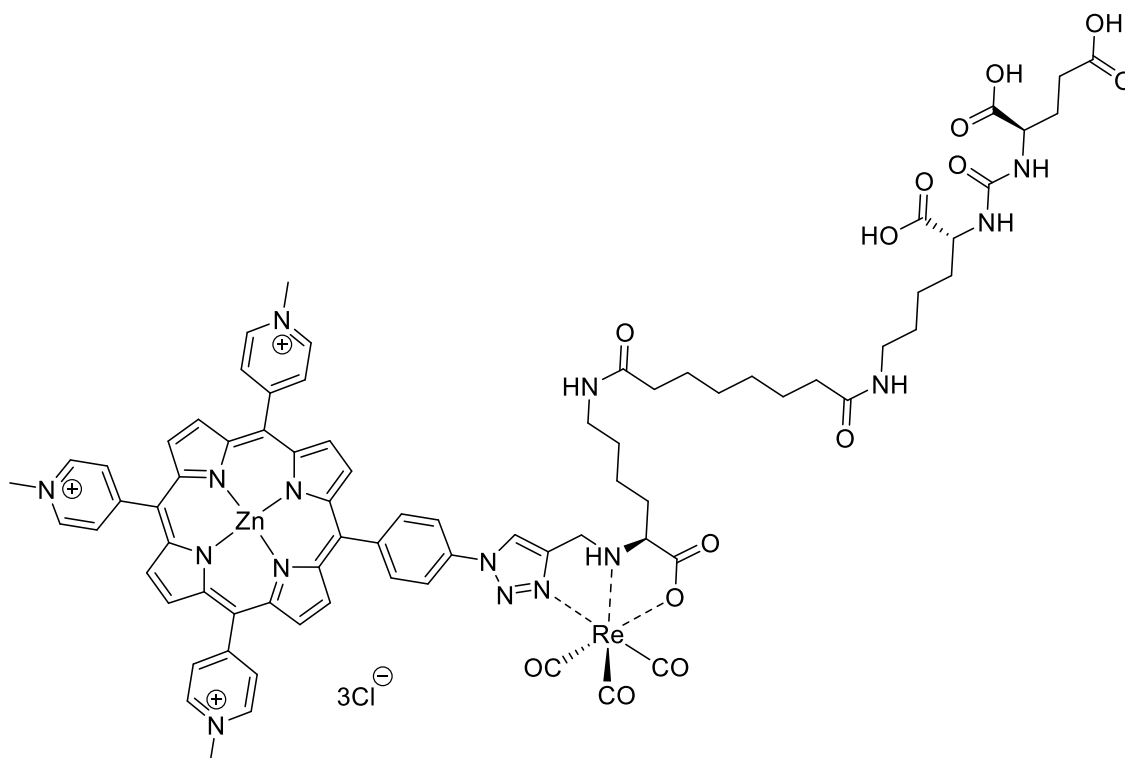


Porphyrin **11** (100 mg, 0.115 mmol) and **44** (115 mg, 0.175 mmol) was taken up in 1:1 t-butanol:water (10 mL). The reaction mixture was added aq. CuSO_4 (10 mM, 500 μL), sodium ascorbate (20 mg), and TBTA (1 mg). The reaction mixture was heated in a microwave reactor (3 hours, 75 W, 70 $^\circ\text{C}$). The reaction mixture was concentrated under reduced pressure. The crude was diluted with water, was added ammonium hexafluorophosphate, and the precipitate isolated via filtration. The residue collected was redissolved in acetone, was added tetrabutylammonium chloride, and the precipitate isolated via filtration. The crude was precipitated from diethyl ether over methanol to yield the product as a purple solid (135 mg, 0.089 mmol, 77%).

HPLC: gradient 3 $R_f = 12.8$ mins, gradient 4 $R_f = 8.6$ mins. ^1H NMR (400 MHz, $\text{DMSO-}d_6$) δ 1.30 (m, 20H), 1.59 (s, 2H), 1.97 (m, 6H), 2.93 (m, 5H), 3.67 (s, 3H, O- CH_3), 3.80 (m, 3H, Lys- αCH), 3.97 (m, 2H, $\alpha\text{CH-NH-CO-NH-}\alpha\text{CH}$), 4.68 (s, 9H, N- CH_3), 6.25 (d, $J = 38.2$ Hz, 2H, $\alpha\text{CH-NH-CO-NH-}\alpha\text{CH}$), 7.76 (d, $J = 52.2$ Hz, 2H, NH-suberate-NH), 8.34 (s, 4H, Ph-H), 8.91 (m, 15H,

115.35, 116.06, 118.75, 122.18, 122.87, 132.22, 132.66 (β C), 132.83, 133.68, 135.81, 136.82, 142.75, 144.16 (β C), 148.46, 148.75, 148.86, 150.55, 157.77, 158.97, 172.45 (C=O), 172.52 (C=O), 174.17 (C=O), 174.69 (C=O), 174.77 (C=O), 175.25 (C=O). MS: (ESI) m/z 490.8 [M-3HCl+3Na] $^{3+}$, HRMS: calcd. for $C_{73}H_{77}N_{15}O_{11}ZnNa_3$ 490.8298 found 490.8288. UV-vis (H_2O , nm): 437, 565, 609. ϵ (437 nm) = 175357 M cm^{-1} .

porphyrin-[$^{nat}Re(Lys)$]-TM complex [^{nat}Re]-47



46 (40 mg, 0.026 mmol) was taken up in phosphate buffer (4 mL, pH 7.4, 0.1 M) and was added [Re(CO) $_3$ Br $_3$][NEt $_4$] $_2$ (30 mg, 0.039 mmol). The reaction mixture was allowed to proceed at 65 °C for 30 mins. Quantitative conversion was observed on TLC (eluate: 2:1:1 MeCN:H $_2$ O:sat. aq. KNO $_3$) and HPLC. The reaction mixture was acidified using 1M HCl, was added ammonium hexafluorophosphate, and the precipitate isolated via filtration. The residue collected was redissolved in acetone, was added tetrabutylammonium chloride, and the precipitate isolated via filtration. The crude was precipitated from diethyl ether over methanol to yield the product as a purple solid (35 mg, 0.020 mmol, 75%).

HPLC: gradient 3 R_f = 16.0 mins, gradient 4 R_f = 10.8 mins. 1H NMR (400 MHz, DMSO- d_6) δ 1.65 (m, 30H), 3.06 (m, 5H), 4.26 (m, 3H, α -CH), 4.66 (s, 9H, N-CH $_3$), 8.39 (s, 4H, o,m-Ph), 8.92 (m, 14H, o-Py, β H), 9.22 (m, 1H, triazole-H), 9.33 (d, J = 5.4 Hz, 6H, m-Py). ^{13}C NMR (100 MHz, DMSO- d_6) δ 23.12, 23.52, 25.74, 28.91, 29.10, 29.30, 29.42, 31.53, 32.39, 32.75, 35.88, 35.92, 38.55, 38.75, 48.32 (N-CH $_3$), 52.75, 52.97, 53.19, 65.98, 115.46, 116.13, 119.58, 121.83, 122.74, 132.48, 132.66 (β C), 133.01, 133.76, 135.86, 135.93, 144.13 (β C), 148.51, 148.81, 148.89, 149.90, 150.45, 157.75, 158.83, 172.83 (C=O), 172.90 (C=O), 173.06 (C=O), 174.71

(C=O), 175.07 (C=O), 175.31 (C=O), 182.65 (C=O), 197.04 (Re-C=O), 197.20 (Re-C=O), 198.52 (Re-C=O). MS: (ESI) m/z 558 $[M-3Cl]^{3+}$, HRMS: calcd. for $C_{76}H_{79}N_{15}O_{14}ReZn$ 558.8252 found 558.8249. UV-vis (H_2O , nm): 437, 565, 615. ϵ (437 nm) = 127473 $M\text{ cm}^{-1}$.

Chapter 8 Reference

- 1 Worldwide cancer statistics, <https://www.cancerresearchuk.org/health-professional/cancer-statistics/worldwide-cancer>, (accessed 24 June 2019).
- 2 C. Hopper, *Lancet Oncol.*, 2000, **1**, 212–219.
- 3 L. B. Josefson and R. W. Boyle, *Theranostics*, 2012, **2**, 916–966.
- 4 J. P. Celli, B. Q. Spring, I. Rizvi, C. L. Evans, K. S. Samkoe, S. Verma, B. W. Pogue and T. Hasan, *Chem. Rev.*, 2010, **110**, 2795–2838.
- 5 A. Mitra and G. I. Stables, *Photodiagnosis Photodyn. Ther.*, 2006, **3**, 116–127.
- 6 A. C. Kübler, *Med. Laser Appl.*, 2005, **20**, 37–45.
- 7 K. L. S. Lane, W. Hovenic, K. Ball and C. B. Zachary, *Lasers Surg. Med.*, 2015, **47**, 168–172.
- 8 A. P. Castano, T. N. Demidova and M. R. Hamblin, *Photodiagnosis Photodyn. Ther.*, 2004, **1**, 279–293.
- 9 E. S. Nyman and P. H. Hynninen, *J. Photochem. Photobiol. B*, 2004, **73**, 1–28.
- 10 B. W. Henderson and T. J. Dougherty, *Photochem. Photobiol.*, 1992, **55**, 145–157.
- 11 C. R. Goodlett and K. H. Horn, *Alcohol Res. Health*, 2001, **25**, 175–184.
- 12 G. Majno and I. Joris, *Am. J. Pathol.*, 1995, **146**, 3–15.
- 13 M. Raffray and C. Gerald M., *Pharmacol. Ther.*, 1997, **75**, 153–177.
- 14 S. Y. Proskuryakov, A. G. Konoplyannikov and V. L. Gabai, *Exp. Cell Res.*, 2003, **283**, 1–16.
- 15 G. Kroemer and J. C. Reed, *Nat. Med.*, 2000, **6**, 513–519.
- 16 H. Endo, H. Hosoya, T. Koyama and M. Ichioka, *Agric. Biol. Chem.*, 1982, **46**, 2183–2193.
- 17 D. Wöhrle, A. Hirth, T. Bogdahn-Rai, G. Schnurpfeil and M. Shopova, *Russ. Chem. Bull.*, 1998, **47**, 807–816.
- 18 W. M. Sharman, C. M. Allen and J. E. van Lier, *Drug Discov. Today*, 1999, **4**, 507–517.
- 19 G. I. Stables and D. V. Ash, *Cancer Treat. Rev.*, 1995, **21**, 311–323.
- 20 J. Trachtenberg, R. A. Weersink, S. R. H. Davidson, M. A. Haider, A. Bogaards, M. R. Gertner, A. Evans, A. Scherz, J. Savard, J. L. Chin, B. C. Wilson and M. Elhilali, *BJU Int.*, 2008, **102**, 556–562.
- 21 J. Trachtenberg, A. Bogaards, R. A. Weersink, M. A. Haider, A. Evans, S. A. McCluskey, A. Scherz, M. R. Gertner, C. Yue, S. Appu, A. Aprikian, J. Savard, B. C. Wilson and M. Elhilali, *J. Urol.*, 2007, **178**, 1974–1979.
- 22 A. Ormond and H. Freeman, *Materials*, 2013, **6**, 817–840.
- 23 F. Borle, A. Radu, P. Monnier, H. den B. Van and G. Wagnières, *Photochem. Photobiol.*, 2003, **78**, 377–383.
- 24 J. C. Kennedy, R. H. Pottier and D. C. Pross, *J. Photochem. Photobiol. B*, 1990, **6**, 143–148.
- 25 T. J. Dougherty, C. J. Gomer, B. W. Henderson, G. Jori, D. Kessel, M. Korbelik, J. Moan and Q. Peng, *J. Natl. Cancer Inst.*, 1998, **90**, 889–905.
- 26 F. Ricchelli, S. Gobbo, G. Jori, G. Moreno, F. Vinzens and C. Salet, *Photochem. Photobiol.*, 1993, **58**, 53–58.
- 27 G. Jori, E. Reddi, I. Cozzani and L. Tomio, *Br. J. Cancer*, 1986, **53**, 615–621.
- 28 A. P. Castano, T. N. Demidova and M. R. Hamblin, *Photodiagnosis Photodyn. Ther.*, 2005, **2**, 91–106.
- 29 S. Bonneau and C. Vever-Bizet, *Expert Opin. Ther. Pat.*, 2008, **18**, 1011–1025.
- 30 A. M. Slomp, S. M. W. Barreira, L. Z. B. Carrenho, C. C. Vandresen, I. F. Zattoni, S. M. S. Ló, J. C. C. Dallagnol, D. R. B. Ducatti, A. Orsato, M. E. R. Duarte, M. D. Nosedá, M. F. Otuki and A. G. Gonçalves, *Bioorg. Med. Chem. Lett.*, 2017, **27**, 156–161.
- 31 G. G. Meng, B. R. James, K. A. Skov and M. Korbelik, *Can. J. Chem.*, 1994, **72**, 2447–2457.
- 32 R. E. Mewis, H. Savoie, S. J. Archibald and R. W. Boyle, *Photodiagnosis Photodyn. Ther.*, 2009, **6**, 200–206.
- 33 J. L. Worlinsky, S. Halepas and C. Brückner, *Org. Biomol. Chem.*, 2014, **12**, 3991–4001.
- 34 Z. Dong and P. J. Scammells, *J. Org. Chem.*, 2007, **72**, 9881–9885.
- 35 A. D. Lammer, M. E. Cook and J. L. Sessler, *J. Porphyr. Phthalocyanines*, 2015, **19**, 398–403.
- 36 H. Abrahamse and M. R. Hamblin, *Biochem. J.*, 2016, **473**, 347–364.
- 37 Y. Matsumura and H. Maeda, *Cancer Res.*, 1986, **46**, 6387–6392.

- 38 F. Danhier, *J. Controlled Release*, 2016, **244**, 108–121.
- 39 J. W. Nichols and Y. H. Bae, *J. Controlled Release*, 2014, **190**, 451–464.
- 40 M. Soncin, L. Polo, E. Reddi, G. Jori, M. Kenney, G. Cheng and M. Rodgers, *Br. J. Cancer*, 1995, **71**, 727–732.
- 41 D. Kessel, *J. Photochem. Photobiol. B*, 1992, **14**, 261–262.
- 42 A. J. Bullous, C. M. A. Alonso and R. W. Boyle, *Photochem. Photobiol. Sci.*, 2011, **10**, 721–750.
- 43 P. M. R. Pereira, B. Korsak, B. Sarmento, R. J. Schneider, R. Fernandes and J. P. C. Tomé, *Org. Biomol. Chem.*, 2015, **13**, 2518–2529.
- 44 J. Taquet, C. Frochot, V. Manneville and M. Barberi-Heyob, *Curr. Med. Chem.*, 2007, **14**, 1673–1687.
- 45 C. Naidoo, C. A. Kruger and H. Abrahamse, *Technol. Cancer Res. Treat.*, 2018, **17**, 1–15.
- 46 S. Osati, H. Ali, B. Guérin and J. E. van Lier, *J. Porphyr. Phthalocyanines*, 2017, **21**, 701–730.
- 47 D. M. Copolovici, K. Langel, E. Eriste and Ü. Langel, *ACS Nano*, 2014, **8**, 1972–1994.
- 48 T. Boulikas, *J. Cell. Biochem.*, 1994, **55**, 32–58.
- 49 M. P. Murphy, *Trends Biotechnol.*, 1997, **15**, 326–330.
- 50 M. Sibrian-Vazquez, T. J. Jensen, R. P. Hammer and M. G. H. Vicente, *J. Med. Chem.*, 2006, **49**, 1364–1372.
- 51 N. L. Oleinick, R. L. Morris and I. Belichenko, *Photochem. Photobiol. Sci.*, 2002, **1**, 1–21.
- 52 O. H. Aina, T. C. Sroka, M.-L. Chen and K. S. Lam, *Pept. Sci.*, 2002, **66**, 184–199.
- 53 A. M. Bugaj, *Photochem. Photobiol. Sci.*, 2011, **10**, 1097.
- 54 F. Biscaglia and M. Gobbo, *Pept. Sci.*, 2018, **110**, e24038.
- 55 Y. Yang, X. Yang, H. Li, C. Li, H. Ding, M. Zhang, Y. Guo and M. Sun, *Colloids Surf. B Biointerfaces*, 2019, **173**, 564–570.
- 56 A. Nunn, K. Linder and H. W. Strauss, *Eur. J. Nucl. Med.*, 1995, **22**, 265–280.
- 57 G. K. Balendiran, R. Dabur and D. Fraser, *Cell Biochem. Funct.*, 2004, **22**, 343–352.
- 58 J. Deng, F. Liu, L. Wang, Y. An, M. Gao, Z. Wang and Y. Zhao, *Biomater. Sci.*, 2019, **7**, 429–441.
- 59 Y. Wang, M. Yang, J. Qian, W. Xu, J. Wang, G. Hou, L. Ji and A. Suo, *Carbohydr. Polym.*, 2019, **203**, 203–213.
- 60 Y. Liu, N. Song, Z. Li, L. Chen and Z. Xie, *Dyes Pigments*, 2019, **160**, 71–78.
- 61 X. Cai, B. Liu, M. Pang and J. Lin, *Dalton Trans.*, 2018, **47**, 16329–16336.
- 62 W. Xu, J. Qian, G. Hou, Y. Wang, J. Wang, T. Sun, L. Ji, A. Suo and Y. Yao, *Acta Biomater.*, 2018, **82**, 171–183.
- 63 R. Ackroyd, C. Kelty, N. Brown and M. Reed, *Photochem. Photobiol.*, 2001, **74**, 656–669.
- 64 T. Nagaya, Y. A. Nakamura, P. L. Choyke and H. Kobayashi, *Front. Oncol.*, 2017, **7**, 314.
- 65 R. N. Bryan, Ed., in *Introduction to the Science of Medical Imaging*, Cambridge University Press, Cambridge, 1 edition., 2009, pp. 13–116.
- 66 G. J. Stasiuk, S. Faulkner and N. J. Long, *Curr. Opin. Pharmacol.*, 2012, **12**, 576–582.
- 67 K. Moghissi, M. R. Stringer and K. Dixon, *Photodiagnosis Photodyn. Ther.*, 2008, **5**, 235–237.
- 68 H. Kasban, M. A. M. El-Bendary and D. H. Salama, *Int. J. Inf. Sci. Intell. Syst.*, 2015, **4**, 37–58.
- 69 A. Corlu, R. Choe, T. Durduran, M. A. Rosen, M. Schweiger, S. R. Arridge, M. D. Schnall and A. G. Yodh, *Opt. Express*, 2007, **15**, 6696–6716.
- 70 P. Suetens, in *Fundamentals of Medical Imaging*, Cambridge University Press, Cambridge, 2nd edn., 2009, pp. 64–104.
- 71 B. M. Dale, M. A. Brown and R. C. Semelka, *MRI: Basic Principles and Applications*, Wiley-Blackwell, Chichester, West Sussex ; Hoboken, NJ, 5th Revised edition edition., 2015.
- 72 V. Jacques and J. F. Desreux, in *Contrast Agents I: Magnetic Resonance Imaging*, ed. W. Krause, Springer Berlin Heidelberg, Berlin, Heidelberg, 2002, pp. 123–164.
- 73 H. Gysling and M. Tsutsui, *Adv. Organomet. Chem.*, 1971, **9**, 361–395.
- 74 M. P. Lowe, *Aust. J. Chem.*, 2002, **55**, 551.
- 75 É. Tóth, L. Helm and A. E. Merbach, in *Contrast Agents I*, ed. W. Krause, Springer Berlin Heidelberg, Berlin, Heidelberg, 2002, vol. 221, pp. 61–101.
- 76 P. Caravan, *Chem. Soc. Rev.*, 2006, **35**, 512.

- 77 P. Caravan, C. T. Farrar, L. Frullano and R. Uppal, *Contrast Media Mol. Imaging*, **4**, 89–100.
- 78 A. D. McLachlan, *Proc. R. Soc. A*, 1964, **280**, 271–288.
- 79 J. Kowalewski, L. Nordenskiöld, N. Benetis and P.-O. Westlund, *Prog. Nucl. Magn. Reson. Spectrosc.*, 1985, **17**, 141–185.
- 80 P. W. Miller, N. J. Long, R. Vilar and A. D. Gee, *Angew. Chem. Int. Ed.*, 2008, **47**, 8998–9033.
- 81 T. W. Price, J. Greenman and G. J. Stasiuk, *Dalton Trans.*, 2016, **45**, 15702–15724.
- 82 L. K. Shankar, J. M. Hoffman, S. Bacharach, M. M. Graham, J. Karp, A. A. Lammertsma, S. Larson, D. A. Mankoff, B. A. Siegel, A. V. den Abbeele, J. Yap and D. Sullivan, *J. Nucl. Med.*, 2006, **47**, 1059–1066.
- 83 S. S. Gambhir, *Nat. Rev. Cancer*, 2002, **2**, 683–693.
- 84 D. Lapointe, N. Brasseur, J. Cadorette, C. La Madeleine and others, *J. Nucl. Med.*, 1999, **40**, 876–882.
- 85 V. Bérard, J. A. Rousseau, J. Cadorette, L. Hubert, M. Bentourkia, J. E. van Lier and R. Lecomte, *J. Nucl. Med.*, 2006, **47**, 1119–1126.
- 86 T. J. Wadas, E. H. Wong, G. R. Weisman and C. J. Anderson, *Chem. Rev.*, 2010, **110**, 2858–2902.
- 87 F. Rösch, in *Theranostics, Gallium-68, and Other Radionuclides: A Pathway to Personalized Diagnosis and Treatment*, eds. R. P. Baum and F. Rösch, Springer Science & Business Media, 1st edn., 2012, pp. 3–16.
- 88 International Atomic Energy Agency, *Production of long lived parent radionuclides for generators, ⁶⁸Ge, ⁸²Sr, ⁹⁰Sr and ¹⁸⁸W.*, International Atomic Energy Agency, Vienna, 2010.
- 89 M. Fani, J. P. André and H. R. Maecke, *Contrast Media Mol. Imaging*, 2008, **3**, 53–63.
- 90 M. Berglund and M. E. Wieser, *Pure Appl. Chem.*, 2011, **83**, 397–410.
- 91 M. A. Green and M. J. Welch, *Int. J. Rad. Appl. Instrum. B*, 1989, **16**, 435–448.
- 92 R. R. Crichton and M. Charlotheaux-Wauters, *Eur. J. Biochem.*, 1987, **164**, 485–506.
- 93 I. Velikyan, A. Sundin, J. Sörensen, M. Lubberink, M. Sandström, U. Garske-Román, H. Lundqvist, D. Granberg and B. Eriksson, *J. Nucl. Med.*, 2014, **55**, 204–210.
- 94 M. Ocak, E. Demirci, L. Kabasakal, A. Aygun, R. O. Tutar, A. Araman and B. Kanmaz, *Nucl. Med. Commun.*, 2013, **34**, 1084–1089.
- 95 A. Romesberg, M. E. Oates and R. E. Khouli, *J. Nucl. Med.*, 2017, **58**, 992.
- 96 I. Kayani, B. G. Conry, A. M. Groves, T. Win, J. Dickson, M. Caplin and J. B. Bomanji, *J. Nucl. Med.*, 2009, **50**, 1927–1932.
- 97 J. Notni, K. Pohle and H.-J. Wester, *EJNMMI Res.*, 2012, **2**, 1–5.
- 98 J. R. Nedrow, A. G. White, J. Modi, K. Nguyen, A. J. Chang and C. J. Anderson, *Mol. Imaging*, 2014, **13**, 1–13.
- 99 J. Notni, J. Šimeček, P. Hermann and H.-J. Wester, *Chem. – Eur. J.*, 2011, **17**, 14718–14722.
- 100 J. Notni, P. Hermann, J. Havlíčková, J. Kotek, V. Kubíček, J. Plutnar, N. Loktionova, P. J. Riss, F. Rösch and I. Lukeš, *Chem. – Eur. J.*, 2010, **16**, 7174–7185.
- 101 Ramunas. Motekaitis, Yizhen. Sun, A. E. Martell and M. J. Welch, *Inorg. Chem.*, 1991, **30**, 2737–2740.
- 102 M. Eder, B. Wängler, S. Knackmuss, F. LeGall, M. Little, U. Haberkorn, W. Mier and M. Eisenhut, *Eur. J. Nucl. Med. Mol. Imaging*, 2008, **35**, 1878–1886.
- 103 M. Eder, M. Schäfer, U. Bauder-Wüst, W.-E. Hull, C. Wängler, W. Mier, U. Haberkorn and M. Eisenhut, *Bioconjug. Chem.*, 2012, **23**, 688–697.
- 104 M. Eiber, T. Maurer, M. Souvatzoglou, A. J. Beer, A. Ruffani, B. Haller, F.-P. Graner, H. Kübler, U. Haberkorn, M. Eisenhut, H.-J. Wester, J. E. Gschwend and M. Schwaiger, *J. Nucl. Med.*, 2015, **56**, 668–674.
- 105 E. Boros, C. L. Ferreira, J. F. Cawthray, E. W. Price, B. O. Patrick, D. W. Wester, M. J. Adam and C. Orvig, *J. Am. Chem. Soc.*, 2010, **132**, 15726–15733.
- 106 L. Tei, G. Gugliotta, M. Fekete, F. K. Kálmán and M. Botta, *Dalton Trans.*, 2011, **40**, 2025–2032.
- 107 Z. Baranyai, F. Uggeri, A. Maiocchi, G. B. Giovenzana, C. Cavallotti, A. Takács, I. Tóth, I. Bányai, A. Bényei, E. Brucher and S. Aime, *Eur. J. Inorg. Chem.*, 2013, **2013**, 147–162.
- 108 J. Seemann, B. P. Waldron, F. Roesch and D. Parker, *ChemMedChem*, 2015, **10**, 1019–1026.

- 109 B. P. Waldron, D. Parker, C. Burchardt, D. S. Yufit, M. Zimny and F. Roesch, *Chem. Commun.*, 2012, **49**, 579–581.
- 110 D. Parker, B. P. Waldron and D. S. Yufit, *Dalton Trans.*, 2013, **42**, 8001–8008.
- 111 D. J. Berry, Y. Ma, J. R. Ballinger, R. Tavaré, A. Koers, K. Sunassee, T. Zhou, S. Nawaz, G. E. D. Mullen, R. C. Hider and P. J. Blower, *Chem. Commun.*, 2011, **47**, 7068–7070.
- 112 M. T. Ma, C. Cullinane, C. Imberti, J. Bagaña Torres, S. Y. A. Terry, P. Roselt, R. J. Hicks and P. J. Blower, *Bioconjug. Chem.*, 2016, **27**, 309–318.
- 113 T. W. Price, J. Gallo, V. Kubíček, Z. Böhmová, T. J. Prior, J. Greenman, P. Hermann and G. J. Stasiuk, *Dalton Trans.*, 2017, **46**, 16973–16982.
- 114 A. Rahmim and H. Zaidi, *Nucl. Med. Commun.*, 2008, **29**, 193–207.
- 115 SPECT, <https://www.cardinalhealth.com/en/product-solutions/pharmaceutical-products/nuclear-medicine/radiopharmaceuticals/spect.html>, (accessed 8 April 2019).
- 116 S. Jurisson, D. Berning, W. Jia and D. Ma, *Chem. Rev.*, 1993, **93**, 1137–1156.
- 117 J. R. Dilworth and S. J. Parrott, *Chem. Soc. Rev.*, 1998, **27**, 43.
- 118 E. Deutsch, K. Libson, S. Jurisson and L. F. Lindoy, *Prog Inorg Chem*, 1983, **30**, 75–139.
- 119 F. N. Von Hippel and L. H. Kahn, *Sci. Glob. Secur.*, 2006, **14**, 151–162.
- 120 K. Schwochau, *Angew. Chem. Int. Ed. Engl.*, 1994, **33**, 2258–2267.
- 121 H. F. Kung, *Semin. Nucl. Med.*, 1990, **20**, 150–158.
- 122 S.-J. Wang, R.-S. Liu, H.-C. Liu, K.-N. Lin, D.-E. Shan, K.-K. Liao, J.-L. Fuh and L.-S. Lee, *Eur. J. Nucl. Med.*, 1993, **20**, 339–344.
- 123 *Technetium - 99 m radiopharmaceuticals: manufacture of kits*, Internat. Atomic Energy Agency, Vienna, 2008.
- 124 J. Lã, R. Taillefer, R. A. Morgan, D. Kupranick and R. C. Walovitch, *J. Nucl. Med.*, 1989, **30**, 1902–1910.
- 125 N. A. Lassen, *Clin. Neuropharmacol.*, 1990, **13**, S1-8.
- 126 M. E. Lancman, H. H. Morris, S. Raja, M. J. Sullivan, G. Saha and R. Go, *Epilepsia*, 1997, **38**, 466–471.
- 127 M. D. Devous, J. K. Payne, J. L. Lowe and R. F. Leroy, *J. Nucl. Med.*, 1993, **34**, 754–761.
- 128 A. Proulx, J. R. Ballinger and K. Y. Gulenchyn, *Int. J. Rad. Appl. Instrum. [A]*, 1989, **40**, 95–97.
- 129 F. J. T. Wackers, D. S. Berman, J. Maddahi, D. D. Watson, G. A. Beller, H. W. Strauss, C. A. Boucher, M. Picard, B. L. Holman, R. Fridrich, E. Inglese, B. Delaloye, A. Bischof-Delaloye, L. Camin and K. McKusick, *J. Nucl. Med.*, 1989, **30**, 301–311.
- 130 R. Schibli and A. Schubiger, *Eur. J. Nucl. Med. Mol. Imaging*, 2002, **29**, 1529–1542.
- 131 J. D. Kelly, A. M. Forster, B. Higley, C. M. Archer, F. S. Booker, L. R. Canning, K. Wai Chiu, B. Edwards, H. K. Gill, M. McPartlin, K. R. Nagle, I. A. Latham, R. D. Pickett, A. E. Storey and P. M. Webbon, *J. Nucl. Med.*, 1993, **2**, 222–227.
- 132 Y. Arano, *Ann. Nucl. Med.*, 2002, **16**, 79–93.
- 133 D. R. Vera, A. M. Wallace, C. K. Hoh and R. F. Mattrey, *J. Nucl. Med.*, 2001, **42**, 951–959.
- 134 S. Jürgens, W. A. Herrmann and F. E. Kühn, *J. Organomet. Chem.*, 2014, **751**, 83–89.
- 135 A. M. Wallace, C. K. Hoh, S. J. Ellner, D. D. Darrah, G. Schulteis and D. R. Vera, *Ann. Surg. Oncol.*, 2007, **14**, 913–921.
- 136 Y. Zhang and J. F. Lovell, *Theranostics*, 2012, **2**, 905–915.
- 137 R. C. Lyon, P. J. Faustino, J. S. Cohen, A. Katz, F. Mornex, D. Colcher, C. Baglin, S. H. Koenig and P. Hambright, *Magn. Reson. Med.*, 1987, **4**, 24–33.
- 138 P. Furmanski and C. Longley, *Cancer Res.*, 1998, **48**, 4604–4610.
- 139 Y. Ni, G. Marchal, Y. Jie, G. Lukito, C. Petré, M. Wevers, A. L. Baert, W. Ebert, C.-S. Hilger, F.-K. Maier and W. Semmler, *Acad. Radiol.*, 1995, **2**, 687–699.
- 140 H. E. Daldrup-Link, M. Rudelius, S. Metz, G. Piontek, B. Pichler, M. Settles, U. Heinzmann, J. Schlegel, R. A. J. Oostendorp and E. J. Rummeny, *Eur. J. Nucl. Med. Mol. Imaging*, 2004, **31**, 1312–1321.
- 141 F. Hindré, M. L. Plouzenec, J. D. de Certaines, M. T. Foulter, T. Patrice and G. Simonneaux, *J. Magn. Reson. Imaging*, 1993, **3**, 59–65.
- 142 J. Luo, L.-F. Chen, P. Hu and Z.-N. Chen, *Inorg. Chem.*, 2014, **53**, 4184–4191.
- 143 A. Sour, S. Jenni, A. Ortí-Suárez, J. Schmitt, V. Heitz, F. Bolze, P. Loureiro de Sousa, C. Po, C. S. Bonnet, A. Pallier, É. Tóth and B. Ventura, *Inorg. Chem.*, 2016, **55**, 4545–4554.
- 144 P. Caravan, *Chem. Soc. Rev.*, 2006, **35**, 512–523.

- 145 Y. Gossuin, Z. Serhan, L. Sandiford, D. Henrard, T. Marquardsen, R. T. M. de Rosales, D. Sakellariou and F. Ferrage, *Appl. Magn. Reson.*, 2016, **47**, 237–246.
- 146 J. Schmitt, V. Heitz, A. Sour, F. Bolze, P. Kessler, L. Flamigni, B. Ventura, C. S. Bonnet and É. Tóth, *Chem. – Eur. J.*, 2016, **22**, 2775–2786.
- 147 J. Schmitt, S. Jenni, A. Sour, V. Heitz, F. Bolze, A. Pallier, C. S. Bonnet, É. Tóth and B. Ventura, *Bioconjug. Chem.*, 2018, **29**, 3726–3738.
- 148 E. Dahlstedt, H. A. Collins, M. Balaz, M. K. Kuimova, M. Khurana, B. C. Wilson, D. Phillips and H. L. Anderson, *Org. Biomol. Chem.*, 2009, **7**, 897–904.
- 149 M. K. Kuimova, H. A. Collins, M. Balaz, E. Dahlstedt, J. A. Levitt, N. Sergent, K. Suhling, M. Drobizhev, N. S. Makarov, A. Rebane, H. L. Anderson and D. Phillips, *Org. Biomol. Chem.*, 2009, **7**, 889–896.
- 150 B. Wu, X.-Q. Li, T. Huang, S.-T. Lu, B. Wan, R.-F. Liao, Y.-S. Li, A. Baidya, Q.-Y. Long and H.-B. Xu, *Biomater. Sci.*, 2017, **5**, 1746–1750.
- 151 Y. Shen, F. L. Goerner, C. Snyder, J. N. Morelli, D. Hao, D. Hu, X. Li and V. M. Runge, *Invest. Radiol.*, 2015, **50**, 330–338.
- 152 Y. Fazaeli, A. R. Jalilian, M. M. Amini, K. Ardaneh, A. Rahiminejad, F. Bolourinovin, S. Moradkhani and A. Majdabadi, *Nucl. Med. Mol. Imaging*, 2012, **46**, 20–26.
- 153 F. Zoller, P. J. Riss, F.-P. Montforts, D. K. Kelleher, E. Eppard and F. Rösch, *Nucl. Med. Biol.*, 2013, **40**, 280–288.
- 154 F. Zoller, P. J. Riss, F.-P. Montforts and F. Rösch, *Radiochim. Acta*, 2010, **98**, 157–160.
- 155 B. Behnam Azad, C.-F. Cho, J. D. Lewis and L. G. Luyt, *Appl. Radiat. Isot.*, 2012, **70**, 505–511.
- 156 E. V. Rosca, R. J. Gillies and M. R. Caplan, *Biotechnol. Bioeng.*, 2009, **104**, 408–417.
- 157 F. Bryden, H. Savoie, E. V. Rosca and R. W. Boyle, *Dalton Trans*, 2015, **44**, 4925–4932.
- 158 J.-X. Zhang, J.-W. Zhou, C.-F. Chan, T. C.-K. Lau, D. W. J. Kwong, H.-L. Tam, N.-K. Mak, K.-L. Wong and W.-K. Wong, *Bioconjug. Chem.*, 2012, **23**, 1623–1638.
- 159 J. Pan, B. I. Harriss, C.-F. Chan, L. Jiang, T.-H. Tsoi, N. J. Long, W.-T. Wong, W.-K. Wong and K.-L. Wong, *Inorg. Chem.*, 2016, **55**, 6839–6841.
- 160 M. Guleria, T. Das, J. Amirdhanayagam, H. D. Sarma and A. Dash, *Cancer Biother. Radiopharm.*, 2018, **33**, 8–16.
- 161 A. K. Babbar, A. K. Singh, H. C. Goel, U. P. S. Chauhan and R. K. Sharma, *Nucl. Med. Biol.*, 2000, **27**, 419–426.
- 162 S. Gupta, B. Dwarakanath, N. Chaudhury, A. Mishra, K. Muralidhar and V. Jain, *J. Cancer Res. Ther.*, 2011, **7**, 314–324.
- 163 M. A. Motaleb and M. Y. Nassar, *J. Radioanal. Nucl. Chem.*, 2014, **299**, 1759–1766.
- 164 M. A. Motaleb, T. El-Kolaly, M. Fayed, L. M. Abdel-Aziz and E. M. Lashine, *Arab J. Nucl. Sci. Appl.*, 2016, **49**, 131–137.
- 165 Y. You, S. L. Gibson, R. Hilf, S. R. Davies, A. R. Oseroff, I. Roy, T. Y. Ohulchanskyy, E. J. Bergey and M. R. Detty, *J. Med. Chem.*, 2003, **46**, 3734–3747.
- 166 M. Subbarayan, S. J. Shetty, T. S. Srivastava, O. P. D. Noronha and A. M. Samuel, *J. Porphyr. Phthalocyanines*, 2001, **5**, 824–828.
- 167 P. M. Santos, M. Laranjo, A. C. Serra, A. M. Abrantes, M. Piñeiro, J. Casalta-Lopes, D. Trindade, J. Maia, A. Rocha-Gonsalves and M. F. Botelho, *J. Label. Compd. Radiopharm.*, 2014, **57**, 141–147.
- 168 R. Waibel, R. Alberto, J. Willuda, R. Finnern, R. Schibli, A. Stichelberger, A. Egli, U. Abram, J.-P. Mach, A. Plückthun and P. A. Schubiger, *Nat. Biotechnol.*, 1999, **17**, 897–901.
- 169 Y. Liu, B. Shen, F. Liu, B. Zhang, T. Chu, J. Bai and S. Bao, *Nucl. Med. Biol.*, 2012, **39**, 579–585.
- 170 T. Gianferrara, C. Spagnul, R. Alberto, G. Gasser, S. Ferrari, V. Pierroz, A. Bergamo and E. Alessio, *ChemMedChem*, 2014, **9**, 1231–1237.
- 171 C. Spagnul, R. Alberto, G. Gasser, S. Ferrari, V. Pierroz, A. Bergamo, T. Gianferrara and E. Alessio, *J. Inorg. Biochem.*, 2013, **122**, 57–65.
- 172 F. Giuntini, C. M. A. Alonso and R. W. Boyle, *Photochem. Photobiol. Sci.*, 2011, **10**, 759–791.
- 173 A. El-Faham and F. Albericio, *Chem. Rev.*, 2011, **111**, 6557–6602.
- 174 L. Liang and D. Astruc, *Coord. Chem. Rev.*, 2011, **255**, 2933–2945.
- 175 R. Huisgen, *Angew. Chem. Int. Ed. Engl.*, 1963, **2**, 565–598.

- 176 V. V. Rostovtsev, L. G. Green, V. V. Fokin and K. B. Sharpless, *Angew. Chem. Int. Ed.*, 2002, **41**, 2596–2599.
- 177 C. W. Tornøe, C. Christensen and M. Meldal, *J. Org. Chem.*, 2002, **67**, 3057–3064.
- 178 T. Lin, Z. Chen, R. Usha, C. V. Stauffacher, J.-B. Dai, T. Schmidt and J. E. Johnson, *Virology*, 1999, **265**, 20–34.
- 179 M. Carrillo-Tripp, C. M. Shepherd, I. A. Borelli, S. Venkataraman, G. Lander, P. Natarajan, J. E. Johnson, C. L. Brooks and V. S. Reddy, *Nucleic Acids Res.*, 2009, **37**, D436–D442.
- 180 Q. Wang, T. Lin, L. Tang, J. E. Johnson and M. G. Finn, *Angew. Chem. Int. Ed.*, 2002, **41**, 459–462.
- 181 K. M. Taylor, V. E. Spall, P. Jonathan, G. Butler and G. P. Lomonosoff, *Virology*, 1999, **255**, 129–137.
- 182 A. E. Czapar and N. F. Steinmetz, *Curr. Opin. Chem. Biol.*, 2017, **38**, 108–116.
- 183 D. J. Evans, *Inorganica Chim. Acta*, 2010, **363**, 1070–1076.
- 184 J. Jeevanandam, K. Pal and M. K. Danquah, *Biochimie*, 2019, **157**, 38–47.
- 185 N. F. Steinmetz and D. J. Evans, *Org. Biomol. Chem.*, 2007, **5**, 2891.
- 186 W. R. Algar, D. E. Prasuhn, M. H. Stewart, T. L. Jennings, J. B. Blanco-Canosa, P. E. Dawson and I. L. Medintz, *Bioconjug. Chem.*, 2011, **22**, 825–858.
- 187 S. Shukla and N. F. Steinmetz, *Wiley Interdiscip. Rev. Nanomed. Nanobiotechnol.*, 2015, **7**, 708–721.
- 188 M. A. Bruckman, X. Yu and N. F. Steinmetz, *Nanotechnology*, 2013, **24**, 462001.
- 189 I. Yildiz, S. Shukla and N. F. Steinmetz, *Curr. Opin. Biotechnol.*, 2011, **22**, 901–908.
- 190 N. F. Steinmetz, *Nanomedicine Nanotechnol. Biol. Med.*, 2010, **6**, 634–641.
- 191 J. K. Pokorski and N. F. Steinmetz, *Mol. Pharm.*, 2011, **8**, 29–43.
- 192 N. F. Steinmetz and M. Manchester, Eds., in *Viral Nanoparticles: Tools for Material Science and Biomedicine*, Pan Stanford, Singapore, 1 edition., 2011, pp. 75–122.
- 193 M. D. Glidden, J. F. Edelbrock, A. M. Wen, S. Shukla, Y. Ma, R. H. French, J. K. Pokorski and N. F. Steinmetz, in *Chemoselective and Bioorthogonal Ligation Reactions*, John Wiley & Sons, Ltd, 2017, pp. 631–710.
- 194 G. P. Lomonosoff and D. J. Evans, in *Plant Viral Vectors*, eds. K. Palmer and Y. Gleba, Springer Berlin Heidelberg, Berlin, Heidelberg, 2011, vol. 375, pp. 61–87.
- 195 Q. Wang, E. Kaltgrad, T. Lin, J. E. Johnson and M. G. Finn, *Chem. Biol.*, 2002, **9**, 805–811.
- 196 A. D. Adler, F. R. Longo, J. D. Finarelli, J. Goldmacher, J. Assour and L. Korsakoff, *J. Org. Chem.*, 1967, **32**, 476–476.
- 197 World Intellectual Property Organization, WO2002000662A1, 2002.
- 198 F. Bryden and R. W. Boyle, *Synlett*, 2013, **24**, 1978–1982.
- 199 F. Le Guern, V. Sol, C. Ouk, P. Arnoux, C. Frochot and T.-S. Ouk, *Bioconjugate Chem.*, 2017, **28**, 2493–2506.
- 200 C. M. A. Alonso, A. Palumbo, A. J. Bullous, F. Pretto, D. Neri and R. W. Boyle, *Bioconjugate Chem.*, 2010, **21**, 302–313.
- 201 R. Schneider, F. Schmitt, C. Frochot, Y. Fort, N. Lourette, F. Guillemain, J.-F. Müller and M. Barberi-Heyob, *Bioorg. Med. Chem.*, 2005, **13**, 2799–2808.
- 202 C. Spagnul, L. C. Turner, F. Giuntini, J. Greenman and R. W. Boyle, *J. Mater. Chem. B*, 2017, **5**, 1834–1845.
- 203 M. Kurupparachchi, H. Savoie, A. Lowry, C. Alonso and R. W. Boyle, *Mol. Pharm.*, 2011, **8**, 920–931.
- 204 J. Duane E. Prasuhn, R. M. Yeh, A. Obenaus, M. Manchester and M. G. Finn, *Chem. Commun.*, 2007, **0**, 1269–1271.
- 205 S. S. Gupta, J. Kuzelka, P. Singh, W. G. Lewis, M. Manchester and M. G. Finn, *Bioconjugate Chem.*, 2005, **16**, 1572–1579.
- 206 G. Destito, R. Yeh, C. S. Rae, M. G. Finn and M. Manchester, *Chem. Biol.*, 2007, **14**, 1152–1162.
- 207 E. Kaltgrad, M. K. O'Reilly, L. Liao, S. Han, J. C. Paulson and M. G. Finn, *J. Am. Chem. Soc.*, 2008, **130**, 4578–4579.
- 208 O. B. Locos, C. C. Heindl, A. Corral, M. O. Senge and E. M. Scanlan, *Eur. J. Org. Chem.*, 2010, 1026–1028.
- 209 C. Pavani, A. F. Uchoa, C. S. Oliveira, Y. Iamamoto and M. S. Baptista, *Photochem. Photobiol. Sci.*, 2009, **8**, 233–240.

- 210 B. G. Maiya, *Resonance*, 2000, **5**, 15–29.
- 211 P. Singh, D. Prasuhn, R. M. Yeh, G. Destito, C. S. Rae, K. Osborn, M. G. Finn and M. Manchester, *J. Controlled Release*, 2007, **120**, 41–50.
- 212 D. E. Prasuhn, P. Singh, E. Strable, S. Brown, M. Manchester and M. G. Finn, *J. Am. Chem. Soc.*, 2008, **130**, 1328–1334.
- 213 T. J. M. Molenaar, I. Michon, S. A. M. de Haas, T. J. C. van Berkel, J. Kuiper and E. A. L. Biessen, *Virology*, 2002, **293**, 182–191.
- 214 T. Kimmerlin and D. Seebach, *J. Pept. Res.*, 2005, **65**, 229–260.
- 215 C. A. G. N. Montalbetti and V. Falque, *Tetrahedron*, 2005, **61**, 10827–10852.
- 216 E. Biron and N. Voyer, *Chem. Commun.*, 2005, **0**, 4652–4654.
- 217 E. Biron and N. Voyer, *Org. Biomol. Chem.*, 2008, **6**, 2507.
- 218 F. Le Guern, T.-S. Ouk, C. Ouk, R. Vanderesse, Y. Champavier, E. Pinault and V. Sol, *ACS Med. Chem. Lett.*, 2018, **9**, 11–16.
- 219 S. Asayama, T. Mori, S. Nagaoka and H. Kawakami, *J. Biomater. Sci. Polym. Ed.*, 2003, **14**, 1169–1179.
- 220 L. Ding, G. Etemad-Moghadam, S. Cros, C. Auclair and B. Meunier, *J. Med. Chem.*, 1991, **34**, 900–906.
- 221 D. Kumar, K. P. Chandra Shekar, B. Mishra, R. Kurihara, M. Ogura and T. Ito, *Bioorg. Med. Chem. Lett.*, 2013, **23**, 3221–3224.
- 222 United States, US20030105130A1, 2003.
- 223 V. Hong, S. I. Presolski, C. Ma and M. G. Finn, *Angew. Chem. Int. Ed.*, 2009, **48**, 9879–9883.
- 224 Q. Wang, T. R. Chan, R. Hilgraf, V. V. Fokin, K. B. Sharpless and M. G. Finn, *J. Am. Chem. Soc.*, 2003, **125**, 3192–3193.
- 225 K. L. Lee, B. L. Carpenter, A. M. Wen, R. A. Ghiladi and N. F. Steinmetz, *ACS Biomater. Sci. Eng.*, 2016, **2**, 838–844.
- 226 A. M. Wen, K. L. Lee, P. Cao, K. Pangilinan, B. L. Carpenter, P. Lam, F. A. Veliz, R. A. Ghiladi, R. C. Advincula and N. F. Steinmetz, *Bioconjugate Chem.*, 2016, **27**, 1227–1235.
- 227 X. Zhang, K. S. Lovejoy, A. Jasanoff and S. J. Lippard, *Proc. Natl. Acad. Sci.*, 2007, **104**, 10780–10785.
- 228 United States, US20030203888A1, 2003.
- 229 F. Giuntini, F. Dumoulin, R. Daly, V. Ahsen, E. M. Scanlan, A. S. P. Lavado, J. W. Aylott, G. A. Rosser, A. Beeby and R. W. Boyle, *Nanoscale*, 2012, **4**, 2034–2045.
- 230 R. J. Young and P. A. Lovell, in *Introduction to Polymers, Third Edition*, Routledge, Boca Raton, 3rd edition., 2011, pp. 61–122.
- 231 S. Zhang, Z. Shi, H. Xu, X. Ma, J. Yin and M. Tian, *Soft Matter*, 2016, **12**, 2575–2582.
- 232 B. A. Moffat, G. R. Reddy, P. McConville, D. E. Hall, T. L. Chenevert, R. R. Kopelman, M. Philbert, R. Weissleder, A. Rehemtulla and B. D. Ross, *Mol. Imaging*, 2003, **2**, 324–332.
- 233 A. S. Desai, V. M. Chauhan, A. P. R. Johnston, T. Esler and J. W. Aylott, *Front. Physiol.*, 2014, **4**, 401.
- 234 H. Xie, L. Zhang, L. Wu and J. Wang, *Part. Part. Syst. Charact.*, 2017, **34**, 1700222.
- 235 A. Gupta, S. Wang, A. Marko, P. Joshi, M. Ethirajan, Y. Chen, R. Yao, M. Sajjad, R. Kopelman and R. K. Pandey, *Theranostics*, 2014, **4**, 614–628.
- 236 Y. Wenger, R. J. Schneider, G. R. Reddy, R. Kopelman, O. Jolliet and M. A. Philbert, *Toxicol. Appl. Pharmacol.*, 2011, **251**, 181–190.
- 237 R. Ruiz-González, R. Bresolí-Obach, Ò. Gulías, M. Agut, H. Savoie, R. W. Boyle, S. Nonell and F. Giuntini, *Angew. Chem. Int. Ed.*, 2017, **56**, 2885–2888.
- 238 L. B. Josefsen, J. W. Aylott, A. Beeby, P. Warburton, J. P. Boyle, C. Peers and R. W. Boyle, *Photochem. Photobiol. Sci.*, 2010, **9**, 801–811.
- 239 B. Söveges, T. Imre, Á. L. Póti, P. Sok, Z. Kele, A. Alexa, P. Kele and K. Németh, *Org. Biomol. Chem.*, 2018, **16**, 5756–5763.
- 240 R. Kopelman, Y.-E. Lee Koo, M. Philbert, B. A. Moffat, G. Ramachandra Reddy, P. McConville, D. E. Hall, T. L. Chenevert, M. S. Bhojani, S. M. Buck, A. Rehemtulla and B. D. Ross, *J. Magn. Magn. Mater.*, 2005, **293**, 404–410.
- 241 Y. Long, Z. Li, Q. Bi, C. Deng, Z. Chen, S. Bhattachayya and C. Li, *Int. J. Pharm.*, 2016, **502**, 232–241.
- 242 X. Dong, C. Wei, L. Lu, T. Liu and F. Lv, *Mater. Sci. Eng. C*, 2016, **61**, 214–219.

- 243 S. Belali, H. Savoie, J. M. O'Brien, A. A. Cafolla, B. O'Connell, A. R. Karimi, R. W. Boyle and M. O. Senge, *Biomacromolecules*, 2018, **19**, 1592–1601.
- 244 H. Sun, T. L. Andresen, R. V. Benjaminsen and K. Almdal, *J. Biomed. Nanotechnol.*, 2009, **5**, 676–682.
- 245 K.-W. Ding, T.-Q. Li, Z.-X. Ge, J.-H. Bu and Y. Liu, *RSC Adv.*, 2018, **8**, 35759–35767.
- 246 S. Belali, A. R. Karimi and M. Hadizadeh, *Polymer*, 2017, **109**, 93–105.
- 247 S. Y. Yap, T. W. Price, H. Savoie, R. W. Boyle and G. J. Stasiuk, *Chem. Commun.*, 2018, **54**, 7952–7954.
- 248 C. Spagnul, J. Greenman, M. Wainwright, Z. Kamil and R. W. Boyle, *J. Mater. Chem. B*, 2016, **4**, 1499–1509.
- 249 F. Bryden, A. Maruani, J. M. M. Rodrigues, M. H. Y. Cheng, H. Savoie, A. Beeby, V. Chudasama and R. W. Boyle, *Bioconjugate Chem.*, 2018, **29**, 176–181.
- 250 W. Wu, W. Driessen and X. Jiang, *J. Am. Chem. Soc.*, 2014, **136**, 3145–3155.
- 251 F. Bryden, A. Maruani, H. Savoie, V. Chudasama, M. E. B. Smith, S. Caddick and R. W. Boyle, *Bioconjugate Chem.*, 2014, **25**, 611–617.
- 252 Information on Gadolinium-Based Contrast Agents, <https://www.fda.gov/Drugs/DrugSafety/PostmarketDrugSafetyInformationforPatientsandProviders/ucm142882.htm>, (accessed 19 November 2018).
- 253 H. Gao, X. Liu, W. Tang, D. Niu, B. Zhou, H. Zhang, W. Liu, B. Gu, X. Zhou, Y. Zheng, Y. Sun, X. Jia and L. Zhou, *Nanoscale*, 2016, **8**, 19573–19580.
- 254 D. J. Hnatowich, W. W. Layne and R. L. Childs, *Int. J. Appl. Radiat. Isot.*, 1982, **33**, 327–332.
- 255 D. J. Hnatowich, R. L. Childs, D. Lanteigne and A. Najafi, *J. Immunol. Methods*, 1983, **65**, 147–157.
- 256 W. C. Eckelman, S. M. Karesh and R. C. Reba, *J. Pharm. Sci.*, 1975, **64**, 704–706.
- 257 C. Daubresse, C. Grandfils, R. Jerome and P. Teyssie, *J. Colloid Interface Sci.*, 1994, **168**, 222–229.
- 258 H. Xu, J. W. Aylott and R. Kopelman, *The Analyst*, 2002, **127**, 1471–1477.
- 259 U. Nobbmann and A. Morfesis, *Mater. Today*, 2009, **12**, 52–54.
- 260 *Zetasizer Nano Series User manual*, Malvern Instrument, Series 1.1., 2013.
- 261 A. Gupta, S. Wang, P. Pera, K. V. R. Rao, N. Patel, T. Y. Ohulchanskyy, J. Missert, J. Morgan, Y.-E. Koo-Lee, R. Kopelman and R. K. Pandey, *Nanomedicine Nanotechnol. Biol. Med.*, 2012, **8**, 941–950.
- 262 C. J. Anderson, P. A. Rocque, C. J. Weinheimer and M. J. Welch, *Nucl. Med. Biol.*, 1993, **20**, 461–467.
- 263 J. Lux, A. G. White, M. Chan, C. J. Anderson and A. Almutairi, *Theranostics*, 2015, **5**, 277–288.
- 264 Y. Ma, Y. Ge and L. Li, *Mater. Sci. Eng. C*, 2017, **71**, 1281–1292.
- 265 A. E. Ekkelenkamp, M. R. Elzes, J. F. J. Engbersen and J. M. J. Paulusse, *J. Mater. Chem. B*, 2018, **6**, 210–235.
- 266 D. M. Corsi, C. Platas-Iglesias, H. van Bekkum and J. A. Peters, *Magn. Reson. Chem.*, 2001, **39**, 723–726.
- 267 A. Hajri, S. Wack, C. Meyer, M. K. Smith, C. Leberquier, M. Kedingier and M. Aprahamian, *Photochem. Photobiol.*, 2007, **75**, 140–148.
- 268 É. Tóth, L. Helm and A. Merbach, in *The Chemistry of Contrast Agents in Medical Magnetic Resonance Imaging*, John Wiley & Sons, Ltd, 2013, pp. 25–81.
- 269 M. Callewaert, V. G. Roullin, C. Cadiou, E. Millart, L. V. Gulik, M. C. Andry, C. Portefaix, C. Hoeffel, S. Laurent, L. V. Elst, R. Muller, M. Molinari and F. Chuburu, *J. Mater. Chem. B*, 2014, **2**, 6397–6405.
- 270 G. Paul, Y. Prado, N. Dia, E. Rivière, S. Laurent, M. Roch, L. V. Elst, R. N. Muller, L. Sancey, P. Perriat, O. Tillement, T. Mallah and L. Catala, *Chem. Commun.*, 2014, **50**, 6740–6743.
- 271 Y. Gossuin, Z. Serhan, L. Sandiford, D. Henrard, T. Marquardsen, R. T. M. de Rosales, D. Sakellariou and F. Ferrage, *Appl. Magn. Reson.*, 2016, **47**, 237–246.
- 272 G. J. Stasiuk, S. Tamang, D. Imbert, C. Gateau, P. Reiss, P. Fries and M. Mazzanti, *Dalton Trans.*, 2013, **42**, 8197–8200.

- 273 S. Sung, H. Holmes, L. Wainwright, A. Toscani, G. J. Stasiuk, A. J. P. White, J. D. Bell and J. D. E. T. Wilton-Ely, *Inorg. Chem.*, 2014, **53**, 1989–2005.
- 274 M. Rohrer, H. Bauer, J. Mintorovitch, M. Requardt and H.-J. Weinmann, *Invest. Radiol.*, 2005, **40**, 715–724.
- 275 J. Pintaske, P. Martirosian, H. Graf, G. Erb, K.-P. Lodemann, C. D. Claussen and F. Schick, *Invest. Radiol.*, 2006, **41**, 213–221.
- 276 A. Beeby, I. M. Clarkson, R. S. Dickins, S. Faulkner, D. Parker, L. Royle, A. S. de Sousa, J. A. G. Williams and M. Woods, *J. Chem. Soc. Perkin Trans. 2*, 1999, **0**, 493–504.
- 277 R. S. Dickins, S. Aime, A. S. Batsanov, A. Beeby, M. Botta, J. I. Bruce, J. A. K. Howard, C. S. Love, D. Parker, R. D. Peacock and H. Puschmann, *J. Am. Chem. Soc.*, 2002, **124**, 12697–12705.
- 278 J. I. Bruce, R. S. Dickins, L. J. Govenlock, T. Gunnlaugsson, S. Lopinski, M. P. Lowe, D. Parker, R. D. Peacock, J. J. B. Perry, S. Aime and M. Botta, *J. Am. Chem. Soc.*, 2000, **122**, 9674–9684.
- 279 S. J. Butler and D. Parker, *Chem Soc Rev*, 2013, **42**, 1652–1666.
- 280 D. H. White, L. A. Delearie, D. A. Moore, R. A. Wallace, T. J. Dunn, W. P. Cacheris, H. Imura and G. R. Choppin, *Invest. Radiol.*, 1991, **26**, S226–S228.
- 281 S. M. Moghimi, A. C. Hunter and J. C. Murray, *Pharmacol Rev*, 2001, **53**, 283–318.
- 282 T. J. Wadas, E. H. Wong, G. R. Weisman and C. J. Anderson, *Chem. Rev.*, 2010, **110**, 2858–2902.
- 283 M. Fani, J. P. André and H. R. Maecke, *Contrast Media Mol. Imaging*, 2008, **3**, 53–63.
- 284 M. I. Tsiou, C. E. Knapp, C. A. Foley, C. R. Munteanu, A. Cakebread, C. Imberti, T. R. Eykyn, J. D. Young, B. M. Paterson, P. J. Blower and M. T. Ma, *RSC Adv.*, 2017, **7**, 49586–49599.
- 285 R. Alberto, R. Schibli, R. Waibel, U. Abram and A. P. Schubiger, *Coord. Chem. Rev.*, 1999, **190–192**, 901–919.
- 286 T. L. Mindt, H. Struthers, L. Brans, T. Anguelov, C. Schweinsberg, V. Maes, D. Tourwé and R. Schibli, *J. Am. Chem. Soc.*, 2006, **128**, 15096–15097.
- 287 A. Barge, S. Tagliapietra, A. Binello and G. Cravotto, *Curr. Org. Chem.*, 2011, **15**, 189–203.
- 288 P. Appukkuttan, W. Dehaen, V. V. Fokin and E. Van der Eycken, *Org. Lett.*, 2004, **6**, 4223–4225.
- 289 T. Mindt, H. Struthers, E. Garcia-Garayoa, D. Desbouis and R. Schibli, *Chim. Int. J. Chem.*, 2007, **61**, 725–731.
- 290 R. Schibli, ETH Zürich, 2003.
- 291 J. R. Dilworth and S. J. Parrott, *Chem. Soc. Rev.*, 1998, **27**, 43–55.
- 292 R. Alberto, A. Egli, U. Abram, K. Hegetschweiler, V. Gramlich and P. A. Schubiger, *J. Chem. Soc. Dalton Trans.*, 1994, **0**, 2815–2820.
- 293 Martin. Karplus, *J. Am. Chem. Soc.*, 1963, **85**, 2870–2871.
- 294 N. Schülke, O. A. Varlamova, G. P. Donovan, D. Ma, J. P. Gardner, D. M. Morrissey, R. R. Arrigale, C. Zhan, A. J. Chodera, K. G. Surowitz, P. J. Maddon, W. D. W. Heston and W. C. Olson, *Proc. Natl. Acad. Sci.*, 2003, **100**, 12590–12595.
- 295 C. Bařinka, M. Rovenska, P. Mleochova, K. Hlouchova, A. Plechanovova, P. Majer, T. Tsukamoto, B. S. Slusher, J. Konvalinka and J. Lubkowski, *J. Med. Chem.*, 2007, **50**, 3267–3273.
- 296 World Intellectual Property Organization, WO2008058192A2, 2008.
- 297 S. R. Banerjee, M. Pullambhatla, Y. Byun, S. Nimmagadda, C. A. Foss, G. Green, J. J. Fox, S. E. Lupold, R. C. Mease and M. G. Pomper, *Angew. Chem. Int. Ed.*, 2011, **50**, 9167–9170.
- 298 M. Felber, M. Bauwens, J. M. Mateos, S. Imstepf, F. M. Mottaghy and R. Alberto, *Chem. – Eur. J.*, **21**, 6090–6099.
- 299 R. Alberto, K. Ortner, N. Wheatley, R. Schibli and A. P. Schubiger, *J. Am. Chem. Soc.*, 2001, **123**, 3135–3136.
- 300 A. Badar, J. Williams, R. T. de Rosales, R. Tavare, F. Kampmeier, P. J. Blower and G. E. Mullen, *EJNMMI Res.*, 2014, **4**, 14.
- 301 R. Schibli, R. La Bella, R. Alberto, E. Garcia-Garayoa, K. Ortner, U. Abram and P. A. Schubiger, *Bioconjug. Chem.*, 2000, **11**, 345–351.
- 302 H. Struthers, B. Spingler, T. L. Mindt and R. Schibli, *Chem. – Eur. J.*, 2008, **14**, 6173–6183.

- 303 F. Kampmeier, J. D. Williams, J. Maher, G. E. Mullen and P. J. Blower, *EJNMMI Res.*, 2014, **4**, 13.
- 304 D. B. G. Williams and M. Lawton, *J. Org. Chem.*, 2010, **75**, 8351–8354.
- 305 E. K. Lumley, C. E. Dyer, N. Pamme and R. W. Boyle, *Org. Lett.*, 2012, **14**, 5724–5727.
- 306 G. M. Entract, F. Bryden, J. Domarkas, H. Savoie, L. Allott, S. J. Archibald, C. Cawthorne and R. W. Boyle, *Mol. Pharm.*, 2015, **12**, 4414–4423.